Università degli Studi di Pisa

Graduate course in Physics

PhD thesis

Studies on $H \to b\bar{b}$ decay and VH production with the ATLAS detector

Advisors:
Prof.ssa Chiara Roda
Dott. Paolo Francavilla

Candidate:
Milène Calvetti

XXXII Ciclo

Contents

Introduction **1**

1 Theoretical aspects **6**

1.1 The Standard Model 6

1.2 The Higgs mechanism 10

1.3 State of the art measurements for $VH(H \to b\bar{b})$ 13

1.4 Simplified Template Cross Sections 14

1.5 Effective Field theories 18

1.5.1 BSM search using STXS 23

1.5.2 EFT at high energies 24

2 The experimental apparatus **26**

2.1 The LHC 26

2.1.1 Luminosity and pile-up 27

2.2 Overview of the ATLAS detector 30

2.2.1 Coordinate system 31

2.2.2 Magnet system 32

2.2.3 The Inner Detector . . . 33
2.2.4 The calorimeter system . . . 36
2.2.5 Muon system . . . 41
2.2.6 Data Acquisition and Trigger . . . 44
2.2.7 Fast Tracker . . . 45

3 Analysis overview 47

3.1 $VH(H \to b\bar{b})$ search . . . 47
3.2 Simplified Template Cross Sections and BSM physics . . . 53

4 Dataset and simulated event samples 55

4.1 Dataset and triggers . . . 55
4.1.1 0-lepton channel triggers . . . 56
4.1.2 1-lepton channel triggers . . . 57
4.1.3 2-lepton channel triggers . . . 58
4.2 Event simulation . . . 59
4.3 Signal processes simulation . . . 63
4.4 Background processes simulation . . . 65
4.4.1 Vector boson+jets . . . 65
4.4.2 Top-Pair . . . 66
4.4.3 Single-Top . . . 67
4.4.4 Diboson . . . 68
4.4.5 Multi-jet background . . . 69

5 Object reconstruction **71**

5.1 Primary vertex and tracks 71

5.2 Leptons 72

5.2.1 Electron reconstruction 73

5.2.2 Electron identification and selection 74

5.2.3 Electron systematic uncertainties 76

5.2.4 Muon reconstruction 76

5.2.5 Muon identification and selection 77

5.2.6 Muon systematic uncertainties 78

5.3 Jets reconstruction 79

5.3.1 Introduction 79

5.3.2 Calorimetric jets 80

5.3.3 Reconstruction algorithms: anti-k_t and k_t 81

5.3.4 Small-R jets calibration and selection 82

5.3.5 Large-R jets grooming and calibration 85

5.3.6 b-jet identification and $H \to b\bar{b}$ tagging 89

5.3.7 Track-jets 93

5.3.8 Large-R jets to track jets association 94

5.4 Missing transverse momentum 94

6 Event selection **98**

6.1 Candidate vector boson selection 98

6.2 Candidate Higgs boson selection 99

6.2.1 *Resolved* analysis 99
6.2.2 *Merged* analysis 100
6.3 Signal and control regions definition 101
6.3.1 0-lepton channel 102
6.3.2 1-lepton channel 105
6.3.3 2-lepton channel 109
6.3.4 Summary of the signal and control regions definition 110
6.4 Jet categorisation in the *merged* analysis 112
6.5 MVA in *resolved* analysis 117
6.5.1 Input variables 118

7 Statistical method **120**

7.1 General statistical treatment 120
7.1.1 Likelihood 121
7.1.2 Signal strength measurement 123
7.1.3 Test statistic 123
7.1.4 Tool for the validation of the fit results 125
7.2 Statistical treatment within STXS framework 129
7.2.1 From the signal strength to the STXS measurements 129
7.2.2 Simplified Template Cross Section bins 131
7.2.3 Comparison to reconstructed categories 132
7.2.4 BDT distributions across the STXS regions 134

8 Systematic uncertainties **136**

8.1 Theoretical cross-sections and related uncertainties 136
8.1.1 Binning scheme for the uncertainties computation 138
8.1.2 Parton Distribution Function and α_S uncertainties 141
8.1.3 Uncertainties due to neglected higher order in the α_s perturbative expansion 142
8.1.4 Summary 148
8.2 $VH(H \to b\bar{b})$ analyses uncertainties 148
8.2.1 Experimental uncertainties 149
8.2.2 Modelling uncertainties for signal and background processes 151
8.2.3 Modelling uncertainties for the *merged* analysis 153
8.3 Signal uncertainties for the STXS measurement 154
8.3.1 Parton-Shower and Underlying Event modelling uncertainties 155
8.3.2 Residual theoretical uncertainties 156

9 Results of the $VH(H \to b\bar{b})$ *resolved* analysis 159
9.1 $H \to b\bar{b}$ and VH observation 159
9.1.1 Observation of $H \to b\bar{b}$ decay 163
9.1.2 Observation of the VH production 164
9.1.3 $VH(H \to b\bar{b})$ results obtained by the CMS collaboration . . 165
9.2 STXS results 166
9.2.1 *5-POI* signal measurements 167
9.2.2 *3-POI* signal measurements 173
9.3 BSM interpretations 176
9.3.1 EFT parameters measurement 177

9.3.2 Future prospects 180

10 Results of the $VH(H \to b\bar{b})$ *merged* analysis 181

10.1 Fit inputs 181

10.2 Cross-section measurement 188

10.2.1 Fit procedure validation 188

10.2.2 Expected performance 190

10.3 STXS 198

10.3.1 Expected performance 198

10.3.2 Future development for the STXS in $VH(H \to b\bar{b})$ 202

11 Conclusions 205

Appendices 208

A FTK and the associative memory system 209

A.1 Hardware for the FTK system 209

A.2 Associative Memory System 210

A.2.1 Test of the Associative Memory System components 213

B Matrix element and MC event generators 215

C Information on selected *resolved* uncertainties 218

C.1 Uncertainties with largest impact on the signal strength for the *resolved* analysis 218

C.2 Naming conventions for the uncertainties with largest impact on the STXS measurement 222

D Validation of the STXS inputs **224**

E Expected significance comparison **229**

F Pull plots for the *merged* analysis **232**

Bibliography **236**

Introduction

The Standard Model (SM) [1] of particle physics provides a description of all the known particles and of their interactions through the strong, weak and electromagnetic forces. The reliability of this theoretical framework has been tested in plenty of physics measurements and the last missing piece, the Higgs boson, was observed in 2012 [2, 3]. The discovery took place at the Large Hadron Collider (LHC) [4], a particle accelerator located at CERN providing proton-proton collisions at unprecedented centre-of-mass energies and at the highest instantaneous luminosity achieved so far in hadron colliders.

Despite the extremely precise predictions provided, the SM is thought to be incomplete. Indeed it only includes three of the four fundamental interactions and it is unable to explain a series of observations, such as the presence of dark matter in the universe [5]. In the last decades, several ideas of physics beyond the SM have been developed to explain these observations, and some of them have been investigated at the LHC. As the LHC reaches unprecedented centre-of-mass energies, it naturally offers a unique opportunity to search for new physics Beyond the Standard Model (BSM). The ATLAS experiment, whose data have been used in this work, is a multi-purpose experiment located on the LHC ring, where it records the particle collisions and allows a detailed study of the produced events. The ATLAS physics program can be summarized into two main goals: the test of the Standard Model and the search for BSM physics signatures. Both aspects are tackled in this thesis as the first part of the work is dedicated to the measurement of the Higgs boson decay to a couple of b-quarks as predicted by the SM, while another part addresses the search for deviations in the Higgs boson production and decay in a phase space highly sensitive to BSM effects.

The Higgs boson branching ratios in various final states are shown in Figure 1 to highlight the importance of the Higgs decay into two b-quarks. This decay is the largest branching ratio channel, with an expected value of about 58% for a SM Higgs boson with a mass of 125 GeV [6]. Additionally, measuring the Higgs boson decay to b-quarks allows a direct measurement of the Higgs coupling to fermions, a crucial probe of the properties of the Higgs sector.

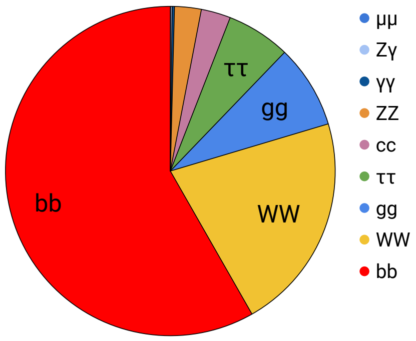

Figure 1: Standard Model Higgs boson decay branching ratio for a Higgs boson mass of 125 GeV. The values of the branching ratios are from Ref. [6].

Despite being the channel with the largest branching ratio, the $H \to b\bar{b}$ decay was not among the first measured decay modes. The decay into two b-quark is indeed not trivial to identify at a hadron collider. As shown in Figure 2, the main Higgs boson production channel is the on-shell gluon-gluon fusion production, $pp \to H$. However, the identification of the Higgs boson produced by the gluon-gluon process and followed by the $H \to b\bar{b}$ decay is extremely difficult, if not impossible, in the overwhelming background from the multi-jet QCD processes. Despite a cross-section more than an order of magnitude lower than the gluon-gluon fusion process, the associated production of the Higgs boson and a vector boson decaying to leptons is the most promising channel to measure the $H \to b\bar{b}$ decay. Indeed,

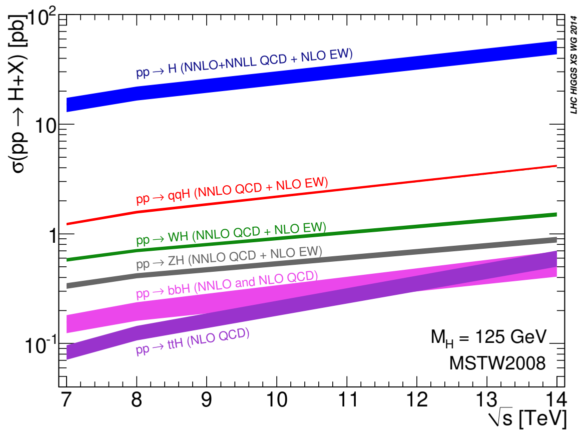

Figure 2: Standard Model Higgs boson production cross sections as a function of the centre-of-mass energy [7].

the selection of events where the V-boson decays leptonically to electrons, muons or neutrinos offers a clear trigger signature to effectively suppress the multi-jet background.

The analyses described in this thesis aim at searching for the decay of the Higgs boson into two b-quarks in the associated production with a V-boson (W or Z) decaying into leptons. For this purpose, two complementary analysis strategies have been developed and they are indicated in the following as *resolved* and *merged* analysis, respectively. In the *resolved* analysis the Higgs boson decay products are reconstructed as two separate objects (b-jets) while in the *merged* analysis, designed for the high energy phase space, the two b-jets produced by the highly boosted Higgs boson tend to coalesce and are reconstructed as a single large jet collecting both decay products. The *resolved* analysis search led in summer 2018 to the first observation of the Higgs boson decay into two b-quarks and to the first observation of the VH production [8]. On the other side, the *merged* analysis is close to final but not completely finalized yet, and the data region most sensitive to signal is thus not shown to avoid biases in the analysis design. For the same reason only the expected results will be shown ("blinded" analysis).
The associated production of a vector boson with a Higgs boson (VH) is also a privileged channel to search for new resonances and to enhance the sensitivity to BSM effects at high energy scales [9, 10]. These effects are encoded into deviations of the VH production cross-section at high masses of the VH system, m_{VH}, or equivalently, at high transverse momentum of the V-boson. For this reason, the data sample used for the $H \to b\bar{b}$ search has also been used to perform measurements of the VH cross-section in bins of the V-boson transverse momentum. This kind of measurements, exploiting the so-called Simplified Template Cross Section (STXS) framework, is designed to investigate possible BSM effects and is as well presented in this thesis.

Structure of the thesis and personal contribution

The results presented in this thesis are the outcome of a joint effort among the components of the ATLAS $VH(H \to b\bar{b})$ analyses team. In this section I present the structure of the thesis, highlighting my contribution to the analyses.
This thesis is divided into eleven chapters. Chapter 1 introduces the thesis subject from the theoretical and phenomenological point of view, giving a short overview of the SM and highlighting those aspects more relevant for the work I have carried out (Higgs mechanism, Higgs boson production and decay).
The LHC and the structure of the ATLAS experiment and its main subsystems are illustrated in Chapter 2. Special attention is dedicated to the FTK system, a track reconstruction processor designed to improve the ATLAS data acquisition system, where I contributed to the commissioning of one of the fundamental electronic board of the system. Details on the electronic boards and on the test performed

are given in Appendix A. I contributed to the commissioning by developing part of the testing procedure, fixing some of the existing software tests and automating the full procedure.
The aim of Chapter 3 is to give a synthetic description of the strategy used to accomplish the measurements described in this thesis.
The data sample used and the trigger strategy followed to select the events are described in Chapter 4. The signal and background processes contributing to the selected events are described as well, together with the Monte Carlo generators and the simulated events used to model such processes.
The isolation of a sample of events enriched in signal events requires the use of physics objects, such as the leptons trajectories and momenta, reconstructed from the detector signals. The methods applied to reconstruct such objects and the performance of the exploited algorithms are described in Chapter 5.
The physics objects are used to select the relevant events, as described in Chapter 6. I have personally contributed to test the event selection and to compute the signal systematics for the *resolved* analysis and I was one of the main contributors to the definition of the event selection for the *merged* analysis. In particular, I have studied in depth the event categorisation according to the jet multiplicity for the *merged* analysis and the definition of the event selection in the leptonic channel aiming at selecting WH events (1-lepton channel).
The selected events are used as input to a maximum likelihood fit to data, from which the value of the measured cross-section is extracted. The statistical procedure and the systematic uncertainties treatment are described in Chapter 7 and Chapter 8, respectively.
The measurement of the Simplified Template Cross Section required dedicated efforts to properly compute the expected signal events and the related uncertainties. My contributions to this topic, described in Chapter 8, was well recognisable in the ATLAS collaboration and in the LHC Higgs Cross Section Working Group. I was one of the authors of the note published by the ATLAS collaboration depicting the evaluation of these uncertainties [11].

The results obtained with the *resolved* analysis that led to the first observation of the VH production process and of the $H \to b\bar{b}$ decay are described in Chapter 9. In the same chapter, a description of the first measurements of the STXS and of the constraints on BSM effects through the EFT formalism is also given. I have started my thesis work giving contributions to the last step of the *resolved* analysis that led to the first observation. The gained experience has allowed me to be one of the main contributors to the STXS measurement, by doing sensitivity studies; participating to the production and testing of the simulated signal split into the exclusive phase-space regions; contributing to the adaptation of the statistical framework used for the $VH(H \to b\bar{b})$ search to the measurement of the STXS and

executing and validating the fitting procedure. I was also one of the three editors of the internal note on which the published result is based on.
From the performed studies it has been shown that the very high energy events are more sensitive to possible BSM deviations compared to the low energy events. This was the main reason to implement the *merged* analysis, for which the results of the $VH(H \to b\bar{b})$ measurement are discussed in Chapter 10. I have dedicated a large part of my work to the production and validation of inputs used in the *merged* analysis fit to data, in particular for the channel aiming at the selection WH events, and to the implementation, execution and validation of the fitting procedure for this analysis. I also contributed to the writing of a minor part of the internal note of the *merged* analysis, and providing materials to the note editors.
Finally, Chapter 11 summarises the results of the work presented in the thesis and includes some remarks on future perspectives.

Chapter 1

Theoretical aspects and current status of the $VH(H \to b\bar{b})$ measurements

After a general overview of the theoretical framework of particle physics, this chapter focuses on the Higgs boson decay into two b-quarks in the Standard Model and on the associated production of a Higgs boson and a massive vector boson (VH). An overview of the most recent results on the Higgs boson decay into two b-quarks, obtained using the ATLAS and CMS detectors, is also presented. The framework adopted to infer information on physics Beyond the Standard Model from the measurement of VH cross-sections in limited phase space regions is introduced in the last sections.

1.1 The Standard Model

The description of the elementary particles and of their interactions is currently based on a relativistic quantum field theory, the Standard Model (SM) of particles Physics [1, 12]. The Standard Model describes the strong, weak and electromagnetic interactions in terms of the exchange of vector boson, the force mediators, among elementary fermions (leptons and quarks). The known elementary particles are 12 spin-1 bosons, mediators of the strong, weak and electromagnetic forces, 12 spin-1/2 fermions plus their corresponding antiparticles and one spin-0 boson, the Higgs boson. Among the fermions there are the leptons: the neutrinos (ν_e, ν_μ, ν_τ) which interact only through the weak interaction, and the charged leptons

(e^-, μ^-, τ^-), which can interact weakly and electromagnetically. The remaining fermions are called quarks (u, d, s, c, t, b) and can interact strongly, weakly and electromagnetically. In addition to charge, spin and mass, quarks are identified by an additional characteristic number called colour. In nature, only uncoloured particles are observed and free quarks have never been detected. The non-observation of free quarks is explained by the *colour confinement*, where the coloured objects are always confined to uncoloured particles and cannot propagate as free particles. Eight bosons, the gluons, are the mediators of the strong interaction, three bosons, W^-,W^+ and Z mediate the weak force and one boson, the photon (γ), mediates the electromagnetic force.
The Higgs boson (H) provides the mechanism by which all other particles acquire mass and it is the only fundamental spin-0 particle discovered to date. The Higgs mechanism is further described in the following section. The properties of the Standard Model particles are summarised in Figure 1.1.

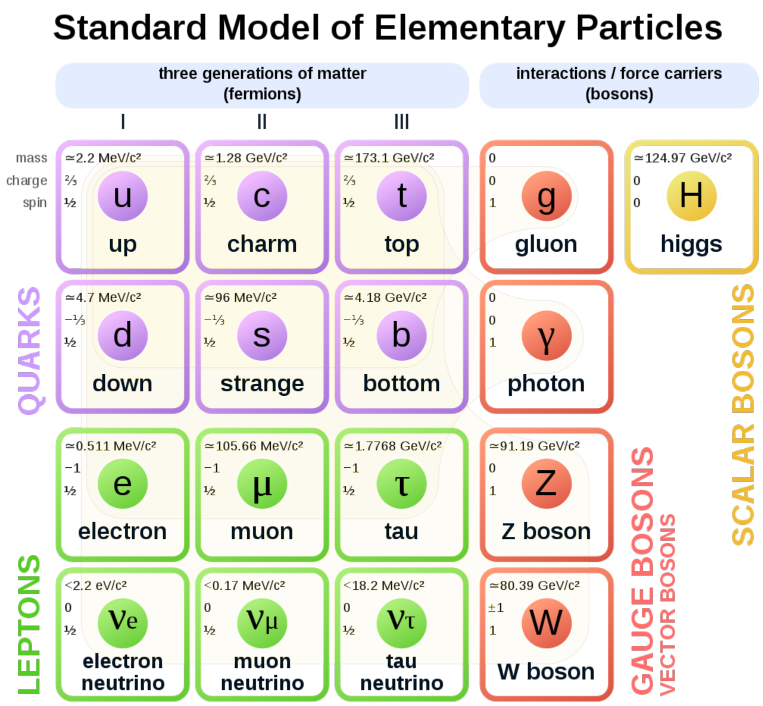

Figure 1.1: Summary of the Standard Model elementary particles and some of their properties. The 12 spin-1/2 fermions and 5 fundamental bosons are shown (the 8 gluons and 2 W bosons are shown in a single g and W box, respectively).

The Standard Model is a relativistic quantum field theory built from the principles of gauge invariance. The gauge symmetry group on which the Standard Model is based is obtained as the direct product of three groups $SU(3)\otimes SU(2)\otimes U(1)$. Each

symmetry of the group corresponds to a conserved quantity (Noether's theorem). Interactions of the SM are interpreted in terms of the fields, ψ, of half-integer spin fermions that interact with integer spin bosons. The symmetries and interactions of the SM are summarised in the following, while a detailed introduction to the Standard Model can be found for example in Ref. [1].
In relativistic quantum mechanics, electromagnetism can be related to a local $U(1)$ gauge invariance. The Dirac Lagrangian equation for a free particle is:

$$\mathcal{L}_D = \bar{\psi}(i\gamma^\mu \partial_\mu - m)\psi$$

where m is the mass of the particle, ψ is the spinor of a spin 1/2 fermion, γ^μ are the Dirac gamma matrices, $\bar{\psi} = \psi^\dagger \gamma^0$ is the Dirac adjoint of the spinor and $\partial_\mu = \partial/\partial x_\mu$. Assuming that there is a symmetry that requires invariance under $U(1)$ local phase transformation, the spinor field transform as:

$$\psi(x) \to e^{ie\theta(x)}\psi(x)$$

where $\theta(x)$ is a generic function and e is the elementary charge. The Dirac Lagrangian becomes:

$$\mathcal{L}'_D = \mathcal{L}_D - e\bar{\psi}\gamma^\mu(\partial_\mu \theta(x))\psi$$

The required invariance can be established only modifying the Dirac Lagrangian and including a new degree of freedom A_μ. The partial derivative ∂_μ is replaced with the covariant derivative, D_μ, which is defined as:

$$D_\mu \psi(x) = (\partial_\mu + ieA_\mu)\psi(x)$$

with A_μ transforming as:

$$A_\mu \to A'_\mu = A_\mu - \partial_\mu \theta(x)$$

A_μ is interpreted as the gauge field for the electromagnetic interaction and e is the interaction strength. Under the mentioned transformation $D_\mu\psi$ trasform as ψ: $D_\mu\psi \to e^{ie\theta(x)} D_\mu\psi$. The quantum electrodynamics QED Lagrangian can then be written as:

$$\mathcal{L}_{QED} = \bar{\psi}(i\gamma^\mu D_\mu - m)\psi - \frac{1}{4}F_{\mu\nu}F^{\mu\nu}$$

where $F_{\mu\nu} = \partial_\mu A_\nu - \partial_\nu A_\mu$ and $F_{\mu\nu}F^{\mu\nu}$ represents the kinetic energy term of the excitation of the gauge field. This Lagrangian describes the interaction between electrons (or any other charged spin 1/2 fermion) and photons. All QED can then be derived by requiring the invariance under local $U(1)$ transformation.
While QED corresponds to a $U(1)$ local gauge symmetry, the underlying symmetry associated to quantum chromodynamics (QCD) is the invariance under the non-Abelian $SU(3)$ local phase transformations. While the QED interaction is mediated

by a massless photon corresponding to the single generator of the $U(1)$ local gauge symmetry, QCD is mediated by eight massless gluons corresponding to the eight generators of the $SU(3)$ local gauge symmetry. Instead of the single charge of the QED, QCD has three conserved *colour* charges. Only the quarks, which carry colour charge, interact with the gluons.

So far it has been shown that QED is associated with the $U(1)$ local gauge symmetry. The charged-current weak interaction, related to $W^{\pm}$, is instead associated with invariance under $SU(2)_L$ local phase transformations. The $SU(2)_L$ local phase transformation that introduces the interaction is:

$$\phi(x) \to \phi'(x) = e^{ig_W \alpha(x)\cdot \frac{1}{2}\sigma}\phi(x)$$

where σ are the Pauli spin matrices and $\alpha(x)$ are three functions specifying the local phase space at each point in space-time. To conserve the symmetry of the Lagrangian it is necessary to introduce four gauge fields analogous to A^{μ}. The three gauge fields of the $SU(2)_L$ group are W^a_{μ} with $a = 1, 2, 3$ and the three corresponding gauge bosons are W^1, W^2 and W^3. The charged currents are expressed as a linear combination of W^1_{μ} and W^2_{μ},

$$W^{\pm}_{\mu} = \frac{1}{\sqrt{2}}(W^1_{\mu} \pm W^2_{\mu})$$

The wave function $\phi(x)$ is written in terms of two components and is named a *weak isospin doublet*. As the weak charged-current interaction associated with the $W^{\pm}$ couples different fermions, the doublets must contain flavours differing by one unit of electric charge, e.g.:

$$q_L = \begin{pmatrix} u \\ d \end{pmatrix}_L, \quad l_L = \begin{pmatrix} \nu_e \\ e^- \end{pmatrix}_L.$$

Left-handed fermions doublets have a weak isospin value $I_W = 1/2$. As the experimentally measured weak charged-current interactions couple only to left-handed particles (and right-handed antiparticles), the gauge transformation can affect only left-handed particles (and right-handed antiparticles). Right-handed particles (and left-handed antiparticles) chiral states are placed in weak isospin singlets with $I_W = 0$ and are unaffected by $SU(2)$ local gauge transformation, which is therefore referred as $SU(2)_L$. The weak isospin singlets are e.g.

$$u_R, \ d_R, \ e_R.$$

Experimental observations indicate that the Z boson couples to both left and right-handed electrons, therefore it cannot be associated with W_3. In the electroweak model of Glashow, Salam and Weinberg, the $U(1)$ gauge symmetry of electromagnetism is replaced with the $U(1)_Y$ local gauge symmetry of weak hypercharge

(Y). In the end, the combination of $SU(2)_L \otimes U(1)_Y$ generates four gauge fields responsible for the electroweak interaction. The physics fields corresponding to the γ, Z, $W^{\pm}$ bosons are linear combinations of these gauge fields. $W^{\pm}_{\mu}$ and Z_{μ} are the fields associated with the weak physics bosons and A_{μ} is the field representing the photon. The weak neutral current and photon are expressed as the product of the mixing of W^3_{μ} and B_{μ}, the boson of the $U(1)_Y$ symmetry, with coupling g'. In the $U(1)_Y$ symmetry, the weak hypercharge is defined as

$$Y = 2Q - 2I$$

where Q is the electromagnetic charge of the fermion and I is the third component of the weak isospin. The relationships between gauge fields W^3_{μ} and B_{μ} and the physics fields Z_{μ} and A_{μ} are reported here:

$$\begin{pmatrix} Z_{\mu} \\ A_{\mu} \end{pmatrix} = \begin{pmatrix} cos\theta_W & -sin\theta_W \\ sin\theta_W & cos\theta_W \end{pmatrix} \begin{pmatrix} W^3_{\mu} \\ B_{\mu} \end{pmatrix} \tag{1.1}$$

where θ_W is the weak mixing angle or Weinberg angle. The relationship between the weak mixing angle and the weak and electromagnetic couplings are:

$$\begin{aligned} e &= g_W sin\theta_W \\ e &= g' cos\theta_W \end{aligned} \tag{1.2}$$

The SM described so far does not include the mass of the bosons and fermions. The procedure by which the masses are included in the SM is known as the Higgs mechanism, described in the following paragraph.

1.2 The Higgs mechanism

The Higgs mechanism is introduced to describe the mass of the particles as a result of the interaction between massless particles and a scalar field, within a gauge-invariant theory. As described in the previous section, the Standard Model Lagrangian can be derived as a Lagrangian that satisfies the Lorentz invariance, the $SU(3)_C \times SU(2)_L \times U(1)_Y$ local gauge invariance, and that is renormalisable. It is not possible to simply add a mass term for the fermion in the Lagrangian. The Dirac mass term could in fact be written as $m\psi\bar{\psi} = m(\bar{\psi}_L + \bar{\psi}_R)(\psi_L + \psi_R) = m(\bar{\psi}_L\psi_R + \bar{\psi}_R\psi_L)$. Such a Dirac mass term contains couplings of left and right-handed fields, which have different transformation properties, spoiling the gauge symmetry. The mass generation of the electroweak gauge bosons and of the fermion can instead be included through the Brout-Englert-Higgs mechanism

(Higgs mechanism) of spontaneous electroweak symmetry breaking, introduced in 1964 [13, 14, 15]. The Higgs mechanism is embedded in the $SU(2)_L \times U(1)_Y$ local gauge symmetry of the electroweak sector of the SM, and it introduces an additional scalar Higgs term in the lagrangian, which can be written as:

$$\mathcal{L}_{Higgs} = (D^\mu \boldsymbol{\phi})^\dagger (D_\mu \boldsymbol{\phi}) - V(\boldsymbol{\phi})$$

The minimal Higgs model consists of two complex scalar fields:

$$\boldsymbol{\phi} = \begin{pmatrix} \phi^+ \\ \phi^0 \end{pmatrix} = \frac{1}{\sqrt{2}} \begin{pmatrix} \phi_1 + i\phi_2 \\ \phi_3 + i\phi_4 \end{pmatrix}$$

The covariant derivative of ϕ is:

$$D_\mu \boldsymbol{\phi} = \left(\partial_\mu + i g_W \frac{\boldsymbol{\sigma}}{2} \cdot \boldsymbol{W_\mu} + i \frac{1}{2} g' B_\mu \right) \phi$$

where W_μ and B_μ are the $SU(2)_L$ and $U(1)_Y$ gauge bosons introduced in the previous section. The square of the covariant derivative involves three and four point interactions between the gauge and the scalar fields. The Higgs potential $V(\phi)$, which respects $SU(2)_L \times U(1)_Y$ invariance, is of the form:

$$V(\boldsymbol{\phi}) = \mu^2 \boldsymbol{\phi}^\dagger \boldsymbol{\phi} + \lambda (\boldsymbol{\phi}^\dagger \boldsymbol{\phi})^2$$

where μ and λ are scalar constants. The λ term describes the quadratic self-interaction among the scalar fields. When $\mu^2 > 0$ the minimum of the potential occurs when all the fields are zero. If $\mu^2 < 0$ the potential has an infinite set of minima defined by:

$$\boldsymbol{\phi}^\dagger \boldsymbol{\phi} = \frac{1}{2}(\phi_1^2 + \phi_2^2 + \phi_3^2 + \phi_4^2) = \frac{v^2}{2} = -\frac{\mu^2}{2\lambda}$$

where v is the vacuum expectation value. A schematic drawing of the potential is shown in Figure 1.2 for the values $\mu^2 > 0$ and $\mu^2 < 0$
Spontaneous symmetry breaking occurs because the minimum of the potential realised in nature is one of such solutions, breaking the initial symmetry of the system. As after symmetry breaking the neutral photon should remain massless, the minimum of the potential corresponds to a non-zero vacuum expectation value only for the neutral scalar field ϕ^0:

$$< 0|\boldsymbol{\phi}|0 >= \frac{1}{\sqrt{2}} \begin{pmatrix} 0 \\ v \end{pmatrix}$$

and the Higgs field itself is given by:

$$\boldsymbol{\phi} = \frac{1}{\sqrt{2}} \begin{pmatrix} 0 \\ v + h \end{pmatrix}$$

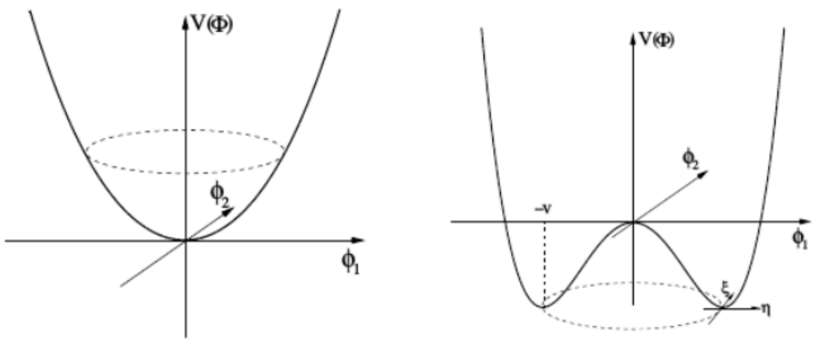

Figure 1.2: The $V(\phi)$ potential for a complex scalar field for $\mu^2 > 0$ and $\mu^2 < 0$.

where v is thus a real constant and h a real scalar field, which in the following is called the Higgs boson field.
The mass term for the gauge bosons can be identified by writing the Lagrangian $\mathcal{L}_{Higgs}$ such that it respects the $SU(2)_L \times U(1)_Y$ local gauge symmetry of the electroweak model, using the appropriate covariant derivative. The values obtained are

$$\begin{aligned} m_W &= \frac{1}{2} g_W v \\ m_A &= 0 \\ m_Z &= \frac{1}{2} v \sqrt{g_W^2 + g'^2} \\ m_H &= \sqrt{2\lambda v^2} \end{aligned}$$

The spontaneous symmetry breaking in the $SU(2)_L \times U(1)_Y$ sector can therefore generate the masses of the W and Z bosons, while ensuring that the photon remains massless. The same mechanism can also be used to describe the masses of the fermions. To generate the masses of the fermions, an additional *Yukawa term* is introduced in the Lagrangian. As mentioned before in the SM left-handed chiral fermions are placed in $SU(2)$ doublets, here named L, and right-handed fermions are placed in singlets, R. As the two complex scalar field of the Higgs mechanism are placed in an $SU(2)$ doublet $\boldsymbol{\phi}(x)$, an infinitesimal local gauge transformation has the same effect on L. The combination $\bar{L}\phi$ is therefore invariant under $SU(2)_L$, where $\bar{L} \equiv L^\dagger \gamma^0$. The combination with a right-handed singlet, $\bar{L}\phi R$, is then invariant under $SU(2)_L$ and $U(1)_Y$ gauge transformations. It is therefore possible to build a Lagrangian term in the form of $-g_f(\bar{L}\phi R + \bar{R}\phi^\dagger L)$ that satisfies the $SU(2)_L \times U(1)_Y$ gauge symmetry. Using the Higgs doublet defined in Equation 1.2, for the $SU(2)_L$ doublet containing the electron this corresponds to:

$$\mathcal{L}_{Yukawa,e} = -\frac{g_e v}{\sqrt{2}}(\bar{e}_L e_R + \bar{e}_R e_L) - \frac{g_e h}{\sqrt{2}}(\bar{e}_L e_R + \bar{e}_R e_L)$$

where e_L is the left-handed fermion $SU(2)$ doublet and e_R the right-handed singlet. The g_e Yukawa coupling is not predicted by the Higgs mechanism but it is chosen to be coherent with the electron mass:

$$g_e = \sqrt{2}\frac{m_e}{v}$$

The Yukawa Lagrangian for the electron becomes:

$$\mathcal{L}_{Yukawa,e} = -m_e \bar{e}e - \frac{m_e}{v}\bar{e}eh$$

where the first term represents the coupling of the electron to the Higgs field through its non-zero vacuum expectation value, generating the electron mass. The second term gives rise to a coupling between the electron and the Higgs boson itself. As the non-zero expectation value occurs only in the neutral component of the Higgs doublet, this mechanism can only generate the masses of the fermion in the lower component of the doublet. It can therefore only explain the masses of the charged leptons and the down-type quarks, but not the neutrinos and the up-type quarks. The mechanism to explain the mass of the up-type quarks requires the introduction of the conjugate doublet $\boldsymbol{\phi}_c$ defined as:

$$\boldsymbol{\phi}_c = \frac{1}{\sqrt{2}}\begin{pmatrix} -\phi_3 + i\phi_4 \\ \phi_1 - i\phi_2 \end{pmatrix}$$

The conjugate doublet $\boldsymbol{\phi}_c$ transforms in the same way as the doublet $\boldsymbol{\phi}$. The Lagrangian term for the up-type quarks, not shown here, is therefore built from $\bar{L}\phi_c R + \bar{R}\phi_c^\dagger L$, following the same procedure followed for the fermions of the lower component of the doublet.

1.3 State of the art measurements for $VH(H \to b\bar{b})$

As mentioned in the introduction the Higgs boson, theorised in 1964, was discovered at the LHC only in 2012. After the discovery of the Higgs boson, many data analyses focused on characterizing the newly discovered particle in order to understand its compatibility with the Standard Model Higgs boson and to study its properties. Among these studies, the search for the decay of the Higgs boson into

two b-quarks is particularly important, as it is the decay channel with the highest branching ratio. The preferred channel to study this process is the associated production of the Higgs boson with a vector boson decaying leptonically. The leptonic decay of the vector boson makes it possible to reduce the large multi-jet background. Despite this, large irreducible backgrounds are still present, and the search for the $H \to b\bar{b}$ decay required many years of data collection and analysis technique optimisations. In summer 2017 the ATLAS and CMS collaborations finally reported the first evidence for the $H \to b\bar{b}$ decay [16, 17]. The mentioned data analyses used about $36 fb^{-1}$ of data collected at a centre-of-mass energy $\sqrt{s} = 13$ TeV (Run 2) during 2015 and 2016, combined with the results of the data collected during the previous data-taking (Run 1) at $\sqrt{s} = 7$ TeV and $\sqrt{s} = 8$ TeV. An excess of events over the expected background from other Standard Model processes was found, with an observed significance of 3.5 standard deviations (that reached 3.6σ after combination with Run 1 data). This result, together with the results presented by the CMS collaboration on the same timescale (with a 3.8σ observed significance) constituted strong evidence for the Higgs boson decay into pairs of b quarks and for the Higgs boson production in association with a vector boson (VH production).
Given the very good performance of the LHC in 2017, a total amount of about $80 fb^{-1}$ of data collected at $\sqrt{s} = 13$ were available at the end of 2017. The $VH(H \to b\bar{b})$ data analyses were therefore improved and repeated by both collaborations on the newly collected data. The results of the ATLAS search, combined with other decay and production channels, led to the observation of the VH production and of the $H \to b\bar{b}$ decay [8]. The observation was shortly followed by the CMS observation of the same Higgs boson decay [18]. The ATLAS data analysis and results are part of this thesis work. The event selection and the analysis technique employed to reach the $H \to b\bar{b}$ observation are therefore described through the thesis and the results are reported in Chapter 9, together with a comparison of the results obtained by the CMS collaboration.

1.4 Simplified Template Cross Sections

Many successful Higgs boson coupling measurements were obtained using Run 1 and early Run 2 data, among which the ATLAS $H \to b\bar{b}$ observation and VH observation. Such analyses presented their main results as measured signal strength and multiplicative coupling modifiers. Given the good performance of the data collection and the analysis technique employed, the signal strength measurement would have naturally evolved in more complex measurements, which make it possible to extract more information and to further test the Standard Model and

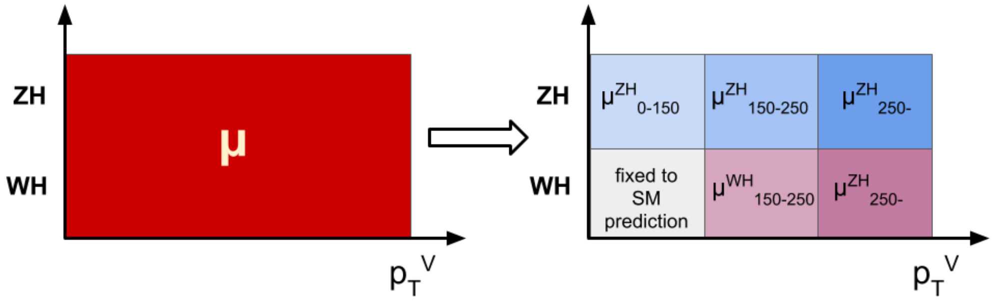

Figure 1.3: Standard signal strength measurement (left) compared with the STXS binning scheme used in this thesis (right). p_T^V is the truth-level V-boson transverse momentum. The WH 0 $< p_T^V <$ 150 GeV bin is fixed to its SM value in the $H \to b\bar{b}$ decay mode, as, with the current analysis, it is not possible to meaningfully measure it given its negligible acceptance.

study the Higgs boson properties. In order to have an optimal and coherent way to present the results a common framework was proposed, the so-called Simplified Template Cross Section (STXS) framework [19, 20]. The STXS framework provides more fine-grained measurements in various kinematic regions, named STXS bins, and at the same time reduces the theoretical uncertainties that are directly folded into the measurements, as explained later in this section. Choosing this common framework has also the advantage to simplify the combination of measurements in different decay channels and between experiments.
For the VH production mode, the goal of the STXS is to measure the production cross-sections, separately for $pp \to WH$ and $pp \to ZH$, in the following regions of the transverse momentum of the vector boson: [75 GeV, 150 GeV], [150 GeV, 250 GeV], >250 GeV. In Figure 1.3 the STXS bins used in this thesis for the VH production mode are shown. This split, shown in Figure 1.3, could help in isolating the effect of BSM deviations. The measurement of the cross-sections for the STXS bins has a clear advantage, compared to the measurement of a single signal strength. While the measurement of a single signal strength only changes the normalisation of the expected Higgs boson signal and forces the shapes of the kinematic distribution used in the analysis to be identical to the SM prediction, the measurement of the STXS bins permits more flexibility. In fact, only the templates of each STXS bin are forced to be identical to the SM prediction, while the measurements of each one of the STXS bins can show deviations from the SM. This flexibility results in two opportunities:

- BSM sensitivity: if there is a deviation from the SM that has a larger effect on the VH events at high energies, it is possible that such deviation produces no measurable effect in the measurement of the signal strength, but has a visible effect in the $VH \geq 250$ GeV bin.

- Reduction of signal systematic uncertainties: the measurement of the signal strength relies completely on the SM expectations. As a consequence, all the systematic uncertainties on the SM predictions have an impact on the measurement. The STXS measurement, instead, relies on the SM expectation only to produce the template in each STXS bin. This allows a reduction of the size of the systematic uncertainties. In fact, a part of the systematic uncertainties are now associated with the prediction of the STXS cross-sections and are decoupled from the measurements. This separation facilitates the comparison between the measured cross-section and the existing or future theoretical calculations.

For this measurement, the simulated signal sample has been used to create one set of histograms for each bin of the STXS bins. Any simulated signal event passing the event selection is assigned to a specific mutually exclusive STXS bin and used to fill a specific histogram. In this way, each set of histograms describes the kinematic distribution of the simulated signal events belonging to a specific STXS bin. One must stress two connected facts:

1. the split into the STXS bins does not utilise measured quantities, but just the so-called truth value of the transverse momentum of the vector boson;
2. based on this split, one can create histograms showing the expected distribution for any measured quantity.

These two facts facilitate the re-interpretation of an existing analysis using the same event selection, event categorisation and background modelling of a standard signal strength analysis. This is possible even when the analysis makes use of a complex multivariate discriminant as final kinematic observable in the statistical procedure. In the STXS framework, in fact, each set of histograms of the selected kinematic observable is used as a template in the statistical procure to measure the cross-section of each desired bin. A re-interpretation of the $VH(H \to b\bar{b})$ analysis published in summer 2018 has been published by the ATLAS collaboration at the end of 2018 and is part of this thesis work [21].
It was mentioned that one of the purposes of the STXS framework is to minimize the theory dependence that is folded into the measurement. The theory dependence is in fact moved (as long as possible) from the first step of determining the STXS from the event categories to the second interpretation step. The cross-section measurement is therefore presented without including the theoretical uncertainties, which can be included at a later step. In this way, the theoretical uncertainties are decoupled from the measurement, and possible future improvement in theoretical

prediction and their uncertainty can be easily propagated and included in the measurement interpretation.
The main difference between STXS measurements and a full fiducial differential measurement is that the fiducial measurement is explicitly optimized for maximal theory independence. In the fiducial measurement acceptance corrections are minimized, a simple event selection is generally applied and the measurements are unfolded to a fiducial volume that is as close as possible to the fiducial volume measured. On the other hand, STXS are optimized for sensitivity while they reduce the dominant theory dependence in the measurement. Instead of precise fiducial volumes, simplified fiducial volumes are used, and larger acceptance corrections are allowed. STXS are also inclusive in the Higgs boson decay, allowing the combination of different decay channels. Additionally, while fiducial and differential measurements are as much as possible agnostic to the production modes, the separation into the production modes is included in the STXS framework to reduce their model dependence.
The criteria followed to define the *STXS bins* are the following:

1. minimize the dependence on theoretical uncertainties;
2. maximize the experimental sensitivity;
3. isolate possible BSM effects;
4. minimize the number of bins without losing experimental sensitivity.

The minimisation of the theory dependence is done avoiding extrapolation from a certain region in phase space to a larger region, whenever this extrapolation carries significant theoretical uncertainties. The bins are therefore preferably defined in terms of quantities that are directly measured by the experiments to reduce the extrapolation. Residual theoretical uncertainties due to the experimental acceptances for each truth bin are of course present. Thus, the reduction of the theory dependence also requires to avoid cases with large variation in the experimental acceptance within one truth bin, as this would introduce a systematic uncertainty on the acceptance. When these systematic uncertainties become big, the bin can be further split into smaller bins. In this way, the impact of this source of systematic uncertainty is reduced.
The maximisation of the experimental sensitivity is done simply by continuing to use event categories that are primarily optimized for sensitivity.
All the mentioned requirements and techniques should naturally be applied minimizing the number of STXS bins. Each bin should have some sensitivity from at least one event category in order to avoid the need to statistically combine several poorly constrained measurements.

1.5 Effective Field theories

Now that the Higgs boson has been discovered, the main focus in particle physics is to extend the SM and look for hints of BSM effects. The study of possible BSM effects extending the SM can be mainly carried on in two different ways. The first is studying specific BSM models (e.g. SUSY), for which different predictions have been investigated. The second is through an effective description, extending the SM Lagrangian with additional operators.
This second approach was followed in looking for BSM effects using the $VH(H \rightarrow b\bar{b})$ STXS measurements. In this approach, deviations from the SM predictions are due to the effects of BSM theories where new particles, with a mass of order Λ, are much heavier than the SM particles and much heavier than the energy scale at which the experiment is conducted. These deviations are encoded in new Lagrangian terms arising from an effective field theory which is intended to parameterize the effects of BSM theories. For this reason, a constraint on these EFT parameters gives valuable constraints on masses and couplings of new particles in these BSM theories. The STXS measurements can be re-casted in the EFT framework, and they can provide useful information on some of the parameters of the new Lagrangian terms. The translation of experimental data into a theoretical framework has then to be done only once rather than for each BSM model separately.
The parametrization is obtained extending the SM Lagrangian by adding new operators with dimensions D larger than 4. The higher-dimensional operators are organized as expansion in D, where each consecutive term is suppressed by a larger power of Λ. The theory has the same field content and the $SU(3) \times SU(2) \times U(1)$ local symmetry as the SM. The EFT Lagrangian can be written as

$$\mathcal{L}_{EFT} = \mathcal{L}_{SM} + \sum_i \frac{c_i^{(5)}}{\Lambda}\mathcal{O}_i^{(5)} + \sum_i \frac{c_i^{(6)}}{\Lambda^2}\mathcal{O}_i^{(6)} + \sum_i \frac{c_i^{(7)}}{\Lambda^3}\mathcal{O}_i^{(7)} ... \tag{1.3}$$

where $\mathcal{O}_i$ are the $SU(3) \times SU(2) \times U(1)$ invariant operators and the parameters c_i are coupling constants, named *Wilson coefficients*. The leading new physics effects from the Lagrangian in equation 1.3 are given by dimension 6 operators. In fact, all $D = 5$ operators violate the lepton number while all $D = 7$ operators violate B-L (barion - lepton number). As experimental constraints on their Wilson coefficients, from previous experiments, suggest that these effects would not be observable at the LHC, their effects on the STXS measurements are not considered. The leading effects are therefore expected from dimension 6 operators, while contributions from operators with dimension 8 or higher are suppressed and assumed to be negligible. The EFT Lagrangian considered is the following, where the SM is only extended by dimension 6 operators:

$$\mathcal{L}_{EFT} = \mathcal{L}_{SM} + \sum_i c_i^{(6)} \mathcal{O}_i^{(6)} / \Lambda^2. \tag{1.4}$$

The dimension 6 operators in equation 1.4 should form a complete, non-redundant set, a so-called *basis*. Any complete basis leads to the same physical predictions concerning possible new physics effects. The basis used to present the results in this thesis is the Strongly Interacting Light Higgs formulation (SILH) [22]. This formalism is defined as the effective theory of a strongly interacting sector in which a light composite Higgs boson arises as a pseudo-Goldstone boson, and is responsible for EW symmetry breaking. There is a total of 59 operators involved in the effective Lagrangian, with an additional seventeen operators for the hermitian conjugate, but only some of them affect Higgs boson physics [23]. Operators not affecting the Higgs boson physics, or that have coefficients tightly constrained by precision electroweak data are not considered. Only 14 operators can be constrained by Higgs boson interactions, but only 4 of them directly affect the VH cross-sections, as they introduce new Higgs boson interactions with W bosons and Z bosons. Additionally, the operator O_d that modifies the coupling between the Higgs boson and down-type quarks, inducing possible variations of the $H \to b\bar{b}$ branching ratio, is considered. This operator affects the measured cross-sections in the same way in each STXS region. All the operators taken into account in this thesis are displayed in Table 1.1.

Operator	Lagrangian term	HEL coefficient	Vertices
$\mathcal{O}_{HW}$	$i\,(D^\mu H)^\dagger\,\sigma^a\,(D^\nu H)\,W^a_{\mu\nu}$	$\frac{g}{m_W{}^2}\texttt{cHW} = \bar{c}_{HW}$	HWW/HZZ
$\mathcal{O}_{HB}$	$i\,(D^\mu H)^\dagger\,(D^\nu H)\,B_{\mu\nu}$	$\frac{g'}{m_W{}^2}\texttt{cHB} = \bar{c}_{HB}$	$H\gamma\gamma/HZZ$
$\mathcal{O}_W$	$i\left(H^\dagger\sigma^a D^\mu H\right)D^\nu W^a_{\mu\nu}$	$\frac{g}{m_W{}^2}\texttt{cWW} = \bar{c}_W$	HWW/HZZ
$\mathcal{O}_B$	$i\left(H^\dagger D^\mu H\right)D^\nu B_{\mu\nu}$	$\frac{g'}{m_W{}^2}\texttt{cB} = \bar{c}_B$	$H\gamma\gamma/HZZ$
$\mathcal{O}_d$	$y_d\|H\|^2\bar{Q}_L H d_R + \text{h.c.}$	$\frac{\texttt{cd}}{v^2} = \bar{c}_d$	Hbb

Table 1.1: Operators and associated parameters included in the model used that could directly affect the VH cross-sections. The Lagrangian term introduced by each operator and the vertex it affects is also shown.

Constraints on the coefficients of the 5 operators of Table 1.1 can be set using the Higgs Effective Lagrangian (HEL) implementation [24] and the known relations between such coefficients and the STXS reported in Ref. [25]. The results presented in this thesis use this exact parametrization. The measurement in STXS model can then be used as input for the subsequent EFT interpretation. In order to establish the relationship between the STXS measurements and the EFT parameters, it is useful to express the cross-section into its SM, interference and BSM components

$$\sigma_{EFT} = \sigma_{SM} + \sigma_{int} + \sigma_{BSM}.$$

where σ_{SM} is the SM component, σ_{BSM} is the BSM component and σ_{int} is the interference component. The deviation from the SM predictions can then be expressed as a function of the EFT parameters, denoted by $\bar{c}_i$, where $\bar{c}_i = c_i^{(6)}/\Lambda^2$:

$$\frac{\sigma_{EFT}}{\sigma_{SM}} = 1 + \sum_i A_i \bar{c}_i + \sum_{ij} B_{ij} \bar{c}_i \bar{c}_j. \tag{1.5}$$

In Equation 1.5, A_i and B_{ij} define the coefficients that are given by $\frac{\sigma_{int}}{\sigma_{SM}} = \sum_i A_i \bar{c}_i$ and $\frac{\sigma_{BSM}}{\sigma_{SM}} = \sum_{ij} B_{ij} \bar{c}_i \bar{c}_j$, which are the linear and quadratic terms in $\bar{c}_i$. The linear term comes from the interference between SM and BSM, while the quadratic term is the leading contribution from BSM only. The A_i and B_{ij} coefficients have been computed by the authors of the note in Ref. [25]. They have been calculated using a Madgraph leading-order generation of the EFT modified cross section σ_{EFT} and of the SM cross section σ_{SM} for each HEL parameter separately in each STXS bin from the ratio of the two cross sections. The uncertainties on the computed coefficients have not been included in the note. Possible sources of uncertainties could arise from the limited number of generated events (statistical uncertainty) and from QCD and EW higher order effects. One of the possible future improvements quoted in the note are the theoretical predictions and simulation of kinematic distributions of some Higgs operators at NLO in QCD. This improvement in the theoretical prediction should be certainly taken into account for future publications.

As the coefficients are computed from the ratio of the EFT and SM cross sections the QCD higher orders effects are expected to partially cancel. These effect should anyhow be included in future analysis as for example QCD corrections start to have sizeble effect for $\bar{\mathtt{c}}_{\mathtt{W}} \sim O(10^{-3})$ [26]. Also non-negligible EW effects could affect the parameters and could be considered in the future. Another point that should be considered in the future is how the coefficients evolve as a function of the energy scale [27].

The equations used for the production cross sections, including linear and quadratic terms, are reported in Table 1.2 and Table 1.3, respectively. Modifications of the $gg \to ZH$ production mode only appears in higher order EFT calculations (starting with dimension 8 operators), hence are not included in this parametrization, and kept fixed to the SM prediction. The equations used for the regions with $p_{\mathrm{T}}^{V} \geq 150$ GeV have been extrapolated from Ref. [25], which in the $150 < p_{\mathrm{T}}^{V} < 250$ GeV region reports separate equations depending on the jet multiplicity, both for ZH and for WH. The overall contribution, independent to the jet multiplicity, is obtained by computing the average between the coefficients in the two categories,

cross-section region	$\sum_i A_i \bar{c}_i$
$pp \to WH,\ W \to \ell\nu$	
150 GeV $\leq p_{\mathrm{T}}^{V} \leq$ 250 GeV	$50\texttt{cHW} + 74\texttt{cWW}$
$p_{\mathrm{T}}^{V} \geq$ 250 GeV	$170\texttt{cHW} + 200\texttt{cWW}$
$pp \to ZH,\ Z(\ell\ell, \nu\nu)$	
75 GeV $\leq p_{\mathrm{T}}^{V} \leq$ 150 GeV	$13\texttt{cHW} + 38\texttt{cWW} + 3.9\texttt{cHB} + 10.5\texttt{cB}$
150 GeV $\leq p_{\mathrm{T}}^{V} \leq$ 250 GeV	$37\texttt{cHW} + 61\texttt{cWW} + 11\texttt{cHB} + 18\texttt{cB}$
$p_{\mathrm{T}}^{V} \geq$ 250 GeV	$130\texttt{cHW} + 150\texttt{cWW} + 38\texttt{cHB} + 46\texttt{cB}$

Table 1.2: Linear terms of the parametrizations for the interference between SM and BSM amplitudes for each STXS region.

cross-section region	$\sum_{ij} B_{ij} \bar{c}_i \bar{c}_j$
$pp \to WH,\ W \to \ell\nu$	
150 GeV $\leq p_{\mathrm{T}}^{V} \leq$ 250 GeV	$839\texttt{cHW}^2 + 1555\texttt{cWW}^2 + \texttt{cHW}(900\texttt{cWW})$
$p_{\mathrm{T}}^{V} \geq$ 250 GeV	$14000\texttt{cHW}^2 + 16000\texttt{cWW}^2 + \texttt{cHW}(30000\texttt{cWW})$
$pp \to ZH,\ Z(\ell\ell, \nu\nu)$	
75 GeV $\leq p_{\mathrm{T}}^{V} \leq$ 150 GeV	$85\texttt{cHW}^2 + 400\texttt{cWW}^2 + 8\texttt{cHB}^2 + 35\texttt{cB}^2$
	$+\texttt{cHW}(150\texttt{cWW} + 20\texttt{cHB} + 42\texttt{cB})$
	$+\texttt{cHB}(44\texttt{cWW} + 12\texttt{cB}) + \texttt{cWW}(140\texttt{cB})$
150 GeV $\leq p_{\mathrm{T}}^{V} \leq$ 250 GeV	$462\texttt{cHW}^2 + 982\texttt{cWW}^2 + 41\texttt{cHB}^2 + 86\texttt{cB}^2$
	$+\texttt{cHW}(1255\texttt{cWW} + 277\texttt{cHB} + 358\texttt{cB})$
	$+\texttt{cHB}(373\texttt{cWW} + 105\texttt{cB}) + \texttt{cWW}(587\texttt{cB})$
$p_{\mathrm{T}}^{V} \geq$ 250 GeV	$8000\texttt{cHW}^2 + 9600\texttt{cWW}^2 + 720\texttt{cHB}^2 + 850\texttt{cB}^2$
	$+\texttt{cHW}(17000\texttt{cWW} + 4800\texttt{cHB} + 5100\texttt{cB})$
	$+\texttt{cHB}(5100\texttt{cWW} + 1500\texttt{cB}) + \texttt{cWW}(5700\texttt{cB})$

Table 1.3: Quadratic terms of the parametrizations for the pure BSM contributions to each STXS region.

weighted with the corresponding cross-sections. The coefficients for ZH in the $75 < p_{\mathrm{T}}^{V} < 150$ GeV range are derived following the procedure suggested in Ref. [20]. The partial widths are parametrized with a procedure identical to the one used for the cross-sections. The BR of the $H \to b\bar{b}$ process can be expressed as a function of linear and quadratic terms of the parameters $\bar{c}_i$ involved, as reported in Equation 1.6.

$$BR_{bb} = \frac{\Gamma_{bb}}{\Gamma_{All}} \approx \frac{\Gamma_{bb}^{SM}}{\Gamma_{All}^{SM}} \left[1 + \sum_i A_i^{bb} \bar{c}_i + \sum_{ij} B_{ij}^{bb} \bar{c}_i \bar{c}_j - \left(\sum_i A_i^{All} \bar{c}_i + \sum_{ij} B_{ij}^{All} \bar{c}_i \bar{c}_j \right) \right] \tag{1.6}$$

Table 1.4 summarize the linear and quadratic dependence of the partial and total widths to the parameters. As shown in the table, the coefficients that affect the

Partial width	$\sum_i A_i \bar{c}_i$
$H \to b\bar{b}$	$3\texttt{cd}$
$H \to$ All	$-2.3\texttt{cd} + 0.37\texttt{cHW} + 1.0\texttt{cWW} + 0.0079\texttt{cHB} + 0.023\texttt{cB}$

Partial width	$\sum_{ij} B_{ij} \bar{c}_i \bar{c}_j$
$H \to b\bar{b}$	$2.3\texttt{cd}^2$
$H \to$ All	$1.7\texttt{cd}^2 + 4.7\texttt{cHW}^2 + 2.6\texttt{cWW}^2 + 4.3\texttt{cHB}^2$

Table 1.4: Parametrizations for the interference between SM and BSM amplitudes (top) and the pure BSM contributions (bottom) for the $H \to b\bar{b}$ Branching Ratio.

VH production cross-sections, such as cHW, cHB, cWW and cB, also enter the BR_{bb} parametrization, with smaller contributions. These contributions have been taken into account in the parametrization used for the fits. The parameters considered for this thesis are therefore: $\bar{\texttt{c}}_{\texttt{HW}}$, $\bar{\texttt{c}}_{\texttt{HB}}$, $\bar{\texttt{c}}_{\texttt{W}} - \bar{\texttt{c}}_{\texttt{B}}$, where $\bar{\texttt{c}}_{\texttt{HW}}$ and $\bar{\texttt{c}}_{\texttt{W}}$ affect the HWW and HZZ vertices, while $\bar{\texttt{c}}_{\texttt{HB}}$ and $\bar{\texttt{c}}_{\texttt{B}}$ are the two leading contributions to the modification of the HZZ vertex. The sum $\bar{\texttt{c}}_{\texttt{W}} + \bar{\texttt{c}}_{\texttt{B}}$ is strongly constrained by precision electroweak data, therefore it is assumed to be zero [28].
In addition to the set of mentioned parameters, related to the operators affecting VH production, the parameter $\bar{\texttt{c}}_{\texttt{d}}$ is also considered, as it affects the partial width Γ_H^{bb} and the total width Γ_H of the Higgs boson, thus modifying the $H \to b\bar{b}$ branching ratio.
The parametrisation used in the fit is a combination of the linear coefficients arising from the interference between SM and BSM amplitudes (Table 1.2) and the quadratic coefficients corresponding to the purely BSM contributions (Table 1.3). The curves corresponding to the parametrization for each kinematic region and each EFT parameter considered have been studied. The curves for the cHW parameters are shown in Figure 1.4 as an example. The other parameters considered have

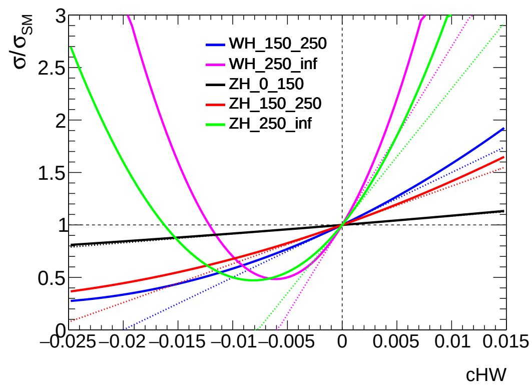

Figure 1.4: Parametrizations induced by the EFT parameters. Dashed lines show the linear parametrization only, the continuous lines show the sum of the linear and quadratic terms.

similar trends. The linear approximation, represented by the dashed lines, is fairly good for the STXS regions with p_{T}^{V} <250 GeV in the range going from -0.01 to 0.01. However the quadratic contributions, represented by the continuous lines, have a dominant impact on the two STXS regions with p_{T}^{V} >250 GeV. The EFT results presented in this thesis have been computed both in the linear only approximation and including the quadratic terms, as shown in Chapter 9.

1.5.1 BSM search using STXS

A measurement within the STXS framework has been recently carried on by the ATLAS collaboration using the $H \to \gamma\gamma$ and $H \to ZZ^* \to 4\ell$ decays [29, 30]. These two analyses have also been combined to extract limits on some EFT parameters [23]. Using this two analyses, constraints have been set on six parameters: `cG`, `cA`, `cu`, `cHW`, `cHB` and `cWW` − `cB`. Other parameters not included in the fit are set to 0 (their SM value). The results of the 68% C.L. intervals are shown in Figure 1.5. All the results are compatible with the Standard Model expected value.
Additionally to the $H \to \gamma\gamma$ and $H \to ZZ^* \to 4\ell$ results, an interesting study is reported in the same paper, showing how much the cross-section of a specific production mode could be modified assuming that one of the EFT parameter value is different from 0. The chosen values of the parameters correspond to the expected constraints shown in Figure 1.5. All the parameters are set to 0, their SM expected value, except from one. The values of the modified cross-sections, divided by the SM value, are shown in Figure 1.6. Two of the channels shown in the Figure are also studied in this thesis: WH and ZH where the V boson decays

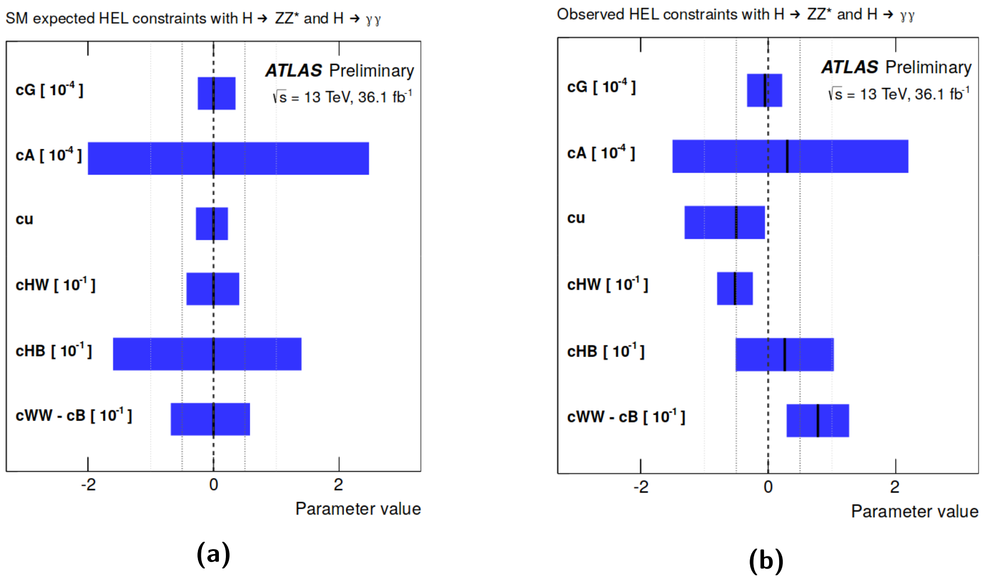

Figure 1.5: The (a) observed and (b) SM predicted best-fit values and 68% C.L. intervals for the parameters `cG`, `cA`, `cu`, `cHW`, `cHB` and `cWW` − `cB` [23].

leptonically. Among all the region shown the WH high p_{T}^{V} region is the one that could potentially be the most sensitive to a `cHW` and `cWW` deviation, while the ZH channel is the most sensitive region for the `cHB` parameter. Both for WH and ZH the high energy regions are more sensitive to the deviation of the investigated parameters with respect to the low energy regions.

1.5.2 EFT at high energies

From the plot in Figure 1.6 it is clear how the bins at high energy are more sensitive to BSM deviations with respect to low energy bins. In the plot, the high p_{T}^{V} regions have a value of the V boson higher than 150 GeV and the low p_{T}^{V} below 150 GeV. This means that even if the bins at high energy are statistically limited, measuring these cross-sections could significantly contribute to measure or set limits on the BSM parameters. This behaviour is the main reason why it has been decided to build another $VH(H \to b\bar{b})$ analysis specifically targeting high energy events, trying to add a bin of the STXS at even higher energies.
The ATLAS experiment collected about 60 fb^{-1} of data in 2018. Adding this up with the data collected between 2015 and 2017 a total of about 140 fb^{-1} is reached for the full Run 2. The STXS analysis depicted in this thesis only makes use of the 2015-2017 dataset, where no categorisation has been done above $p_{\mathrm{T}}^{V} = 250$ GeV. On the other side, the full Run 2 dataset is considered sufficient to try to measure an

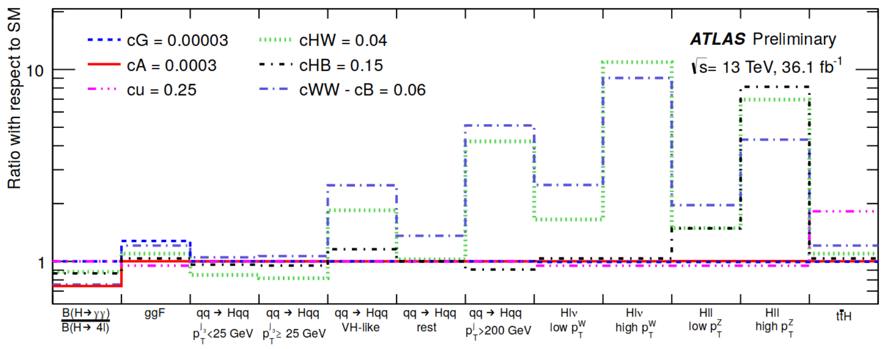

Figure 1.6: The values of the cross-section, divided by the SM cross-section, of some STXS regions for $\approx +1\sigma$ expected SM values of $\texttt{cG}$ (3×10^{-5}), $\texttt{cA}$ (3×10^{-4}), $\texttt{cu}$ (0.25), $\texttt{cWW} - \texttt{cB}$ (0.06), $\texttt{cHW}$(0.04), and $\texttt{cHB}$(0.15). The high p_{T}^{V} category includes events with a value of the vector boson tranverse momentum higher than 150 GeV [23]. In the x-axis $Hl\nu$ includes $pp \to WH$ events where the W decays leptonically and $Hl\nu$ includes $pp \to ZH$ events where the Z decays leptonically.

additional bin at very high energies, at p_{T}^{V} >400 GeV. Additionally to the increased dataset, specific techniques have been developed to measure events with hadronic decays at very high energies. The main idea is that some events are produced in a high energy regime where it is not possible to reconstruct separately the two b-hadrons from the Higgs boson decay. The Higgs boson is therefore reconstructed with a single jet with a large radius, including both the b-hadrons from the decay, instead of using two separate cones, which would merge at very high energies. This analysis, performed with the full Run 2 dataset and targeting high energy events, is called in this thesis *merged* analysis. Instead in the aforementioned analysis, which led to the $H \to b\bar{b}$ observation, the candidate Higgs boson is reconstructed with two separate jets and the analysis is called *resolved* analysis.

Chapter 2

The experimental apparatus

In this chapter, the experimental apparatus is described. In the first part, the Large Hadron Collider is briefly introduced. In the second part the structure of the ATLAS experiment is illustrated.

2.1 The LHC

The Large Hadron Collider (LHC) is a particle accelerator located at CERN, near Geneva, Switzerland. It has been designed as a high energy, high-intensity collider for hadrons, namely for proton-proton, lead-lead and proton-lead collisions. It is installed in an underground ring and it has a circumference of 27 km.
The accelerator complex at CERN is a succession of machines that accelerate particles to increasingly high energies. Each machine boosts the energy of a beam of particles, before injecting the beam into the next machine in the sequence. The LHC is the last element in this accelerator chain.
In the LHC two beams travel in the ring in opposite directions, in two separate beam pipes at ultra-high vacuum, before they collide. The proton beams are bent by 1232 superconducting dipole magnets providing fields of up to 8.3 T, while multipole magnets focus the beams.
There are four locations, so-called interaction points, where the beams cross and collisions occur. At each of these locations there is a large detector experiment, as shown in Figure 2.1.
The ATLAS (A Toroidal LHC ApparatuS) [32] and CMS (Compact Muon Solenoid) [33] detectors are two multi-purpose detectors; LHCb (Large Hadron Collider beauty) [34] is a specialized detector designed for studying bottom quark physics; and the AL-

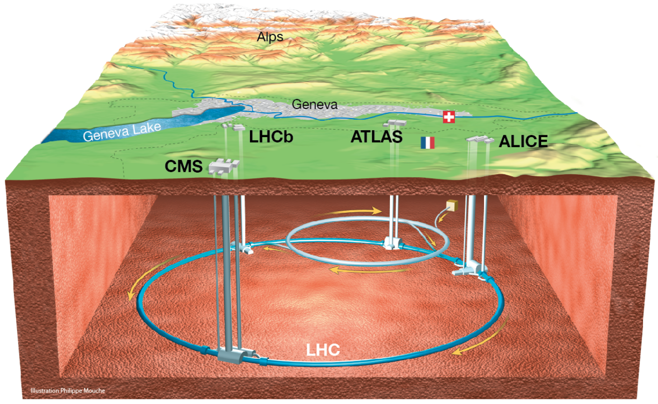

Figure 2.1: Schematic LHC layout: four experiments are installed in correspondence of four collision points: ATLAS, CMS, LHCb and ALICE [31].

ICE (A Large Ion Collider Experiment) detector [35] is designed for studying heavy ion collisions. An overview of the ATLAS detector is given in Section 2.2.
The LHC was designed to collide proton beams with a centre-of-mass energy up to 14 TeV, and with an instantaneous luminosity of $10^{34}\text{cm}^{-2}\text{s}^{-1}$. Up to now, the LHC delivered proton-proton collisions (*pp* collisions) at centre-of-mass energies of 7, 8 and 13 TeV, with a peak luminosity of $\sim 2 \cdot 10^{34}\text{cm}^{-2}\text{s}^{-1}$ [36]. The LHC first run, Run 1, lasted from 2009 to 2012. During Run I LHC delivered *pp* collisions at centre-of-mass energies of 7 TeV and 8 TeV. After a scheduled long shutdown, the second run, Run 2, started in 2015 and lasted until the end of 2018. The centre-of-mass energy of the proton-proton collisions during Run 2 was 13 TeV. The work presented in this thesis almost exclusively exploits the set of data collected during Run 2. However, some of the presented results are given by the combination of the Run 2 results, depicted in the thesis, with the Run 1 results exploiting the data collected in 2011 and 2012. The centre-of-mass energy, together with some other important parameters, are summarised in Table 2.1 for the dataset used in this thesis.

2.1.1 Luminosity and pile-up

Protons at LHC are accelerated in bunches of up to $\sim 10^{11}$ protons, which are simply referred to as *bunches*. Collisions between bunches occur every 25 ns (50 ns for the Run I collisions).
The collision rate $\dot{N}$ for a given process of cross-section σ produced by a machine

Years	Run	Centre-of-mass energy [TeV]	Integrated luminosity [fb^{-1}]	$< \mu >$	Bunch spacing [ns]
2011	Run 1	7 TeV	4.7 fb^{-1}	9.1	50
2012	Run 1	8 TeV	20.3 fb^{-1}	20.7	50
2015-16	Run 2	13 TeV	36.1 fb^{-1}	23.7	25
2017	Run 2	13 TeV	43.8 fb^{-1}	37.8	25
2018	Run 2	13 TeV	58.5 fb^{-1}	36.1	25

Table 2.1: LHC centre-of-mass energy, integrated luminosity, average number of interactions per crossing and bunch spacing for the years 2011-2012 [37] and 2015-2018 [36].

functioning with luminosity $\mathcal{L}$ is given by: $\dot{N} = \mathcal{L}\sigma$. Accurate measurement of the delivered luminosity is crucial for many physics measurements, as the uncertainty on the delivered luminosity is often a relevant source of systematic uncertainty. One way to express the luminosity $\mathcal{L}$ of a proton-proton collider is:

$$\mathcal{L} = \frac{N_1 N_2 n_b f_r}{2\pi\sqrt{(\sigma_{1x}^2 + \sigma_{2x}^2)(\sigma_{1y}^2 + \sigma_{2y}^2)}}$$

where N_1 and N_2 are the protons in each bunch, n_b is the number of colliding bunch pairs, f_r is the machine revolution frequency, and, assuming to have gaussian beams, $\sigma_u = \sqrt{\sigma_{1u}^2 + \sigma_{2y}^2}$ with $u = x, y$ for each separation plane [38]. The size and shape of the interaction region are measured with the van der Meer method [39], by moving the beams across each other in the two transverse planes and recording the relative interaction rates as a function of the transverse beam separation. The measured interaction rates as a function of the separation allow a determination of the effective beam size. The delivered luminosity is monitored, both during the van der Meer scan and during the ordinary data-taking, by measuring with several algorithms the observed interaction rate per crossing independently with a variety of detectors [40]. For Run 2, the primary bunch-by-bunch luminosity measurement was performed with the LUCID2 detector [41]. LUCID2 is a detector composed of 16 photomultiplier tubes (PMTs) placed in each forward arm of the ATLAS detector, at approximately $z = \pm 17$ m from the interaction point. Cherenkov light is produced in the quartz windows of the PMTs and the detector provides luminosity counts for each of the bunch crossing. These counts are integrated over time periods of about 60 seconds, called *luminosity blocks*.
The *integrated luminosity* is the integral of luminosity with respect to time. Some of the physics processes that are measured or searched for by ATLAS and CMS have very low cross-sections. The excellent LHC performance has been therefore

essential to collect the integrated luminosity necessary to study such processes. During Run 2 an integrated luminosity of 156 fb^{-1} was delivered by the LHC, of which ATLAS recorded 147 fb^{-1}. The integrated luminosity of data certified to be good enough to use them in physics analysis (good quality data) is 139 fb^{-1}. Figure 2.2a shows the cumulative luminosity versus time for the full Run 2. The uncertainty on the integrated luminosity for the full Run 2 dataset is 1.7% [40].

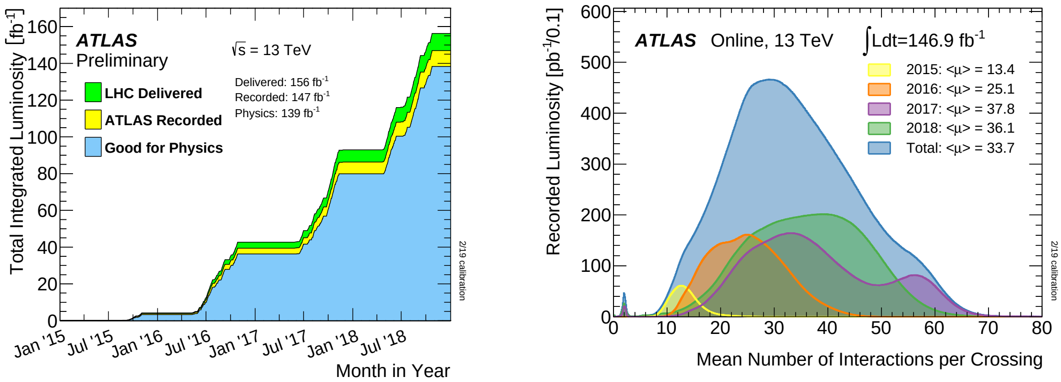

(a) (b)

Figure 2.2: (a) Cumulative luminosity versus time delivered by LHC (green), recorded by ATLAS (yellow), and certified to be good quality data (blue) during stable beams and for proton-proton collisions for the full Run 2 [36].
(b) Luminosity-weighted distribution of the mean number of interactions per crossing for Run 2. The mean number of interactions per crossing corresponds to the mean of the Poisson distribution of the number of interactions per crossing for each bunch. The distribution for the total Run 2 data-taking is shown in blue, while the distributions for the data recorded in 2015, 2016, 2017 and 2018 are shown in yellow, orange, purple and green, respectively [36].

The high instantaneous luminosity achieved at LHC has the side effect of producing a large number of proton interactions per bunch crossing. The mean number of interactions per crossing μ for Run 2 is shown in Figure 2.2b. Particles produced in multiple interactions, either coincident with the event of interest or in adjacent bunch crossings, are referred to as *pile-up*. Pile-up events occurring simultaneously with the interaction of interest, are indicated as *in-time pile-up*. In order to isolate the interaction of interest from in-time pile-up, experiments are designed to distinguish the different interaction vertices and their associated particles. One of the requirements of the ATLAS detector is high granularity, needed to handle the particle fluxes and to reduce the influence of pile-up events. Additionally to the in-time pile-up, adjacent bunch crossings might produce overlapping signals. This happens in particular in the slower components of the detector and in the read-out electronics. Pile-up events occurring before or after the interaction of interest but within the detector integration time are named *out-of-time pile-up*. The out-of-time pile-up effect is largely determined by the response function of the detector and the inclusion of these effects is critical to an accurate simulation of the detector response.

2.2 Overview of the ATLAS detector

The ATLAS detector is one of the two general-purpose particle detectors located on the LHC ring [4, 32]. General-purpose detectors are designed to study many different aspects of particle physics. ATLAS is designed to cover the widest possible range of physics studies, from the search and measurements of the Higgs boson to the search for new physics, and also pursues a considerable program of Standard Model measurements and heavy-ion physics. A schematic view of the detector is shown in Figure 2.3.

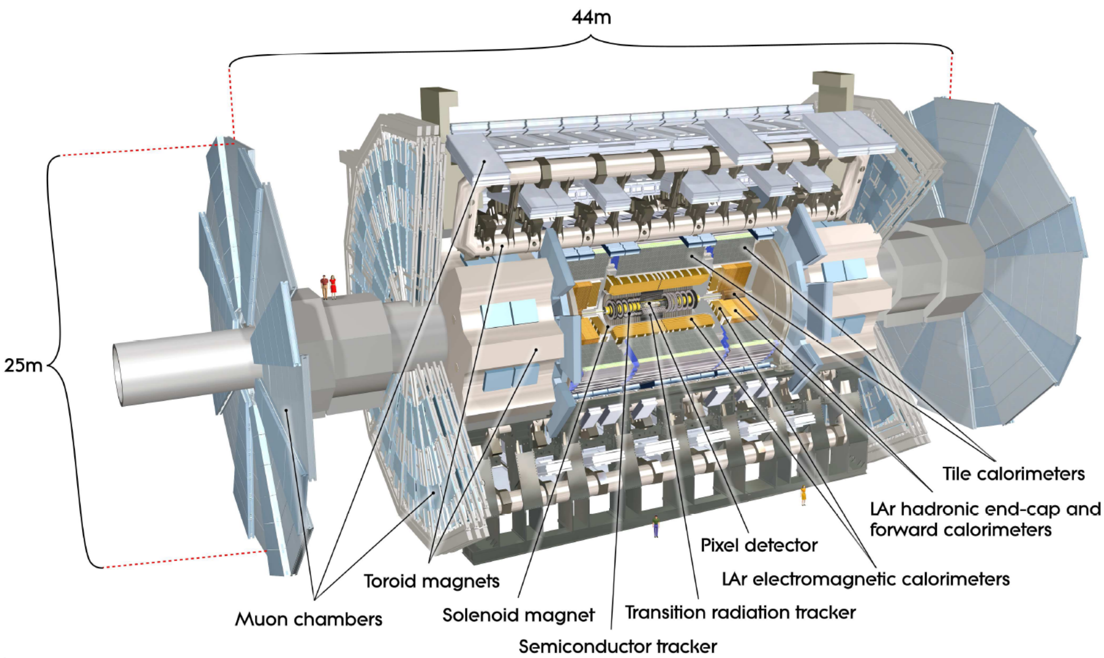

Figure 2.3: Cut-away view of the ATLAS detector and of the main sub-detector structures [32].

ATLAS has an approximately cylindrical geometry which consists of several sub-detectors surrounding the interaction point and covering almost the full solid angle. The detector is built in layers. The innermost layer is a tracking system surrounding the interaction point. The tracking system is immersed in a magnetic field and is enclosed by electromagnetic and hadronic calorimeters. The outermost layer is constituted by a muon spectrometer.

The structure of the detector can be divided into the *barrel* and the *end-cap* regions. The barrel region is cylindrically symmetric around the beam pipe while the endcaps close the open sides of the barrel, allowing the coverage of almost the full solid angle of 4π. This geometry with wide coverage is designed so that almost all the particles produced in the collisions fall within the detector acceptance.
The search for the Higgs boson has been used as a benchmark to establish the performance of the main sub-detectors of ATLAS. It is a particularly important process since it involves many production and decay mechanisms. Additionally, before the Higgs discovery at LHC, its mass was not known and the preferred decay modes widely vary depending on the Higgs mass, forcing the construction of a detector sensitive to a wide range of decays. The main ATLAS sub-detectors are described in more detail in the next sections.

2.2.1 Coordinate system

The nominal interaction point is defined as the origin of the coordinate system used in ATLAS, while the beam direction defines the z-axis, and the x-y plane is transverse to the beam direction. The positive x-axis is defined as pointing from the interaction point to the centre of the LHC ring, and the positive y-axis is defined as pointing upwards. The azimuthal angle ϕ is measured around the beam axis, and the polar angle θ is the angle from the beam axis.
The rapidity of a particle is defined as $y = \frac{1}{2}ln(\frac{E+p_z}{E-p_z})$, where E is the energy of the particle and p_z is the projection of the particle momentum along the z axis. This quantity is additive under boost along z, hence distributions in rapidity are invariant. The pseudorapidity is defined as

$$\eta = -\ln[\tan(\theta/2)]$$

and it approximates the rapidity y when it is possible to neglect the mass of the particle with respect to the energy. The pseudorapidity is more widely used because it is experimentally easier to measure it and because it is a geometric quantity, and therefore does not depend on the particle.
Often in this work, the angular distance between two objects i and j is used. It is defined as

$$\Delta R_{ij} = \sqrt{(\eta_i - \eta_j)^2 + (\phi_i - \phi_j)^2}$$

where η_i and η_j are the pseudorapidities of the two objects, while ϕ_i and ϕ_j represent their azimuthal angles.
Since the longitudinal momentum of the colliding partons is not known a priori in proton-proton collisions, and the detector acceptance does not allow the reconstruction of the momentum component along the beam pipe, transverse observables are

defined in the x-y plane, such as transverse momentum, p_T and missing transverse momentum, E_{T}^{miss}.

2.2.2 Magnet system

One of the key features of the ATLAS detector is the unique hybrid superconducting magnet system. It is an arrangement of a central solenoid surrounded by a system of three large toroids, one barrel and two end-caps. The crucial choice of having two separate magnetic systems, one for the internal tracking, and one for the outer muon tracker, has driven the design of large part of the rest of the detector. The reason for implementing such system was to obtain precise measurements for muons at high rapidity [42]. Toroids allow covering an acceptance not reachable with a solenoid system. Moreover the toroids allow measuring particles momenta, which is particularly relevant for forward-going particles, since they can carry high momentum and low p_T.
The full magnetic system is 26 m in length and 22 m in diameter [32]. A sketch of the ATLAS magnet system is shown in Figure 2.4.

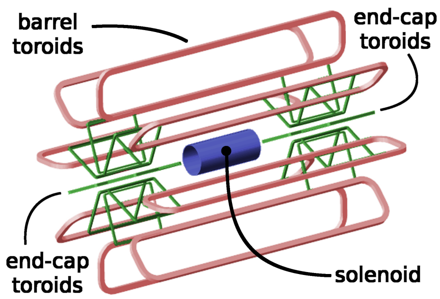

Figure 2.4: Sketch of the ATLAS magnet system: the central solenoid (blue), the barrel toroid (red) and the end-cap toroids (green) [43].

The central superconducting solenoid provides the magnetic field for particle bending in the inner detector and extends over a length of 5.3 m with a diameter of 2.5 m. It provides a 2 T axial magnetic field for the inner detector.
The three superconducting toroids provide the magnetic field for the muon detectors. They are arranged with an eight-fold azimuthal symmetry around the calorimeters. As mentioned, the main reason for using toroids for muon bending is to have the best possible measuring acceptance at high rapidity. The large barrel toroid provides magnetic bending over the range $|\eta| < 1.4$. End-cap magnets are smaller than the barrel magnet and are inserted into both ends of the barrel toroid, they provide magnetic bending over the range $1.6 < |\eta| < 2.7$. Over $1.4 < |\eta| < 1.6$,

usually referred to as the transition region, magnetic deflection is provided by a combination of barrel and end-cap fields. This magnet configuration provides a field which is mostly orthogonal to the muon trajectories and at the same time it minimizes the degradation of resolution due to multiple scattering.
The barrel toroid provides 1.5 to 5.5 Tm of bending power in the range $0 < |\eta| < 1.4$, and the end-cap toroids 1 to 7.5 Tm in the region $1.6 < |\eta| < 2.7$. The bending power is lower in the transition regions where the two magnets overlap.

2.2.3 The Inner Detector

The ATLAS Inner Detector tracker (ID) records information on the charged particle trajectories. It was designed to reconstruct the tracks with an excellent momentum and position resolution, using as little material as possible to minimise the energy loss before the calorimeters. A precise track measurement is essential to reconstruct the primary and secondary vertices, allowing the discrimination of the hard-scatter vertices from the pile-up vertices and the identification of the tracks from b-hadron decays. The required ID precision is reached in a dense tracking environment. It is in fact designed to work in an environment of $\sim$ 1000 particles produced every 25 ns within $|\eta| < 2.5$. In this challenging environment, the ID provides a few high precision measurements close to the interaction point and a large number of lower precision measurements in the outer volume.
The whole ID is immersed in a 2 T magnetic field generated by the central solenoid, which provides the track bending power (Section 2.2.2). The precise measurement of the trajectory and the high magnetic field allows reaching a high resolution on the measurement of the transverse momentum of charged particles with p_T as low as 500 MeV [44]. Moreover, the position of the vertices (from the hard scattering interaction and from the in-time pile-up events) are reconstructed with high spatial resolution. This is achieved by installing very high-granularity silicon pixel detectors as close as possible to the beam axis.
The ID consists of four tracking devices: the Insertable B-Layer (IBL), the Pixel detector (PIXEL), the silicon microstrip tracker (Semi-Conductor Tracker SCT) and the Transition Radiation Tracker (TRT) [32, 45]. A schematic of the ATLAS Inner Detector is shown in Figure 2.5.
To better match the topology of the tracks emerging from the proton-proton collisions all the devices, except for IBL, are separated into a barrel and two end-caps sections, measuring particles laying at $|\eta| < 1.2$ and $1.2 \lesssim |\eta| \leq 2.5$, respectively. In the barrel region, the sensors are arranged in concentric cylinders around the beam axis while in the end-cap regions they are located on disks perpendicular to the beam axis [32].

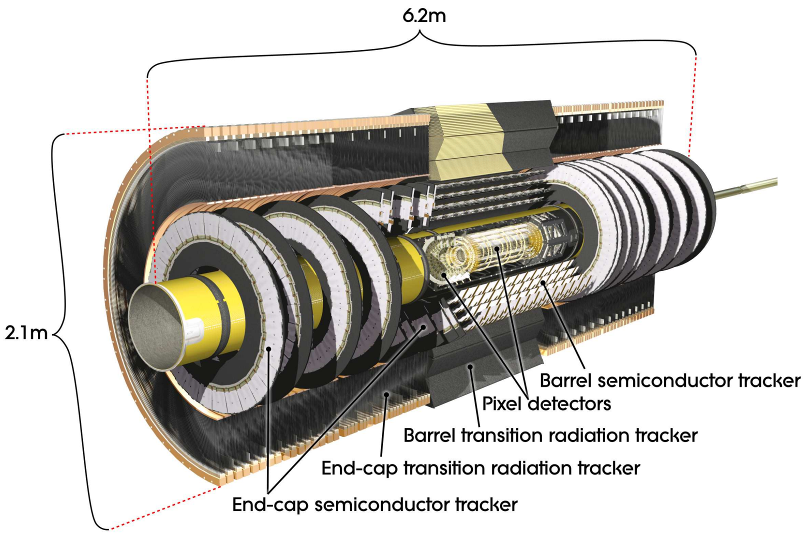

Figure 2.5: Cut-away view of the ATLAS inner detector [32].

IBL

The innermost part of the ID is the IBL, which was installed during the shutdown between Run 1 and Run 2. It is a very-high-resolution semiconductor pixel detector, extending up to $|\eta| < 2.9$ [45]. In order to improve vertex reconstruction as much as possible, it was installed as close as possible to the interaction point, around a new thin beam pipe at a radial distance of only 3.3 cm from the beam axis. This low distance from the interaction point requires the sensors to be very robust against ionising radiation.
The IBL pixel size of (50, 250) µm in $(\phi,\ z)$ contributes to the excellent track parameters resolution. The transverse impact parameter resolution measured on data collected in 2012, before the IBL installation, and in 2015, after the IBL installation, is shown in Figure 2.6a. This parameter is crucial for the identification of jets from b-hadrons. The parameters resolution worsen for low p_T values, below about 10 GeV, where the resolution is governed by multiple scattering in the beam pipe and first pixel layers. For higher momenta, the impact parameter resolutions approach an asymptotic limit given by the intrinsic detector resolution and residual misalignments [46]. A clear improvement in the resolution for the 2015 data is observed in the figure and it is particularly significant for the low p_T tracks ($\sim 40\%$ for tracks with $p_T < 1$ GeV). Additionally to the improved resolution, the installation of the IBL strengthens the robustness of the tracking against detector problems and helps in the pileup rejection.

Pixel

The IBL is surrounded by the Pixel detector, which is placed between five and 12 cm radial distance from the interaction point. It is made up of silicon pixels of the typical size of $50\,\mu m \times 400\,\mu m$ to obtain high precision measurements in the region close to the interaction point. The pixel detector is made up of three barrel layers and three disks per side. Each track typically crosses three pixel layers.

SCT

The trajectories in the intermediate region (radii from 30 to 60 cm) are measured by the SCT. The SCT is a silicon microstrips detector that provides excellent spatial resolution over a large area. At this radii, the expected particle density is lower and the silicon microstrips were chosen over silicon pixels. This choice allowed a cost reduction and a reduction of the number of readout channels while maintaining a good spatial resolution. The barrel region of the SCT detector, covering $|\eta| < 1.4$, is composed of silicon microstrip modules arranged in eight coaxial cylinders. While a pixel layer can measure both the ϕ and the z coordinates of a hit, it takes two SCT layers, installed with an angle between them of 40 mrad, to form one stereo strip. This allows the measurement of both ϕ and z. Eight strip layers, corresponding to four space points, are crossed by each track in the barrel region. The two end-caps of the detector are instead formed by nine disk layers per side and cover the region $1.4 < |\eta| < 2.5$.
The positions of the clusters on the transverse plane in the IBL, the Pixel detector and the SCT are shown in Figure 2.6b. The innermost circle represents the clusters in the IBL, the three layers surrounding the IBL are the clusters in the Pixel detector and the last four layers represent the clusters in the SCT.

Transition Radiation Tracker

The Transition Radiation Tracker is placed at outer radii with respect to the SCT (60 to 100 cm). It is designed to provide continuous tracking to enhance pattern recognition and improve the momentum resolution over $|\eta| < 2.0$ and electron identification complementary to that of the calorimeter. It is made up of a large number of small diameter (44 mm) drift tubes (straws) which provide good spatial resolution in the track bending plane and greatly contribute to pattern recognition. Each track typically produces about 36 hits in the TRT. In the barrel region, the straws are parallel to the beam axis while in the end-cap regions, the straws

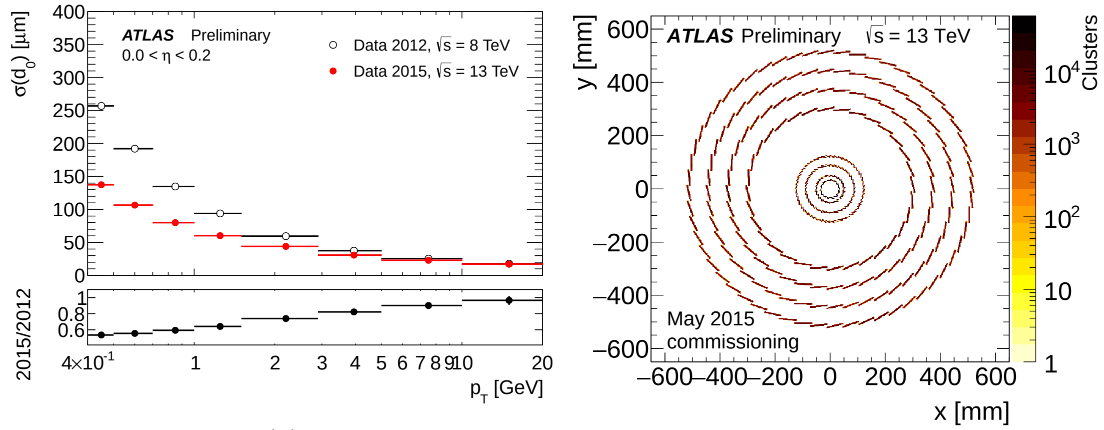

(a) (b)

Figure 2.6: (a) Transverse impact parameter resolution measured from data in 2015, at $\sqrt{s} = 13$ TeV with the ID including the IBL, as a function of p_T, for values of $0.0 < \eta < 0.2$ compared to that measured from data in 2012, $\sqrt{s} = 8$ TeV [47].
(b) Global X and Y position of clusters in the IBL, the Pixel detector and the SCT detector in the barrel region [48].

are arranged radially in wheels. Electron identification capability is added by employing Xenon gas to detect transition radiation photons created in a radiator between the straws. Diagrams of the ID barrel and of the end-caps of the ID are shown in Figure 2.7a and 2.7b.
The combination of precision trackers at small radii with the TRT at a larger radius gives very robust pattern recognition and high precision in both $R - \phi$ and z coordinates. The straw hits at the outer radius contribute significantly to the momentum measurement. Indeed, the lower precision per point compared to the silicon is compensated by a large number of measurements and by the longer measured track length.

2.2.4 The calorimeter system

The ATLAS calorimeter system is divided into two sections: the electromagnetic calorimeter and the hadronic calorimeter. The electromagnetic section must provide a good measurement and containment of the electromagnetic showers. The hadronic showers are instead measured by the ensemble of the electromagnetic and hadronic sections. A schematic layout of the ATLAS calorimeter system is shown in Figure 2.8.
The ATLAS calorimeter system makes use of sampling calorimeters, in which layers

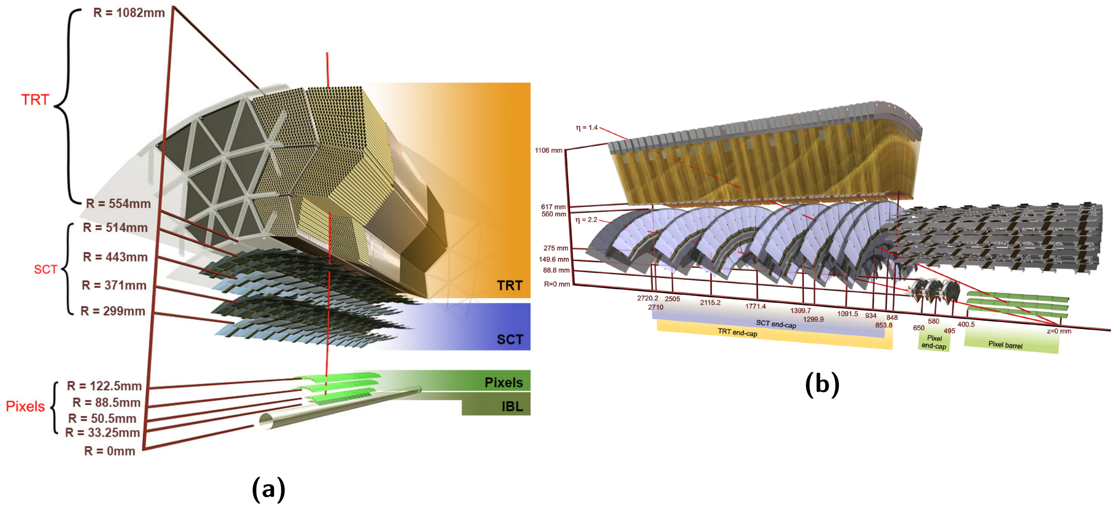

Figure 2.7: (a) ID barrel diagram: the beam-pipe, the IBL, the three cylindrical silicon Pixel layers, the four cylindrical layers of barrel silicon micro-strip modules (SCT) and 72 straw layers in the barrel TRT modules within their support structure [49].
(b) ID end-cap diagram: the three silicon-pixel disks, the nine disks of the end-cap SCT and the forty planes of TRT wheels [32].

of passive and active material alternate. The electromagnetic section is constituted by a high granularity Liquid-Argon (LAr) electromagnetic sampling calorimeter, with excellent performance in terms of energy and position resolution, and covers the pseudorapidity range $|\eta| < 3.2$. The hadronic calorimetry in the range $|\eta| < 1.7$ is provided by a scintillator-tile calorimeter (TileCal). In the end-caps ($|\eta| > 1.5$), LAr technology is also used for the hadronic calorimeters thanks to its radiation hardness. The LAr forward calorimeters provide both electromagnetic and hadronic energy measurements and extend the pseudorapidity coverage to $|\eta| = 4.9$. Over the η region matched to the ID, the fine granularity of the electromagnetic calorimeter is ideally suited for precision measurements of electrons and photons. Very good electron and photon identification and measurements are important requirements as these objects are the basis of many physics studies, e.g. the $H \to \gamma\gamma$ channel that has been crucial for the first Higgs observation [50]. The coarser granularity of the rest of the calorimeter is sufficient to satisfy the physics requirements for jet reconstruction and E_{T}^{miss} measurements. The electromagnetic calorimeter, the hadronic calorimeter and the forward calorimeter are further discussed in the next sections. The jet, MET and other objects reconstruction are instead described in Chapter 5.
The quality of a calorimeter system is mainly assessed by two parameters: the energy linearity and the energy resolution. The resolution of calorimeters can be

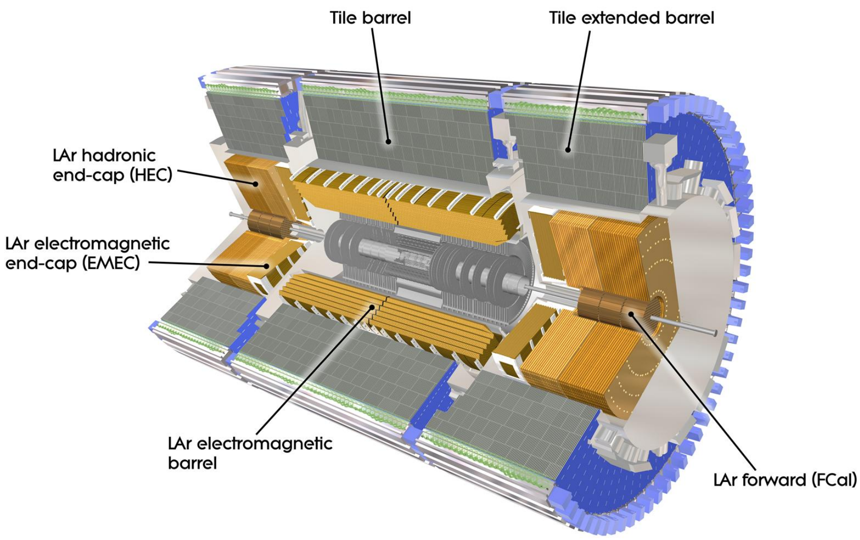

Figure 2.8: Cut-away view of the ATLAS calorimeter system [32].

parametrized as [51]:

$$\frac{\sigma(E)}{E} = \frac{a}{\sqrt{E(\mathrm{GeV})}} \oplus \frac{b}{E(\mathrm{GeV})} \oplus c$$

where E is the energy released by the particle in the calorimeter. The a term is the *stochastic term* accounting for all the Poisson statistics-related fluctuations such as the intrinsic shower fluctuations and sampling fluctuations. The parameter b accounts for contributions not depending on the energy of the detected particle, such as electronic noise in the read-out system. The constant parameter c takes into account the systematic effects due to non-perfect calibration and the non-full containment of the showers. The pion energy resolutions for the combined ATLAS calorimeters are shown Figure 2.9. The performance requirements of the calorimeters were driven by the ATLAS physics programme. The calorimeters performance shown in Figure 2.9 with $a \sim 50\%$, $b \sim 3\%$ and $c \sim 2$ guarantees good sensitivity for measurements of physics processes at the TeV scale. The response linearity within 2% up to about 4 TeV is crucial for searching for new physics phenomena.

A good E_{T}^{miss} measurement is important for many physics signatures, including $VH(H \to b\bar{b})$, and is particularly important for SUSY particle searches and new physics. This is ensured by a sufficient total calorimeter thickness, a large η coverage and a small fraction of dead detector regions (which create fake E_{T}^{miss}). The total thickness of the electromagnetic calorimeter is about 22 radiation lengths

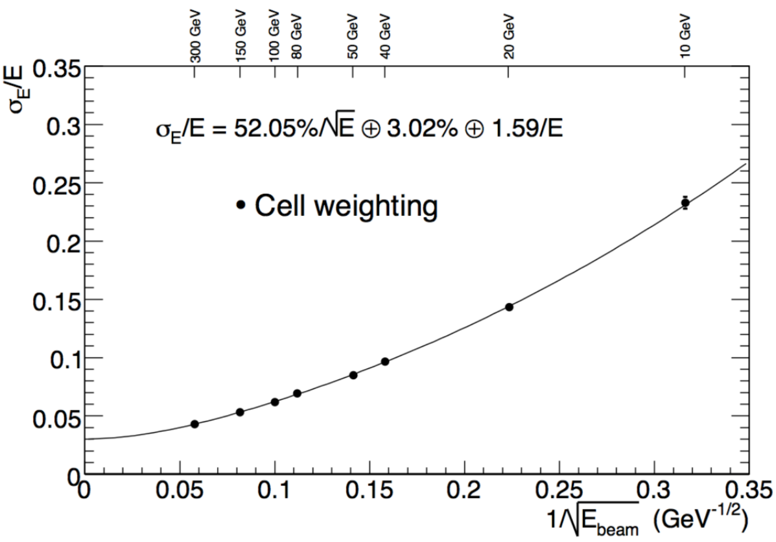

Figure 2.9: Fractional energy resolution measured using pions as a function of the inverse square root of the beam energy, for the combined ATLAS electromagnetic and hadronic calorimeters at $|\eta| = 0.25$. [52]. The energy E in the formula is expressed in GeV.

(X_0) in the barrel and about $24X_0$ in the end-caps. The total thickness of the calorimeter system is above 11 interaction lengths (λ) and has been shown to be sufficient to reduce particle leakage in the muon spectrometer below the irreducible level of prompt or decay muons.

Electromagnetic calorimeter

The LAr electromagnetic calorimeter is divided into a barrel part and two end-cap components. The barrel calorimeter consists of two identical half-barrels, separated by a small gap at z = 0.

The electromagnetic calorimeter is a lead-LAr detector with accordion-shaped electrodes and lead absorber plates over its full coverage. The liquid argon has been chosen for its intrinsic linear behaviour, its stability of response over time and its intrinsic radiation-hardness. The calorimeter is segmented into layers to observe the longitudinal development of the showers and determine their direction. Over the region devoted to precision physics ($|\eta| < 2.5$, corresponding to the ID coverage), it is segmented into three sections in depth, while in the higher η region ($2.5 < |\eta| < 3.2$) it is segmented into two sections.

In the precision measurement region, an accurate position measurement is obtained by finely segmenting the first layer in η. The direction of photons is determined by the position of the energy cluster in the first and the second layers. The first layer consists of fine-grained strips segmented in the η-direction with a coarser granularity in ϕ. The second layer collects the largest fraction of the energy of the electromagnetic shower, while the third layer collects only the tail of the electromagnetic shower and it is, therefore, less segmented in η. In the region of $|\eta| < 1.8$, a presampler detector is used to correct for the energy lost by electrons and photons upstream of the calorimeter. The three LAr layers are visible in Figure 2.10.

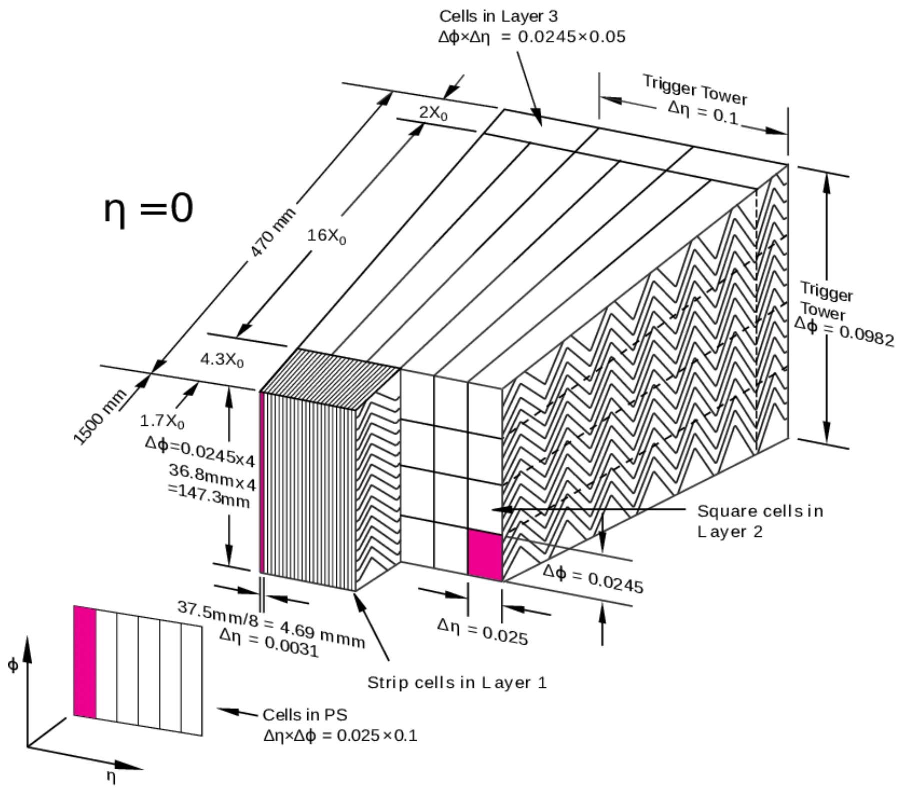

Figure 2.10: Sketch of the lateral and longitudinal segmentation of the ATLAS electromagnetic calorimeter around $\eta = 0$. The different layers are visible and the granularity in η and ϕ of the cells of each of the three layers is also shown [53].

Hadronic calorimeter

TileCal is the central hadronic calorimeter. It is placed directly outside the electromagnetic calorimeter envelope and is divided into a barrel section, which covers the region $|\eta| < 1.0$, and two extended barrels, which cover the range $0.8 < |\eta| < 1.7$. It is a sampling calorimeter using steel as the absorber and

scintillating tiles as the active material. This choice maximises the depth while minimizing the cost.
The Hadronic End-cap Calorimeter (HEC) is a sampling calorimeter as well and consists of two independent wheels per end-cap, located directly behind the end-cap electromagnetic calorimeter. Each wheel is divided into two segments in depth, for a total of four layers per end-cap. The wheels are built from parallel copper plates, interleaved with LAr gaps, providing the active medium. To improve the performance in the transition region between the end-cap and the forward calorimeter (around $|\eta| = 3.1$), the HEC extends out to $|\eta| = 3.2$, overlapping with the forward calorimeter. Similarly, the HEC η range also slightly overlaps the TileCal range ($|\eta| < 1.7$) by extending to $|\eta| = 1.5$.

Forward Calorimeter

The Forward Calorimeter (FCal) is copper-tungsten/liquid-argon detector which consists of three modules in each end-cap: the first, made of copper, is optimised for electromagnetic measurements, while the other two, made of tungsten, measure predominantly the energy of hadronic interactions. Each module consists of a metal matrix, with regularly spaced longitudinal channels. The channels are filled with an electrode structure consisting of concentric rods and tubes parallel to the beam axis. The gap between the rod and the tube is filled with LAr, the sensitive medium. The region covered by the Fcal is $3.1 < |\eta| < 4.9$.

2.2.5 Muon system

The ATLAS muon system has two functions: it provides precise measurements of trajectories of muons and it provides fast signals to trigger events containing muon candidates. The system is based on the magnetic deflection of muon tracks in the large superconducting toroid magnets. It is instrumented with a hybrid system of tracking chambers that provides fast information for trigger implementation, and high precision measurement for high-resolution tracking. A schematic view of the muon system is shown in Figure 2.11.
Since most muons pass the ID and the calorimeters without decaying or being absorbed, they can be measured in the outer part of the detector. The muon spectrometer is therefore placed around the calorimeter. The toroid system, described in Section 2.2.2, generates strong bending power in age volume within a light and open structure. Multiple-scattering effects are thereby minimised, and excellent muon momentum resolution is achieved by three layers of high precision

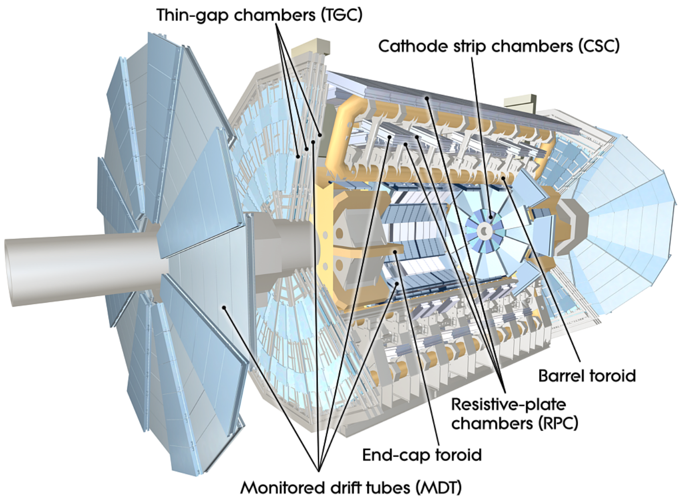

Figure 2.11: Cut-away view of the ATLAS muon system [32].

tracking chambers.

The performance goal of the muon system is a transverse momentum resolution of approximately 10% for 1 TeV tracks, which translates into a sagitta along the z (beam) axis of about 500 μm, to be measured with a resolution of ≤50 μm [32].

In the barrel region tracks are measured in chambers arranged in three cylindrical concentric layers around the beam axis; at radii of approximately 5 m, 7.5 m, and 10 m. The intermediate layer of chambers is placed inside the magnet structure, allowing the measurement of the muons at the inner field boundary, inside the field volume and at the outermost field boundary. In the end-cap regions, the chambers form four large wheels and are installed in planes perpendicular to the beam, located at distances of $|z| \simeq 7$ m, 11 m, 14 m, and 21 m from the interaction point. The inner chamber is placed before the barrel toroid and the two outer wheels after it.

Over most of the η-range, a precision measurement of the track coordinates is provided by Monitored Drift Tubes. These chambers consist of three to eight layers of drift tubes. They cover the pseudorapidity range $|\eta| < 2.7$, except in the innermost end-cap layer where their coverage is limited to $|\eta| < 2.0$. The Monitored Drift Tubes achieve an average resolution of about 35 μm per chamber.

At large pseudorapidities, $2 < |\eta| < 2.7$, Cathode Strip Chambers (CSC) are used in the innermost tracking layer due to their higher rate capability and time resolution. The CSC are multiwire proportional chambers with cathode planes segmented into strips in orthogonal directions.

The muons can be reconstructed either from the ID, the muon spectrometer (MS), or a combination of the two. The resolution of the muon tracks reconstructed with the ID and with the muon spectrometer are shown in Figure 2.12. While the

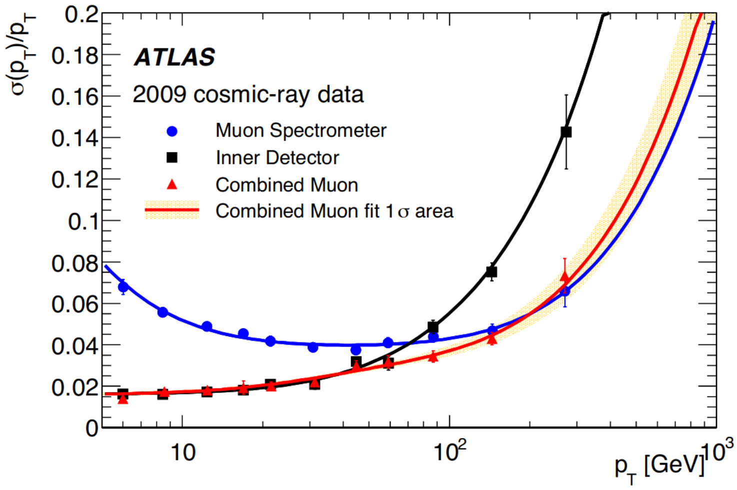

Figure 2.12: Resolution on relative p_T as a function of p_T muon tracks reconstructed using the ID information (black squares), muon tracks reconstructed using muon spectrometer information (blue triangles) and muon reconstructed combining the information from both subdetectors (red triangles) [54].

resolution at low p_T is dominated by the ID (black dots) the muon spectrometer, placed at large distance from the interaction point, dominates the resolution at high p_T. In the intermediate region, for p_T from about 50 to 150 GeV, both systems are required to reach the best resolution. The relative p_T resolution for the particles reconstructed in a tracker can be parameterized as follows

$$\frac{\sigma(p_T)}{p_T} = \frac{r_0}{p_T} \oplus r_1 \oplus r_2 \cdot p_T$$

where the first term accounts mainly for fluctuations of the energy loss in the traversed material, the second term accounts predominantly for multiple scattering and the third term describes intrinsic resolution effects caused by the spatial resolution of the hit measurements and by residual misalignment of the muon spectrometer [55]. As the energy loss in the ID is negligible, the r_0 therm can be neglected for the fit of the tracks reconstructed with the ID. The fit results for the multiple scattering term and the intrinsic resolution term for the tracks reconstructed with the ID, muon spectrometer and a combination of the two are shown in Table 2.2. For the combined tracks the multiple scattering term is determined mainly by the ID contribution, while the intrinsic high-energy resolution largely comes from the muon spectrometer measurement.
As mentioned the muon system also provides trigger signals. The muon trigger

Fitted resolution	r_1	r_2
Inner Detector	$1.6 \pm 0.1\%$	$(53 \pm 2) \times 10^{-5}$ GeV^{-1}
Muon Spectrometer	$3.8 \pm 0.1\%$	$(20 \pm 3) \times 10^{-5}$ GeV^{-1}
Combined Muon	$1.6 \pm 0.1\%$	$(23 \pm 3) \times 10^{-5}$ GeV^{-1}

Table 2.2: Fitted values of the multiple scattering and intrinsic momentum resolution terms for muons reconstructed with the ID, muon spectrometer and a combination of the information from the two subdetectors [54].

system covers the pseudorapidity range $|\eta| < 2.4$. Since the collection time of MDTs is low (maximum drift time is about 700 ns) they cannot be used for the trigger system. Faster Resistive Plate Chambers (RPC) have been chosen instead to trigger the muons in the barrel region ($|\eta| < 1$), while Thin Gap Chambers (TGC) are used in the end-cap regions ($1 < |\eta| < 2.4$). This system of fast trigger chambers is capable of delivering track information within a few tens of nanoseconds after the passage of the particle.

2.2.6 Data Acquisition and Trigger

The bunches in the LHC cross every 25 ns, at a rate of 40 MHz. However, only a small fraction of the collision events contain physics processes that are of interest for the physics analyses. In general, processes interesting for physics analysis have cross-sections many orders of magnitude smaller than the common multi-jet QCD production. As an example the Higgs boson production cross-section is ~ 50 pb while the total proton-proton cross-section is about 10^{11} pb [56]. Bandwidth and data storage are limited and it is therefore necessary to implement an efficient triggering system able to reject large part of the events. Such a system performs a decision of whether an event seems interesting enough to be recorded or not and it reduces the event rate from 40 MHz to about 1 kHz. An important feature of the trigger system is that trigger algorithms should cover all relevant physics scenarios, and it must be ensured that the trigger does not introduce any kind of bias. A non-trivial balance has then to be found between the physics coverage and the rate.

The ATLAS trigger system is organised into two levels: a hardware-based first-Level trigger (L1) and a software-based High-Level Trigger (HLT) implemented on standard CPUs [57]. The L1 trigger, using input from the calorimeters and the muon system, reduces the event rate from about 40 MHz to about 100 kHz, providing a decision within 2.5 μs. While the L1 trigger performs the decision,

all detector information is stored in temporary pipeline memories. To achieve the required speed the decision is purely hardware-based, using custom-built electronics. The Central Trigger Processor (CTP) combines information provided by the calorimeter and the muon chambers to identify interesting events, searching for signatures such as large electromagnetic energy deposits or high-p_T muon tracks. If the event is accepted at L1, Regions Of Interest (ROIs) are built around relevant objects identified by the CTP and are communicated to the second level of the trigger. This information allows the HLT to narrow data requests to areas of the detector where L1 has identified interesting objects. The second level of the trigger, the HLT, is software-based and exploits algorithms very close to offline algorithms, which allows reducing the output rate to about 1kHz.
The trigger selection requirements for every step are combined into trigger chains. The trigger chains are collected in the so-called *trigger menu*, defining which triggers are applied. In some cases, triggers that would lead to very large rates, but are needed e.g. for calibration and validation purposes, are pre-scaled. This means that only a randomly selected fraction of the triggered events are recorded.

2.2.7 Fast Tracker

During Run 2 data-taking the accelerator performances steadily increased, and the experiments operating at the LHC faced more and more challenging data-taking conditions. A critical parameter for the experiments is the mean number of interactions per bunch crossing. As shown in Figure 2.2b, this parameter has reached a maximum of ≈ 60 interactions per bunch crossing during Run 2. During the next data-taking phase, foreseen for 2021 (Run 3), the luminosity will be levelled at or above pile-up of 60. Track-based trigger selection is fundamental for selecting events with good purity and efficiency. At the same time, high pile-up constitutes a major combinatorial challenge to tracking, which is currently limited by available CPU resources. This challenge has been addressed in ATLAS by designing the FTK system. FTK is a track processor designed to provide full event track reconstruction at the HTL input at 100 kHZ with a latency of about 200 μs.
The FTK system is being installed, and it will be fully integrated into the ATLAS trigger during the shutdown period in 2019-2020. A schematic diagram of the trigger, including the FTK system, is shown in Figure 2.13. The information from the tracking detectors is presently exploited in the HLT only for a subset of the events or for limited detector regions (ROIs) due to timing limitations. The FTK system will process data from the ID for the full event and it will perform tracking for all events accepted by L1 [58].
The key idea the FTK system is based on is to calculate all possible track-patterns

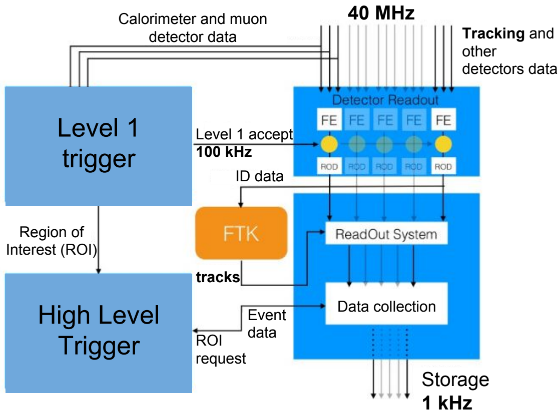

Figure 2.13: ATLAS trigger diagram including the FTK system.

with simulation and store them in dedicated memories of the system. Track reconstruction is accomplished by comparing the ID hits as they are readout with the expected hits from the stored track-patterns. Every time all the hits for track-pattern are found this track is considered as reconstructed. The comparison is performed using a dedicated content addressable memory chip, the associative memory, and using high-performance Field Programmable Gate Arrays to provide the needed computing power. More details on the operating principle of the FTK system and on its structure are described in Appendix A.
The FTK system is designed to provide full-event reconstruction of all tracks with $p_T > 1$ GeV with resolutions close to those found by offline track reconstruction. Extensive use of FTK tracking, including vertexing using those tracks, will be exploited by HLT algorithms to improve the identification of physics objects such as b-jets and τ leptons [59]. Information from tracks provided by the FTK system will also improve secondary vertex identification and help to mitigate the effects of the pile-up. It will as well allow the use of looser HLT jet thresholds and therefore help to refine the missing transverse momentum. The system will allow the design of new trigger algorithms specific for analysis channels using objects that will be better identified with FTK, such as $hh \to b\bar{b}b\bar{b}$, fundamental channel to study the Higgs boson self-coupling at the LHC.

At the time this thesis was written the FTK project was under installation. Unfortunately, meanwhile, the ATLAS collaboration decided to close the project for a number of reasons, mainly related to funding of US institutes participating in the project.

Chapter 3

Analysis overview

In this chapter, a synthetic description of the whole analysis is given to introduce the reader to the complete strategy to measure the signal cross-section and to define limits to BSM effects. All the details of the analysis are deferred to later sections.

3.1 $VH(H \to b\bar{b})$ search

As mentioned in Chapter 1 the most promising production mode to measure the $H \to b\bar{b}$ decay is the associated production of the Higgs boson with a vector boson V, exploiting the V leptonic decays. Event topologies characteristic of these processes, $ZH \to \nu\nu b\bar{b}$, $WH \to \ell\nu b\bar{b}$ and $ZH \to \ell\ell b\bar{b}$, contain zero, one or two charged leptons from the V boson decay and jets from the Higgs boson decay. The event selection aims therefore at choosing events containing a candidate Higgs boson associated with a candidate V boson.

In this thesis, two $VH(H \to b\bar{b})$ searches are described and indicated as *resolved* and *merged* analysis. Both analyses aim at measuring the $VH(H \to b\bar{b})$ cross-section, but with some differences briefly summarised here. In the *resolved* analysis, the candidate Higgs boson is reconstructed through two b-tagged jets of radius $R = 0.4$ (small-R jets). This reconstruction method is efficient up to a value of the Higgs boson transverse momentum of about ~ 500 GeV, but for higher energies the requirement of detecting two separate jets is responsible for a drop in efficiency. As high energy events are crucial to gain information on possible scenarios Beyond the Standard Model, a so-called *merged* analysis has been developed. Such analysis is optimised to select very high energy events, reconstructing the Higgs boson candidate through a single jet of radius $R = 1.0$ (large-R jets).

Even if the *resolved* and the *merged* analyses differ in the event selection and in the variables used to extract the cross-section, the general strategy described in this section applies to both cases and is schematically shown in Figure 3.1.

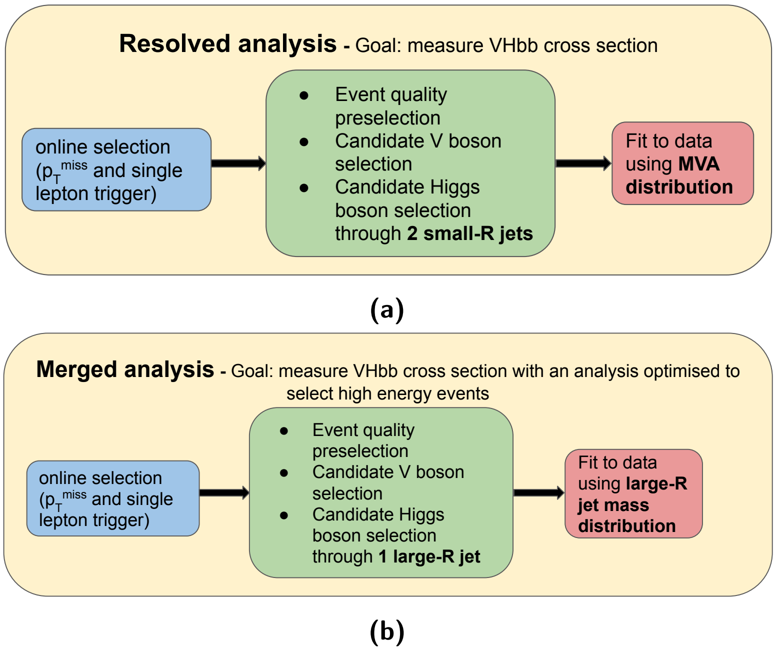

Figure 3.1: Schematic summary of the steps necessary to measure the cross-section in the *resolved* (a) and *merged* (b) analyses.

The first step to select $VH(H \to b\bar{b})$ events, shown in blue in Figure 3.1, is the online event selection. It exploits the signature given by the vector boson leptonic decays, and relies either on the missing transverse momentum or on the single-charged-lepton triggers. A more detailed description of the triggers used to select the events is presented in Chapter 4.
The second step is the offline event selection, shown in green in Figure 3.1, which is performed using physics objects (electrons, muons, jets...) reconstructed from the detector signals. In Chapter 5 the methods applied to reconstruct the physics objects are presented. Such objects are used to reconstruct the candidate Higgs boson, as described above, and the candidate V boson. The selection of the candidate V boson is the same for the *resolved* and *merged* analysis, but it differs significantly depending on the selected V decay mode ($Z \to \nu\bar{\nu}$, $W \to \ell\nu$ or $Z \to ll$). For this reason, events are categorised in the 0-, 1- and 2-lepton channels, based on the number of charged leptons (electrons or muons), to explore the $ZH \to \nu\nu b\bar{b}$, $WH \to \ell\nu b\bar{b}$ and $ZH \to \ell\ell b\bar{b}$ signatures, respectively. In the 2-lepton channel the V boson is simply represented by the two charged leptons system, while it requires the use of the E_{T}^{miss} for the 1-lepton ($p_{\mathrm{T}}^{V} = E_{\mathrm{T}}^{miss}$ + lepton) and

0-lepton channels ($p_{\mathrm{T}}^{V} = E_{\mathrm{T}}^{miss}$).

As the signal cross-section is much smaller than the background cross-section the sensitivity is optimized with a twofold strategy. On one side, an offline event selection is applied to reject phase space regions with large background and null or negligible signal thus improving the total signal to background ratio. Secondly, events passing this selection are divided in several categories with different signal to background ratios. The second step, indicated in the following with *categorization*, allows improving the sensitivity exploiting at best the complete phase space sensitive to the signal. The complete event selection and categorization is described in Chapter 6. The large-R jet mass distribution after having applied the *merged* event selection, in the 1-lepton channel, is shown in Figure 3.2 to give an example of agreement between data and prediction. The selected data are drawn as black dots,

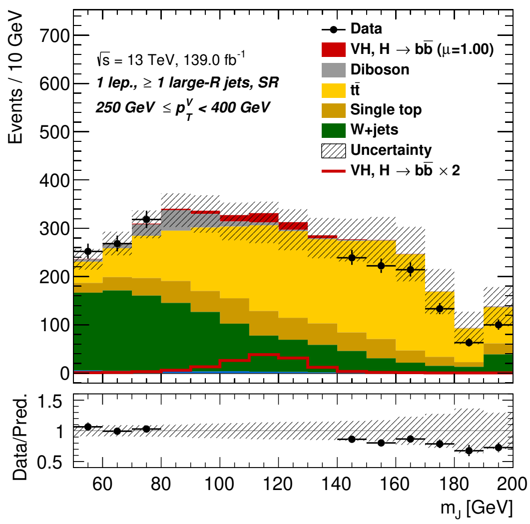

Figure 3.2: Large-R jet mass distribution, m_J, in the 1-lepton channel of the *merged* analysis, for data and simulated events. Data between 80 GeV and 140 GeV are not shown. For the events shown the vector boson transverse momentum is between 250 GeV and 400 GeV.

except for the region between 80 GeV and 140 GeV where they are not shown, as the analysis is still blinded. The simulated distributions for the signal and background processes are shown as coloured filled histograms.

All the selected data and simulated events are used in the fit to extract the cross-section, as schematised in the red box in Figure 3.1. The measured cross-section is obtained by performing a binned maximum-likelihood fit to data using templates based on the simulations. As shown for example in Figure 3.2, the signal events represent a small fraction of all the selected events. In order to measure the signal cross-section, it is therefore important to choose a fit variable that provides good separation between signal and background events. The fit relies in fact on these shape differences to extract the signal cross-section. The shapes used in the fit for the different signal and background processes are obtained from the simulations or from data-driven methods, as described in Chapter 4.

The candidate Higgs mass distribution is expected to be a good discriminant both for the *resolved* and the *merged* selection. It is represented by the two b-jets invariant mass, m_{bb}, for the *resolved* analysis, and by the large-R jet mass, m_{J}, for the *merged* analysis. m_{J} is in fact chosen as discriminating variable in the fit for the *merged* analysis. The m_{J} shapes of the simulated events for the signal and for the main background processes are shown in Figure 3.3.

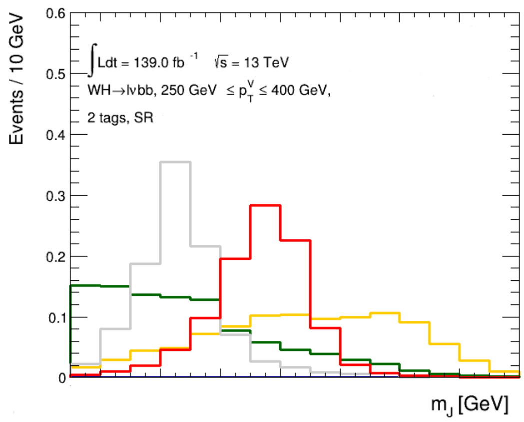

Figure 3.3: Simulation of the shape of the signal processes and of the main background processes for the large-R jet mass distribution. The signal is drawn in red, the $t\bar{t}$ background in yellow, the diboson background in grey and the W+jets background in green. All the histograms are normalised to unit area.

All the histograms in the figure are normalised to the same area, to highlight the shape comparison. The simulated shape of the signal for the m_{J} variable peaks at the value of the Higgs mass, differently from the shape of the main background processes, allowing to extract the signal cross-section.

After having applied the event selection the overall signal over background ratio is still small, it is therefore crucial to carefully control the background processes. The *control regions* are categories especially defined, and included in the fit, to evaluate the contributions of the dominant background processes. The event selection in the control regions is as close as possible to the signal selection, with small selection differences aimed at enriching the fraction of events for a specific background.

All the signal regions (SRs) and the control regions (CRs) are fitted at the same time. There is no fundamental difference between the *signal regions* and the control regions. The first ones are enriched in signal events while the second ones are designed to be enriched in a specific background process, but they are all treated in exactly the same way in the fit procedure. One of the control regions for the

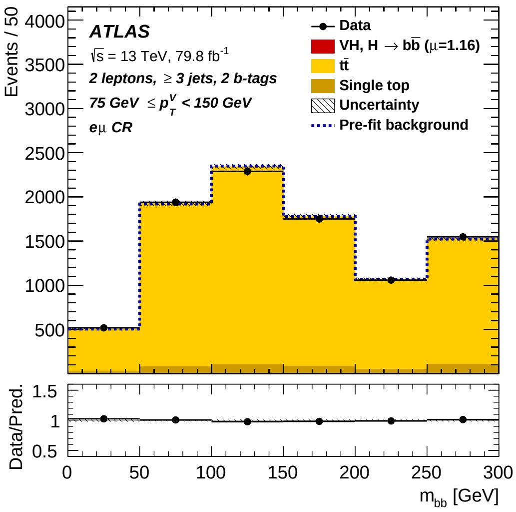

Figure 3.4: Distribution of the m_{bb} variable in one of the control regions. Shown are the data (points with error bars) and expectation (histograms) [60].

resolved analysis is shown in Figure 3.4. In this case, the selection is designed to have a region enriched in $t\bar{t}$ events by requiring events with one electron and one muon. The $t\bar{t}$ normalisation would have a large uncertainty if only SRs were included in the fit. By using this CR in the fit, one can extract precious information for the description of the $t\bar{t}$ background in the SR, and, as a consequence, it is possible to improve the precision in the measurement of the VH signal.

Finally the distributions of the discriminant variables in all the SRs and CRs are used for the fit. The binned maximum likelihood fit extracts the measurement of the signal strength (μ), a parameter which scale the SM predicted simulated template. E.g. a measured value of $\mu = 0$ correspond to complete absence of measured signal while a value of $\mu = 1$ correspond to a measured signal normalisation identical to the predicted SM signal.
The measured signal strength is then exploited to extract the measured cross section, following:

$$(\sigma \cdot BR(H \to b\bar{b}))_{\text{measured}} = \mu \cdot (\sigma \cdot BR(H \to b\bar{b}))_{\text{expected (SM)}}$$

where $(\sigma \cdot BR(H \to b\bar{b}))_{\text{measured}}$ is the measured $VH(H \to b\bar{b})$ cross-section times branching ratio and $(\sigma \cdot BR(H \to b\bar{b}))_{\text{expected (SM)}}$ is the predicted SM cross-section times branching ratio. More details about the statistical treatment used both for the *resolved* and the *merged* analyses are given in Chapter 7, while the description of the systematic uncertainties on the shape and normalization of the templates are included in Chapter 8. The results of the cross-section measurement are presented in Chapter 9 for the *resolved* analysis and in Chapter 10 for the *merged* analysis.

Using the candidate Higgs boson mass distribution is the simplest way to discriminate between the signal and background processes. However, other kinematic variables, such as the vector boson transverse momentum and the jet multiplicity, carry useful discriminating information. For the *resolved* analysis, which is the more advanced analysis, several kinematic variables are exploited to construct a multivariate discriminant [16] to be used in the final fit. This allows optimizing the sensitivity to the signal. The distribution of the candidate Higgs boson mass (m_{bb}) for the *resolved* analysis is shown in Figure 3.5 together with the BDT distribution in one of the 1-lepton categories, as an example. The simulated signal events,

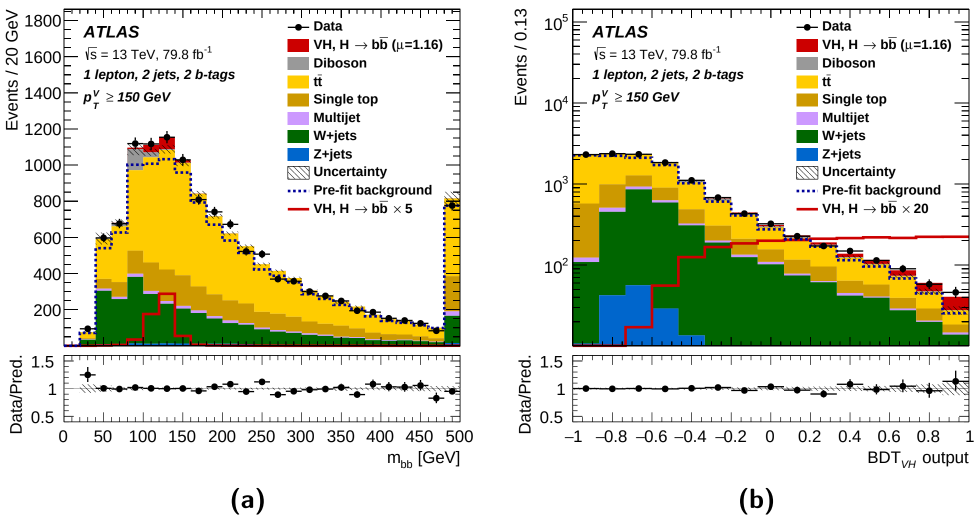

Figure 3.5: Distribution of the m_{bb} (a) and the BDT (b) variable. The distributions refer to one signal region of the 1-lepton channel. Shown are the data (points with error bars) and expectation (histograms). The background contributions and the Higgs boson signal are shown as filled histograms [60].

shown in red, are clearly visible in both distributions: close to the Higgs boson mass for the m_{bb} distribution and close to 1 for the BDT. However, while for the m_{bb} distribution also other background processes have a shape peaking close to the Higgs boson mass, in the BDT distribution the signal simulated shape is peaking in a region where the background shape is smoother. The BDT distribution for the background processes has in fact a peak close to -1, resulting in a higher signal sensitivity in the fit.

3.2 Simplified Template Cross Sections and BSM physics

As already mentioned in Chapter 1, the STXS framework is an evolution of the standard signal strength measurement. The reasons for adopting such framework have already been described and can be summarised stating that it allows to increase the experimental sensitivity and isolate possible BSM effects. The general strategy for the fit procedure, followed to perform the cross-section measurement in the STXS framework, and to extract information on BSM physics, is given in this section. Details are deferred to Chapter 7.
In the STXS measurement the event selection, event categorisation and background modelling are unchanged with respect to the standard signal strength measurement described above. The main difference lays in the treatment of the simulated signal, which is split into mutually exclusive phase space regions. Therefore, each template adopted to describe a signal process (as the one shown in Figure 3.3) is split into several templates. An important point to stress is that the splitting of the STXS bins is done at truth level while the analysis categories are defined at the reconstructed level. Splitting at truth level allows having a direct measurement of the cross-sections, with no unfolding procedure. The level of coherence between the STXS regions and the reconstructed categories of the analysis needs to be checked to ensure that there are no large migrations (e.g. events in the 1-lepton channel at truth level ending up in the 0-lepton channel at reconstructed level).

The fit procedure adopted in the STXS framework for measuring the cross-section is almost identical to the procedure adopted for the $VH(H \to b\bar{b})$ search. However, instead of extracting only one parameter of interest from the fit (the signal strength), there is one parameter of interest for each STXS bin. The ability of the fit to discriminate between the signal from the different phase space regions arises in part from the analysis categorisation at reconstructed level, which largely match the STXS categorisations, and partially (in the *resolved* analysis) from the shape differences between the BDT distributions of the signal from different phase space regions.

The STXS framework is ideal to explore possible BSM effects, which can be interpreted using the EFT formalism introduced in Chapter 1. In EFT the SM Lagrangian is extended to include terms describing possible BSM effects. The presence of these extra terms in Nature could modify the production cross-sections, the branching ratios, and the kinematic distributions of the signal events. Set of equations have been developed to describe the deviation of the STXS expectations as a function of the parameters used in the EFT. In order to extract information on

BSM physics, each STXS parameter of interest is substituted in the likelihood by the specific set of equations derived from the EFT equations. The fit will therefore directly result in a measurement of the EFT parameters.

The measurement performed so far in the STXS framework have been carried out reinterpreting the *resolved* analysis that has been developed for the $VH(H \to b\bar{b})$ search. The results for this measurement are presented in Chapter 9. Given the high sensitivity to BSM deviations of high energy events, the possibility to select events at even higher energy has been studied. This was the main reason to push towards the development of the *merged* analysis, optimised to select very high energy events. STXS measurement using the *merged* analysis are foreseen as the next step and preliminary performance are presented in this thesis in Chapter 10. Exploiting the *merged* analysis, or a combination of events selected with the *resolved* and *merged* analyses, will result in increased information on the EFT parameters.

Chapter 4

Dataset and simulated event samples

In this chapter details are given on the dataset used and on the trigger strategy followed to select the events. The signal and background processes contributing to the selected events are described as well, together with the Monte Carlo generators and the simulated events used.

4.1 Dataset and triggers

The data used in this thesis correspond to proton-proton collisions [36] collected at $\sqrt{s} = 13$ TeV during 2015-2018. The *merged* analysis exploits the full Run 2 dataset with an integrated luminosity of 139 fb^{-1}, while the *resolved* analysis used for the $H \to b\bar{b}$ observation and its reinterpretation within the STXS framework is based on the 79.8 fb^{-1} data sample collected between 2015 and 2017.
As mentioned in Chapter 3, events are categorised in the 0-lepton, 1-lepton and 2-lepton channels, aiming at selecting $ZH \to \nu\nu b\bar{b}$, $WH \to \ell\nu b\bar{b}$ and $ZH \to \ell\ell b\bar{b}$ events. The trigger used to select such events exploits the signatures from the leptonic decay of V boson and thus it varies depending on the leptonic channel, as described in the three following sections.
The events used in the data analyses are required to belong to a list named *Good Run List* (GRL), where all the recorded *luminosity blocks* (introduced in Section 2.1) not affected by relevant detector problems are registered. Luminosity blocks which are not listed in the GRL are not used, ensuring the good quality of the dataset.

4.1.1 0-lepton channel triggers

As in the 0-lepton channel signal events are characterised by the Z boson decay into two neutrinos, events were recorded with missing transverse momentum triggers (E_{T}^{miss} triggers). The trigger threshold was increased from 70 GeV to 110 GeV between the 2015 and 2018 data-taking periods [61, 62, 63]. This choice allowed coping with the increasing level of pile-up, strongly affecting the rate of E_{T}^{miss} triggers.
The turn-on efficiency curves for the E_{T}^{miss} triggers used in 2016 and 2017 are shown in Figure 4.1a as an example. The efficiency is computed as the fraction of events

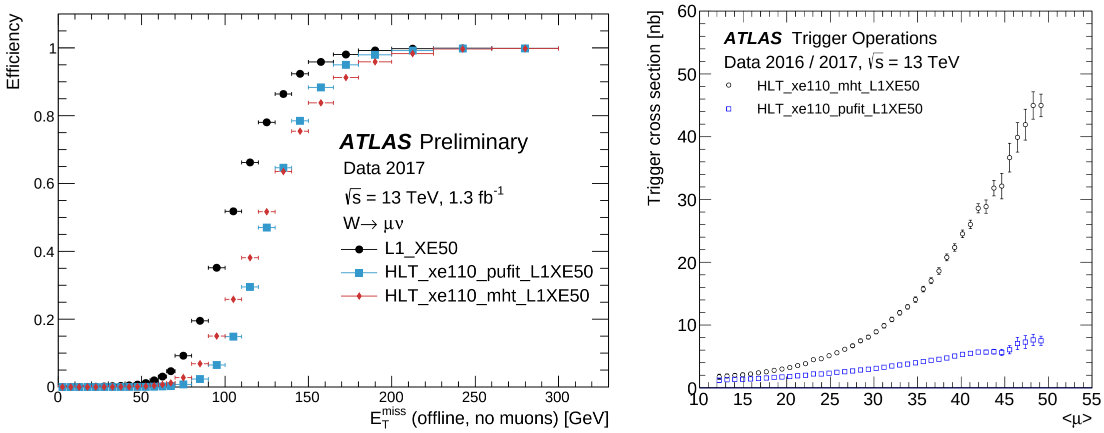

(a) (b)

Figure 4.1: E_{T}^{miss} trigger efficiency turn-on curves (left) and trigger cross-section (trigger rates normalised to the instantaneous luminosity) as a function of the average number of interactions per bunch crossing (right) for E_{T}^{miss} trigger using the MHT or *pufit* algorithms. All triggers also require the E_{T}^{miss} calculated at L1 to exceed 50 GeV. The efficiencies are evaluated in an event sample passing a loose $W \to \mu\nu$ selection [61].

passing the E_{T}^{miss} trigger as a function of the offline E_{T}^{miss}. The efficiencies are evaluated on a sample of data recorded by the muon triggers and passing a loose $W \to \mu\nu$ selection, to provide a sample enriched in real E_{T}^{miss}. The efficiencies are shown as a function of a modified offline E_{T}^{miss} calculation with no muon correction, emulating the calorimeter-only E_{T}^{miss} calculation used in the trigger.
Due to the poor online E_{T}^{miss} resolution, the efficiency as a function of the offline reconstructed E_{T}^{miss} grows slowly. Figure 4.1a shows that for a trigger E_{T}^{miss} threshold of 110 GeV the efficiency curve reaches 100% efficiency for $E_{\mathrm{T}}^{miss} > 180$ GeV.
The two colored curves shown in Figure 4.1a allow comparing the trigger efficiencies obtained with the missing H_T (MHT) and *pufit* algorithms. The MHT algorithm, used in 2016, calculates E_{T}^{miss} as the negative vector sum of the transverse energy

of calibrated $R = 0.4$ anti-k_t jets. The pufit algorithm, used in 2017 and 2018, is designed to disentangle calorimeter deposits from the hard-scatter from those originating from pile-up interactions. This is done by grouping towers made out of topological clusters into a pile-up and a hard-scatter category. The pile-up dependence of the two algorithms is shown in Figure 4.1b on the right. Observing the two curves it is clear that the E_{T}^{miss} rate is strongly affected by the number of collisions per bunch crossing. In fact, each proton-proton collision adds to the total energy deposited in the calorimeter, and cause increasing fluctuations in the calorimeter response [64]. These resolution effects lead to a strong increase in the trigger rate with rising pile-up. For this reason the *pufit* has been used as the baseline E_{T}^{miss} trigger starting in 2017, as it has a slightly sharper efficiency turn-on curve while yielding a much smaller rate and a smaller dependence on the pile-up.
The trigger efficiency compared to the offline *merged* selection is 85–90% efficient at $E_{\mathrm{T}}^{miss} = 150$ GeV and fully efficient above 180 GeV. The E_{T}^{miss} trigger efficiencies are computed both for data and for simulated events. The scale factors extracted from the ratio of these efficiencies, as a function of E_{T}^{miss}, are used to correct for the differences between the data and the simulations. An uncertainty on these scale factors, which is about 2%, is propagated in the analyses.

4.1.2 1-lepton channel triggers

In the 1-lepton channel, in order to select $W \to e\nu$ and $W \to \mu\nu$ events, different triggers are used for the electron and muon decays. In the 1-lepton electron sub-channel, aiming at selecting $W \to e\nu$ events, the lowest-p_T threshold un-prescaled single electron triggers are used. These triggers apply loose isolation and identification requirements that are tighter at the analysis level. The nominal p_T threshold was 24 GeV in 2015 and increased to 26 GeV in 2016, 2017 and 2018 [61, 62, 63]. The efficiencies of the trigger algorithms used in 2015 and in 2016-2018 are shown in Figure 4.2. The trigger used is a combination of all the lowest un-prescaled single electron triggers (e.g. the logical OR between an online cut $p_T > 26$ GeV with a tight identification criteria and an online cut $p_T > 60$ GeV and a medium identification criteria). The efficiency is determined using the tag-and-probe method selecting $Z \to ee$ events. The highest trigger efficiency was obtained in 2015 since no online isolation was required and the identification criteria were looser. The inefficiency observed in 2016 is due to too stringent online identification criteria. The efficiency improvements in 2017-2018 are obtained thanks to the implementation of more effective online algorithms better matched to the offline selection.

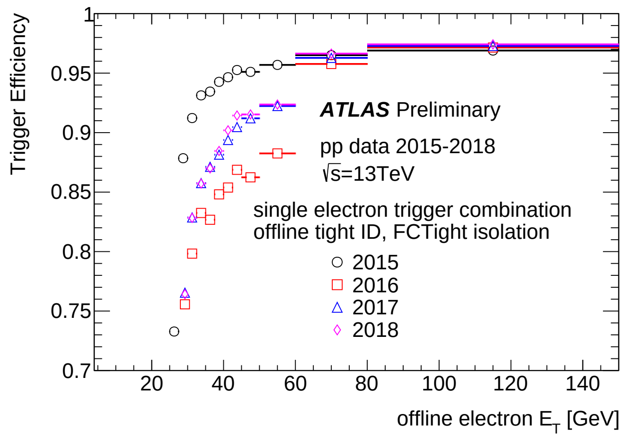

Figure 4.2: Efficiency of the lowest un-prescaled single electron trigger combination in 2015 and 2016-2018 data. The efficiency is given as a function of the offline electron transverse energy, where the offline electron fulfils a tight offline identification requirement as well as a tight offline isolation requirement.

In the 1-lepton muon sub-channel events are recorded using the same E_{T}^{miss} triggers used for the 0-lepton channel. This choice is motivated by the low muon trigger efficiency both for $|\eta|$ >2.4, due to the TGC coverage, and some gaps needed for the inner detector services. On the other hand, E_{T}^{miss} triggers effectively select muon events since muons, differently from electrons, are not included in the online E_{T}^{miss} calculation. The E_{T}^{miss} trigger provides a 98% efficiency for the signal passing the offline *resolved* selection, compared to a $\sim$ 80% efficiency for the combination of single-muon triggers. This high acceptance is obtained thanks to the requirement $p_{\mathrm{T}}^{V} > 150$ GeV, where p_{T}^{V} is computed from the muon transverse momentum and the E_{T}^{miss} vector. As the trigger is in effect selecting events based on p_{T}^{V}, it is fully efficient for values of p_{T}^{V} above 180 GeV and rather highly efficient also for $150 < p_{\mathrm{T}}^{V} < 180$ GeV.

4.1.3 2-lepton channel triggers

In the 2-lepton channel, events are recorded using the lowest-p_T threshold un-prescaled single electron and muon triggers. Similarly to the electron trigger, the muon trigger includes isolation and identification requirements looser than those applied offline. In the muon sub-channel, the lowest p_T threshold increased from 2015 to 2018, ranging from 20 GeV to 26 GeV. The muon momentum resolution in the trigger system is sufficiently good that the trigger is fully efficient for reconstructed muons with offline p_T at least one GeV higher than the nominal online threshold. The trigger efficiency with respect to the offline *resolved* selection depends on the p_{T}^{V} region and is $\sim 98\%$ for the electron sub-channel of $\sim 87\% - 90\%$ for the muon sub-channel. It has been decided to not use di-lepton triggers as it has been found that the signal gain acceptance from adding such items in the logical OR of single lepton trigger is only around 2%.

4.2 Event simulation

The results obtained in this analysis heavily rely on the ability to describe the expected kinematic distributions with simulated events. The simulated samples are used both to establish the analysis selection criteria and to determine the expected signal and background distributions of the discriminant used in the final fit. Furthermore, simulations allow estimating the systematic uncertainties caused by different sources. All simulated processes used in this thesis are normalised using the most accurate theoretical cross-section predictions currently available and are generated at least at next-to-leading order (NLO) accuracy.
Given the large number of particles produced in hadron collisions, with momenta ranging over several orders of magnitude, the simulation procedure is not trivial. The description of the non-perturbative soft QCD processes is particularly complex and requires a phenomenological approach. Simulated events are obtained with multiple processing including all steps from event generation up to the detector signal simulation. The Monte-Carlo programs and event generators used to implement all the steps are state-of-the-art. The main steps are:

- primary **hard process** generation;
- generation of the **parton showers** associated with the incoming and outgoing coloured participants in the subprocess;
- simulation of the **hadronisation**: to convert the parton showers into outgoing hadrons and connect them to the incoming beam hadrons;
- simulation of the partons non participating to the hard scatter, giving rise to the **underlying event**;
- simulation of the **decays** of unstable particles that do not escape from the detector;
- simulation of the interaction of the particles with the **detector**.

All the simulation steps are schematically shown in Figure 4.3 and briefly summarised in the following. A brief description of the MC event generators used in this analysis is given in Appendix B.

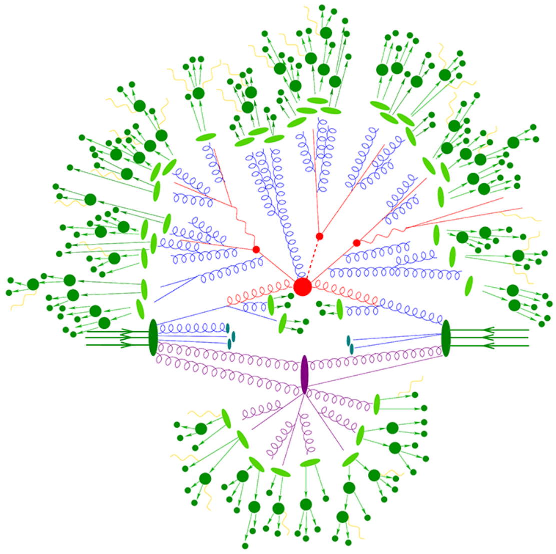

Figure 4.3: Schematic diagram of the main steps of an event simulation [65]. The simulation of the hard process is shown in red, the parton showers are shown with blue lines, the hadrons are shown with light green dots and the decay of the hadrons is represented by dark green arrows and dots. The purple lines represent the simulation of the underlying events.

Hard process simulation

Many LHC processes of interest involve large momentum transfers. The simulation of processes with large momentum transfer named *hard scatter* processes, is thus at the core of simulations of collider events through Monte Carlo event generators. As QCD quanta are asymptotically free, such reactions can be described by perturbation theory, thus allowing to compute many features of such processes. The factorisation formula in Equation 4.1 is employed to calculate cross-sections (σ):

$$\sigma = \sum_{a,b} \int_0^1 \int_0^1 dx_a dx_b \int f_a^{h1}(x_a, \mu_F) f_b^{h2}(x_b, \mu_F) d\hat{\sigma}_{ab\to n}(\mu_F, \mu_R) \tag{4.1}$$

where $f_{a,b}^{h1,h2}h(x_{a,b}, \mu_F)$ are the parton distribution functions (PDFs) of hadrons $h1$ and $h2$, which parametrize the distributions of parton of type a carrying momentum fraction x of a hadron h, when probing the distribution at the factorization scale

μ_F. The factorisation scale marks the transition between the perturbative and non-perturbative regime. $\hat{\sigma}_{ab\to n}$ is the parton-level cross-section for the production of the final state n from the initial partons a and b. This cross-section depends on the momenta given by the final-state phase space, on the factorisation scale μ_F and on the renormalization scale μ_R. The cross-section defined by 4.1 is therefore fully specified only for a given PDF set and a certain choice for the factorization and renormalization scales. Both scales are unphysical and their impact on the result decreases with each additional order of perturbation theory that is taken into account.

Parton shower

What has been described for the hard process simulation is the generation according to lowest-order matrix elements. These can describe the momenta of the outgoing jets well, but to give a complete picture of the process, including the internal structure of the jets and the distributions of accompanying particles, any fixed order is not sufficient. The effect the higher orders can be approximated through a *parton shower* algorithm. The partons involved in the hard process are coloured particles, quarks and gluons. These partons, scattered from the collision, radiate gluons that can themselves trigger new radiations. The parton shower algorithms describe these processes. The algorithms are typically formulated as an evolution in momentum transfer from the high scales associated with the hard process to the low scales associated with the confinement of the partons into hadrons (~ 1 GeV). At this scale events are simulated with *hadronisation* models.

Hadronisation

As the event is evolved downwards in momentum scales it ultimately reaches the region in which QCD becomes strongly interacting and perturbation theory breaks down. At this scale, the perturbative evolution must be terminated and replaced by a non-perturbative hadronization model. This model describes how coloured partons are confined into colourless hadron. Individual partons do not hadronize independently, but rather colour-connected systems of partons hadronize collectively. As these models are not derived directly from QCD, they have more free parameters than the preceding steps. An important feature is that, to a good approximation, the hadronization of a given coloured system is independent of how that system is produced, so that once tuned on one data set the models are predictive for new collision types or energies.

Decay

Many hadrons that are produced during hadronization are unstable resonances. Sophisticated models are used to simulate their decay to the lighter hadrons that are long-lived enough to be considered stable on the time-scales of particle physics detectors.

Underlying events

The steps described so-far of the hard process, parton shower, hadronisation and decay, are sufficient to describe the final state of the hard process. However, the hard process involves the extraction of coloured partons from each hadron, which are colourless bound states of partons. The hadron remnants, which evolve, hadronise, and can interact with each other, need therefore to be modelled. This part of the event structure is the so-called *underlying events* simulation.

Pile-up

All simulated samples include the effect of pile-up from multiple interactions in the same bunch (in-time pile-up) and neighbouring bunch crossing (out-of-time pile-up). This is achieved by overlaying simulated minimum bias events to the simulated process prior to the conversion of energy deposits to detector signals [66].

Detector simulation

The last step of the MC samples production is the simulation of the interaction between the particles emerging from the proton collisions and the ATLAS detector material. This simulation is based on Geant4 [67] and events are reconstructed with the ATLAS reconstruction software [68]. The ATLAS detectors are modeled in terms of basic shapes with properties (e.g. the material) and a position, named physical volumes. A very detailed description of the detector is crucial for an accurate simulation. The full detector is thus modelled with hundreds of materials and hundreds of thousands of physical volumes. As the detector simulation is quite slower than the event generation it is sometimes convenient to simulate the interaction with the ATLAS detector only for events that are likely to pass the full analysis chain, thus introducing *MC filters* between the generation and simulation steps.

4.3 Signal processes simulation

The VH signals include three main Higgs production modes: $ZH \to \nu\nu b\bar{b}$, $WH \to \ell\nu b\bar{b}$ and $ZH \to \ell\ell b\bar{b}$, where $\ell = e,\ \mu,\ \tau$. The leading order Feynman diagrams for the $ZH \to \nu\nu b\bar{b}$, $WH \to \ell\nu b\bar{b}$ and $ZH \to \ell\ell b\bar{b}$ processes are shown in Figure 4.4. The ZH production modes are furthermore split into two contributions depending

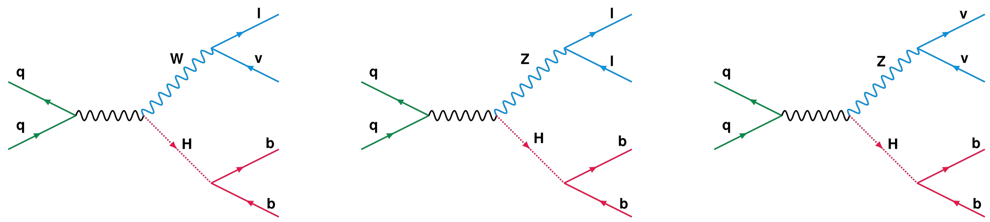

Figure 4.4: Leading order Feynman diagrams for the $ZH \to \nu\nu b\bar{b}$, $WH \to \ell\nu b\bar{b}$ and $ZH \to \ell\ell b\bar{b}$ processes.

on the partonic initial state: $qq \to ZH$ and $gg \to ZH$. Two Feynman diagrams for the $gg \to ZH$ process are shown in Figure 4.5.

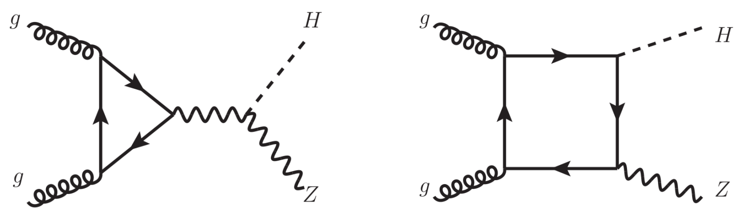

Figure 4.5: Two leading order Feynman diagrams for the $gg \to ZH$ process.

All $q\bar{q}$-initiated production processes are simulated using the `Powheg` generator with the `MiNLO` [69] procedure applied, interfaced to the Pythia 8.212 [70] generator and using the NNPDF3.0 PDF set [71]. The simulation of the $q\bar{q}$-initiated production processes, called $q\bar{q}$-initiated for simplicity, actually also includes qg-initiated events, appearing at NLO. One of the qg-initiated diagrams included in the simulation is shown in Figure 4.6.

The gg-initiated ZH contributions are simulated using the `Powheg` prediction interfaced with Pythia 8.212 for the modelling of parton shower, underlying event and multiple parton interactions and using the NNPDF3.0 PDF [71] for both the matrix-element and the parton shower. The computation of the gg-initiated ZH contribution is in fact currently not available at NLO.
All VH signal processes are listed in Table 4.1, along with the generators used to produce the samples. All samples are normalised to the best theoretical prediction

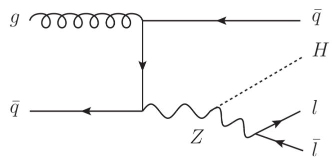

Figure 4.6: One of the qg-initiated Feynman diagrams included in the $qq \to VH$ simulation [69].

Process	Generator
qq-initiated (nominal)	
$qq \to W^+H \to l^+\nu b\bar{b}$	Powheg +MiNLO +Pythia 8
$qq \to W^-H \to l^-\nu b\bar{b}$	Powheg +MiNLO +Pythia 8
$qq \to ZH \to llb\bar{b}$	Powheg +MiNLO +Pythia 8
$qq \to ZH \to llb\bar{b}$	Powheg +MiNLO +Pythia 8
gg-initiated (nominal)	
$gg \to ZH \to llb\bar{b}$	Powheg +Pythia 8
$gg \to ZH \to llb\bar{b}$	Powheg +Pythia 8

Table 4.1: Standard Model VH samples used in the analyses.

of the cross-section for the different processes. All cross-section numbers for WH and ZH are obtained from the *LHC Higgs Cross-Section Working Group* prescriptions for the SM Higgs boson with mass $m_H = 125$ GeV [20, 72]. The inclusive cross-sections are calculated at NNLO in QCD [73, 74] and NLO in EW [75], and are listed, for the various signal processes, in Table 4.2. The listed values do not include the decay branching ratio.

The ZH signal samples are normalised as follows: the $gg \to ZH$ samples use the cross-section calculated from NLO+NNL QCD corrections; the cross-section of the $qq \to ZH$ sample is obtained from the difference between the total ZH production cross-section and the $gg \to ZH$ cross-section. This is done to avoid double counting when merging $qq \to ZH$ and $gg \to ZH$ samples together.

The uncertainties listed in Table 4.2 take into account QCD scale, PDF and α_s uncertainties. These uncertainties are added in quadrature to obtain the uncertainties shown in the table, but are considered as separate contributions in the fit, as is described in Chapter 8.

Process	order	cross-section [pb]
WH	NNLO(QCD)+NLO(EW)	1.37 ± 0.04
W^+H	NNLO(QCD)+NLO(EW)	0.84
W^-H	NNLO(QCD)+NLO(EW)	0.53
ZH	NNLO(QCD)+NLO(EW)	$0.88^{+0.04}_{-0.03}$
$gg \to ZH$	NLO+NNL(QCD)	0.12
$qq \to ZH$		0.76

Table 4.2: Inclusive cross-sections for the signal processes.

4.4 Background processes simulation

4.4.1 Vector boson+jets

The production of V ($V = W$ or Z) bosons in association with jets (V+jets) is one of the main backgrounds for all the lepton channels considered (0-lepton, 1-lepton, 2-lepton). The availability of reliable V+jets MC samples with high statistics is therefore important for these and many other analyses. Efforts have therefore been made by the ATLAS Collaboration to update the simulation of this process to the latest MC generators, including moving from LO to NLO generation [76].
The V+jets processes are simulated with `Sherpa` interfaced with the NNPDFs [77] for both the matrix element calculation and the parton shower tuning. In order to provide a good modelling of events with many jets produced in association with the W or Z boson, `Sherpa` provides a combination of different matrix elements with different parton multiplicities: up to two extra partons are included in the NLO matrix elements, and 3 or 4 extra partons are included at LO in QCD. A list of the V+jets samples used and of the relative cross-sections is given in Table 4.3. A conservative 5% theoretical uncertainty is assigned to the cross-sections [78].

Process	Generator	$\sigma\times$ BR [pb]
$Z \to \nu\nu$	`Sherpa` 2.2.1	1914
$W \to l\nu$	`Sherpa` 2.2.1	20080
$Z\gamma^* \to ll$	`Sherpa` 2.2.1	2107 ($m_{\ell\ell} > 40$ GeV)

Table 4.3: Monte Carlo samples used for the V+jets processes and the cross-section times branching ratio (BR) used to normalise the different processes at $\sqrt{s} = 13$ TeV [78].

The analyses discussed in this thesis include phase spaces corresponding to high p_T of the vector boson or large values of the invariant mass. In order to be able to fully exploit the sensitivity of these regions, it is important to ensure that statistical fluctuations of the background prediction are small compared to those in data. To achieve this, the generation of the `Sherpa` V+jets samples is done splitting the events according to the p_T of the vector boson and to the scalar sum of the p_T of the jets in the event, H_T. The split is obtained by introducing a cut at generation level, and producing samples for different ranges of max(H_T, p_{T}^V):

$$[0-70, 70-140, 140-280, 280-500, 500-1000, > 1000] \text{ GeV}$$

As in the analysis event selection, it is required to have final states with b-tagged jets, it is also important to make sure that the MC statistics for this heavy-flavour enriched phase space is large enough. The V+jets samples are therefore generated by applying different filters to select the flavour composition of the jets produced in association with the V boson. The filters used for these samples are outlined in Table 4.4.

Filter	Description
BFilter	at least 1 b-hadron with $p_T > 0$ GeV and $\|\eta\| <4$
CFilterBVeto	at least 1 c-hadron with $p_T >4$ GeV and $\|\eta\| <3$
	veto events which pass the BFilter
CVetoBVeto	veto events which pass the BFilter or the CFilterBVeto

Table 4.4: Heavy flavour filters used for V+jets.

Within the V+jets background the dominant component in the $VH(H \to b\bar{b})$ analyses is the heavy-flavour jets component (bb, bc, bl and cc), abbreviated with "HF". In the thesis W+HF and Z+HF are used to indicate W+jets and Z+jets events for the sum of the bb, bc, cc and bl components. As the fit has sufficient constraining power the parameter associated to the normalisation of the W+HF and Z+HF component are left unconstrained in the fit. A 30% uncertainty is instead associated to the normalisation of the V+ll and V+cl components.

4.4.2 Top-Pair

The top-pair process is among the main background for both the 0-lepton and 1-lepton channels. The default MC sample for the $t\bar{t}$ process is `Powheg` +Pythia 8, which is generated with the `Powheg` generator using a NLO calculation for the

matrix element and interfaced to PYTHIA 8.230 [79]. In this sample, the PDF set used in the matrix element calculation is NNPDF3.0 (NLO) while the PDF set used in the parton shower is NNPDF2.3 (LO) [77].
The $t\bar{t}$ cross-section for pp collisions at a centre-of-mass energy of $\sqrt{s} = 13$ TeV is $\sigma_{t\bar{t}} = 831.76^{+40}_{-46}$ pb for a top quark mass of 172.5 GeV. It has been calculated at next-to-next-to leading order (NNLO) in QCD including resummation of next-to-next-to-leading logarithmic (NNLL) soft gluon terms [80].
The $t\bar{t}$ samples used for the nominal prediction are listed in Table 4.5. Samples listed as "non-all-had" are required to contain at least one W boson decaying leptonically, while the "dilepton" ones are required to contain both W bosons decaying leptonically. In the 0-lepton channel, the $E_{\mathrm{T}}^{miss} > 150$ GeV selection requirement removes a large number of events from the non-all hadronic sample. Therefore, generating events with a E_{T}^{miss} filter within this selection greatly increases the efficiency of events passing the selection. A number of E_{T}^{miss} filtered $t\bar{t}$ samples have been produced and used for this channel and are listed in the same table. The listed $t\bar{t}$ samples are normalised to the best NNLO+NNLL prediction of the

Process	Generator	$\sigma \times BR$ [nb]	ϵ_{filter}
non-all-had $t\bar{t}$	POWHEG + PYTHIA 8	0.832	0.5438
dilepton $t\bar{t}$	POWHEG + PYTHIA 8	0.832	0.1054
non-all-had $t\bar{t}$, E_{T}^{miss} [100-200] GeV	POWHEG + PYTHIA 8	0.832	0.0952
non-all-had $t\bar{t}$, E_{T}^{miss} [200-300] GeV	POWHEG + PYTHIA 8	0.832	0.0080
non-all-had $t\bar{t}$, E_{T}^{miss} [300-400] GeV	POWHEG + PYTHIA 8	0.832	0.0011
non-all-had $t\bar{t}$, $E_{\mathrm{T}}^{miss} > 400$ GeV	POWHEG + PYTHIA 8	0.832	0.0003

Table 4.5: $t\bar{t}$ samples used in the analysis for the nominal prediction. The MC generator, production cross-section and filter efficiency are shown. All samples are normalised to the same NNLO cross-section value. The E_{T}^{miss} filtered $t\bar{t}$ samples are utilised in the 0-lepton channel to increase the number of simulated $t\bar{t}$ events

cross-section, therefore the total normalisation does not vary across the different samples (Table 4.5).

4.4.3 Single-Top

The single-top processes are relevant background processes both in the 0-lepton and 1-lepton channels. Three different channels are generated: s-channel, t-channel and Wt-channel. Among these, the channel giving the more relevant contribution is the

Wt-channel. The channels are generated separately, using the Powheg generator for the hard scattering prediction with CT10 NLO PDFs, interfaced with the PYTHIA 8.230 algorithm for the simulation of parton shower, underlying event and multiple parton interactions. Single top samples in the t- and s-channels are generated applying a lepton filter to require the leptonic decay of the W boson.
The predicted t-channel single-top cross-section for proton-proton collisions at $\sqrt{s} = 13$ TeV is $\sigma_t = 136.02^{+5.4}_{-4.6}$ pb for the top quark and $\sigma_{\bar{t}} = 80.95^{+4.1}_{-3.6}$ pb the anti-top quark. For the same scenario the s-channel single-top cross-section is $\sigma_t = 6.35 \pm 0.2$ pb for the top quark and $\sigma_t = 3.97^{+0.19}_{-0.17}$ pb for the anti-top quark. The Wt-channel single-top cross-section is $\sigma_t = 71.7 \pm 3.8$ pb for the top quark plus the anti-top quark processes. This cross-section is the result of an approximate NNLO calculation, with $m_{top} = 172.5$ GeV.

Process	Generator	$\sigma\times$ BR [nb]
Single top W t incl t	POWHEG + PYTHIA 8	0.0380
Single top W t incl $\bar{t}$	POWHEG + PYTHIA 8	0.0379
Single top DS W t incl t	POWHEG + PYTHIA 8	0.0369
Single top DS W t incl $\bar{t}$	POWHEG + PYTHIA 8	0.0376
Single top t-chan t	POWHEG + PYTHIA 8	0.0370
Single top t-chan $\bar{t}$	POWHEG + PYTHIA 8	0.0222
Single top s-chan t	POWHEG + PYTHIA 8	0.0020
Single top s-chan $\bar{t}$	POWHEG + PYTHIA 8	0.0013

Table 4.6: Single-top samples used as nominal in the fit inputs. The MC generator and production cross-section are shown. *DS* refers to the diagram subtraction event generation technique, detailed at Ref. [81].

4.4.4 Diboson

The diboson background consists of final states arising from WW, WZ, and ZZ events. Several of these diboson processes are likely to be selected in the 0-lepton channels; the $Z \to b\bar{b}$ and $W \to \ell\nu$ processes in the 1-lepton channel; and the $Z \to b\bar{b}$ and $Z \to ll$ processes in the 2-lepton channel. Additional processes can give smaller contributions arising from the mistagging of a jet from the W decay or the failed reconstruction of one of the leptons, for example in $Z \to \nu\bar{\nu}$ and $W \to q\bar{q}$, $Z \to ll$ and $W \to q\bar{q}$, and $W \to \ell\nu$ and $W \to q\bar{q}$ production.
The nominal simulation for modelling all these diboson processes [82] is the Sherpa generator, interfaced with the NNPDF 3.0 PDF sets for both the matrix element

calculation and the parton shower. `Sherpa` provides a combination of different matrix elements with different parton multiplicities: processes with zero or one additional partons are calculated at NLO in the matrix element for WW, WZ, and ZZ, while 2 or 3 additional partons are included at LO in QCD.
The inclusive cross-section for the various diboson processes are summarised in Table 4.7.

Process	Generator	$\sigma\times$ BR [pb]
$qq \to W^+ l\nu W^- qq$	`Sherpa` 2.2.1	24.71
$qq \to W^+ qq W^- l\nu$	`Sherpa` 2.2.1	24.73
$qq \to Wl\nu Zqq$	`Sherpa` 2.2.1	11.4
$qq \to WqqZll$	`Sherpa` 2.2.1	3.44
$qq \to WqqZ\nu\nu$	`Sherpa` 2.2.1	6.80
$qq \to ZqqZll$	`Sherpa` 2.2.1	15.56
$qq \to Wl\nu Zbb$	`Sherpa` 2.2.1	2.50
$qq \to ZllZbb$	`Sherpa` 2.2.1	15.54
$qq \to Z\nu\nu Zbb$	`Sherpa` 2.2.1	15.57
$qq \to ZqqZ\nu\nu$	`Sherpa` 2.2.1	15.56
$gg \to W^- l\nu W^+ qq$	`Sherpa` 2.2.1	0.6224
$gg \to W^+ l\nu W^- qq$	`Sherpa` 2.2.1	0.6225
$gg \to ZllZqq$	`Sherpa` 2.2.1	0.923
$gg \to Z\nu\nu Zqq$	`Sherpa` 2.2.1	0.925

Table 4.7: Nominal diboson samples. The MC generator and production cross-section are shown. The `Sherpa` generator has been used for the production of all the diboson simulation used in this thesis.

4.4.5 Multi-jet background

QCD multijet events can pass the signal selection either because jets can fake the lepton signatures or because of electrons/muons produced via non-prompt weak decays. Such processes often result in a miscalibrated physics object, thereby yielding a fake non-negligible E_{T}^{miss} signature. In fact, the production cross-section of QCD multi-jet events and the rejection of such events by the analysis selection are so large that a prohibitively large number of simulated events would need to be generated, in order to obtain a statistically significant sample. An additional complexity would be the simulation of the rate at which light-quark or gluon jets are selected as b-jets (mis-tag rate). Both in the 0-lepton and 2-lepton channels the multi-jet contribution is suppressed to a negligible level and is not considered in the fit. In the 1-lepton channel, the multi-jet background is instead included in the fit and is modelled with a data-driven method. To model the multi-jet process a selection, as close as possible to the signal selection but with inverted lepton isolation cuts, is adopted to select an enriched multi-jet sample. The transverse W-candidate mass, m_{T}^{W}, is chosen as the variable offering the best discrimination between pure strong multi-jet production and electroweak induced processes, while not being excessively sensitive to systematics. A multi-jet template for this variable is obtained in the inverted isolation region. The contribution from electroweak background processes in the inverted isolation region is subtracted based on Monte Carlo predictions. Systematic variations of the MC predictions are later applied as a source of systematic uncertainty. A fit to the transverse W-candidate mass distribution is carried out in the signal region to extract simultaneously the normalization factors for both the multi-jet and the electroweak components. Separate templates for the multi-jet contributions are obtained depending on lepton flavour (e, μ), jet multiplicity and p_{T}^{V} category. For each of these signal regions, a corresponding multi-jet control region is thus defined. While this procedure is used to determine the normalization of the multi-jet background in the signal regions, the distribution of the discriminating variable used in the signal extraction fit is obtained in the same way as the m_{T}^{W} distribution used in the template fit.

Chapter 5

Object reconstruction

This chapter focuses on the methods applied to reconstruct the characteristics of the physical objects from the detector signals. The described procedures are applied to both simulated events and data samples.

The signals recorded by the various ATLAS sub-detectors are analysed by event reconstruction algorithms to identify individual particles and determine their kinematics. The reconstructed objects (electrons, muons, jets and missing transverse momentum) are used to select the events with a certain kinematic and topology. Such events are in turn used to extract the cross-section measurements.
The $VH(H \to b\bar{b})$ analyses here presented exploit in particular the reconstructed charged leptons and the missing transverse momentum to identify the decay products of the vector boson; while the Higgs boson decay products are identified by jets containing b-hadron decays (b-jets). The reconstruction of the physical objects used in the event selection is briefly described in this chapter.

5.1 Primary vertex and tracks

Primary vertices are defined as the points in space where proton-proton interactions have occurred. Their efficient and precise reconstruction is an important element of data analysis, as it is of direct relevance to the reconstruction of hard-scatter interactions. The correct assignment of charged-particle trajectories to the hard-scatter primary vertex is, in fact, essential in reconstructing the full kinematic properties of the event [83, 84].
Interaction vertices are reconstructed from good quality tracks measured in the

inner detector. The selection criteria applied to the tracks require no missing hit in the Pixel detector, a minimum number of hits in the silicon detectors, small transverse impact parameter, well-measured impact parameters and $p_T > 400$ MeV. Among the reconstructed vertices, the vertex with the highest sum of squared transverse momenta of associated tracks is selected as the primary vertex [83, 85]. The remaining reconstructed vertices comprise vertices from pile up and secondary vertices, which are fundamental for b-jet identification. The primary vertex reconstruction efficiency is shown in Figure 5.1 as a function of the number of tracks. Such efficiency is determined from data by taking the ratio between

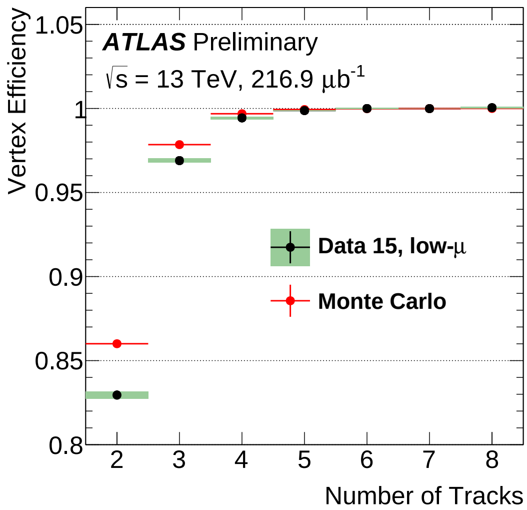

Figure 5.1: Vertex reconstruction efficiency as a function of the number of tracks in low-μ data compared to MC simulation [84].

events with a reconstructed vertex and events with at least two reconstructed tracks. The efficiency has been computed using data collected when the ATLAS detector was collecting data in a special condition with a low number of pile-up events (low-μ) [84]. The reconstruction efficiency is higher than 99% for vertexes with four or more tracks.

5.2 Leptons

The events selected in the $VH(H \to b\bar{b})$ analysis are categorized by the number of observed charged leptons (e or μ). The presence of isolated leptons is crucial to reduce fake-lepton background (e.g. QCD multi-jets in 1-lepton channel). In this section, the reconstruction, identification and selection criteria for electrons and muons are described.

5.2.1 Electron reconstruction

Electrons are reconstructed as energy deposits (clusters) in the EM calorimeter associated to a well-reconstructed ID track originating from a primary interaction vertex [86, 87]. A schematic illustration of the subdetectors crossed by an electron is shown in Figure 5.2. The electron first traverses the tracking system (pixel detectors, then silicon-strip detectors and lastly the TRT) and then enters the electromagnetic calorimeter.

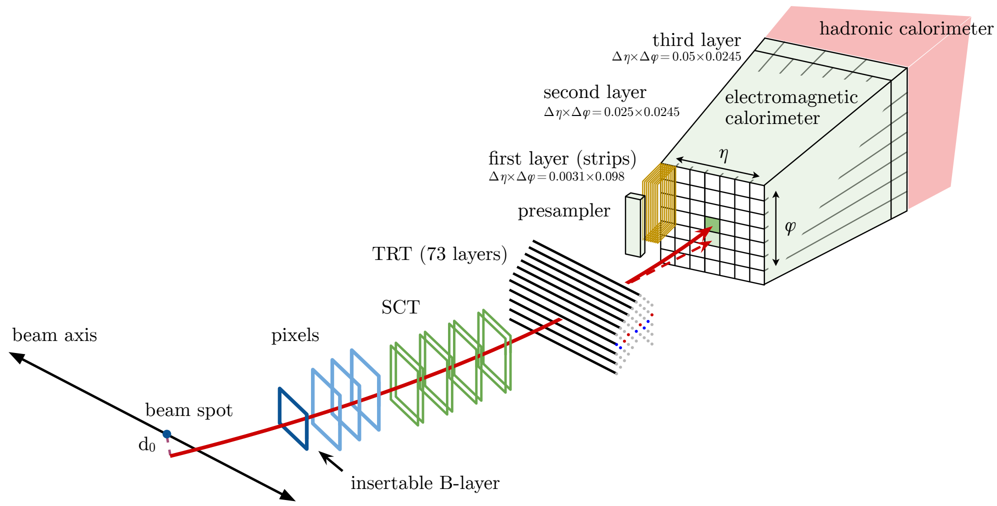

Figure 5.2: A schematic illustration of the path of an electron through the detector. The red trajectory shows the hypothetical path of an electron. The dashed red trajectory indicates the path of a photon produced by the interaction of the electron with the material in the tracking system [88].

To reconstruct the electromagnetic clusters the EM calorimeter is divided into a grid of $N_\eta \times N_\phi = 200 \times 256$ towers of size $\Delta\eta \times \Delta\phi = 0.025 \times 0.025$, corresponding to the granularity of the EM calorimeter middle layer. The tower energy is obtained by summing the cell energies of all the longitudinal layers (the front, middle and back EM calorimeter layers and, for $|\eta| < 1.8$, also the presampler detector). The energy of cells spanning several towers is distributed uniformly among the participating elements. In order to reconstruct the EM clusters, seed clusters of longitudinal towers with total cluster transverse energy above 2.5 GeV are searched for, using a sliding-window algorithm [89]. This algorithm is based on the clustering of calorimeter cells within rectangles of size 3×5 towers in the $\eta - \phi$ space. A duplicate removal algorithm is applied on close-by seed clusters.

5.2.2 Electron identification and selection

In order to be labelled as an electron, the clusters associated with electron candidates must satisfy a set of identification criteria, requiring their longitudinal and transverse profiles to be consistent with those expected for EM showers induced by electrons. Three levels of identification criteria, labelled *loose*, *medium* and *tight*, have been defined to identify electrons [90]. They provide an increasing level of background rejection at the cost of some efficiency loss. The *medium* identified electrons are a subset of the *loose* selection and the *tight* identified electrons are a subset of the *medium* selection. The selections are tightened by considering more variables and by using more stringent cuts.
A brief description of the electron selections:

- *loose*: simple shower-shape cuts and very loose matching cuts between the reconstructed track and the calorimeter cluster;
- *medium*: tightened requirements on the discriminating variables used in the *loose* selection together with a relaxed selection on the transverse impact parameter and on the number of track hits in the TRT. Moreover, a track hit in the innermost layer of the pixel detector is requested to discriminate against photon conversions;
- *tight*: a selection is added on the ratio between the candidate electron energy and the matched track momentum; stricter requirements on the discriminating variables and TRT information with respect to those applied in the *medium* selection are used; a veto is also applied on reconstructed photon conversion vertices associated with the cluster.

The electron reconstruction efficiency is defined as the ratio of the number of electrons reconstructed as a cluster matched to a track passing the track quality criteria (numerator) to the number of clusters with or without a matching track (denominator). Measured reconstruction efficiencies are shown as a function of the electron E_T and η in Figure 5.3 respectively. Such efficiencies are obtained by applying the *tag-and-probe* method [91] on $Z \to ee$ events. The ratios of efficiencies measured in data and the simulation, the so-called scale factors, are used in physics analyses to correct the yield of electrons in simulated samples, together with their

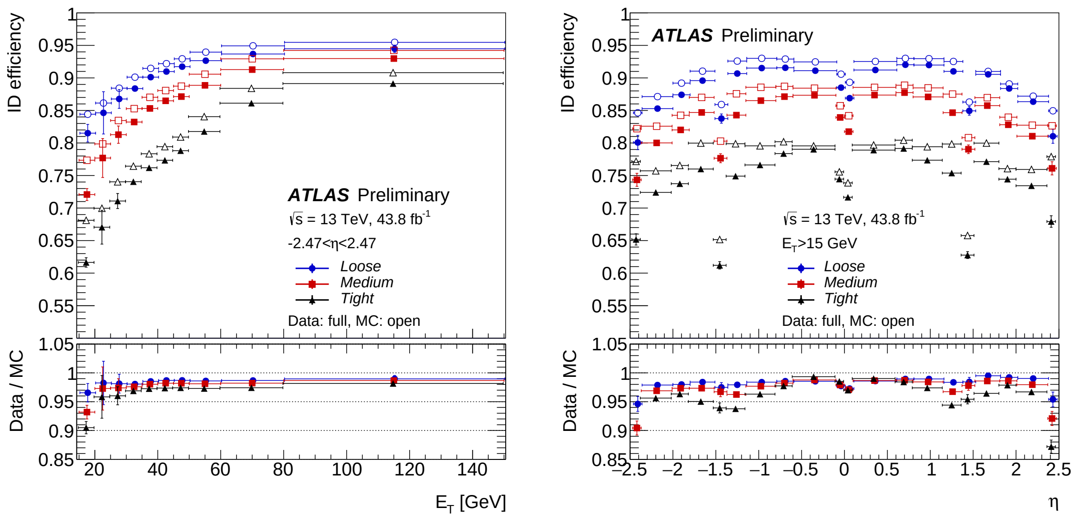

(a) **(b)**

Figure 5.3: Measured reconstruction efficiencies as a function of $E_T = Esin\theta$ integrated over the pseudorapidity range $|\eta| < 2.47$ (a) and as a function of η for $E_T > 15$ GeV (b) for the simulation (open) and data (full) [92].

associated uncertainties.
Electrons used in the event selection are required to have $p_T > 7$ GeV and $|\eta| < 2.47$. Non-prompt and pile-up tracks are rejected by requiring the electrons to have small transverse ($IP_{r\phi}$) and longitudinal (IP_z) impact parameters, defined with respect to the primary vertex position: tracks must have $|IP_{r\phi}|/\sigma_{IP_{r\phi}}$ <5 and $|IP_z| < 0.5$ mm, with $\sigma_{IP_{r\phi}}$ representing the uncertainty in the transverse impact parameter. A loose isolation requirement is applied: the electron track must be isolated from other tracks reconstructed in the inner detector, based on a variable cone size with $\Delta R_{max} = 0.2$. The isolation requirement is tuned as a function of electron p_T and η to yield an approximately constant 99% isolation efficiency, corresponding to making the requirement looser with increasing values of p_T [88, 93]. The isolation efficiencies, computed with the tag-and-probe method in $Z \to ee$ events, are shown in Figure 5.4. The isolation efficiency corresponding to the isolation requirement applied to electrons in this analysis is shown as black dots.
Tight electrons are also required to pass a calorimeter-based isolation requirement, where the sum of the transverse energy of all the clusters of calorimeter cells, not associated with the electron candidate but found within a cone of $\Delta R = 0.2$ around the electron track, is required to be below 3.5 GeV.
Loose electrons are used in the event selection of the 0- and 2-leptons channels. For the 1-lepton channel events are selected requiring electrons with tight selection criteria to reject the high multi-jet background.

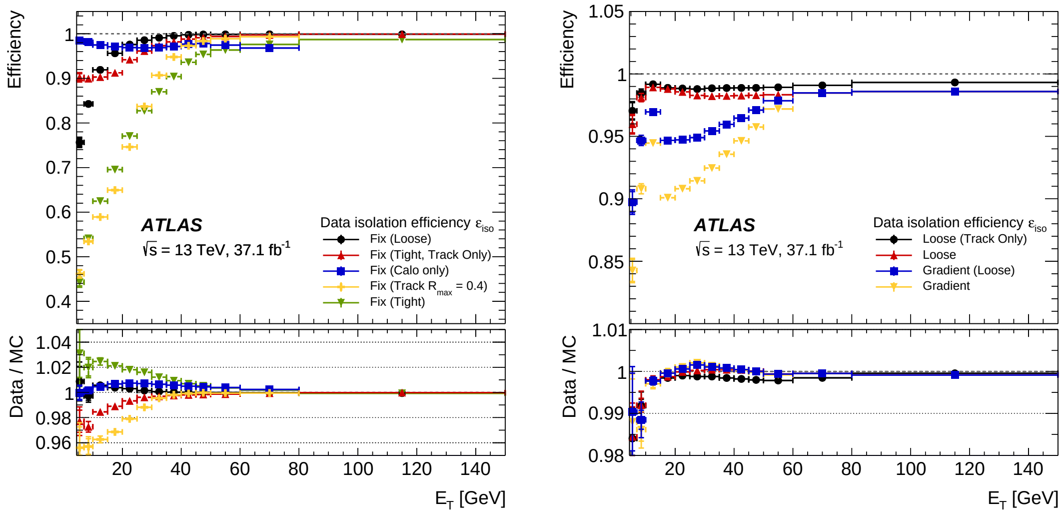

(a) **(b)**

Figure 5.4: Isolation efficiencies for data (in the upper panels) and the ratio to simulation (lower panels) as a function of candidate-electron E_T (left) and η (right). The maximum cone size is $R_{max} = 0.2$ for track isolation [88].

5.2.3 Electron systematic uncertainties

The uncertainties on the reconstruction and identification efficiency are determined in bins of transverse momentum and rapidity from data and MC using $Z \to ee$, $W \to e\nu$, and $J/\psi \to ee$ events. Systematic uncertainties on the electron reconstruction efficiency are of the order of 1% for $E_T = 15 - 20$ GeV and reach the per-mille level at higher E_T. The uncertainties on the identification efficiencies [88] for the *loose* (*tight*) operating point range from 3% (4%) at $E_T = 4.5$ GeV to 0.1% (0.3%) for $E_T = 40$ GeV.
The uncertainties in the electron energy scale are determined in $Z \to ee$ events, comparing the invariant mass distribution in data and simulation. The accuracy of the energy scale measurement varies from 0.03% to 0.2% depending on $|\eta|$. All the mentioned uncertainties are included in the fit model. However, this analysis is very weakly sensitive to the electron systematic uncertainties, which have a negligible impact on the cross-section uncertainty.

5.2.4 Muon reconstruction

Muons are reconstructed and identified using the information from the muon spectrometer (MS) and from the ID and, to a lesser extent, from the calorimeter [55].

The reconstruction is first performed independently in the ID and in the MS. The information from individual subdetectors is then combined to form the muon tracks used in physics analyses.
Muons are reconstructed as tracks in the ID matched to tracks in the MS up to $|\eta| = 2.5$, corresponding to the region covered by the ID. Tracks in the MS are required to have at least three hits in two monitored drift tube (MDT) chambers layers. Some acceptance is gained up to $|\eta| = 2.7$ using the muon spectrometer alone, as this region is not covered by the ID. Within the region $|\eta| < 0.1$, of limited muon-chamber acceptance, tracks in the MS are only required to have at least one hit in the MDT chambers, but in addition should have deposited energy in the calorimeter that is consistent with the energy loss of a muon.

5.2.5 Muon identification and selection

Also for muons several levels of identification criteria are defined. Two of the three selection categories are used in this analysis: *loose* and *medium*.
Figure 5.5 shows the muon reconstruction efficiency as a function of η, for $p_T >$10 GeV, as measured using the tag-and-probe method with $Z \to \mu\mu$ events. The efficiency for muons identified with *loose*, *medium* and *tight* selection criteria are shown. The *loose* muons have a uniform muon reconstruction efficiency of about 99% over most detector regions. The reconstruction efficiency of *medium* muons is affected by acceptance losses mainly in the region at $\eta \sim 0$, where the MS is only partially equipped with muon chambers in order to provide space for the services for the ID and the calorimeters.
All muon candidates are required to have $p_T > 7$ GeV, and not to be matched to ID tracks that are likely to arise from non-prompt muons or from pile-up, by applying impact parameters requirements similar to those applied to the electron selection: $|IP_{r\phi}|/\sigma_{IP_{r\phi}} < 3$ and $|IP_z| < 0.5$ mm. A loose isolation requirement is applied as well. Muons originating from the decay of heavy particles, such as W or Z, are in fact often produced isolated from other particles in the event. Differently, muons from semileptonic decays are embedded in jets. Applying muon isolation requirement is therefore a powerful tool for background rejection. The requirement applied is based on the momenta of tracks in the ID which lie within a variable-size cone around the muon track, with $\Delta R_{max} = 0.3$. Analogously to what is done in the electron case, the requirement is tuned to yield an approximately 99% efficiency for any value of p_T. Such efficiency is measured with the tag-and-probe method in $Z \to \mu\mu$ events.
The above-described isolation criterium is applied to all muons (including *loose* muons). For *medium* quality muons an additional more stringent track-based

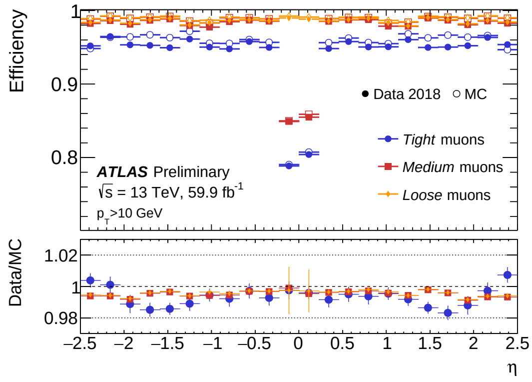

Figure 5.5: Muon reconstruction efficiency as a function of η measured in $Z \to \mu\mu$ events for muons with $p_T > 10$ GeV shown for the *loose*, *medium* and *tight* muon selection. The predicted efficiency is depicted as open circles, while filled dots indicate the observation in collision data with statistical uncertainties. Panels at the bottom show the ratio of the measured to predicted efficiencies, with statistical and systematic uncertainties [94].

isolation requirement is applied, where the sum of the p_T of all the tracks found within a cone of $\Delta R = 0.2$ around the muon track is required to be below 1.25 GeV. The efficiency of *medium* muons is above $\sim 98\%$.
Similarly to what is done for the electron selection *loose* muons are used in the 0- and 2-lepton channels and *tight* muons are used in the 1-lepton channel.

5.2.6 Muon systematic uncertainties

The muon momentum scale and reconstruction uncertainties are computed using $J/\Psi \to \mu\mu$ events for the low p_T region ($p_T < 20$ GeV) and using $Z \to \mu\mu$ decays for the high p_T region ($p_T \geq 20$ GeV).
The muon reconstruction uncertainty for muons with p_T between 5 GeV and 20 GeV is lower than 1% and for muons with p_T >20 GeV is lower than 0.2%.
The uncertainty on the momentum scale varies from a minimum of 0.05% for $|\eta| < 1$ to a maximum of 0.3%(0.1%) for $|\eta| \sim 2.5$ for $Z \to \mu\mu$ ($J/\Psi \to \mu\mu$) decays.
The use of isolation requirements to reject fake muons requires the introduction of simulation to data scale factors to correct for possible mismodelling. The systematic uncertainties in the SFs are estimated by varying the background contributions within their uncertainties and by varying some of the selection criteria. The measured uncertainty is at the per mille level over a wide range of p_T.

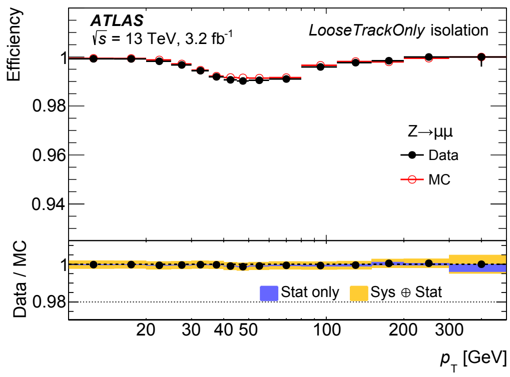

Figure 5.6: Muons isolation efficiency as a function of the muon p_T measured in $Z \to \mu\mu$ events. The full (empty) markers indicate the efficiency measured in data (MC) samples. The errors shown on the efficiency are statistical only. The bottom panel shows the ratio of the efficiency measured in data and simulation, as well as the statistical uncertainties and combination of statistical and systematic uncertainties [55].

5.3 Jets reconstruction

5.3.1 Introduction

Jets are the experimental manifestation of partons. Because of confinement quarks and gluons can not be observed directly but they are observed through the sprays of particles that emerge from their hadronisation. These particles interact with the calorimeters and with the ID producing energy "showers".

Jets are typically reconstructed by grouping topologically related energy deposits in the calorimeters. In the following such jets are referred to as calorimeter jets (calo-jets) or simply as jets. For some measurements the calorimeter jets are not optimal and the information is complemented exploiting track-jets. Track-jets are built applying exactly the same algorithms used for calorimeter jets but using tracks emerging from the hard scatter vertex instead of energy deposits. The reconstruction algorithms to build the calorimeter and the tracks jets are two: the anti-k_t and the k_t algorithms. These algorithms and the motivations for using them are discussed in Section 5.3.3. The reconstruction of the calo-jets and the preliminary calibration steps are described in Section 5.3.2 while the track-jets reconstruction and the motivations for employing such jets are illustrated in Section 5.3.7.

The high energy collisions at the LHC can result in the production of particles having transverse momenta much larger than their masses. Such particles are boosted, therefore their decay products are highly collimated and, for fully hadronic decays, they can be reconstructed as a single hadronic jet, as shown in Figure 5.7.

A helpful rule of thumb is $2M/p_T \sim \Delta R$: twice the particle mass divided by

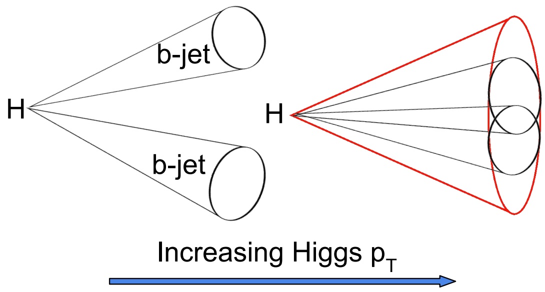

Figure 5.7: Illustration showing the two reconstruction modes for the Higgs boson. In the figure on the left, the candidate Higgs boson is reconstructed through two small-R jets. In some events the Higgs boson is produced with very high energy and the two small-R jets tend to merge. In such a case, it is not possible to reconstruct the Higgs with two small-R jets and a single large-R jet is used instead.

its p_T is roughly equal to the maximum opening angle (ΔR) of the two decay products. In this analysis two kinds of jets are used to reconstruct the Higgs boson: in the *resolved* analysis two small-R calo-jets are employed, while in the *merged* analysis a single large-R jet. The small-R jets selection and calibration is described in Section 5.3.4 while the reconstruction through a large-R jet is depicted in Section 5.3.5.
In order to identify the candidate Higgs boson it is crucial to check that the selected jets are compatible with having been produced by two b-hadrons, as discussed in Section 5.3.6.

5.3.2 Calorimetric jets

Jets are reconstructed from noise-suppressed energy clusters in the calorimeter. Single-cell energy depositions are merged into topological clusters (topo- clusters) with an iterative algorithm designed to group cell deposits belonging to the same particle [95, 96]. The topo-cluster energy is calibrated to account for the effects of the non-compensating calorimeter response to hadrons, for the energy deposited outside the cluster and in inactive material in the vicinity of the topo-cluster [96, 97]. This calibration is performed without any particular assumption about the kind of object the cluster will be part of. Topological clusters are then used as input to a jet reconstruction algorithm which, for this analysis, is the anti-k_t algorithm [98]. A further calibration, described in the next sections, is then applied to the reconstructed jets [99].

5.3.3 Reconstruction algorithms: anti-k_t and k_t

To apply the anti-k_t jet clustering algorithm two distances are introduced: the distance d_{ij} between the topo-clusters i and j and the distance d_{iB} between the topo-cluster i and the beam (B):

$$d_{ij} = min(\frac{1}{p_{Ti}^2}, \frac{1}{p_{Tj}^2}) \cdot \frac{\Delta R_{ij}^2}{R^2}$$

$$d_{iB} = \frac{1}{p_{Ti}^2}$$

where $\Delta R_{ij}^2 = (\eta_i - \eta_j)^2 + (\phi_i - \phi_j)^2$; p_{Ti} , η_i, ϕ_i and are the transverse momentum, pseudorapidity and azimuth of particle i and R is the distance parameter.
The clustering proceeds by identifying the smallest of the distances among d_{ij} and d_{iB}, and if it is a d_{ij} the topo-clusters i and j are recombined, whereas if it is d_{iB} i is classified as a jet and is removed from the list of constituents. The distances are recalculated and the procedure repeated until no topo-clusters are left. The mechanism with which jets are formed using the anti-k_t algorithm is briefly described in the following.
The $d_{1i} = min(\frac{1}{p_{T1}^2}, \frac{1}{p_{Ti}^2}) \cdot \frac{\Delta R_{1i}^2}{R^2}$ between a hard particle 1 and a soft particle i is exclusively determined by the transverse momentum of the hard particle and the ΔR_{1i} separation. The d_{ij} between similarly separated soft particles will instead be much larger. Therefore soft particles will tend to cluster with hard ones long before they cluster among themselves. If a hard particle has no hard neighbours within a distance $2R$, then it will simply accumulate all the soft particles within a circle of radius R, resulting in a perfectly conical jet. The key feature of this algorithm is that the soft particles do not modify the shape of the jet, while hard particles do; this means that the jet boundaries are resilient with respect to soft radiation but flexible with respect to hard radiation.
In this analysis, two kinds of jets are reconstructed with the anti-k_t algorithm: small-radius jets (small-R jets) with distance parameter $R = 0.4$ and large-R jets with distance parameter $R = 1.0$. The Higgs boson decaying into two b-hadron is in fact typically reconstructed through two small-R jets. For boosted Higgs boson the decay products are instead reconstructed as a single large-R jet.
The second jet algorithm used in the analysis, the k_t algorithm, is used to disentangle the sub-jets within a single larger-R jet. The k_t algorithm, contrary to the anti-k_t one, cluster energy deposits into jets starting from the softest up to the hardest one. This algorithm proceeds exactly as the anti-k_t algorithm but distances are defined as:

$$d_{ij} = min(p_{Ti}^2, p_{Tj}^2) \cdot \frac{\Delta R_{ij}^2}{R^2}$$

$$d_{iB} = p_{Ti}^2$$

The k_t algorithm has the peculiarity that the reconstructed jets tend to better share the energy between them.

5.3.4 Small-R jets calibration and selection

In this section, the calibration and the selection applied to the small-R calo-jets is described. The calorimeter cell energies used to build the topo-clusters are measured at the EM scale, corresponding to the energy deposited by electromagnetically interacting particles. Reconstructed calo-jets are then calibrated using a multi-step procedure [99, 100], for which an overview is given in Figure 5.8.

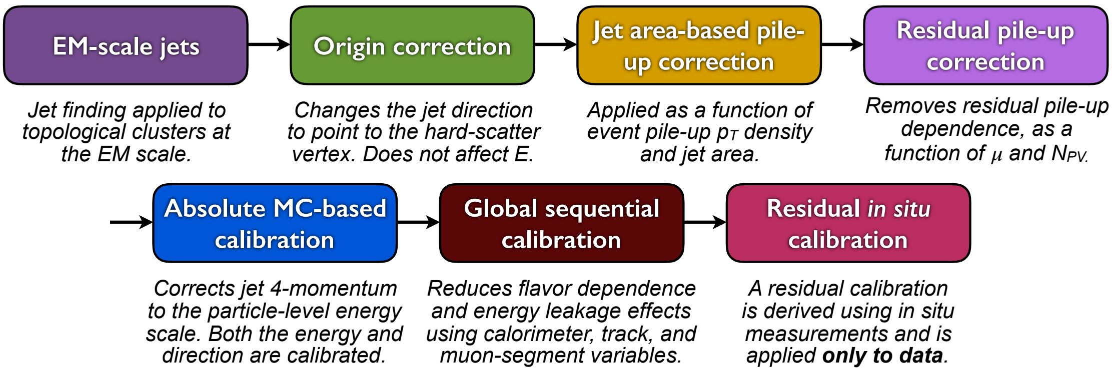

Figure 5.8: Overview of the small-R jet calibration procedure. Other than the origin correction, each stage of the calibration is applied to the four-momentum of the jet [101].

First, the direction of the jet is adjusted imposing that the jet points back to the hard-scatter vertex. Secondly, the pile-up dependence of the calorimeter response to jets is reduced by subtracting the average expected pile-up contribution, defined as the expected energy density of soft contributions multiplied by the jet area. Any remaining pile-up dependence is removed by residual corrections parametrized as a function of the number of primary vertices (NPV), sensitive to in-time pile-up, and the expected average number of interactions $\langle\mu\rangle$, sensitive to out-of-time pile-up. Such corrections are derived from MC simulations, comparing the reconstructed jet p_T and truth jet p_T, with the latter being insensitive to pile-up. The effect of the area-based correction and the effect of the residual pile-up correction is shown in Figure 5.9 as a function of $|\eta|$.
Thirdly, the *absolute* jet energy scale and η calibration is applied. It corrects the reconstructed jet four-momentum to the true jet energy scale and accounts for biases in the jet η reconstruction. Such biases are primarily caused by the transition

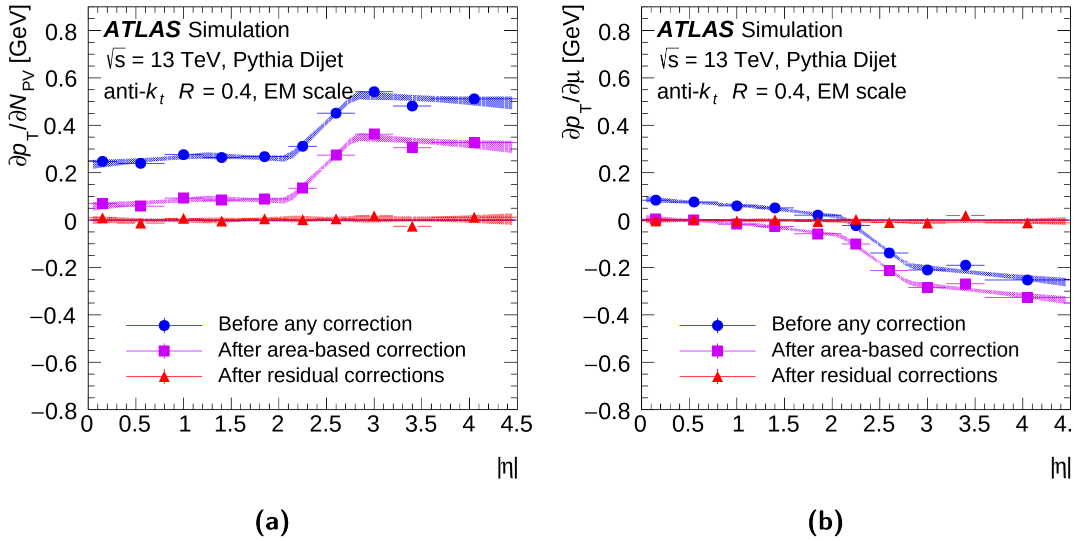

Figure 5.9: Dependence of the reconstructed jet p_T on in-time pile-up (a) and out-of-time pile-up (b) at various correction stages as a function of jet $|\eta|$ for $p_T^{true} = 25$ GeV. The dependence is shown in bins of $|\eta|$ before pile-up corrections (blue circle), after the area-based correction (violet square), and after the residual correction (red triangle) [101].

between different calorimeter technologies and sudden changes in calorimeter granularity. In addition to these steps, further corrections are applied to the jets to reduce the dependence of the jet energy measurement on the longitudinal and transverse structure of the jets and also to correct for jets that are not fully contained in the calorimeter. This is the global sequential calibration [101], which make use of calorimeter, muon spectrometer, and track-based variables.

Lastly, jets in data are further corrected by applying scale factors based on *in situ* studies. The in situ corrections account for differences between data and MC simulation in the jet p_T measurement. Such corrections are calculated using γ+jets, Z+jet and multijet processes exploiting the transverse momentum balance between the jet and a reference object.

The calibrated jets are finally used in the analysis to reconstruct the candidate Higgs bosons. The selection applied to the calibrated jets is described in the following. Jets with $p_T < 60$ GeV and with $|\eta| < 2.4$ associated with vertices other than the primary are removed using the jet vertex tagger (JVT) [102, 103], a discriminant that uses track and vertex information in order to suppress jets originating from pile-up activity. The effect of a cut on JVT is shown in Figure 5.10 for jets with $p_T > 20$ GeV. The number of jets has a clear pile-up dependence, both in data and in MC simulated events. Such dependence is removed by applying a cut on JVT.

In this analysis jets reconstructed in the central region $|\eta| < 2.5$, covered by the

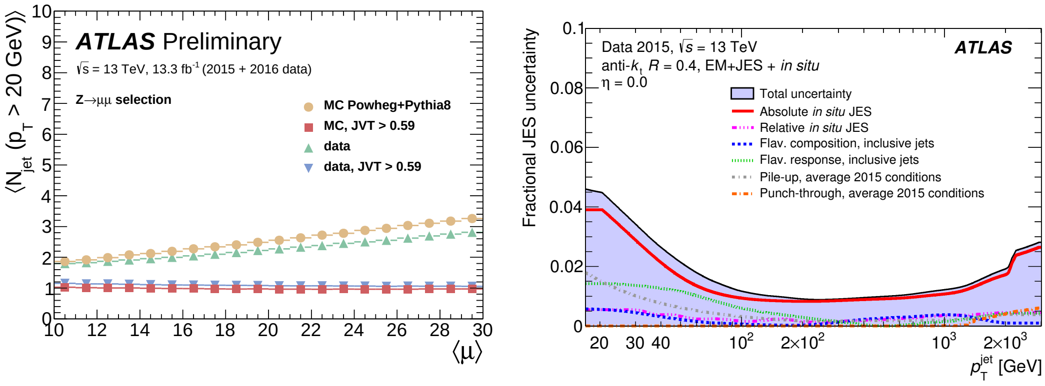

(a) **(b)**

Figure 5.10: (a) The average number of jets with $p_T > 20$ GeV in MC simulation and in data before and after a cut of JVT > 0.59. The selected events are jets balanced against a Z decaying into two μ [104].
(b) Combined uncertainty in the JES of fully calibrated jets as a function of jet p_T at $\eta = 0$. Systematic uncertainty components include pile-up, punch-through, and uncertainties propagated from the Z/γ-jet and multi-jet in situ calibrations [101].

tracker, are required to have $p_T > 20$ GeV. Jets reconstructed at $2.5 < |\eta| < 4.5$, are required to pass the stricter requirement $p_T > 30$ GeV in order to suppress jets from pile-up activity.
The most prominent sources of jet-related uncertainty are the uncertainties from the jet energy resolution (JER) and jet energy scale (JES). The JER in the simulation is similar to the resolution observed in data [105]. In order to assess the impact of the JER the jet energies in simulated events are smeared using a Gaussian function with width set to the JER uncertainty measured in the data. The difference between the calibrations obtained with nominal and smeared simulation is taken as the JER uncertainty. The determination of the JES uncertainty is the result of the combination of several components of the uncertainty. The JES uncertainty as a function of jet p_T for jets at $\eta = 0$ is shown in Figure 5.10 on the right. A large part of the JES uncertainty comes from the in situ calibrations and accounts for assumptions made in the event topology, MC simulation, sample statistics, and propagated uncertainties of the electron, muon, and photon energy scales. The remaining contribution is derived from several other sources, including pile-up uncertainties, statistical uncertainties, and differences in the jet response and simulated jet composition of light-quark, b-quark, and gluon-initiated jets. The total JES uncertainty is lower than 5% for low p_T jets and about 1% for jets with p_T between 100 GeV and 1 TeV.

5.3.5 Large-R jets grooming and calibration

The reconstruction algorithm used for the boosted boson is the anti-k_t algorithm described in Section 5.3.2 with a distance parameter $R = 1.0$. Large-R jets tend to collect energy depositions from soft and pile-up particles. A *grooming algorithm* is therefore applied to the resulting jet, in order to remove pile-up contributions and to reveal the hard substructure by removing the soft component of the radiation. Various grooming algorithms have been developed in the last years, and the one used in this analysis is the trimming algorithm [106]. The inputs to the trimming are the topo-clusters composing the jet. The algorithm consists of two steps. Firstly, the topo-clusters of the jets are clustered in smaller "sub-jets" using the k_t algorithm described in Section 5.3.2, with a distance parameter R_{sub}. Secondly, the sub-jets are removed if they carry less than a fraction f_{cut} of the original, ungroomed, jet p_T. This procedure is illustrated in Figure 5.11.

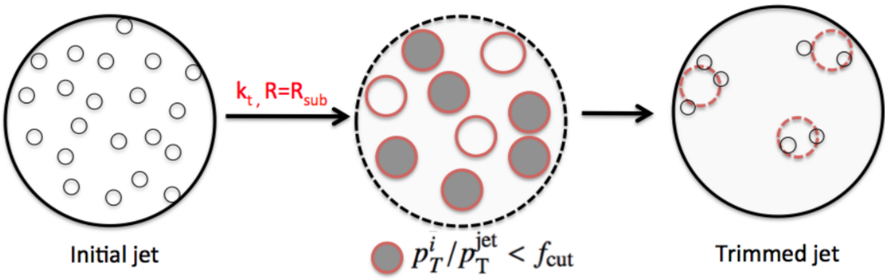

Figure 5.11: Diagram depicting the jet trimming algorithm. The inputs for the trimming are the topo-clusters (left). Smaller sub-jets are then reconstructed using the k_t algorithm with a distance parameter R_{sub} (center). The sub-jets are then removed if they carry less than a fraction f_{cut} of the original, ungroomed, jet p_T (right) [106, 107].

The trimming algorithm configuration used for this work is $R_{sub} = 0.2$ and $f_{cut} = 0.05$ and is the result of the performance assessment of several grooming algorithms and parameters [107]. The trimmed large-R jets are then calibrated, similarly to what is done for the small-R jets.
In the following the techniques used to calibrate large-R jets are briefly described [108]. The results of several methods are combined to provide a calibration that defines the nominal large-R jet energy scale (JES) and the jet mass scale (JMS). The stages of the jet calibration are schematically shown in Figure 5.12.
Jet reconstruction starts with the topo-clusters. Topo-clusters are brought to the hadronic scale using the local hadronic cell weighting scheme (LCW) [96]. Large-R jets are then reconstructed with the anti-k_t algorithm and groomed with the trimming algorithm described above. The trimmed large-R jets are calibrated to the energy scale of stable final-state particles using corrections based on simulations. This jet-level correction is referred to as the simulation-based calibration and

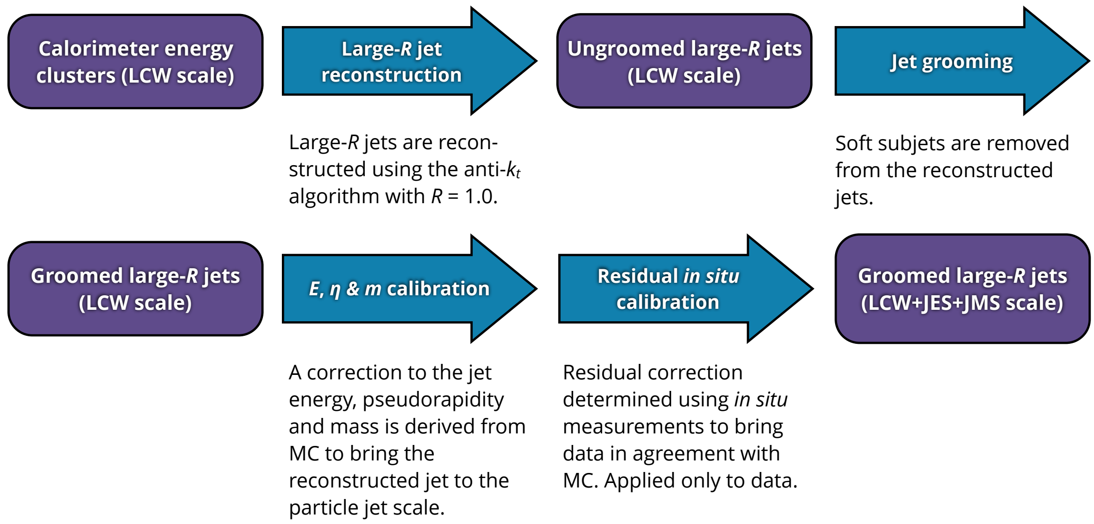

Figure 5.12: Overview of the large-R jet reconstruction and calibration procedure. The calorimeter energy clusters from which jets are reconstructed have already been adjusted to point at the event's primary hard-scatter vertex [108].

includes a correction to the jet mass [109]. Finally, the jets are calibrated *in situ* using response measurements. A correction based on a statistical combination of data-to-simulation ratios of these response measurements is applied only to data and adjusts for the residual mismodelling of the response. The in situ calibration is determined in two steps. The first step consists in measuring the JES by relying on the transverse momentum balance in a variety of final states: Z+jet, γ+jet, and multijet. With this method, the calibration is propagated from the well-measured central JES into the forward region of the detector. The JES correction is applied as a four-momentum scale factor to jets in data and therefore also affects the jet mass calibration.
The second step of the in situ calibration consists in measuring the jet mass response with the R-track method [107]. This method takes advantage of the independent measurements by the calorimeter and the inner tracker and provides a calibration for the calorimeter jet mass measurement over a broad p_T range. The same method is also exploited to compute the uncertainties on the jet mass scale and is described in more details in the following.

Large-R jet uncertainties and the R-track procedure

The uncertainties related the large-R jets can be roughly classified into *scale uncertainties*, which take into account systematic uncertainties on the jet mass scale, and *resolution uncertainties*, which take into account the uncertainty on the jet mass resolution and on the jet p_T resolution.

The jet mass scale uncertainties are derived in situ using the *R-track procedure*. The R-track procedure is a method for evaluating the large-R jet mass scale (JMS) uncertainty using the tracks. The primary assumption in this approach is that the systematic uncertainties associated with the tracking measurements are largely uncorrelated with the calorimeter uncertainties. There is no assumption that the track-jet mass is better measured than the calorimeter jet mass. The method exploits the fact that the difference between observables measured in the calorimeter compared to the tracker gives information about the modelling of both. Of course, systematic uncertainties on both measurements need to be included.
The basic element of the R-track procedure is the ratio between the calorimetric jet mass and the jet mass computed with tracks:

$$r^m_{\text{track-jet}} = \frac{m^{\text{jet}}}{m^{\text{track-jet}}} \tag{5.1}$$

where m^{jet} is the large-R jet mass computed with the calorimeter information and $m^{\text{track-jet}}$ is the large-R jet mass computed with tracks. Their ratio is in turn used to compute the calorimeter-to-track-jet mass double ratios:

$$R^m_{r \text{ track jet}} = \frac{r^{m,\text{data}}_{\text{track jet}}}{r^{m,\text{MC}}_{\text{track jet}}} \tag{5.2}$$

where $r^{m,\text{data}}_{\text{track jet}}$ and $r^{m,\text{MC}}_{\text{track jet}}$ are the ratios computed with data and with simulated samples, respectively. The double ratios are computed both comparing the data and a baseline simulation as well as comparing various simulations among them. The most important part is the comparison between the calorimeter-to-track-jet ratio in data and simulation. If detector effects are well modelled in the simulations, the double-ratio should be unity. The comparisons of the nominal simulation to alternative simulations are instead exploited to take into account uncertainties due to differences in the fragmentation and hadronisation models.
It is important to evaluate these ratios and the modelling of the data in various kinematic ranges. The systematic uncertainties are generally derived in bins of the jet mass over the calorimeter jet transverse momentum, m/p_T. This variable is chosen as it provides a handle on the boost of the jet and thus its collimation.

The distribution in Figure 5.13 shows, as an example, the full spectrum of the $r^m_{\text{track jet}}$ ratio for a $p_T > 200$ GeV and $m/p_T = 0.2$ for data, the nominal simulation and two alternative simulations. The $r^m_{\text{track-jet}}$ distribution is mostly expected to be larger than one because the track-jet only accounts for charged particles. The lower panel on Figure 5.13 shows the double ratios of $r^m_{\text{track jet}}$ computed with the simulations and with data ($1/R^m_{r \text{ track jet}}$). All the double ratios, computed with

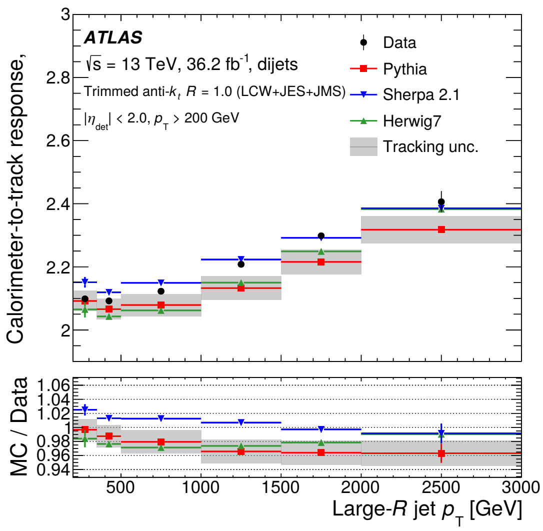

Figure 5.13: Measurement of $r^m_{\text{track jet}}$ as a function of the large-R jet p_T for large-R jets with $m/p_T = 0.2$. Data are compared with three generators and with three tracking variations for the default generator PYTHIA 8. The double ratio of $r^m_{\text{track jet}}$ measured in simulations and data is shown in the lower panel [108].

three different simulations, depend on the large-R jet p_T and are lower at high energy.
Using the R-track procedure four sources of scale uncertainties are obtained:

- the *baseline* variation accounts for the base difference of $R^m_{r\text{ track jet}}$ between data and the nominal Pythia8 simulation. This accounts for all the difference between the data and the simulated jets and the simulation of the interaction of the particles with the detector;
- the *modelling* variation accounts for deviation of the $R^m_{r\text{ track jet}}$ from unity using alternative simulated events. The maximum difference between Pythia8 and Herwig7 or Pythia8 and Sherpa is chosen as modelling uncertainty;
- the *tracking* uncertainty is the quadratic sum of the effect of the various tracking uncertainty sources;
- the *statistical* uncertainty accounts for the statistical uncertainty of the simulated samples and dataset. This uncertainty is typically small at low p_T and only relevant at very high p_T.

The total scale uncertainty computed with the R-track method is shown in Figure 5.14. The contributions from the four mentioned sources are indicated. The

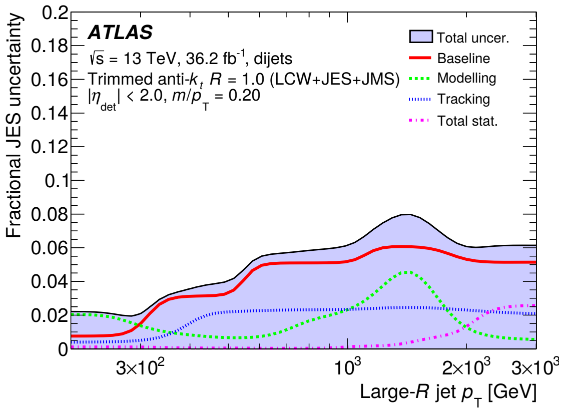

Figure 5.14: The total uncertainty in the relative JES in data and simulations associated with the R-track method is plotted as a function of jet transverse momentum p_T. The large-R jet p_T is corrected using the simulation calibration, η-intercalibration, and a combination of in situ direct balance techniques. The contributions from several sources are indicated [108].

statistical uncertainty only has a relevant effect for jet p_T larger than 2 TeV. The tracking uncertainty contribution is constant for $p_T \gtrsim 400$ GeV and with a $\sim 2\%$ contribution. The modelling uncertainty is also of the order of 2%, with a larger impact at about 1 TeV. The baseline uncertainty is the more relevant source of uncertainty and is about 5%.

For the p_T resolution uncertainty, a gaussian with a width of 0.02 (an absolute 2% uncertainty) is used to smear the simulated distribution. The resulting difference with respect to the unsmeared distribution is taken as resolution uncertainty.
For the jet mass resolution uncertainty, a relative jet mass resolution smearing of 20% is applied to each jet. In order to apply relative smearing, it is necessary to have the approximate resolution of each jet. This is obtained through resolution maps that depend on the assumption of the origin of the jet: a top-jet, W/Z-jet, or $H \to b\bar{b}$-jet. The simulated jets are therefore truth-matched jet-by-jet to determine which of the three different sample topologies is relevant for the jet mass resolution.

5.3.6 b-jet identification and $H \to b\bar{b}$ tagging

To identify jets generated by b-hadrons, named b-jets, several b-tagging algorithms have been developed. Such algorithms take as an input the charged particle tracks produced in the b-quark decay and hadronisation. The principle of identification of the b-jets is shown in Figure 5.15. The lifetime of b quarks is of the order of 1.5 ps. This implies that b-hadrons with a transverse momentum of a few tens of

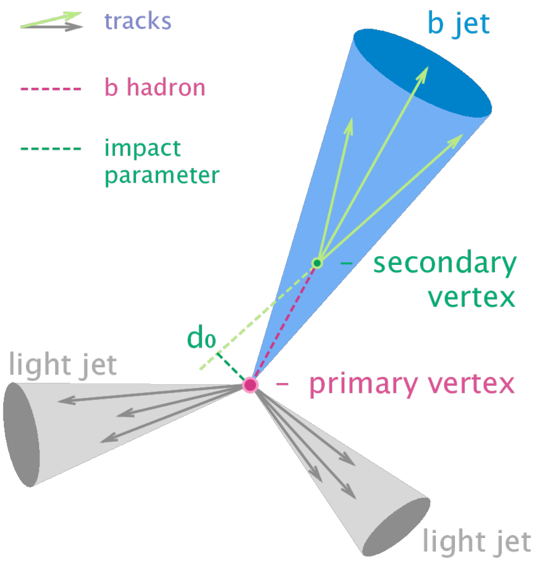

Figure 5.15: Diagram showing the principle of identification of jets initiated by b-hadron decays [110].

GeV travel on average a few *mm* in the detector before decaying. This lead to topologies with at least one *secondary vertex* separated from the *primary vertex*. Additionally, b-hadrons have a relatively heavy mass (around 4 GeV) and tracks from the b-hadron decays will have on average larger invariant mass and larger multiplicity with respect to the tracks from light quarks decays. The long lifetime, high mass and high decay multiplicity of b-hadrons are exploited by the b-tagging algorithms to distinguish the b-jets from the jets produced by light flavour hadrons. The tracks used by the b-tagging algorithm are associated with the jets based on their angular separation ΔR and are required to have p_T >1 GeV [111]. The ΔR cut varies as a function of the jet p_T, with a narrower cone for jets at high p_T, which are more collimated.
Several low-level b-tagging algorithms have been developed in ATLAS. The output of these b-tagging algorithms has been later combined by high-level taggers using a multivariate classifier to maximise the b-tagging performance. In this analysis, the multivariate discriminant named MV2 is used [112]. MV2 combines (i) variables based on the impact parameter measurement, (ii) variables obtained from the reconstruction of the secondary vertices and (iii) variables built from the attempt to reconstruct the full b-to-c-hadron decay chain. The distributions of the MV2 discriminant for the b-jets, c-jets and light-flavour jets are shown in Figure 5.16 (left). Such distributions are computed using simulated $t\bar{t}$ events. In the simulation the jet flavour labels are attributed looking at the truth particles. Jets are labelled as b-jets if they are matched to at least one weakly decaying b-hadron having

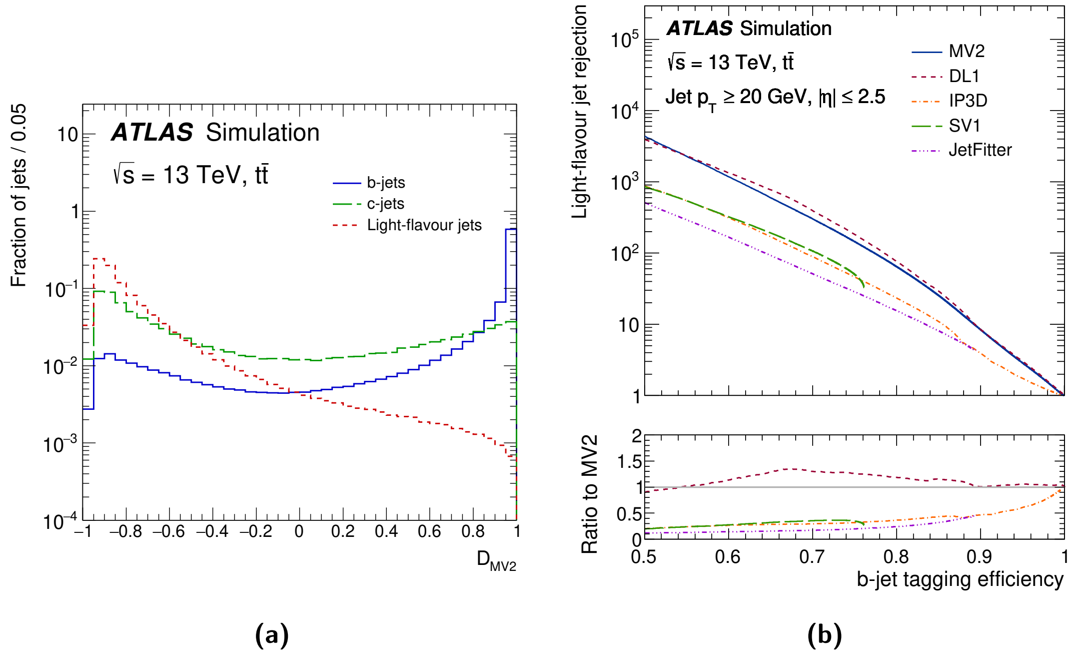

Figure 5.16: (a) Distribution of the b-tagging discriminant MV2 for b-jets, c-jets and light-flavour jets in the $t\bar{t}$ simulated events.
The light-flavour jet rejections versus the b-jet tagging efficiency for the MV2, IP3D, SV1, JetFitter and DL1 b-tagging algorithms evaluated on the $t\bar{t}$ events [113].

$p_T \geq 5$ GeV within a cone of size $\Delta R = 0.3$ around the jet axis. If no b-hadrons are found, c-hadrons and (then τ-leptons) are searched for. The jets matched to a c-hadron (τ-lepton) are labelled as c-jets (τ-jets). The remaining jets are labelled as light-flavour jets. The MV2 variable distribution is built to separate b-jets, peaking at high value of MV2, from light jets, peaking at low values of MV2. The MV2 cut is tuned to produce an average efficiency of 70% for b-jets in simulated $t\bar{t}$ events. The b-tagging efficiency vs. light-flavour jet rejection is shown in Figure 5.16 (right). The 70% b-jet efficiency corresponds to c-jet rejection equal to 8.9 and to a light-flavour jet rejection equal to 300 [113].
The b-tagging algorithm described above can be applied in the same way to small-R calo-jets and to track-jets. The tracks used in the b-tagging algorithms, of course, do not include all the tracks of the events but only tracks associated with the jet. The association is performed looking at the angular separation ΔR between the track and the jet axis. The ΔR requirement varies as a function of jet p_T and it is wider for low p_T values (0.45 for jet p_T of 20 GeV) and narrower for high values (0.26 for jet p_T of 150 GeV) [113].

$H \rightarrow b\bar{b}$ tagging and jets correction in the resolved analysis

Higgs bosons decaying into two b-quarks are typically identified by b-tagging two small-R calo-jets. This is what is done in the *resolved* analysis, using jets with cone R=0.4. b-tagged jets are further corrected to take into account the presence of muon from b- and c-hadron decays, which do not deposit their full energy in the calorimeter. This procedure is named *muon-in-jet* correction. When medium quality muon with $p_T > 5$ GeV is found within $\Delta R = 0.4$ of a jet no isolation criteria are applied on such muons. When more than one muon is found, the one closest to the jet axis is chosen. The muon four-momentum is added to that of the jet, and the energy deposited by the muon in the calorimeter is removed, allowing a better evaluation of the jet p_T and direction.
To further improve the jet response, a second correction, denoted *PtReco*, is applied. This correction, applied as a function of jet p_T, is derived separately for jets with or without a lepton (muon or electron) found within $\Delta R = 0.4$ of the jet axis. It is based on the difference in jet response expected from the signal simulation between the reconstructed b-jets (with the *muon-in-jet* correction already applied) and the corresponding truth jets. For jets without a matching lepton, the *PtReco* correction increases the energy of jets with $p_T \sim 20$ GeV by 12% and the energy of those with $p_T > 100$ GeV by 1%, while a larger correction is observed for jets matched to a lepton, due to the missing neutrino energy.

$H \rightarrow b\bar{b}$ tagging in the merged analysis

As already mentioned, in the *merged* analysis the Higgs boson is reconstructed through a single, large-R jet. The b-tagging algorithms described above cannot be trivially applied to the large-R jet, as they are optimised to identify a small-R jet from a single b-hadron decay. In order to identify the boosted Higgs and have a good background rejection, it is paramount to understand the large-R jet substructure and identify two b-hadrons within the large-R jet. At the moment the ATLAS collaboration has not developed a dedicated tagging algorithm to identify boosted Higgs bosons decaying to b-hadrons. The Higgs boson is instead identified in two steps: first, identifying the track-jets associated to the large-R and secondly applying the b-tagging algorithms to the matched track-jets. More details about b-tagging track-jets are given in the following chapter.

5.3.7 Track-jets

Track-jets are jets reconstructed by applying the jet clustering algorithm on the tracks emerging from the hard scatter vertex. Track-jets used in this analysis are reconstructed from ID tracks using the anti-k_t algorithm with a jet p_T dependent distance parameter $R(p_T) = \rho/p_T$ where the parameter ρ determines how rapid the effective jet size decreases with p_T. The upper and lower bounds R_{max} and R_{min} are set as cut-offs [114, 115]. The parameters chosen for this thesis are $\rho = 30$ GeV, $R_{max} = 0.4$ and $R_{min} = 0.02$ [116]. These parameters have been chosen to optimize the double b-tagging efficiency in boosted $H \to b\bar{b}$ decays [117]. The tracks composing the jets are required to have $p_T > 0.5$ GeV, at least 1 hit in the PIXEL detector and 6 hits in the SCT, and to be tightly matched to the hard scatter vertex using impact parameter thresholds on the tracks. Such requirements greatly reduce the number of tracks from pile-up vertices whilst being highly efficient for tracks from the hard scatter vertex.

The track-jets are required to have $p_T > 10$ GeV, $|\eta| < 2.5$, and they need to have more than one track as a constituent.

Track-jets are used in this analysis only to tag jets containing b-hadrons within large-R jets. In fact, it has been shown that there are several benefits of b-tagging track-jets instead of b-tagging calo-jets, especially in boosted topologies, as detailed in the following [114, 115].

As track-jets are explicitly chosen to originate from the primary vertex the performance dependence on pile-up is significantly reduced compared to the calorimeter jets performance. Such pile-up reduction allows using track-jets with a low p_T threshold. This feature is especially important when reconstructing low p_T b-hadrons. In fact low p_T b-hadrons that can be present in events where one of the b-hadron from the Higgs decay is produced in the opposite direction with respect to the boost of the Higgs. These relatively low-p_T b-hadrons might otherwise be lost due to the higher p_T-threshold that is imposed on calorimeter jets in order to reduce pile-up.

Additionally, as b-tagging algorithms only use information from the ID, they can be decoupled from calorimeter jet finding in order to identify b-hadrons. The track-jet algorithm can therefore be optimized and calibrated specifically for b-tagging, independent of the calorimeter jet algorithm, which can be optimized separately to interpret the hadronic final state. The b-tagging information provided by the track-jets can be then integrated with the calorimeter jet algorithm using the ghost-association technique described in Section 5.3.8.

Finally, ATLAS b-tagging algorithms look for b-hadrons locally around a seed direction defined by the jet axis. Track-jets have good angular resolution with respect to the b-hadron, even in environments with dense hadronic activity. This allows for the accurate determination of the seed direction for b-hadron identification within boosted topologies.

5.3.8 Large-R jets to track jets association

In events with a dense hadronic environment, there can often be ambiguity when trying to match track-jets to the calorimeter large-R jets. To overcome this ambiguity the track-jet association to large-R jets is performed using ghost-association technique, which provides a robust matching procedure that makes use of the catchment area of the jet [118]. Using this technique the matching to jets with irregular boundaries is less ambiguous than a simple geometric (i.e. ΔR) matching. In this procedure, the "ghosts" are the track-jet 4-vectors with the track-jet p_T set to an infinitesimal amount. Thus the 4-vectors only retain the direction of the track-jets. The association proceeds by performing again the jet clustering algorithm, which in this case is anti-k_t, fed with both the calorimeter clusters and the ghosts track-jets. A track-jet is considered ghost-associated with a jet if its ghost version is contained in the jet after reclustering. The infinitesimal p_T of the ghosts and the resilience of the jet algorithm to soft particles ensures that no difference is obtained in the final jet with respect to the one clustered without ghosts.

5.4 Missing transverse momentum

The missing transverse momentum, E_{T}^{miss}, is an important observable serving as an experimental proxy for the transverse momentum carried by undetected particles produced in the collisions. It is reconstructed from the signals of reconstructed objects in the event and obtained as the momentum imbalance in the plane transverse to the beam axis. Such an imbalance may signal the presence of undetectable particles, such as neutrinos.
E_{T}^{miss} variable plays a key role in both the 0- and 1-lepton channels. Indeed, these channels contain a vector boson that decays either to two neutrinos or to one charged lepton plus a neutrino. In both cases, the neutrino appears as an imbalance in transverse momentum. In the 2-lepton channel, the E_{T}^{miss} is instead used to suppress background.
The reconstruction of E_{T}^{miss} is challenging because it involves all detector subsystems and requires a complete and unambiguous representation of the hard interaction of interest by calorimeter and tracking signals. This representation is complicated by the limitations introduced by the detector acceptance and by the impact of online

and offline pile-up.
The reconstructed E_{T}^{miss} in ATLAS is characterised by two contributions[119]. The first one is from the *hard-event* signals, comprising fully reconstructed and calibrated particles and jets (hard objects). The reconstructed particles are electrons, photons, τ-leptons, and muons. The second contribution originates from the *soft-event* signals consisting of reconstructed charged-particle tracks (soft signals) associated with the hard-scatter vertex but not with hard objects.
A dedicated reconstruction procedure is carried out for each kind of particle as well as for jets, casting a particle or jet hypothesis on the origin of a group of detector signals. These procedures are independent of one another. This means that e.g. the same calorimeter signal used to reconstruct an electron is likely also used to reconstruct a jet, thus potentially introducing double counting. This issue is addressed by applying the *signal ambiguity resolution* procedure, which rejects already used signals when combining the various E_{T}^{miss} contributions [119].

The E_{T}^{miss} reconstruction performance is assessed by comparing the E_{T}^{miss} distributions in data and MC simulations, applying the same object and event selections. Systematic uncertainties in the E_{T}^{miss} response and resolution are then derived from these comparisons. The E_{T}^{miss} distributions obtained by applying a selection aimed at identifying $W \to e\nu$ (left) and $Z \to \mu\mu$ (right) events are shown in Figure 5.17. In the first case a genuine missing transverse momentum is expected while in the second it is not. For the $W \to e\nu$ distribution the data and MC simulations agree within 20% for most of the E_{T}^{miss} distribution, with larger differences not accommodated by the total uncertainties for high E_{T}^{miss} values. These differences suggest a mismodelling in $t\bar{t}$ events, which is the dominant background at high E_{T}^{miss} values. The level of agreement for the $Z \to \mu\mu$ selection is at $\sim \pm 20\%$.

The deviation from linearity in E_{T}^{miss} reconstruction, is measured by

$$\Delta_T^{lin}(E_{\mathrm{T}}^{miss,true}) = \frac{E_{\mathrm{T}}^{miss} - E_{\mathrm{T}}^{miss,true}}{E_{\mathrm{T}}^{miss}}$$

The deviation from linearity as a function of $E_{\mathrm{T}}^{miss,true}$ for MC simulations of $W \to e\nu$, $W \to \mu\nu$ and $t\bar{t}$ production is shown in Figure 5.18 on the left.
The observed $\Delta_T^{lin} > 0$ at low values of $E_{\mathrm{T}}^{miss,true}$ indicates an overestimation of $E_{\mathrm{T}}^{miss,true}$ by the reconstructed E_{T}^{miss} due to the so-called *observation biases*. As not all relevant p_T from the hard-scatter interaction can be included in the E_{T}^{miss} and the reconstructed p_T from each contribution is affected by the limited resolution of the detector, an observation bias towards non-vanishing values for E_{T}^{miss} is introduced. For $E_{\mathrm{T}}^{miss,true} > 70$ GeV the E_{T}^{miss} response is directly proportional to $E_{\mathrm{T}}^{miss,true}$, with the reconstructed recoil being approximately 2% too small. The $W \to e\nu$ and $W \to \mu\nu$ final states show very similar deviations from linearity as

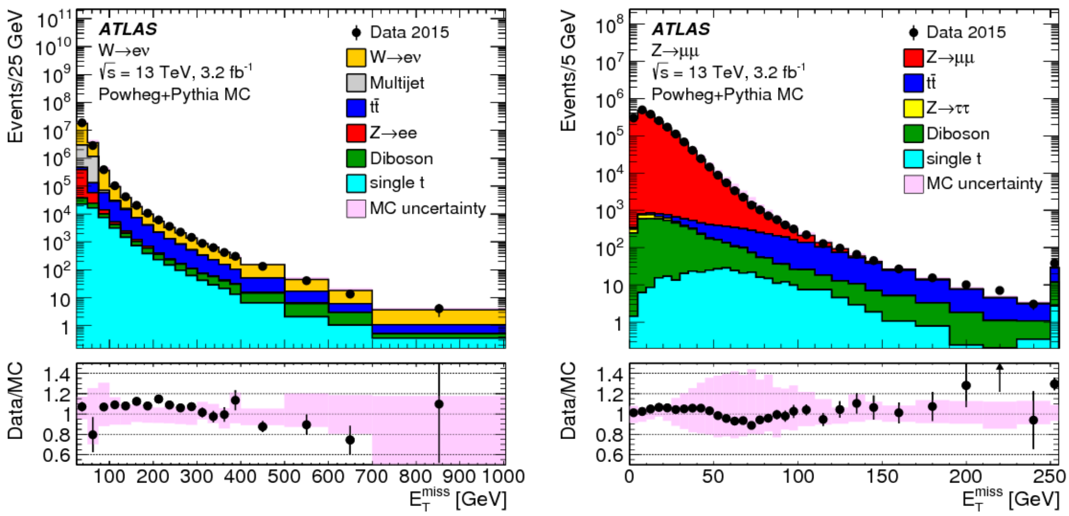

(a) (b)

Figure 5.17: Distributions of E_{T}^{miss} a $W \to e\nu$ (left) and $Z \to \mu\mu$ selection in data, compared to MC simulations including all relevant backgrounds. The shaded areas indicate the total uncertainty from MC simulations, including the overall statistical uncertainty combined with the p_T scale and resolution which are contributed by muons, jets, and the soft term. The respective ratios between data and MC simulations are shown below the distributions, with the shaded areas showing the corresponding total uncertainties from MC simulations [119].

a function of $E_{\mathrm{T}}^{miss,true}$, indicating the independence on the lepton flavour of the reconstructed E_{T}^{miss} in a low-multiplicity final state with $E_{\mathrm{T}}^{miss,true} > 0$.
In $t\bar{t}$ final-state reconstruction, Δ_T^{lin} is dominated by resolution effects up to $\sim$ 120 GeV. The poorer E_{T}^{miss} resolution (compared to $W \to e\nu$ and $W \to \mu\nu$) is due to the presence of at least four jets with relatively low p_T and high sensitivity to pile-up-induced fluctuations in each event of the $t\bar{t}$ sample. For $E_{\mathrm{T}}^{miss,true} \gtrsim$ 120 GeV, $\Delta_T^{lin}(E_{\mathrm{T}}^{miss,true}) \sim 2\%$ indicates a proportional E_{T}^{miss} response with a systematic shift similar to the one observed in $W \to e\nu$ and $W \to \mu\nu$.
The E_{T}^{miss} resolution is determined by the width of the distribution of the differences between the measured E_{T}^{miss} components and the components of the true missing transverse momentum vector $E^{miss,true}$.

$$RMS_{x(y)}^{miss} = RMS(E_{x(y)}^{miss} - E_{x(y)}^{miss,true})$$

The E_{T}^{miss} resolution for final states with $E_{\mathrm{T}}^{miss,true} > 0$ is measured using dedicated inclusive $W \to e\nu$, $W \to \mu\nu$ and $t\bar{t}$ samples from MC simulations. The $RMS_{x(y)}^{miss}$ is shown in Figure 5.18 (right) as a function of $E_{\mathrm{T}}^{miss,true}$. As already observed in Figure 5.18 (left), the E_{T}^{miss} resolution is very similar for $W \to e\nu$ and $W \to \mu\nu$ final states, while it is poorer in $t\bar{t}$ final states.

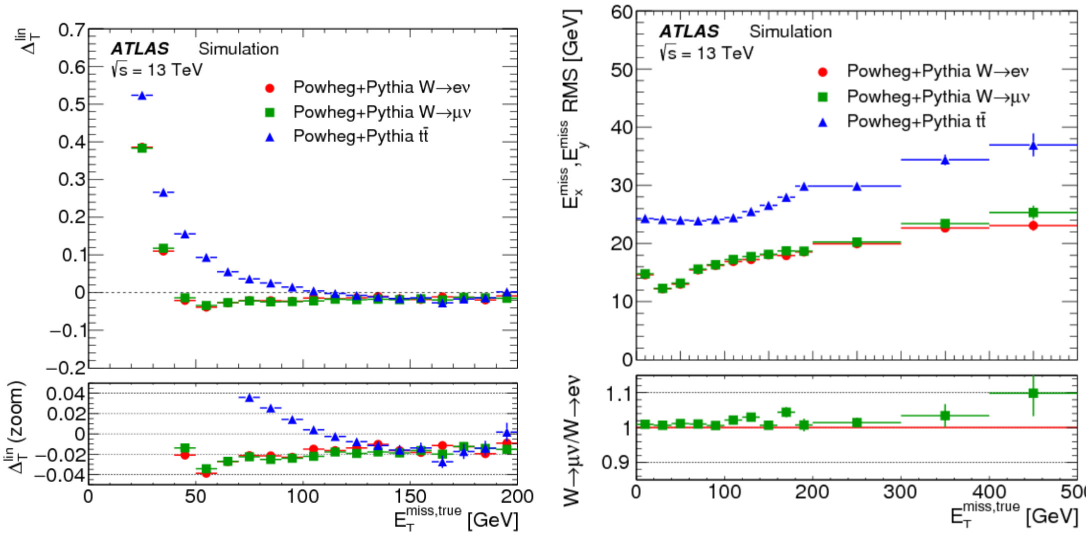

(a) **(b)**

Figure 5.18: The deviation of the E_{T}^{miss} response from linearity, measured as a function of the expected $E_{\mathrm{T}}^{miss,true}$ in $W \to e\nu$, $W \to \mu\nu$ and $t\bar{t}$ final states in MC simulations. The lower plot shows a zoomed-in view of the same distribution with a suppressed ordinate [119].

E_{T}^{miss} uncertainties are mainly related to the soft term in the E_{T}^{miss} calculation, as the uncertainties on the hard terms are already included in the systematics related to the other physics objects mentioned, and propagated to the E_{T}^{miss} calculation. These uncertainties, associated to the E_{T}^{miss} scale and resolution for the soft term, are derived by comparing data to MC simulations.

Chapter 6

Event selection

In this chapter, the selection of candidate $VH(H \to b\bar{b})$ events is described. The first part discusses the criteria aiming at identifying the VH events at trigger level. In the second section, the selection of the candidate Higgs boson is described, highlighting the differences between the selection in the resolved and merged analyses. All the signal regions and control regions included in the fit are described in the third section, together with the selections implemented in the three lepton channels. In the fourth section, some details are given about the event categorization according to the number of jets, in particular within the merged analysis event selection. Finally, the multivariate technique used to increase the signal-background separation is illustrated.

6.1 Candidate vector boson selection

The selection of the candidate $VH(H \to b\bar{b})$ events includes an online selection, described in detail in Section 4.1 and summarised in this section, and an offline selection, described in the next two sections. The online event selection relies on the E_{T}^{miss} in the 0-lepton channel. In the 1-lepton channel, the electron sub-channel relies on the single-electron triggers, while events in the muon sub-channel are selected using E_{T}^{miss} triggers. The online selection in the 2-lepton channel relies on single-electron and muons triggers.
Events passing the trigger selection and satisfying basic quality requirements are assigned to the 0-lepton, 1-lepton and 2-lepton channels depending on the number of charged leptons. This observable, used in the event selection, corresponds to E_{T}^{miss} in the 0-lepton channel, to the magnitude of the vectorial sum of E_{T}^{miss}

and the charged lepton transverse momentum in the 1-lepton channel, and to the transverse momentum of the 2-lepton system in the 2-lepton channel. The selection of the candidate Higgs boson is instead common to the three channels and described in the next section.

6.2 Candidate Higgs boson selection

The event selections of the *resolved* and the *merged* analyses differ in three main aspects. The first one is the selection of the candidate Higgs boson, which has been already mentioned and is described in details in the following. The other two are the vector boson transverse momentum magnitude and the categorisation, described in the next section. The candidate Higgs selection is summarised in Table 6.1 both for the *merged* and the *resolved* selection.

6.2.1 *Resolved* analysis

In the *resolved* analysis, the candidate Higgs boson is selected through two b-tagged jets with radius parameter $R = 0.4$. The jets are required to satisfy the quality and selection criteria detailed in Chapter 5. Jets reconstructed in the region $|\eta| < 2.5$ are required to have $p_T > 20$ GeV and jets reconstructed at 2.5$< |\eta| < 4.5$, are required to have $p_T > 30$ GeV. The variable used for the b-tagging is MV2, tuned to produce an average efficiency on p_T of 70% for b-jets. Selected events contain exactly two b-tagged jets, and at least one of them is required to have $p_T > 45$ GeV.
b-tagged jets are corrected to take into account the presence of muons from b- and c-hadron decays, which give a few GeV energy loss in the calorimeter, with the *muon-in-jet* correction (described in Section 5.3.6). To further improve the jet response, the *PtReco* correction is applied as well (Section 5.3.6). These two corrections result in an improved m_{bb} mass resolution of about 20%.
In the 2-lepton channel, the energy calibration of the jets is further improved by a kinematic likelihood fit, in place of the *PtReco* correction. This correction is possible in this channel as the $ZH \to \ell\ell b\bar{b}$ event kinematics can be fully reconstructed. The kinematic fit includes a Breit–Wigner constraint on the dilepton mass, a Gaussian constraints on each of the transverse components of the two b-jets system momentum, a dedicated transfer functions relating the true jet transverse momenta to their reconstructed values as well as a prior built from the expected true jet p_T spectrum in ZH events. The combination of the *muon-in-jet* and kinematic fit

corrections results in an improved m_{bb} mass distribution resolution of about 40%.

6.2.2 *Merged* analysis

As discussed in Section 5.3, as the Higgs boson transverse momentum (p_{T}^{H}) increases the two b-jets produced in its decay tend to coalesce, and the *resolved* analysis efficiency consequently decreases. To overcome this problem the *merged* analysis has been designed to select the decay products using a single large-R jet.
The approximate angular distance between the decay products is $\Delta R \sim 2M/p_T^H$ therefore for $p_{\mathrm{T}}^{H} \sim 250$ GeV a jet with $R = 1$ would collect both decay products. For this reason, in the *merged* analysis, events are selected if they contain at least one large-R jet with $p_T > 250$ GeV and $|\eta|<2.0$; the leading large-R jet is chosen as Higgs candidate. As about 20% of $H \to b\bar{b}$ large-R jets have semileptonic decay muons, also for large-R jet the *muon-in-jet* correction is applied to recover the jet response using reconstructed muons (Section 5.3.6). This correction results in a m_{J} resolution improved by about 10%.
As for the *resolved* analysis, a kinematic likelihood fit correction is applied in the 2-lepton channel, resulting in an improved m_{J} resolution up to $\sim$ 40%.
The large-R jet, candidate Higgs boson, is also required to be matched to at least two track jets with $p_T >$10 GeV. The matching between the large-R jet and the track jets is obtained using the ghost association technique (Section 5.3.8). The b-tagging is performed on the associated track jets, which allows accessing all the information needed for MV2. The two leading track jets associated with the selected large-R jet are required to be b-tagged.

	Resolved	*Merged*
jets	2+jets, $R = 0.4$	1+jet, $R = 1.0$
jet p_T	p_{Tj}>20 GeV ($\|\eta\| < 2.5$) p_{Tj}>30 GeV ($2.5 < \|\eta\| < 4.5$)	$p_{TJ} > 250$ GeV
η	$\|\eta_j\| < 2.5$	$\|\eta_J\| < 2.0$
b-tagging	exactly two b-tagged jets	the two leading track jets matched to large-R jets are b-tagged
b-jets	$p_{Tb1} > 45$ GeV	$p_{T\text{track jets}} > 10$ GeV

Table 6.1: Summary of the candidate Higgs boson selection for the *resolved* and *merged* analysis.

6.3 Signal and control regions definition

As each lepton channel is dominated by different background processes, additional selections are defined in each of these channels and are described in this section. These selections have first been studied and optimised in the *resolved* analysis and then adapted to the *merged* analysis. As there are not many differences between the *resolved* and *merged* selection both is described below, highlighting the most relevant differences.
For each lepton channel, events are categorised in several *signal regions* (SRs) to enhance the significance. Moreover, to evaluate the contributions of the dominant background processes, several *control regions* (CRs) are defined as well. It is not always possible to define CRs for all background processes and all lepton channels. However, since both for the *resolved* and *merged* analysis all the SRs and CRs are fit simultaneously, the top and V+HF CRs, even if defined for a specific lepton channel, are useful to control the background processes in signal regions with similar characteristics. All the SRs and CRs included in the fit are defined in this section.
At first, categorisation is done based on the reconstructed transverse momentum of the vector boson, p_{T}^{V}, as described in Table 6.2. The phase space with the highest signal-to-background ratio is in fact at large values of the candidate Higgs boson transverse momentum, also corresponding to large values of p_{T}^{V}. The chosen p_{T}^{V} categorisation is coherent with the categorisation adopted in the Simplified Template Cross Section (Chapter 7).

	Resolved	*Merged*
0-lepton, 1-lepton	p_{T}^{V} >150 GeV	250 GeV $<p_{\mathrm{T}}^{V}<$400 GeV p_{T}^{V} >250 GeV
2-lepton	75 GeV$<p_{\mathrm{T}}^{V}<$150 GeV p_{T}^{V} >150 GeV	250 GeV $<p_{\mathrm{T}}^{V}<$400 GeV p_{T}^{V} >250 GeV

Table 6.2: Summary of the vector boson transverse momentum categorisation.

The selection applied to the electrons and muons used in the event selection is summarised in Table 6.3. The VH-loose leptons defined in the table are used to categorise the events into the three lepton categories (0-lepton, 1-lepton, 2-lepton). The events that have more than two VH-loose leptons are discarded. In 1-lepton channel the lepton is also required to pass the WH-signal selection, while in the 2-lepton channel at least one lepton needs to pass the ZH-signal selection.

Electron Selection	p_T	η	ID	d_0^{sig}
VH-loose	>7 GeV	$\lvert\eta\rvert < 2.47$	*loose*	< 5
ZH-signal	>27 GeV	$\lvert\eta\rvert < 2.47$	*loose*	< 5
WH-signal	>27 GeV	$\lvert\eta\rvert < 2.47$	*tight*	< 5
Muon Selection	p_T	η	ID	d_0^{sig}
VH-loose	>7 GeV	$\lvert\eta\rvert < 2.7$	*loose*	< 3
ZH-signal	>27 GeV	$\lvert\eta\rvert < 2.5$	*loose*	< 3
WH-signal	>25 GeV	$\lvert\eta\rvert < 2.5$	*medium*	< 3

Table 6.3: Electron and muon selection requirements. All leptons also respect the requirement $|\Delta z_0 \sin\theta| < 0.5$ mm and the isolation requirement mentioned in Section 5.2. The lepton identification criteria, *loose*, *medium* and *tight*, have been defined in Section 5.2.

6.3.1 0-lepton channel

Signal regions

Events passing the online selection in the 0-lepton channel are required to have no loose leptons. The missing transverse momentum is required to be E_{T}^{miss} >150 GeV for the *resolved* analysis and E_{T}^{miss} >250 GeV for the *merged* analysis. In the *resolved* analysis, events are selected with exactly two or exactly three jets, including the two b-jet candidates. Events with four or more jets are rejected to reduce the background arising from $t\bar{t}$ production. The events are categorised according to the jet multiplicity (2-jets and 3-jets categories). Also in the *merged* analysis events are categorised according to the jet multiplicity, in this case, defined as the number of additional jets outside of the large-R jet. Such additional jets are calorimeter jets with radius $R = 0.4$ and $p_T > 30$ GeV. This categorisation allows increasing the analysis sensitivity isolating a region with higher expected significance (0 additional jets) from a region with lower expected significance (1 or more additional jets). A study justifying this categorisation is described in Section 6.4.

In the *resolved* analysis 2-jet events are required to have the scalar sum of the transverse momenta of the jets $H_T > 120$ GeV while 3-jet events are required to have $H_T > 150$ GeV. This criterion is designed to remove a region mis-modelled in simulation due to a non-trivial dependence of the trigger efficiency on the jet activity.

High E_{T}^{miss} in multi-jet events is mostly due to mismeasured jets in the calorimeters. Such events are produced with a large cross-section and give rise to potentially large backgrounds. Multi-jet events are therefore removed by applying dedicated angular selection criteria:

- $\Delta\phi(E_{\mathrm{T}}^{miss}, H_{cand}) > 120°$, where E_{T}^{miss} is the missing transverse momentum and H_{cand} is the Higgs boson candidate, calculated from the kinematic variables of the two selected b-jets (large-R jet) in the *resolved* (*merged*) selection;

- $\Delta\phi(E_{\mathrm{T}}^{miss}, p_{T,trk}^{miss}) < 90°$, where $p_{T,trk}^{miss}$ is the missing transverse momentum calculated using only tracks associated to the primary vertex of the event;

- $\Delta\phi(b_1, b_2) < 140°$, where b_1 and b_2 indicates the two b-jets;

- $min[\Delta\phi(E_{\mathrm{T}}^{miss}, jets)] > 20°$ for 2-jets category and $> 30°$ for 3-jets category for the *merged* analysis. This selection requires a minimum azimuthal separation between the E_{T}^{miss} and any jet in the event. In the *merged* analysis only small-R calo-jets outside the large-R jet with $p_T > 70$ GeV are considered.

The angular selection described is applied both in the *resolved* and *merged* analysis. The only small difference is the angular cut on $min[\Delta\phi(E_{\mathrm{T}}^{miss}, jets)]$ that is always set at 30° in the *merged* analysis. The event selection is summarised in Table 6.4.

Resolved	Merged
no loose leptons	
$E_{\mathrm{T}}^{miss} > 150$ GeV $H_T >$120 GeV for 2-jets, $H_T >$120>150 GeV for 3-jets	$E_{\mathrm{T}}^{miss} > 250$ GeV
$\Delta\phi(E_{\mathrm{T}}^{miss}, p_{T,trk}) < 90°$	
$\Delta\phi(b_1, b_2) < 140°$	
$\Delta\phi(E_{\mathrm{T}}^{miss}, bb) > 120°$	
$min[\Delta\phi(E_{\mathrm{T}}^{miss}, jets)] > 20°$ for 2-jets, $min[\Delta\phi(E_{\mathrm{T}}^{miss}, jets)] > 30°$ for 3-jets	$min[\Delta\phi(E_{\mathrm{T}}^{miss}, jets)] > 20°$

Table 6.4: Summary of the event selection in the 0-lepton channel. This summary does not include the candidate Higgs boson selection.

The post-fit m_{bb} distribution for data and simulation in *resolved* 2-jet SR is shown in Figure 6.1a to give an idea of the main background processes in the 0-lepton channel. The data are shown as back dots, while the signal and background contributions after the global likelihood fit are shown as filled histograms. The Higgs boson signal is also shown unstacked as an unfilled histogram, scaled by the factor indicated in the legend. The size of the combined statistical and systematic uncertainty for the sum of the signal and background is indicated by the hatched band. The ratio of the data to the sum of the signal and background is shown in the lower panel. The same style and convention are used also for the following pre-fit and post-fit plots in this chapter. The dominant backgrounds are the $V + HF$

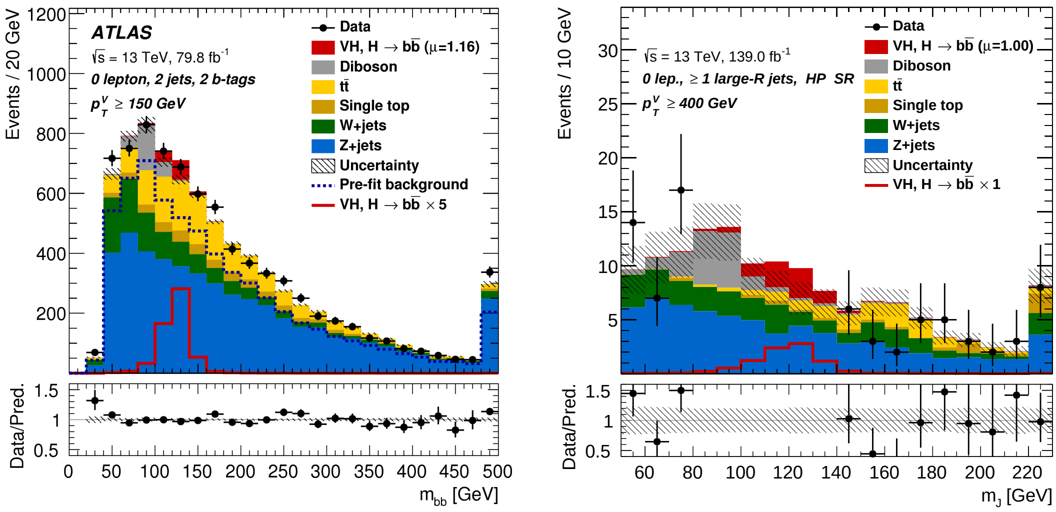

(a) **(b)**

Figure 6.1: The post-fit distributions for m_{bb} in the 0-lepton channel for the *resolved* analysis channels for 2-jet events (left). The pre-fit distribution of the large-R jets mass, m_{J}, in the 0-lepton channel for the *merged* analysis in the SR with p_{T}^{V} >400 GeV and 0 additional jets. The data are shown as back dots. The signal and background contributions are shown as filled histograms. The Higgs boson signal is also shown unstacked as an unfilled histogram, scaled by the factor indicated in the legend. The size of the combined statistical and systematic uncertainty for the sum of the signal and background is indicated by the hatched band.

and top processes. The pre-fit distribution of the large-R jet mass, m_{J}, for data and simulation in the 0-lepton channel *merged* SR is shown in Figure 6.1b. This region has p_{T}^{V} >400 GeV and no additional jets. In this and in the following m_{J} distributions in the *merged* SR the data are shown for the region m_{J} = [80,140] GeV of the, as the analysis is still "blinded". Differently from the resolved case, the m_{J} distribution is only studied starting at 50 GeV, as the large-R jet calibration below this value is affected by large uncertainties. The background composition in the SR for the *resolved* and *merged* analyses are very similar. A dedicated top CR is included in the fit both for the *resolved* and *merged* analyses.

Control regions

An important difference between the *merged* and the *resolved* analysis is the definition of the $t\bar{t}$ control regions. In the merged analysis, it is possible to define a data-sample enriched of top background by selecting events according to the number of b-tagged track jets not overlapping with the large-R jet. The SRs contain only events with no b-tagged track jets outside of the large-R jet while the CRs contain events with at least one b-tagged track jet outside of the large-R jet. With this definition, most of the events in the CRs are from the $t\bar{t}$ background process ($\sim$ 80% in the region 250 GeV $< p_{\mathrm{T}}^{V} <$ 400 GeV and $\sim$ 56% in the region p_{T}^{V} >400 GeV). The pre-fit plots of the CRs for the *merged* analysis in the 0-lepton channel are shown in Figure 6.2. A coarser binning has been chosen w.r.t. the SRs due to the low statistic. The *resolved* top CR will instead be defined in the

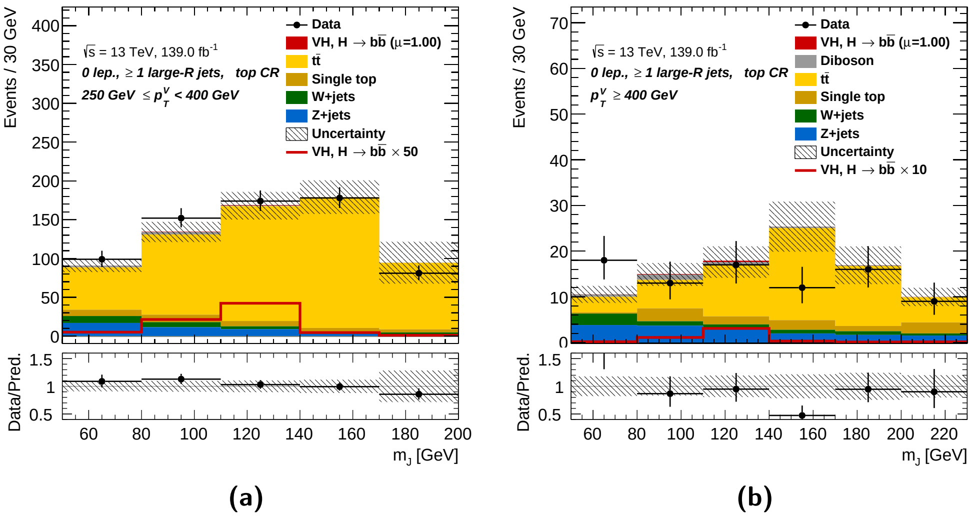

Figure 6.2: The pre-fit distributions for m_J in the 0 lepton channel for the 250<p_{T}^{V} <400 GeV category (left) and the p_{T}^{V} >400 GeV category (right). The data are shown as back dots. The signal and background contributions are shown as filled histograms. The Higgs boson signal is also shown unstacked as an unfilled histogram, scaled by the factor indicated in the legend. The size of the combined statistical and systematic uncertainty for the sum of the signal and background is indicated by the hatched band.

2-lepton channel.

6.3.2 1-lepton channel

Signal regions

Events in the 1-lepton channel are required to contain exactly one tight electron or muon (with p_T above 27 GeV and 25 GeV, respectively) and no additional loose leptons. They are required to have p_{T}^{V} >150 GeV for the *resolved* analysis and p_T^V >250 GeV for the *merged* analysis. The event selection in this channel is divided into the electron and muon sub-channels. In the electron sub-channel, the requirement $E_T^{miss} > 30$ GeV is applied to reduce the multi-jet background. The event selection is summarised in Table 6.5.

Resolved	Merged
$p_T^V > 150$ GeV	$p_T^V > 250$ GeV
exactly one tight electron or muon and no additional loose leptons	
$E_T^{miss} > 30$ GeV	

Table 6.5: Summary of the event selection in the 1-lepton channel. This summary does not include the candidate Higgs boson selection.

As for the 0-lepton channel, in the *resolved* analysis events are considered with exactly two or exactly three jets, including the two b-jets candidate. Events with four or more jets are rejected to reduce the background arising from $t\bar{t}$ production. In the *merged* analysis events are categorised according to the number of additional calo-jets outside of the large-R jet. Additionally, for the *resolved* analysis events selected in the 1-lepton CRs, described in next section, are vetoed.
The post-fit m_{bb} distribution in the 2-jet signal region is shown in Figure 6.3a. The dominant background processes are $t\bar{t}$ and $W + HF$. The pre-fit distribution of the large-R jet mass, m_J, in the *merged* analysis is shown in Figure 6.3b. Also in this case the background composition of the SRs in the *merged* analysis is very similar to the background composition in the *resolved* analysis.

Control regions

In the *resolved* analysis, control regions enhanced in the $W + HF$ background are obtained by applying two additional selection requirements: $m_{bb} < 75$ GeV and $m_{top} > 225$ GeV. The top mass (m_{top})is calculated as the invariant mass of the lepton, the reconstructed neutrino and the b-jet that yields the lowest value. The requirement on the top quark mass significantly reduces the $t\bar{t}$ and single-top-quark events in the $W + HF$ CRs. Events satisfying the CR selection are not included in the signal regions. The $W + HF$ CR for the 2-jet events is shown in Figure 6.4a. The resulting purity of the W+HF control region is about 75%. No equivalent dedicated $W + HF$ CR is used in the *merged* analysis, which relies uniquely in the SRs to control the $W + HF$ background.
As for the 0-lepton analysis, in the *merged* analysis the CR enriched in $t\bar{t}$ events is obtained by selecting events according to the number of b-tagged track jets. The

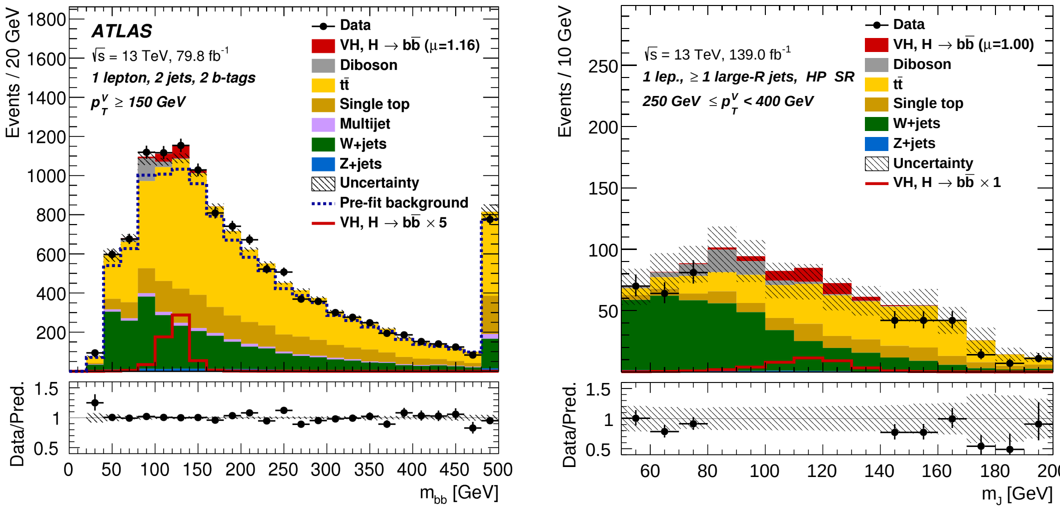

(a) (b)

Figure 6.3: The post-fit distributions for m_{bb} for 2-jet events in the *resolved* analysis [60]. The pre-fit distribution for the large-R jet mass, m_J, in the 0 additional jets category with p_{T}^{V} >400 GeV, for the *merged* analysis. The data are shown as back dots. The signal and background contributions are shown as filled histograms. The Higgs boson signal is also shown unstacked as an unfilled histogram, scaled by the factor indicated in the legend. The size of the combined statistical and systematic uncertainty for the sum of the signal and background is indicated by the hatched band.

CRs for the 1-lepton channel are shown in Figure 6.5. The fraction of $t\bar{t}$ events in the CRs is $\sim 90\%$. The available number of $t\bar{t}$ events is much higher in the 1-lepton channel than in the 0-lepton channel since the signal final state is more similar to the $t\bar{t}$ final state. As in the *merged* analysis CRs can be easily defined for both the 0-lepton and 1-lepton analysis, the normalisation of the $t\bar{t}$ background is kept uncorrelated between the two channels.

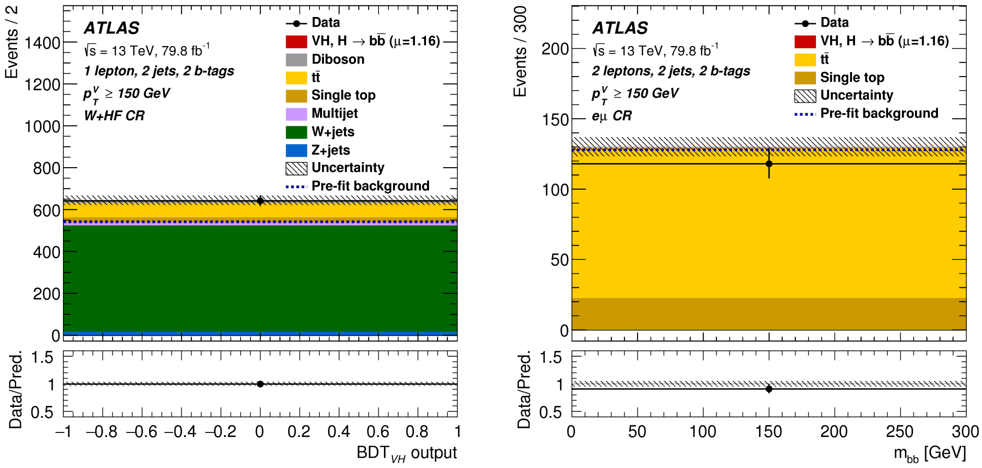

(a) (b)

Figure 6.4: Event yields in the $W + HF$ control regions in the 1-lepton (left) channel and in the top CR in the 2-lepton channel (right) for 2-jet events in the $p_T^V > 150$ GeV kinematic region [60]. The data are shown as back dots. The signal and background contributions are shown as filled histograms. The Higgs boson signal is also shown unstacked as an unfilled histogram, scaled by the factor indicated in the legend. The size of the combined statistical and systematic uncertainty for the sum of the signal and background is indicated by the hatched band.

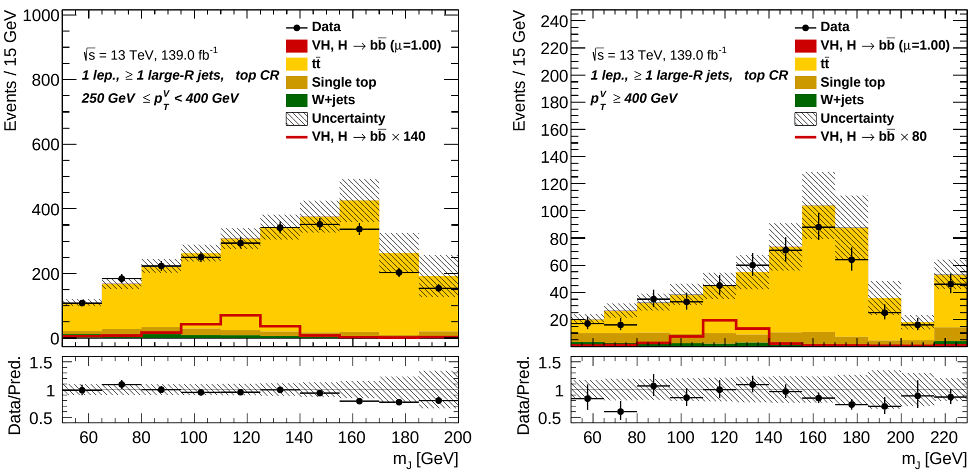

(a) (b)

Figure 6.5: The post-fit distributions for the large-R jet mass, m_J, in the 1-lepton channel CRs. The 250$<p_{\mathrm{T}}^{V}<$400 GeV category (left) and $p_{\mathrm{T}}^{V}>$400 GeV category are shown. The data are shown as back dots. The signal and background contributions are shown as filled histograms. The Higgs boson signal is also shown unstacked as an unfilled histogram, scaled by the factor indicated in the legend. The size of the combined statistical and systematic uncertainty for the sum of the signal and background is indicated by the hatched band.

6.3.3 2-lepton channel

Signal regions

In the 2-lepton channel, exactly two loose leptons of the same flavour are required. In the muon sub-channels, the two muons are required to have an opposite-sign charge. This is not applied in the electron sub-channel, where the charge misidentification rate is not negligible. Events passing the online selection in the 2-lepton channel are required to have p_{T}^{V} >75 GeV for the *resolved* analysis and p_{T}^{V} >250 GeV for the *merged* analysis. Differently from the other lepton channels, due to the lower level of the $t\bar{t}$ background, events with high jet multiplicity are accepted in the *resolved* analysis. Thus, the categories are either exactly two jets or three or more jets.
In the *resolved* analysis, to suppress backgrounds with non-resonant lepton pairs, such as $t\bar{t}$ and multi-jet production, the invariant mass of the dilepton system must be consistent with the Z boson mass (81 GeV$< m_{ll} <$ 101 GeV for the *resolved* analysis and 66 GeV$< m_{ll} <$ 116 GeV for the *merged* analysis). A summary of the event selection is shown in Table 6.6.

Resolved	Merged
$p_{\mathrm{T}}^{V} > 75$ GeV	$p_{\mathrm{T}}^{V} > 250$ GeV
two loose leptons of the same flavour	
81 GeV$< m_{ll} <$ 101 GeV	66 GeV$< m_{ll} <$ 116 GeV
In the muon sub-channels, the two muons with opposite-sign charge.	

Table 6.6: Summary of the event selection in the 2-lepton channel. This summary does not include the candidate Higgs boson selection.

The m_{bb} distribution for $p_{\mathrm{T}}^{V} > 150$ GeV in the *resolved* analysis is shown in Figure 6.6a. The large-R jet distribution for the *merged* analysis for p_{T}^{V} >400 GeV is shown in Figure 6.6b. The dominant background process in both cases is the $Z + HF$ process. As for the *merged* analysis the statistic in the 2-lepton channel is very low, no jet categorisation has been applied.

Control regions

The 2-lepton event selection in the *resolved* analysis allows a definition of very pure top CRs keeping the requirement unchanged except for inverting the lepton

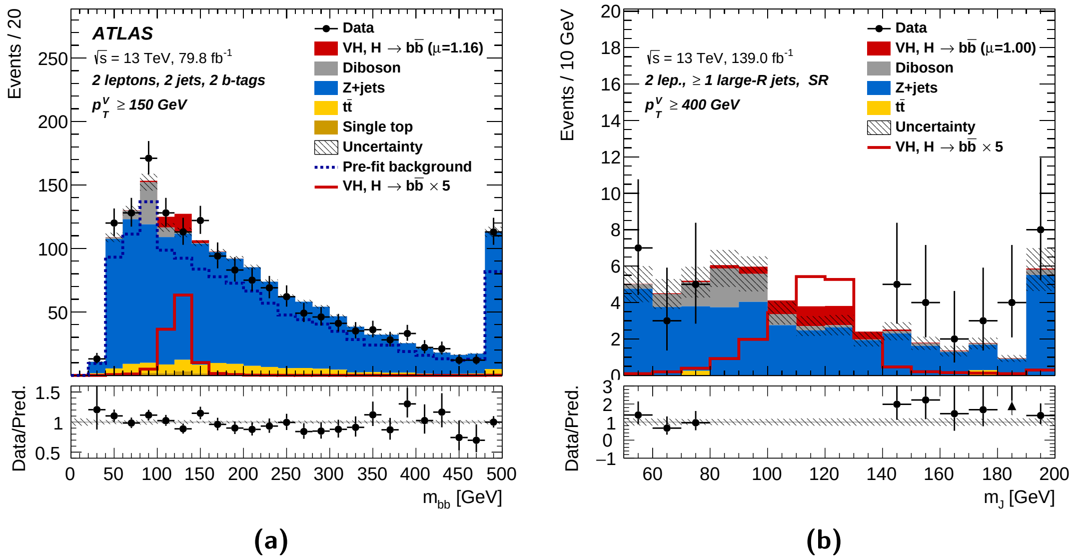

Figure 6.6: The post-fit distributions for m_{bb} in the 2 lepton channel for the *resolved* analysis (left) and the pre-fit m_{J} distribution for the *merged* analysis (right). Only the region $p_{\mathrm{T}}^{V} > 150$ GeV ($p_{\mathrm{T}}^{V} > 400$ GeV) is shown for the *resolved* (*merged*) analysis. The data are shown as back dots. The signal and background contributions are shown as filled histograms. The Higgs boson signal is also shown unstacked as an unfilled histogram, scaled by the factor indicated in the legend. The size of the combined statistical and systematic uncertainty for the sum of the signal and background is indicated by the hatched band.

flavour selection. An $e\mu$ lepton flavour combination is requested, instead of ee or $\mu\mu$, and no opposite-charge requirement is applied. The top CR for the 2-jet events is shown in Figure 6.4b and is over 99% pure in $t\bar{t}$ and single top-quark events.

6.3.4 Summary of the signal and control regions definition

The eight SRs and six CRs of the *resolved* analysis are summarized in Table 6.7, while the ten SRs and four CRs of the *merged* analysis are summarised in Table 6.8.

The selection efficiencies for the *resolved* and *merged* analysis as a function of the truth p_{T}^{V} in the 1-lepton channel are shown in Figure 6.7. The efficiency is defined as the number of $qq \to WH$ events that are reconstructed in the signal regions, divided by the number of generated events. The efficiency of the resolved analysis drops at ~ 500 GeV. In Section 5.3 a helpful rule of thumb has been introduced, the average distance between the decay products of a boosted particle of mass M and transverse momentum p_T is $\Delta R \sim 2M/p_T$. Considering a Higgs boson mass of

Channel	$p^V_{T[75\text{-}150]}$ GeV			$p^V_{T[150\text{-}]}$ GeV		
	2 jet	3 jet	3+jet	2 jet	3 jet	3+jet
0-lepton	–	–	–	SR	SR	–
1-lepton						
→ $m_{bb} \geq 75$ GeV or $m_{\text{top}} \leq 225$ GeV	–	–	–	SR	SR	–
→ $m_{bb} < 75$ GeV and $m_{\text{top}} > 225$ GeV	–	–	–	CR	CR	–
2-lepton						
→ ee and $\mu\mu$ channels	SR	–	SR	SR	–	SR
→ $e\mu$ channel	CR	–	CR	CR	–	CR

Table 6.7: Summary of the definition of the *resolved* analysis regions. Regions with relatively large signal purity are marked with the label SR. Regions designed to constrain the background uncertainties are marked with the label CR.

Channel	$p^V_{T[250\text{-}400]}$ GeV		$p^V_{T[400\text{-}]}$ GeV	
	0 jet	≥ 1 jet	0 jet	≥ 1 jet
0-lepton				
No additional b-tagged track jet	SR	SR	SR	SR
≥ 1 additional b-tagged track jet	CR		CR	
1-lepton				
No additional b-tagged track jet	SR	SR	SR	SR
≥ 1 additional b-tagged track jet	CR		CR	
2-lepton	SR		SR	

Table 6.8: Summary of the definition of the *merged* analysis regions. Regions with relatively large signal purity are marked with the label SR. Regions designed to constrain the background uncertainties are marked with the label CR.

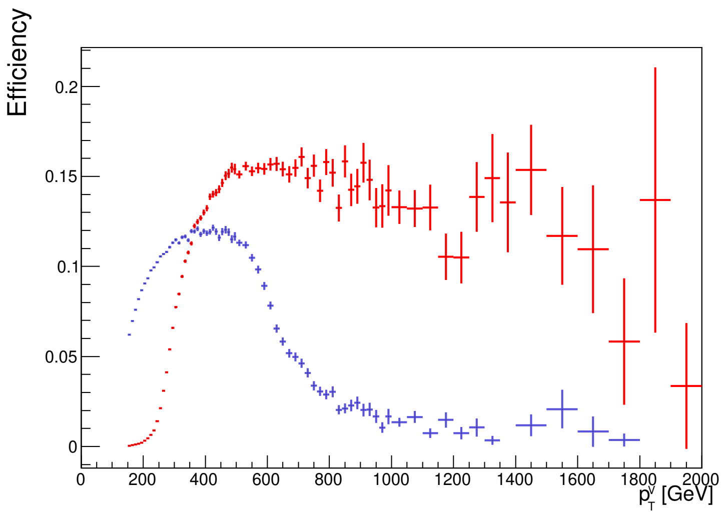

Figure 6.7: Selection efficiencies of the *resolved* (blue) and *merged* (red) analyses for $qq \to WH$ events in the signal region of the 1-lepton channel. The efficiencies are shown as a function of the W transverse momentum, computed at truth level. A cut at $p_T^{\text{truth V}}$ >150 GeV has been applied to both analyses for an easier comparison.

125 GeV, at $p_T = 500$ GeV the average distance between the decay products is 0.5. As in the *resolved* analysis, the radius of the jets used to reconstruct the candidate Higgs is $R = 0.4$, at 500 GeV the two jets are on average completely overlapping and an efficiency drop is therefore expected. On the other side, the radius of the large-R jet used in the *merged* analysis is $R = 1.0$. The decay products of the Higgs boson start therefore to be both reconstructed within the jet radius at $p_T \sim 250$ GeV. It is important to remember that in the *resolved* analysis the 1-lepton channel has a selection cut at $p_{\mathrm{T}}^V > 150$ GeV, while the *merged* analysis has a cut at $p_{\mathrm{T}}^V > 250$ GeV. While the event selection is applied at the reconstructed level, the p_{T}^V shown in the plot is at truth level. Events of the *merged* analysis drown below the 250 GeV cut have therefore reconstructed p_{T}^V that pass the event selection.

6.4 Jet categorisation in the *merged* analysis

The jet multiplicity is an important variable in the event selection. As already mentioned, in the *resolved* analysis events with four or more jets are discarded, both in the 0-lepton and 1-lepton channels. This selection reduces the number of $t\bar{t}$ events, which have on average a higher jet multiplicity with respect to signal events. The jet multiplicity is also used to categorise the events in the resolved analysis. Categorizing the events in purity and lower purity regions increases the overall

significance without reducing the number of selected signal events. Starting from this consideration, the jet multiplicity categorization has been studied also for the *merged* analysis, since the $t\bar{t}$ process gives a large contribution to the background also for this topology.
The choice of the categorisation is the result of a detailed study that has been first carried out on the 1-lepton channel and then, given the good performance, tested also on the 0-lepton channel.
The difference in jet multiplicity between the $t\bar{t}$ and WH processes can be easily deduced from the leading order Feynman diagrams for these two processes shown in Figure 6.8. The $t\bar{t}$ events passing the event selection are mainly constituted by

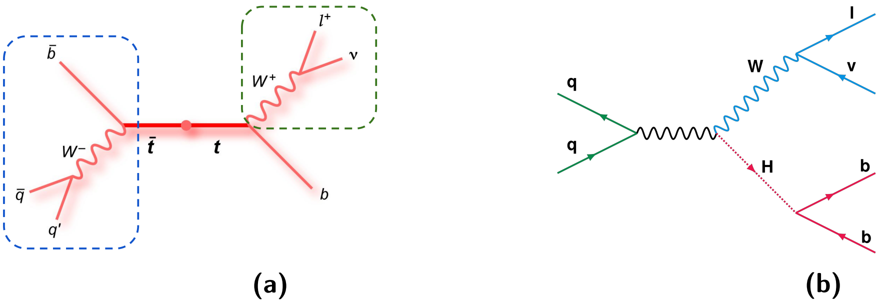

Figure 6.8: Leading order Feynman diagram for the $t\bar{t}$ (a) and WH (b) processes. The blue box indicates the decay product of a hadronically decaying top quark, which could be wrongly selected as a Higgs boson candidate. The green box includes the decay products of a W boson, expected to be reconstructed as a candidate V boson.

events where one of the W bosons decays hadronically and the other one decays leptonically. In this case, one of the W is expected to be correctly identified by the vector boson selection (green box in Figure 6.8). On the other hand, one of the two jets from the hadronically decaying W could be misidentified as a b-jet, and the decay product of the high energy top could thus be wrongly selected as a Higgs candidate (blue box in Figure 6.8).
In order to measure the jet activity additional to the Higgs boson decay products the number N_{add} of small-R jets lying outside the large-R jet (ΔR>1) is considered. The N_{add} distributions for data and simulation are shown in Figure 6.9, left. The N_{add} distributions for the most important processes are also shown normalized to the same area (Figure 6.9 right) to highlight the difference in shape. As expected, N_{add} is on average larger for the $t\bar{t}$ background with respect to the signal, for which the distribution is peaking at $N_{add} = 0$.
In order to define the precise categorization strategy various selections have been studied and are summarized in the plots shown in Figure 6.10 for the two SRs 250 GeV $<p_{\mathrm{T}}^{V}<$400 GeV (left) and $p_{\mathrm{T}}^{V}>$400 (right). The plots show the fraction of signal events surviving the various selections. The x axis represents the minimum p_T cut applied to the jets used to calculate N_{add}. The y axis is the cut on N_{add}.

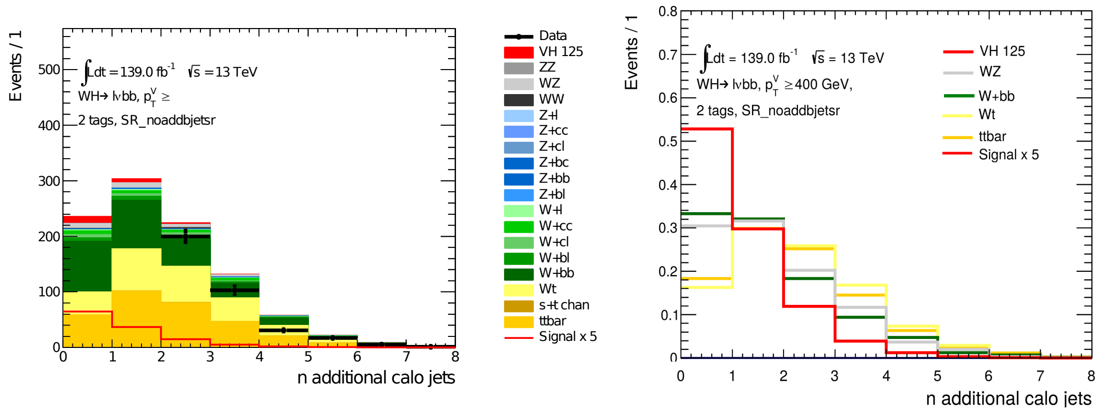

Figure 6.9: Distribution of the number of additional calorimetric jets, N_{add}, in the 1 lepton channel for the events with $p_{\rm T}^V > 400$ GeV (left) and comparison of the shape of the histograms for the signal and the main background processes (right). The minimum p_T of the additional jets used in the plot is 30 GeV.

E.g., assuming to use the cut at 30 GeV to define the additional jet multiplicity, $\sim$ 66% of the signal events in the category 250<$p_{\rm T}^V$ <400 GeV have 0 additional jets.

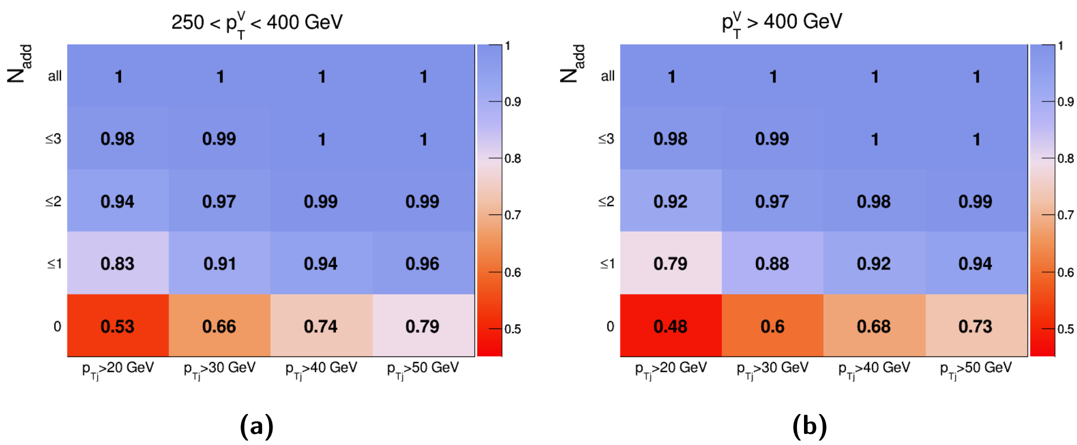

Figure 6.10: Fraction of signal events passing the selection in the region $250 < p_T^V < 400$ GeV (a) and $p_T^V > 400$ (b) GeV assuming to add a cut on the number of additional jets. The first row corresponds to not applying any cut on the number of additional jets. Both the number of additional jets and the cut applied on the additional jets p_T are varied.

The equivalent plots for the number of events for all background processes are shown in Figure 6.11. Only $\sim$ 30% of the background events are in the bin with $p_{Tj} > 30$ GeV and 0 additional jet.
A rough estimate of the improvement in significance is obtained by computing the significance bin by bin from the SRs m_J distribution and summing the result

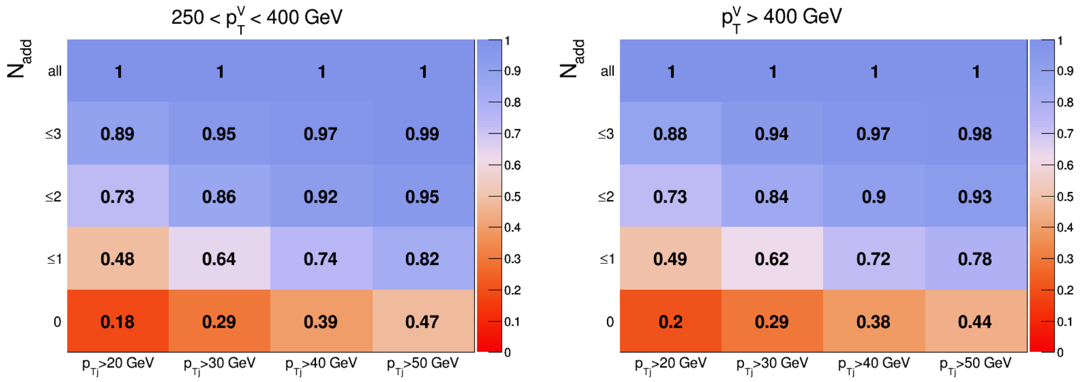

(a) (b)

Figure 6.11: Fraction of background events passing the selection in the region $250 < p_T^V < 400$ GeV (a) and $p_T^V > 400$ (b) GeV assuming to add a cut on the number of additional jets. The first raw correspond to not applying any cut on the number of additional jets. Both the number of additional jets and the cut applied on the additional jets p_T are varied.

in quadrature. The formula used to compute the significance in each bin is $S = \sqrt{2((s+b)ln(1+s/b)-s}$. The plots showing the expected significance applying a cut on the number of additional jets are shown in Figure 6.12. In this

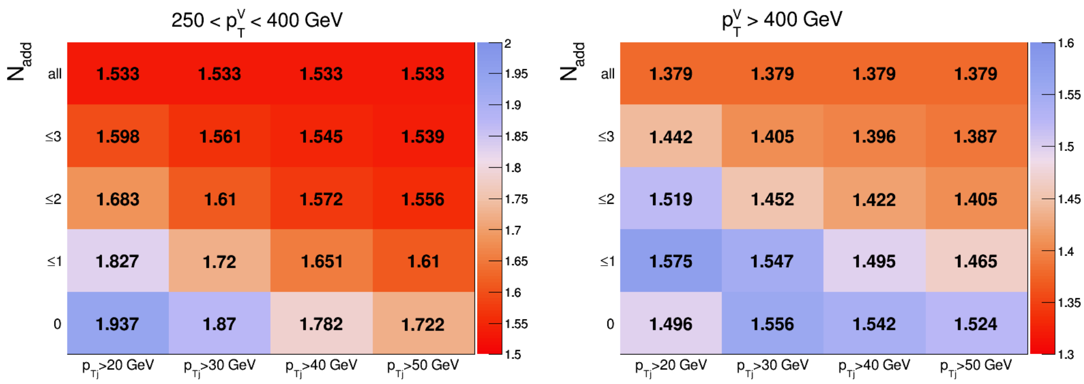

(a) (b)

Figure 6.12: Expected significance in the region $250 < p_T^V < 400$ GeV (a) and $p_T^V > 400$ (b) GeV assuming to add a cut on the number of additional jets. The first raw correspond to not applying any cut on the number of additional jets. Both the number of additional jets and the cut applied on the additional jets p_T are varied.

preliminary study, a simple cut on the number of additional jets is applied while in the final implementation events are categorised to avoid discarding signal events and increase the final significance.

The bin on the top left corner of the plots indicates the significance without any additional cuts. It can be seen that the regions on the bottom left of the plots correspond to the selections giving the largest significance improvements. Given the promising results, a more complete performance assessment was implemented using the full fit procedure with events divided into two categories. The chosen p_T threshold is 30 GeV and events are categorised according to N_{add} as follows:

- high sensitivity category: $N_{add} = 0$;
- low sensitivity category: $N_{add} \geq 1$.

The chosen p_T threshold is the best compromise to define a uniform selection across the analyses and to use jets in a phase space region not strongly affected by pile-up effects. Figure 6.13 summarizes the event categories in the reference scheme (left) and the new scheme (right). The new scheme corresponds to the one used in this thesis and described in the previous sections. The fit procedure, defined in

		0L	1L	2L
250-400 GeV	no add b-tagged jets	SR	SR	SR
	add b-tagged jets	CR	CR	
>400 GeV	no add b-tagged jets	SR	SR	SR
	add b-tagged jets	CR	CR	

		0L		1L		2L
		# add. small-R jets		# add small-R jets		
		0	>=1	0	>=1	
250-400 GeV	no add b-tagged jets	SR	SR	SR	SR	SR
	add b-tagged jets	CR		CR		
>400 GeV	no add b-tagged jets	SR	SR	SR	SR	SR
	add b-tagged jets	CR		CR		

Figure 6.13: Schematic summary of the signal regions and control regions of the *merged* analysis without (left) and with (right) the categorisation in the additional jets multiplicity.

Chapter 7, has been implemented for the two schemes using Asimov data. In this section only the results on the significance comparison are shown, while a complete description of the full fit procedure and of the systematic uncertainties taken into account is presented in the next chapters of this thesis.
The first comparison of the significances for the two schemes was obtained without considering systematic uncertainties, this is called a *stat only* fit. The results obtained for the two schemes in the 0-lepton and 1-lepton channels are summarized in Table 6.9. As expected the largest significance improvement, of about 28%, is found in the 1L channel, where the $t\bar{t}$ represents the largest contribution to the background. However, also the 0-lepton categorization gives good results bringing a significance improvement of about 15%. As in the 2-lepton channel the contribution of the $t\bar{t}$ background is negligible the new categorization has not been used. The global sensitivity improvement when the categorization is used for all channels is reported in the last line of Table 6.9. Given the improvement in the expected significance, it was decided to implement the jet multiplicity categorisation both in

	No jet mult. categor.	jet mult. categor.	improvement
1L, Stat only	2.17	2.77	28%
0L, Stat only	2.56	2.94	15%
012L, Stat only	3.77	4.39	16%

Table 6.9: Expected significance for a fit not including nuisance parameters (Stat Only fit), for a fit model with and without a categorisation in the number of additional jets outside of the selected large-R jet. The improvement in the expected significance is quoted as well.

the 1-lepton and 0-lepton channel. In the following the region with zero additional jets is referred to as high purity signal region (HP SR) and the region with one or more additional jets is referred to as low purity signal region (LP SR).

6.5 Multivariate approach in the resolved analysis

In this section a brief description of the multivariate approach followed in the *resolved* analysis is described. Multivariate analyses (MVAs) are used in a variety of high energy physics analyses to optimize the signal purity and the background rejection. This is achieved through the combination of a wide set of input variables which the multivariate algorithm is trained on, by constructing a one-dimensional discriminant. Such an approach is quite complex, but results in an increased separation between signal and background events and therefore in an increased expected significance. Multivariate techniques have been used in the *resolved* analysis but not in the *merged* analysis. In fact, as the *merged* analysis is completely new, it was chosen to follow a simpler approach that is easier to inspect, and defer the implementation of an MVA analysis to the future.
The MVA algorithm is set up taking into account the available MC statistics so that the final result does not depend on the random statistical fluctuations in the input distributions. On the other hand, multivariate algorithms must be trained and evaluated on separate MC samples to ensure an unbiased result: in this analysis, 2-fold cross-validation of the training is implemented. One training is performed using even (odd) event-numbered MC events and then applied to odd (even) events, thereby ensuring orthogonality between the samples the algorithm is trained on and evaluated on. The final discriminant is then built by summing the multivariate discriminant of the even and odd events since no difference in the physics is expected between them.
For this analysis, a Boosted Decision Tree (BDT) provided by the TMVA package of ROOT is used [120]. For each SR of the analysis, separate training is performed in the aforementioned 2-fold way. As the kinematics and background compositions

are different in each category, training the BDT in the separate categories increases the sensitivity of the analysis. An example of the m_{bb} and BDT distribution in the 1-lepton channel was shown in Figure 3.5, in Chapter 3.

6.5.1 Input variables

The BDT input variables are defined after the selection requirements are applied. The input variables used in each channel are summarised in Table 6.10. They were

Variable	0-lepton	1-lepton	2-lepton
m_{jj}	✓	✓	✓
$\Delta R(jet_1, jet_2)$	✓	✓	✓
p_T^{jet1}	✓	✓	✓
p_T^{jet2}	✓	✓	✓
p_T^V	✓	✓	✓
$\Delta\phi(V, H)$	✓	✓	✓
$\|\Delta\eta(jet_1, jet_2)\|$	✓		
$M_{eff}(M_{eff3})$	✓		
E_T^{miss}	$= p_T^V$	✓	
$min(\Delta\phi(l, jet))$		✓	
m_T^W		✓	
$\Delta Y(W, H)$		✓	
m_{top}		✓	
E_T^{miss} significance			✓
$\Delta\eta(V, H)$			✓
m_{ll}			✓
	Only in 3-jet Events		
p_T^{jet3}	✓	✓	✓
m_{jjj}	✓	✓	✓

Table 6.10: Variables used to train the multivariate discriminant.

chosen based on studies conducted during Run 1, where an iterative procedure was adopted to find the optimal set of variables and ranking to use [121]. Initially, the BDT was constructed using simply the invariant mass of the two b-tagged jets and ΔR between them, which provide the most discriminating distributions. Each candidate variable was then added to the MVA in turn, with the variable offering the best improvement in significance being added to the MVA as the third

variable. The final optimal MVA is then constructed when all variables have been studied and no further improvement is seen. This was done separately for each lepton channel.
Since most of the kinematic variables have tails towards very high values the range of the input variables is limited to a range that includes 99% of all signal events. All events above those limits are artificially set to the maximum value. This procedure is introduced to avoid that the BDT wastes degrees of freedom to categorise the small number of events that accumulate in the tails of these distributions.

Chapter 7

Statistical method for the cross-section measurements

The statistical treatment used to extract the $VH(H \to b\bar{b})$ cross-section is described in this chapter. The likelihood and the statistical test exploited are described in the first section. In the same section, the plots displaying the nuisance parameter pulls and the ranking of the impact of the uncertainties are described. The statistical method followed to measure the $VH(H \to b\bar{b})$ inclusive cross-section is very similar to the one adopted for the STXS measurements. However, some differences are present and are described in the second section of this chapter, together with some additional studies needed for the STXS measurements.

7.1 General statistical treatment

The main fit strategy is common to all the measurements presented in this thesis. The signal yield in the selected data is extracted by a binned maximum likelihood fit. A significant difference between the *resolved* and the *merged* analyses is that the observable used in the fit as a final discriminant is the BDT distribution for the *resolved* analysis and the large-R jet mass for the *merged* analysis. The structure of the likelihood function is instead the same for the two analyses and is introduced in this section.

7.1.1 Likelihood

The fit is based on a binned likelihood fit, which is obtained as the product of different components. The first component of the likelihood is the *Poissonian component* ($\mathcal{L}_{Poiss}$). It is built as the product, over all the bins, of the Poisson probability to observe n_i events in bin i, when m_i events are expected. The $\mathcal{L}_{Poiss}$ equation is:

$$\begin{aligned}\mathcal{L}_{Poiss}(\mu, \boldsymbol{\alpha}, \boldsymbol{\gamma}, \boldsymbol{\tau}) &= \prod_{i \in \text{bins}} \text{Poiss}(n_i | m_i(\boldsymbol{\alpha}, \boldsymbol{\gamma}, \boldsymbol{\tau})) \\ &= \prod_{i \in \text{bins}} \text{Poiss}(n_i | \mu s_i(\boldsymbol{\alpha}) + b_i(\boldsymbol{\alpha}, \boldsymbol{\gamma}, \boldsymbol{\tau})) \\ &= \prod_{i \in \text{bins}} \frac{(\mu s_i + b_i)^{n_i}}{n_i!} e^{-(\mu s_i + b_i)}\end{aligned} \tag{7.1}$$

where the number of predicted events m_i in bin i is obtained as the sum of μs_i and b_i, which are the expected signal yield s_i scaled by the parameter μ, and the background yield b_i. In addition to the parameter μ, the likelihood depends on other parameters ($\boldsymbol{\alpha}$, $\boldsymbol{\gamma}$, $\boldsymbol{\tau}$). In order to distinguish the parameter μ from these additional parameters needed by the model, the first one is named parameter of interest (POI), while the second ones are named nuisance parameters (NP). Systematic uncertainties from various sources enter the likelihood function through these NPs. The NP set can be divided into three sub-sets: $\boldsymbol{\alpha} = (\alpha_1, \alpha_2, ...)$, $\boldsymbol{\gamma} = (\gamma_1, \gamma_2, ...)$ and $\boldsymbol{\tau} = (\tau_1, \tau_2, ...)$, each referring to a different type of nuisance parameters. The background normalisations, $\boldsymbol{\tau}$, are parameters that are free to float in the fit, and they correspond to global rescaling factors of some background components. The NPs $\boldsymbol{\gamma}$ represent the statistical uncertainty caused by the limited size of the simulated background samples. The modelling and experimental uncertainties instead enter the fit through the $\boldsymbol{\alpha}$ NPs and affect both the signal and background processes.

Auxiliary measurements (e.g. the measurement of the jet energy scale) are used to evaluate the $\boldsymbol{\alpha}$ NPs uncertainties. As discussed in detail in Ref. [122], when evaluating a systematic effect parameterized by $\boldsymbol{\alpha}$, usually only an estimate of its "central value", or of its "best guess", and some notion of uncertainty on it are available. In these cases, an approximated term in the likelihood is used, named *penalty term* or *constraint term*. This term is generally approximated with a Gaussian (with mean zero and a variance of unity for convenience) or with a log-normal constraint. The case of the Gaussian is represented in the following equation:

$$\begin{aligned}\mathcal{L}_{syst}(\alpha) &= \prod_{\alpha\in\boldsymbol{\alpha}} Gauss(\boldsymbol{\alpha}|0,1) \\ &= \prod_{\alpha\in\boldsymbol{\alpha}} \frac{1}{\sqrt{2\pi}} e^{-\alpha^2/2} \quad .\end{aligned} \tag{7.2}$$

where the product is extended over all the systematic uncertainties treated with this method and the nuisance parameters are expressed in units of σ_α (i.e. moving the parameter α of the jet energy scale by 1 correspond in shifting the energy calibration of the jet by 1 σ). In this way as the fit *moves* the value of α away from the nominal value (0) the likelihood is *penalized* with a factor that is smaller than 1.

This way of using the parameters $\boldsymbol{\alpha}$ allows correlating the systematic uncertainties across physics processes, or analysis regions, as it is done for example for the uncertainties on the jet energy scale. Other uncertainties, e.g. the background modelling uncertainties, can be uncorrelated across the processes.

Even if most constraint terms are extracted from auxiliary measurements, some systematic effects included in the likelihood are not measured in this way. In particular, some theoretical uncertainties are not statistical in nature, e.g. the uncertainty associated with the choice of the renormalisation and factorisation scale. Even if the use of such NPs as constraint terms is not fully coherent, they are usually included in this way for convenience, and in this thesis this approach is followed as well.

The uncertainties on the background predictions due to the limited number of MC simulated events are taken into account in the likelihood function by including an additional NP γ per bin [123]. The NP is used to modify the likelihood with a Poisson probability that gives for each bin i the probability to have b_i predicted events when the true number of events is $\gamma_i b_i$ [1].

$$\mathcal{L}_{stat}(\boldsymbol{\gamma}) = \prod_{i\in\text{bins}} \frac{(\gamma_i b_i)^{b_i} e^{-(\gamma_i b_i)}}{\Gamma(b_i+1)} \quad , \tag{7.3}$$

with

$$\Gamma(x) = \int dt \quad t^{x-1} e^{-t} \quad .$$

There is one γ_i NP for each bin of the histograms, it therefore represents the uncertainty on the sum of all background processes in that bin.

[1]The following formula is a Poissonian term using the Γ-function to express the factorial. This is needed as the simulation yields may be not of integer value. For integer values the expression is equal to the Poisson distribution.

As mentioned above the likelihood function is the product of all the described components:

$$\mathcal{L}(\mu, \boldsymbol{\alpha}, \boldsymbol{\gamma}, \boldsymbol{\tau}) = \mathcal{L}_{Poiss}(\mu, \boldsymbol{\alpha}, \boldsymbol{\gamma}, \boldsymbol{\tau}) \cdot \mathcal{L}_{syst}(\boldsymbol{\alpha}) \cdot \mathcal{L}_{stat}(\boldsymbol{\gamma}). \tag{7.4}$$

7.1.2 Signal strength measurement

The binned maximum-likelihood fit results in the measurement of the signal strength (μ). The measured signal strength and the measured nuisance parameters are obtained as the values of the parameters that maximize the likelihood function $\mathcal{L}(\mu, \boldsymbol{\alpha}, \boldsymbol{\gamma}, \boldsymbol{\tau}) = \mathcal{L}(\mu, \boldsymbol{\theta})$ or, equivalently, minimize $-ln\mathcal{L}(\mu, \boldsymbol{\theta})$. Here $\boldsymbol{\theta}$ represents the set of NPs introduced in the previous section ($\boldsymbol{\gamma}$, $\boldsymbol{\alpha}$, $\boldsymbol{\tau}$).
The uncertainty on the signal strength is assessed evaluating $\mu_{+/-} = \hat{\mu} \pm \sigma_\mu$ as the value the satisfies:

$$-2(ln\mathcal{L}(\mu_{+/-}, \hat{\hat{\boldsymbol{\theta}}}_\mu) - ln\mathcal{L}(\hat{\mu}, \hat{\boldsymbol{\theta}})) = -2ln\frac{\mathcal{L}(\mu_{+/-}, \hat{\hat{\boldsymbol{\theta}}}_\mu)}{\mathcal{L}(\hat{\mu}, \hat{\boldsymbol{\theta}})} = 1$$

where $\hat{\mu}$ and $\hat{\boldsymbol{\theta}}$ are the parameters that maximise the overall likelihood, while $\hat{\hat{\boldsymbol{\theta}}}_\mu$ are the NP values that maximise the likelihood for a particular value of μ. In the asymptotic limit, this corresponds to a 68% confidence level interval, as it will be clarified below. The signal strength and its uncertainty computation are schematically represented in Figure 7.1. Some of the variables used in the figure will be introduced in the next section.

7.1.3 Test statistic

An important aspect in the search for the $H \to b\bar{b}$ decay is to differentiate the background-only hypothesis $\mu = 0$, from the alternative hypothesis $\mu > 0$. More in general, these tests are interesting to state the degree to which data supports a particular value of the signal strength (where $\mu = 0$ is a special case). This is done through a profile likelihood ratio test statistic, q_μ , defined as follows:

$$q_\mu = -2ln\frac{\mathcal{L}(\mu, \hat{\hat{\boldsymbol{\theta}}}_\mu)}{\mathcal{L}(\hat{\mu}, \hat{\boldsymbol{\theta}})} = -2ln\lambda(\mu) \tag{7.5}$$

where $\hat{\mu}$ and $\hat{\boldsymbol{\theta}}$ are the parameters that maximise the overall likelihood, and $\hat{\hat{\boldsymbol{\theta}}}_\mu$ are the NP values that maximise the likelihood for a particular value of μ, as mentioned

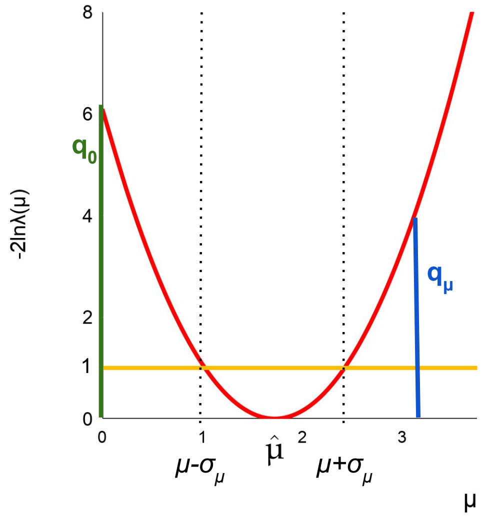

Figure 7.1: Schematic representation of the profile likelihood ratio test statistic as a function of the signal strength (red line). The measured signal strength corresponds to the maximum of the likelihood. The uncertainty on the signal strength correspond to the value of the likelihood ratio function for $-2(ln\mathcal{L}(\mu,\hat{\hat{\boldsymbol{\theta}}}_{\mu}) - ln\mathcal{L}(\hat{\mu},\hat{\boldsymbol{\theta}})) = -2ln\lambda(\mu) = 1$. The yellow horizontal line is drawn at 1. q_0 corresponds to the value of the likelihood ratio function for $\mu = 0$.

above. The likelihood maximization without fixing the value of the signal strength is named *unconditional fit*. Instead, the *conditional fit* is performed maximising the likelihood for a particular value of μ. The likelihood ratio q_{μ} depends explicitly on the parameter of interest μ and implicitly on the data.
The compatibility of the data with the background-only hypothesis, used to identify the presence of a significant excess, is evaluated with the test statistic q_0:

$$q_0 = -2ln\frac{\mathcal{L}(\mu = 0, \hat{\hat{\boldsymbol{\theta}}}_{\mu=0})}{\mathcal{L}(\hat{\mu}, \hat{\boldsymbol{\theta}})} \tag{7.6}$$

In the background-only hypothesis the signal strength μ is equal to 0. For data compatible with a background-only hypothesis the minimum of the likelihood and the minimum of the likelihood fixing $\mu = 0$ are close, implying that the likelihood ratio is close to 1 and q_0 is close to 0. A visual representation of q_0 is shown in Figure 7.1.
The distribution of q_0 can be explicitly determined calculating q_0 on an ensemble of experiments statistically compatible with the nominal distribution used to build the likelihood (toy Monte Carlo simulations). Nevertheless, assuming the null hypothesis to be true, the *Wilks theorem* [124] ensures that q_0 is asymptotically distributed as a chi-square with one degree of freedom. This means that it is

possible to easily compare the value of q_0 to the chi-square value. This technique is particularly convenient to measure an approximate p-value, that corresponds to $p_0 = \int_{q_0^{obs}}^{\infty} f(q_0|0)dq_0$, where $f(q_0|0)$ denotes the probability density function of the statistic q_0 under the $\mu = 0$ assumption [125]. The p-value allows measuring the eventual incompatibility of the data with the tested hypothesis: the hypothesis can be considered as excluded if its p-value is observed below a specified threshold. The p-value is then converted into an equivalent significance Z defined such that a Gaussian distributed variable found Z standard deviations above its mean has an upper-tail probability equal to p_0. In what follows all the statistical tests are done using the asymptotic approximation ensured by the Wilks theorem.

7.1.4 Tool for the validation of the fit results

Nuisance parameters play a fundamental role in the fit. As a large number of systematic uncertainties are included in the fit, some typical plots are used to easily visualize information from the fit results. These plots allow spotting eventual problems or simply aspects that need to be understood. Among these there are the *pull plots*, displaying the *pulls* of the NPs [126].
For a normalised nuisance parameter θ, with an expectation value and a standard deviation equal to $\theta_0 = 0$ and $\sigma_\theta = 1$ respectively, the pull is defined as

$$pull(\theta) = \frac{\hat{\theta} - \theta_0}{\sigma_\theta} = \hat{\theta}$$

where $\hat{\theta}$ is the NP value obtained from the maximum likelihood fit. The pull quantifies how far from its expected value the NP was "pulled" by the fit in number of σ_θ. A healthy situation is when the pull average is close to zero. A pull value of +1(-1) corresponds to a NP pulled by $+\sigma(-\sigma)$. A large pull, indicating that the NP value extracted from the fit is far from the expected NP value, does not necessarily imply that there is an issue, but further investigation or understanding is required.
In addition to this point parameter estimation, one can study the profiled likelihood ratio as a function of the parameter θ around $\hat{\theta}$ to estimate an interval for the parameter. The interval is estimated applying the same method used to evaluate the μ uncertainty. In the case of the Gaussian constraint term in the likelihood, this interval is $[-1, 1]$. The use of the combined likelihood can, in principle, add information on a certain parameter, reducing the size of this interval. If this interval is significantly smaller than $[-1, 1]$, the systematic uncertainty is said to be constrained by the data. This means that the performed measurement results in a more accurate measurement of the NP with respect to the auxiliary measurement

used to extract the uncertainty on the NP. This behaviour is possible but needs to be understood.

A first estimate of all the information described above is obtained using the *Asimov* dataset. This dataset is obtained by replacing the data in each input bin with the expected yields predicted from the simulation, using the nominal values of the nuisance parameters. While the values of the pulls will not change when using the Asimov dataset, possible constraints become evident and allow identifying suspicious behaviours prior to the use of the measured data. The use of the Asimov dataset is also useful to predict the expected precision of the measurement of the floating normalisations $\boldsymbol{\tau}$ as well as the expected precision on the measurement of the POI.

By construction, the Asimov dataset is not giving information on the presence of pulls of the NP. The need to use the measured data to measure them and, consequently, to study if there are potential errors or problems to be fixed, is particularly delicate. The use of data at this stage must respect the principle that no information can be gathered on the value of the POI since this could bias the final result. For this reason, the fit is performed fixing the POI to its expected value (post-fit, conditional $\mu = 1$ expected results). An example of a pull plot, from the fit result of the *merged* analysis, is shown in Figure 7.2. The parameters

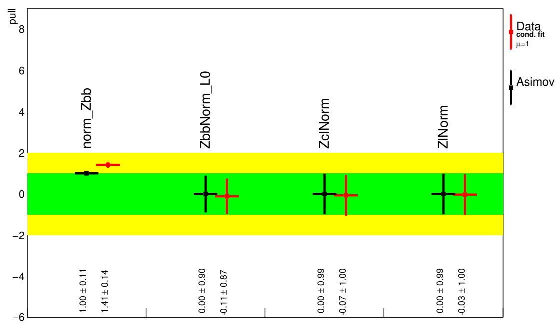

Figure 7.2: Example of a pull plot from the *merged* analysis results. Results from the Asimov fit are shown in black and the results from the conditional fit to data (with $\mu = 1$ are shown in red.

corresponding to the floating normalisations are presented in the pull plots following a different convention. The value shown is not the pull of the parameter, but the parameter absolute value with its uncertainty, as these normalisations do not have a prior. The expected normalisation value is set to one in the Asimov fit, meaning that the normalisation is one of the simulated processes. Deviations from 1 of the parameter value extracted from the fit to data are therefore expected.

Another important information to be assessed in the fit results is how much the value of the POI varies when changing the value of a NP. The impact of a nuisance parameter θ on the fitted POI is defined as:

$$impact(\theta) = \Delta\mu^{\pm} = \hat{\hat{\mu}}_{\theta_0 \pm \sigma_\theta} - \hat{\mu}$$

where $\hat{\mu}$ is the value maximising the likelihood, while $\hat{\hat{\mu}}_{\theta_0 \pm \sigma_\theta}$ are the values of the POI extracted from a fit where all the NP except from θ are allowed to vary, while θ is fixed to the values at the edge of the intervals of the pull introduced above. Obviously, not all NPs have the same impact, and *ranking plots* are used to study the NPs that have larger impact. In Figure 7.3 the ranking plot for the *resolved* analysis is shown as an example. The systematic uncertainties are listed in decreasing order of their impact on the signal strength μ. The boxes show the impacts on μ, referring to the top x-axis. The hatched and open areas correspond to the upwards and downwards variations, respectively. The filled circles, referring to the bottom x-axis, show the pulls of the nuisance parameters. The associated error bars show the interval obtained from the fitted uncertainties of the nuisance parameters, relative to their nominal uncertainties. The dotted vertical lines are also associated with the bottom x-axis and are placed at -1 and $+1$, corresponding to the pre-fit nuisance parameters interval.

All the tools described in this section are used to gain experience with the statistical analysis, to identify potential problems and errors, and they are mandatory to arrive at a solid result.

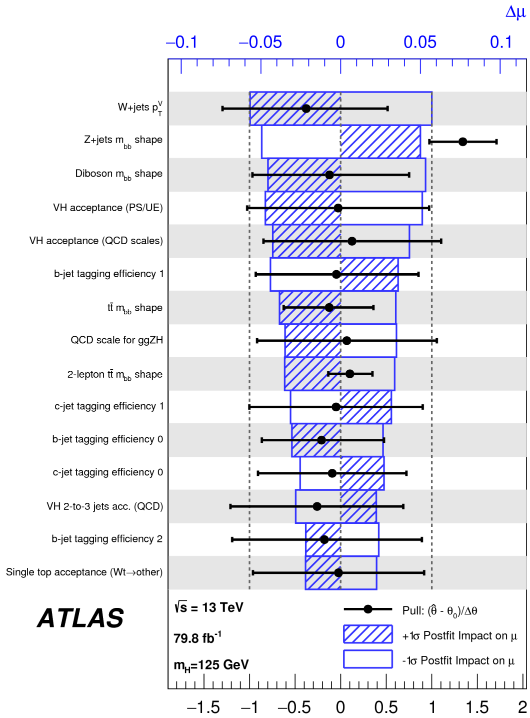

Figure 7.3: Impact of systematic uncertainties for the fitted Higgs boson signal strength μ in the *resolved* analysis [60]. The systematic uncertainties are listed in decreasing order of their impact on μ. The boxes show the variations of μ, referring to the top x-axis, when fixing the corresponding individual nuisance parameter θ to its fitted value $\hat{\theta}$ modified upwards or downwards by its fitted uncertainty, and performing the fit again, with all the other parameters allowed to vary, so as to take correlations between systematic uncertainties properly into account. The hatched and open areas correspond to the upwards and downwards variations, respectively. The filled circles, referring to the bottom x-axis, show the deviations of the fitted nuisance parameters $\hat{\theta}$ from their nominal values θ_0, expressed in terms of standard deviations with respect to their nominal uncertainties Δ_θ. The associated error bars show the fitted uncertainties of the nuisance parameters, relative to their nominal uncertainties.

7.2 Statistical treatment within STXS framework

The signal strength data analysis, which led to the observation of the $H \to b\bar{b}$ decay and VH production, can be re-interpreted in the STXS framework introduced in Chapter 1. The fit strategy for the STXS measurements is very similar to the one followed for the $VH(H \to b\bar{b})$ search, detailed in the previous section. The main difference is that instead of a single parameter of interest (POI), a set of POIs is extracted from the fit, corresponding to the cross-sections in the various STXS bins defined.
The peculiarities of the fit strategy for the STXS measurement are presented in more detail in Section 7.2.1. The STXS bins adopted for the *resolved* analysis are instead described in more detail in Section 7.2.2. As the STXS bins are built at truth level, while the analysis categories are built at reconstructed level, it is important to study the level of matching between the STXS bins and the analysis event categorisations. This study is presented in Section 7.2.3, where the plots of the fraction of signal events from each STXS bins in every reconstructed category and the acceptance of each bin are presented. In the *resolved* analysis the categorisation of the STXS bins at $p_{\mathrm{T}}^{V} = 250$ GeV does not correspond to an equivalent categorisation at reconstructed level. The sensitivity allowing isolation of this high energy region can only arise from the differences in the BDT shapes in the regions below and above the p_{T}^{V} cut. The study of this aspect is presented in Section 7.2.4.

7.2.1 From the signal strength to the STXS measurements

The crucial difference in the fit strategy between the STXS measurements and the signal strength analysis is the POI parametrization, which needs to be adapted for the measurement of several POIs instead of a single POI (signal strength). As described in Chapter 1, the signal strength analysis uses a single signal template (histogram) for each analysis region and the factor μ scales all these templates by the same amount. Calling $n_{r,i}^{SM}$ the number of expected signal events in a reconstructed category r in the bin i of the discriminant variable histogram (the BDT score for the resolved analysis), the signal strength fit parametrises the number of signal events as:

$$\mu \times n_{r,i}^{SM}.$$

The STXS framework, on the contrary, divides the expected signal events in bins, so that the template used in the signal strength measurement is replaced by a set of templates, one for each STXS bin. The number of events per category r per bin of the histogram i is now a sum over the STXS bins (j):

$$\mu \times n^{SM}_{r,i} = \sum_j \mu_j \times n^{SM}_{r,i,j}$$

This means that each STXS bin has its set of templates (a template for each analysis category), and each set of templates can be scaled up by an independent parameter μ_j. The STXS measurement consists in measuring simultaneously all these μ_j parameters. By multiplying the measured $\hat{\mu}_j$ by the expected cross sections times branching ratio for a certain STXS bin j, it is possible to obtain the measurement of the $(\sigma_j \times BR)^{measured}$ for the STXS:

$$(\sigma_j \times BR)^{measured} = \hat{\mu}_j \times (\sigma_j \times BR)^{SM}$$

The signal parametrisation for the signal strength measurement and for the STXS measurement is summarised in Table 7.1.

	POI	Signal parametrization
standard signal strength	1	$\mu \times n^{SM}_{r,i}$
STXS	5	$\sum_{j=1}^{5} \mu_j \times n^{SM}_{r,i,j}$

Table 7.1: Differences in the signal parametrization between the standard signal strength and the STXS fit. The index j specifies the STXS bin, the index r refers to the reconstructed category and i is a BDT histogram bin. The number of POI for a STXS measurement depends on the data-analysis and dataset. Most STXS results in this thesis are obtained using *5-POI*.

This change in the signal parametrisation pushes to reconsider which is the proper scheme of uncertainties to be used for the signal in the STXS measurement. The measurement of the signal strength considers, in fact, different sources of systematics uncertainties (neglected higher order in the α_s expansion, electro-weak effects, ...) which can affect the signal template in three ways:

1. a change in the overall signal normalisation (i.e. the uncertainty on the signal $(\sigma \times BR)^{SM}$ prediction);
2. a change in the acceptance of the signal in the analysis categories;
3. a change in the shape of the templates.

While this approach is consistent with the strategy adopted for the discovery of the Higgs boson in 2012, it includes a group of systematics uncertainties (group 1 in the list above) which is not strictly necessary when measuring a cross-section. The uncertainties in group 1, in fact, quantify the accuracy of the theoretical predictions which the measured cross-section should be compared to. In this optic, the STXS framework overcomes the signal strength approach, by limiting the systematics uncertainties propagated to the STXS measurement to group 2 and to group 3. In addition, the split of the STXS bins is designed to significantly mitigate the effect of these two groups of systematics. Clearly, the number of phase space regions in which the cross-section is measured (*STXS bins*) depends on the available statistics. A larger data sample allows to meaningfully measure more STXS bins and therefore to extract more differential information. The binning schemes used in this thesis for the *resolved* analysis are described in the next section.

7.2.2 Simplified Template Cross Section bins

The categorisation scheme chosen to measure the STXS in the *resolved* analysis is denoted as *5-POI scheme*. This scheme, which only includes eight bins, is shown on the left in Figure 7.4. The bins WH $0 < p_{\mathrm{T}}^{V} < 75$ GeV, WH $75 < p_{\mathrm{T}}^{V} < 150$ GeV

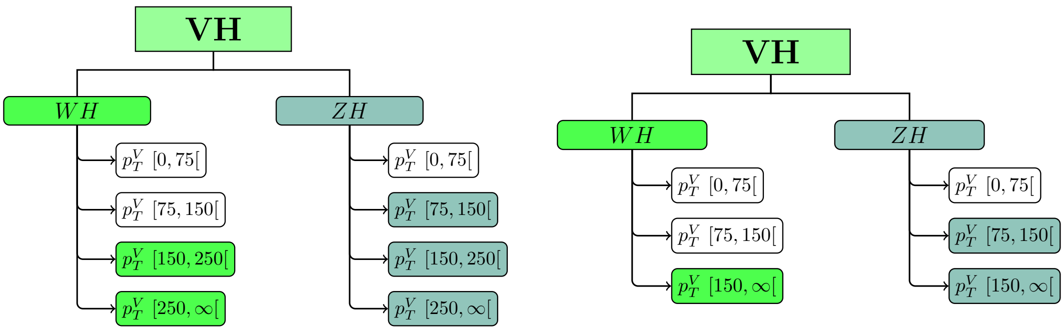

Figure 7.4: Splitting of the $VH(H \to b\bar{b})$ candidates in the STXS bins for the *5-POI* split categorisation (left) and the *3-POI* categorisation (right). The WH $0 < p_{\mathrm{T}}^{V} < 75$ GeV, WH $75 < p_{\mathrm{T}}^{V} < 150$ GeV and ZH $0 < p_{\mathrm{T}}^{V} < 75$ GeV bins, shown in white, are fixed to their Standard Model values in the fit.

and ZH $0 < p_{\mathrm{T}}^{V} < 75$ GeV, shown in white in Figure 7.4, are fixed in the fit to their Standard Model value, as there is not enough statistics to meaningfully measure them with the current analysis selection and available data sample. Therefore, only five cross-section values are measured with this scheme. The forward Higgs region ($|y_H| > 2.5$) has not been included in the measurement as the acceptance for these events is too small.

Additionally to the *5-POI* splitting another scheme, the *3-POI scheme*, shown in Figure 7.4, has been studied. The only difference with respect to the *5-POI* scheme is that the p_T^V cut at 250 GeV is not included. The reason to study this configuration is that there is no split in the event selection at $p_T^V = 250$ GeV, and it could therefore be difficult to measure separately the cross-section above and below 250 GeV. More information about this topic is given in Section 7.2.4.

7.2.3 Comparison to reconstructed categories

In this section, the study to evaluate the level of matching between the reconstructed signal regions and the STXS bins (defined at truth level) is described. For this study the 5-POI splitting scheme is used. This matching is shown in Figure 7.5a, where each bin represents the number of events selected both in a single reconstructed category (y-axis) and in a single STXS bin (x-axis). As mentioned before, the number of reconstructed events for WH $p_T^V < 150$ GeV and ZH $p_T^V < 75$ GeV is low and the cross-section in these regions cannot be measured with the available data sample and the current event selection. Among the remaining regions, the one with the lowest number of signal events is ZH, $p_T^V >$250 GeV with $\sim$ 70 signal events.
For each reconstructed category, the fraction of signal events belonging to a specific STXS bin is shown in Figure 7.5b.
In the 2-lepton and 1-lepton signal regions, almost all events are from ZH and WH bins, respectively. On the contrary in the 0-lepton signal regions even if most of the events are from ZH bins there is a significant contribution ($\sim$ 20%) also from WH bins. The WH events reconstructed in the 0-lepton channel are for example events where the W decays in $\tau\nu$, and the τ decays hadronically and is reconstructed as a jet. In the 1-lepton signal regions a small amount of events belongs to a ZH STXS bin ($\sim$ 2%). Differently, in the 2-lepton signal regions the fraction of events that belong to a WH STXS bin is negligible.
From the plot in Figure 7.5b it is clear that various production channels can have contributions, sometimes tiny, in all the reconstructed categories. By using the templates, all these migrations are automatically taken into account in the fit.
The acceptance times efficiency (referred to as "acceptance" in the following) of each reconstructed category for signal events from the different STXS bins is shown in Figure 7.5c (ratios between the numbers in Figure 7.5a and the corresponding initial numbers for each bin). The bins with the highest acceptance are the high-p_T^V bins, which reach an acceptance of about 6%.

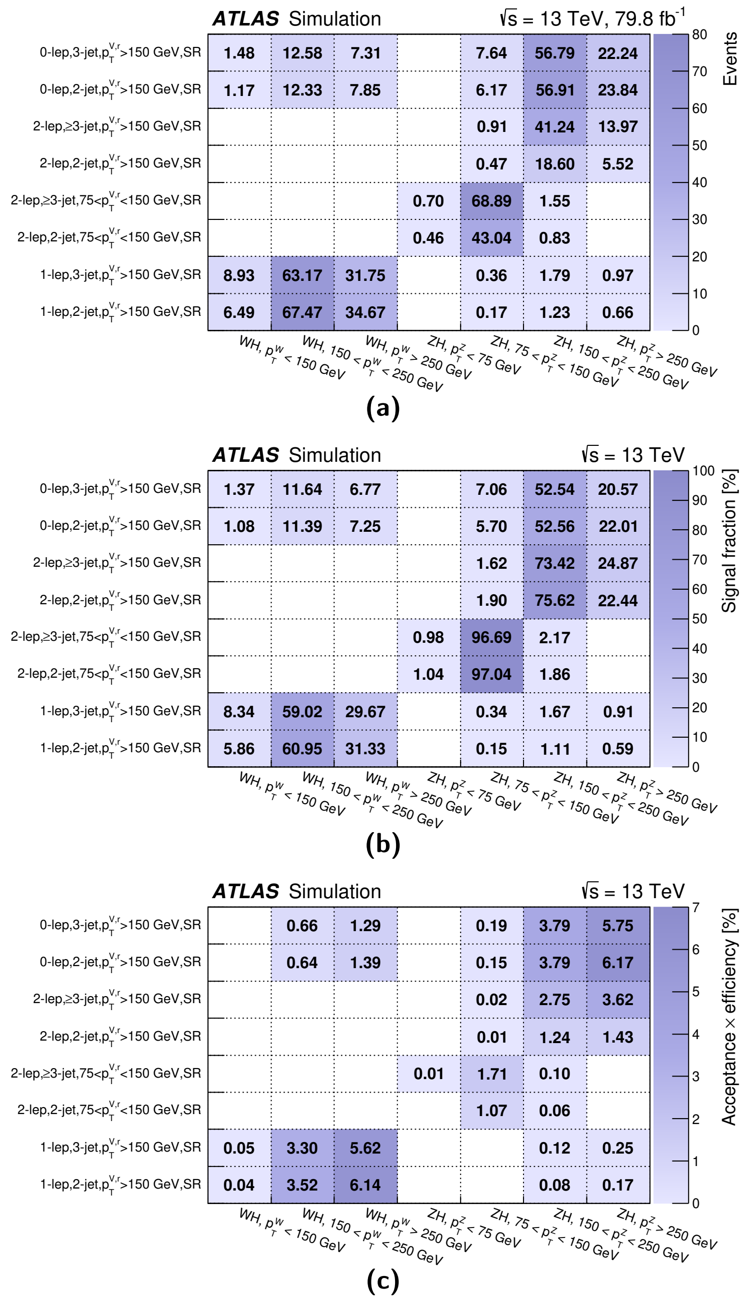

Figure 7.5: With the 5-POI splitting categorisation scheme, (a) the surviving events from each STXS signal region (x-axis) in every reconstructed category (y-axis); (b) the fraction of signal (in percent) from each STXS signal region (x-axis) in every reconstructed category (y-axis); (c) the acceptance (including the efficiency of the experimental selection) for VH, $V \to$ leptons, $H \to b\bar{b}$ events of each reconstructed-event category (y-axis) for each STXS signal region (x-axis), in percent. The control regions are not shown due to negligible contributions. Entries with acceptance times efficiency below 0.01% or signal fractions below 0.1% are not shown [127].

7.2.4 BDT distributions across the STXS regions

The event selection of the *resolved* analysis does not categorize the events with a cut at $p_{\mathrm{T}}^{V} = 250$ GeV. Nonetheless the cross-section can be measured separately in the region below and above 250 GeV. The fit discrimination power between the two p_{T}^{V} regions can only be provided by the different shapes of the BDT discriminant across STXS bins. A difference in shape is expected to arise from the fact that the reconstructed p_{T}^{V} is largely correlated with the BDT score. Actually, p_{T}^{V} constitutes one of the input variables that provides the strongest discrimination between signal and background events, together with m_{bb} and the angular separation of the two b-jets. Signal events tend to have higher p_{T}^{V} with respect to background events. This implies that events with high p_{T}^{V} are expected to peak at higher values of the BDT, with respect to events with low p_{T}^{V}.
In order to understand the sensitivity of the BDT variable to the STXS binning, the shapes of the BDT distributions have been compared. As the goal was only to study the sensitivity to the split at $p_{T}^{V} = 250$ GeV cut, only two regions have been used: $150 < p_{T}^{V} < 250$ GeV and $p_{T}^{V} > 250$ GeV, merging the WH and the ZH production channels. In Figure 7.6 the BDT distributions for the 1-lepton channel is shown as an example, in the 2 jets signal region. The BDT distributions

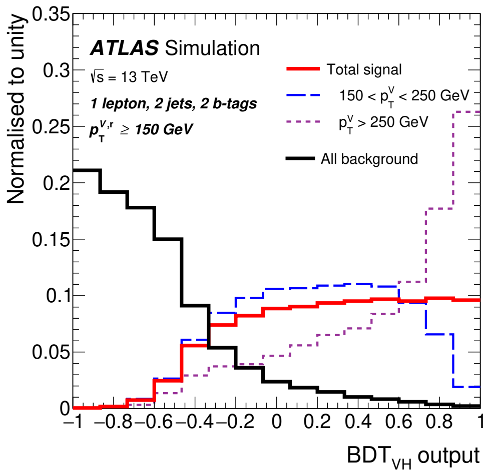

Figure 7.6: *BDT* distributions for p_{T}^{V} bins for the 1-lepton channel in the signal regions 2 jets category. The distributions of the total signal processes (red line) and background processes (black line) are also shown. All the distributions are normalised to unitary areas.

are scaled to the same area in order to highlight the shape differences. A clear difference between the shape of the BDT distribution for events with $p_{\mathrm{T}}^{V} < 250$ GeV and $p_{\mathrm{T}}^{V} > 250$ GeV is observed, with the shape of events with $p_{T}^{V} > 250$ GeV peaking at higher values, as expected. The BDT shape of all the signal events selected in the 1-lepton channel is shown in the same figure in red, together with the shape of all the background events, shown in black and peaking at low BDT values.

The number of events in each category can be assessed from the plot in Figure 7.5a, which suggests that the number of events in the regions below and above 250 GeV is of the same order (e.g. for WH in the 1-lepton 2-jet region is $\sim$ 67 events in the p_{T}^{V} region [150,250] GeV and $\sim$ 35 in the region p_{T}^{V} >250 GeV). The differences of the BDT shapes thus allow a measurement of the cross-section above and below p_{T}^{V} = 250 GeV, as described in the next chapters. In the future, a simple optimisation for these measurements could consist in replicating the analysis adding a cut at p_{T}^{V} = 250 GeV in the categorisation.

Chapter 8

Systematic uncertainties

The measurement of the STXSs presented in this thesis has been the first measurement of the $VH(H \to b\bar{b})$ cross-section as a function of the vector-boson transverse momentum, p_T^V. The theoretical predictions on the cross-sections as a function of p_T^V and their uncertainties had to be specifically computed for the STXS measurement and are presented in the first section of this chapter. The systematic uncertainties for the resolved and merged analyses are described in the second section. The last section is dedicated to the systematic uncertainties specifically needed for the STXS measurements.

8.1 Theoretical cross-sections and related uncertainties

The STXS framework has been designed to maximize the sensitivity of the Higgs boson cross-section measurements while minimizing their theory dependence. In this framework, cross-sections are measured in mutually exclusive phase space regions. At the time of the measurement, the theoretical predictions of the cross-sections in these regions were not available, and they have been hence derived for this purpose. Similarly, the uncertainties on these predictions were only available on the inclusive cross-sections. The uncertainties on the predictions that should be taken into account are:

- uncertainties on the branching ratio;

- unaccounted higher-order electro-weak (EW) corrections;
- uncertainties from neglected higher orders in QCD (QCD scale variations);
- parton distribution function (PDF) and α_s uncertainties.

The predicted cross-sections for WH and ZH, available when this thesis started, are shown in Table 8.1 together with their associated uncertainties due to the QCD scale variations, unaccounted higher-order EW corrections, PDF and α_s uncertainties. Another systematic uncertainty on the overall VH cross-section

Process	σ[fb]	QCD scale unc. [%]	PDF/α_s [%]	δ_{EW} [%]	σ_γ [fb]
$W^+(\to \ell^+\nu)H$	94.26	${}^{+0.5}_{-0.7}$	$\pm1.6/\ \pm0.9$	-7.4	$3.09^{+3.33}_{-0.37}$
$W^-(\to \ell^-\nu)H$	59.83	${}^{+0.4}_{-0.7}$	$\pm1.8/\ \pm0.8$	-7.3	$2.00^{+2.34}_{-0.22}$
$Z(\to \ell\ell)H$	29.82	${}^{+3.8}_{-3.1}$	$\pm1.3/\ \pm0.9$	-5.3	$0.11^{+0.12}_{-0.01}$
$Z(\to \nu\nu)H$	177.62	${}^{+3.8}_{-3.1}$	$\pm1.3/\ \pm0.9$	-4.4	0.00

Table 8.1: Total cross-sections σ for $W^+(\to \ell^+\nu)H$, $W^-(\to \ell^-\nu)H$, $Z(\to \nu\nu)H$ and $Z(\to \nu\nu)H$. The cross-section values are scaled by the branching ratios for the leptonic V decays $Z(\ell\ell,\nu\nu)$ and $W \to \ell\nu$. σ_γ is the photon-induced contribution to the cross-section. δ_{EW} are the NLO EW corrections. The uncertainties due to the QCD scale variations, PDF and α_s variations are reported as well. All the numbers are from Ref. [20].

originates from unaccounted higher-order electro-weak effects. It is determined in the following way:

$$\Delta_{EW} = max\{1\%, \delta^2_{EW}, \Delta_\gamma\} \tag{8.1}$$

with the maximum of the generic size of the neglected NNLO EW effects 1%, the relative NLO EW correction δ_{EW} and the uncertainty of the photon-induced cross-section relative to the total (W/Z)H cross-section, Δ_γ.
The theoretical predictions for the $VH(H \to b\bar{b})$ process are completed by the $H \to b\bar{b}$ branching ratio, equal to 0.582 (for $m_H = 125$ GeV). Its uncertainty is equal to 1.7% and takes into account missing higher-order effects in QCD and EW theory calculation as well as uncertainties on the b-quark mass and α_s [20].

The predictions and uncertainties presented so far are not sufficient for the granularity of the STXS measurements. Therefore, the theoretically predicted cross-sections, the PDF, α_s and QCD scale uncertainties on the more granular STXS regions have been specifically derived for the $VH(H \to b\bar{b})$ measurements. These estimates have been obtained following the recommendations and ideas available in the literature, and are presented in the following paragraphs of this section.

8.1.1 Binning scheme for the uncertainties computation

In STXS measurements the signal simulated samples are split at truth level into several STXS bins. The number of bins that is possible to measure depends on the size of the data sample. In order to have a flexible setup, it was chosen to evaluate SM predicted cross-sections and their uncertainties using a very fine binning, named *maximum splitting*, and to establish a procedure to easily re-evaluate the cross-sections and their uncertainties when reducing the number of bins (e.g. reducing to the *3-POI* and *5-POI* schemes presented in Section 7.2.2 for the *resolved* analysis). In the maximum splitting scheme, the VH signal is divided into three production modes: $qq \to Z(\ell\ell, \nu\nu)H$ denoted as $qq \to ZH$, loop-induced $gg \to Z(\ell\ell, \nu\nu)H$ or $gg \to ZH$, $qq \to WH$ or WH. For each production mode the phase space is divided into a central and forward (FWD) region according to the value of the Higgs boson rapidity: $|y_H| > 2.5$ and $|y_H| \leq 2.5$. The central region is further divided into intervals based on the vector boson transverse momentum at truth level, p_{T}^{V}. The five p_{T}^{V} intervals are defined by cuts at 75, 150, 250 and 400 GeV; each interval is further split according to the number of extra jets (exactly 0, exactly 1 and ≥ 2, denoted as 0J, 1J and GE2J). Jets are defined at truth level using the anti-k_t algorithm with a radius parameter of R = 0.4. Truth jets are built from final state hadrons excluding those produced in the Higgs boson decay, and are required to have $p_T > 30$ GeV. The *maximum splitting* bins are schematically shown in Figure 8.1. In summary, 16 regions are defined for each production mode (5 p_{T}^{V} regions × 3 n_{jet} regions + FWD).

The cross-section measured in the STXS bins needs to be compared with the SM theoretical predictions. The predicted cross-sections for the maximum splitting categorisation scheme have therefore been computed and can be easily merged to obtain the values on coarser categorisation schemes. The predicted values have been obtained, at a centre of mass energy $\sqrt{s} = 13$ TeV, from the following event generators. All $q\bar{q}$-initiated production processes are simulated using the `Powheg` generator with the `MiNLO` procedure, interfaced to the Pythia 8 generator, normalized to the most accurate theoretical cross-section predictions currently available (NNLO (QCD) and NLO (EW)). An additional scale factor, computed using the Hawk generator [128], is applied to the $q\bar{q}$-initiated processes as a function of p_{T}^{V} to account for electroweak corrections at NLO. The $gg \to ZH$ contribution relies on the `Powheg` prediction, computed at LO in QCD, interfaced with Pythia 8 for the modelling of parton shower, underlying event and multiple parton interactions, normalized to the NLO order and next-to-leading-logarithm (NLO+NLL) (QCD) cross-section. The values obtained for the WH production cross-sections are shown in Figure 8.2. The equivalent plots for $qq \to ZH$ and $gg \to ZH$ are available at Ref. [11].

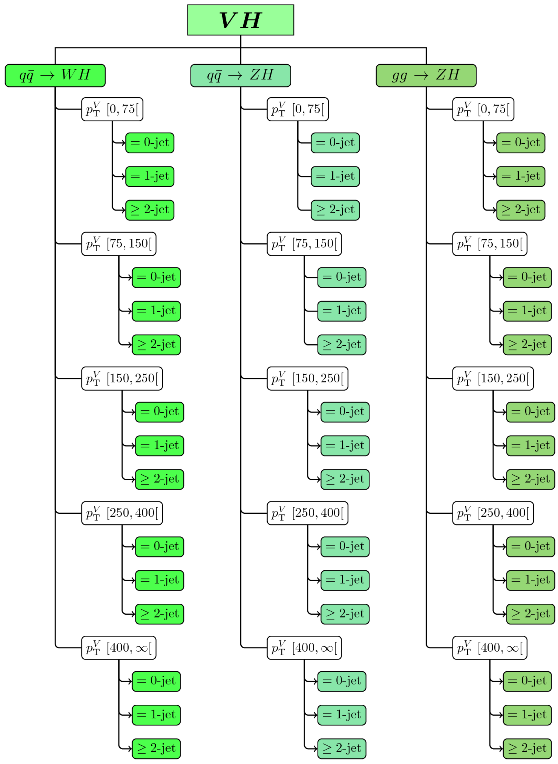

Figure 8.1: STXS bins for the VH processes in the *maximum splitting* categorisation scheme. The leptonic decay of the vector boson V is not shown for simplicity. Forward region bins are not shown in this figure. The boundaries of the p_{T}^{V} regions are expressed in GeV.

The predicted SM cross-sections for the *5-POI* splitting categorisation scheme, adopted in the *resolved* STXS measurement, are shown in Figure 8.3. The values for the *3-POI* scheme can be easily computed from the same plot, summing the cross-section values in the regions of the *5-POI* scheme, and are not shown.

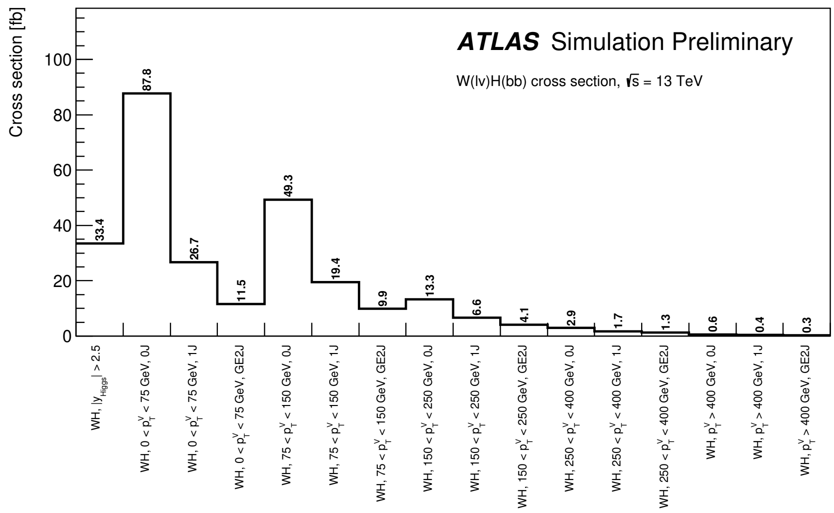

Figure 8.2: Expected SM cross-section in each *maximum splitting* bin for WH. The first bin includes all contributions from the forward Higgs region ($|y_H| > 2.5$). No uncertainties on the predictions are considered in this plot. The cross-section values are scaled by the Higgs branching ratio to bottom quark pairs BR($H \to b\bar{b}$) = 0.582, and by the branching ratios for the leptonic $W \to \ell\nu$ decay [11].

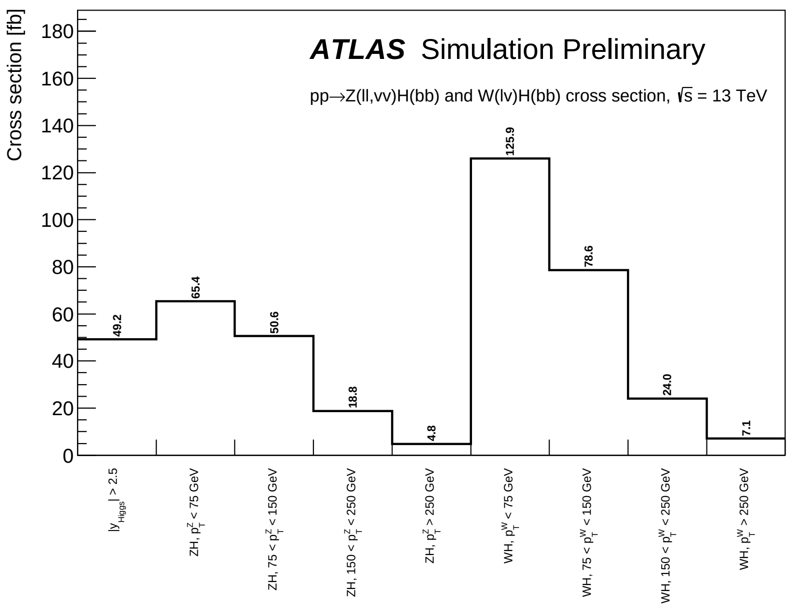

Figure 8.3: Expected SM cross-section in each *5-POI* splitting bin. The first bin includes all contributions from the forward Higgs region ($|y_H| > 2.5$). No uncertainties on the predictions are considered in this plot. The cross-section values are scaled by the Higgs branching ratio to bottom quark pairs BR($H \to b\bar{b}$)=0.582, and by the branching ratios for the leptonic decays $Z(\ell\ell, \nu\nu)$ and $W \to \ell\nu$ [11].

8.1.2 Parton Distribution Function and α_S uncertainties

As shown in Table 8.1, uncertainties accounting for the Parton Distribution Functions (PDF) variations were only available on the inclusive VH cross-sections when the work on the STXS measurement began. The uncertainties due to the PDF variations have therefore been re-computed to adapt for the STXS framework, adopting the *maximum splitting* categorisation scheme introduced in the previous section. PDF uncertainties have been implemented using the PDF4LHC15_30 set from Ref. [129]. The PDF set used includes a nominal value and 30 PDF variations, assuming $\alpha_s(m_Z^2) = 0.1180 \pm 0.0015$. In addition to the 30 PDF variations, the set includes two variations of $\alpha_s(m_Z^2)$: $\alpha_s(m_Z^2) = 0.1165$ and $\alpha_s(m_Z^2) = 0.1195$, corresponding to a central value variation equal to ± 0.0015.
The percent yield variations ($Var_{i,j}$) induced by the PDF uncertainty are computed in each STXS bin j and for each PDF i using as nominal PDF the first PDF sample of the set (PDF0):

$$\mathrm{Var}_{i,j} = \frac{y_{\mathrm{PDFi},j} - y_{\mathrm{PDF0},j}}{y_{\mathrm{PDF0},j}}$$

where $y_{\mathrm{PDFi},j}$ is the yield in bin j calculated with PDF set i.
The α_S variation is computed as the average of the absolute value of the relative variations $\alpha_s(m_Z^2) = 0.1165$ and $\alpha_s(m_Z^2) = 0.1195$ with respect to PDF0:

$$\mathrm{Var}_{\alpha_s} = \frac{|\mathrm{Var}_{\alpha_s=0.1165}| + |\mathrm{Var}_{\alpha_s=0.1195}|}{2}$$

where $\mathrm{Var}_{\alpha_s=0.1165}$ and $\mathrm{Var}_{\alpha_s=0.1195}$ are the relative variations of the samples with $\alpha_s(m_Z^2) = 0.1165$ and $\alpha_s(m_Z^2) = 0.1195$ with respect to the nominal sample PDF0.
The PDF and α_S relative variations in all STXS bins are shown in Figure 8.4 for the WH production mode. Most of the PDF variations have a negligible contribution. For WH only five of the 31 variations have an impact larger that 1%, and only in some bins. The α_s variation is represented with a black dotted line and is among the largest variations. The variations for $qq \to ZH$ and $gg \to ZH$, which are not shown here, have a similar behavior and have an impact below $\sim 2\%$ (see Ref. [11]).
The described implementation allows to simplify the possible combination of the $VH(H \to b\bar{b})$ fit framework with ATLAS analyses exploring other production-decay channels, where the PDF contribution could potentially be large. Therefore even if in the VH channel most contributions are negligible, all the PDF variations are propagated in the fit. There are therefore 31 nuisance parameters accounting for variations of PDF+α_S.

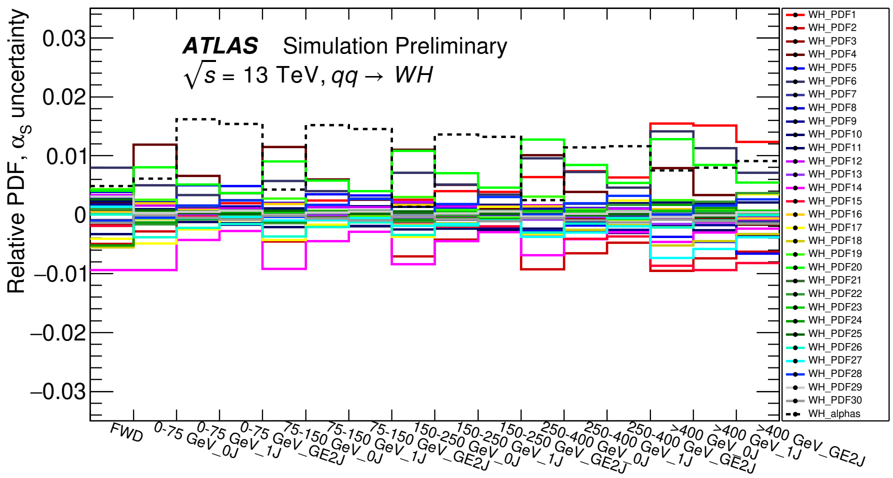

Figure 8.4: Relative yield variations across STXS WH bins for PDF (colored lines) and α_s (black dotted line) uncertainties. The x-axis labeling indicates the p_{T}^{V} bin boundaries in GeV, the n_{jet} multiplicity (0, 1 and $\geq$ 2 jets, as 0J, 1J and GE2J). The FWD bin includes all contributions from the forward Higgs region ($|y_H| > 2.5$) [11].

8.1.3 Uncertainties due to neglected higher order in the α_s perturbative expansion

As for the PDF variations, also the uncertainties from missing higher orders in QCD were only available as variations on the inclusive VH cross-sections and have been re-computed to adapt to the STXS framework. These uncertainties are evaluated by assessing the dependence of the yields on the renormalisation and factorisation scale values. In what follows, the parametrization scheme adopted for the computation is described.

In the calculation of the nominal cross-sections, the renormalization and factorization scales are set to a value close to the energy scale of the process, e.g. the invariant mass of the VH system, m_{VH} [69]. The QCD scale uncertainties are estimated by varying the renormalisation scale μ_R and factorisation scale μ_F independently between $1/2$ and 2 times their original values μ_R^{nom} and μ_F^{nom}. The six scale variations considered are:

$$[\frac{\mu_R}{\mu_R^{nom}}, \frac{\mu_F}{\mu_F^{nom}}] : [0.5, 1][1, 0.5][2, 1][1, 2][0.5, 0.5][2, 2]$$

The computed variations are relative variations with respect to the nominal values $[\frac{\mu_R}{\mu_R^{nom}}, \frac{\mu_F}{\mu_F^{nom}}] = [1, 1]$. The parametrization of these uncertainties across the STXS bins is obtained following the recommendations of Ref. [20, 130]. The effect of these variations on the STXS bins is arranged into two sources. The first source describes the total event rate variation, while the second source describes migration

uncertainties, introduced by the binning cuts. Hence, every split based on the vector boson transverse momentum p_{T}^{V} or on the number of jets n_{jet} introduces an uncertainty.
The example of a two-bin measurement and its generalisation to a N-bin case are used to illustrate the method. Consider a single boundary a/b that splits the cross-section into two bins $\sigma_{ab} = \sigma_a + \sigma_b$. This binning can introduce a migration uncertainty, which affects each bin, and it should cancel when the bins are merged together. In the following, the absolute uncertainty on the expected value σ_{ab} is referred to as Δ_{ab}^{y}. With the introduction of a boundary a/b, two sources of uncertainties are necessary:

- Δ_a^y and Δ_b^y: the absolute uncertainties on σ_a and σ_b;
- $\Delta_{a/b}$: the uncertainty on the migration at the boundary a/b;

where Δ_a^y and Δ_b^y satisfies $\Delta_{ab}^y = \Delta_a^y + \Delta_b^y$ as they are completely correlated. These uncertainties are implemented as two independent sources: θ^y called the *correlated source*, and $\theta_{a/b}$ called the *anti-correlated source*. They are defined as shown in Table 8.2. The choice of the separation into independent sources, which are fully

	σ_{ab}	σ_a	σ_b
θ^y	Δ_{ab}^y	Δ_a^y	Δ_b^y
$\theta_{a/b}$	0	$\Delta_{a/b}$	$-\Delta_{a/b}$

Table 8.2: Impact of the overall uncertainty, θ^y, and of the migration uncertainty, $\theta_{a/b}$, on the σ_a, σ_b and σ_{ab} cross-sections.

correlated or anti-correlated between the different observables, allows for easy implementation in terms of independent nuisance parameters for each component.
Consider now the general case of multiple bins. Each bin can have more than one boundary, and each boundary can be shared by different bins. To treat this case the uncertainties in Table 8.2 are used for any single bin boundary a/b, ignoring all additional subdivisions. Then, given the bin boundary a/b, additional binning cuts that further subdivide σ_a and σ_b as $\sigma_a = \sum_i \sigma_{ai}$ and $\sigma_b = \sum_j \sigma_{bj}$ can be included. Since the a/b boundary is interpreted as a common uncertainty source, it is considered as fully correlated among each set of sub-bins and implemented via a single source $\theta_{a/b}$. The corresponding uncertainty amplitudes for all the bins are now given as:

$$\theta_{a/b} : \Delta_{a/b} \times \{\{x_{ai}\}, \{-x_{bj}\}\} \text{ with } \sum_i x_{ai} = \sum_j x_{bj} = 1$$

where the parameters x_{ai} and x_{bj} specify how the absolute uncertainty $\Delta_{a/b}$ gets distributed among the sub-bins. For example, assuming that the STXS bins are split at $p_T^V = 150$ GeV, the migration uncertainty induced by the split will be fully anti-correlated between the bins $0 < p_T^V < 150$ GeV and $p_T^V > 150$ GeV. If the bin $p_T^V > 150$ GeV is further split at 250 GeV the migration uncertainty induced by the cut at 150 GeV is fully correlated between bins $150 < p_{\mathrm{T}}^V < 250$ GeV and $p_{\mathrm{T}}^V > 250$ GeV.

At this point, the estimate of the sources of uncertainties on the theoretical predictions for the STXS bins passes by the determination of the appropriate $\Delta^y_{a/b}$ and $x_{ai,bj}$. While the uncertainties on the scale variations introduced before can be used to determine the values of Δ^y_{ab} and $\Delta_{a/b}$, more freedom is left on the values of x_{ai} and x_{bj}. In this thesis, the adopted scheme uniformly distributes the uncertainties across sub-bins, so that the value of x_{ai} (x_{bj}) is equal to the fraction of events in the sub bin $i(j)$ with respect to the number of events in the bin $a(b)$. This is equivalent to use a constant relative uncertainty on all the sub-bins of a certain bin. This strategy automatically ensures that in any merging of adjacent bins, the resulting systematic uncertainty can be easily obtained.
The estimates of the $\Delta_{a/b}$ have been performed starting from the scale variation introduced before. The scale variations have been performed in inclusive p_{T}^V bins to compute the uncertainties due to p_{T}^V boundaries, and inclusive in n_{jet} to compute the uncertainties due to n_{jet} boundaries. The basic idea behind this choice is that the scale uncertainties cannot be directly computed in bins that are exclusive in p_{T}^V or in the number of jets, as scale variations in exclusive fixed-order predictions have been found to underestimates the perturbative uncertainty for these cross-sections. This is due to the cancellation of large and predominantly independent perturbative series. The uncertainties are therefore first computed in inclusive bins and then propagated to the exclusive bins. More details about this procedure and the theoretical argument can be found in Ref. [131].

To compute the uncertainties due to p_{T}^V boundaries the six scale variations of equation 8.1.3 are evaluated in inclusive p_{T}^V bins: $p_T^V > 75$ GeV, $p_T^V > 150$ GeV, $p_T^V > 250$ GeV and $p_T^V > 400$ GeV. The variations are shown in Figure 8.5 for the WH production mode. Similar variations have been computed for the $qq \to ZH$ and $gg \to ZH$ production modes. The maximum scale variations in inclusive bins for WH and $qq \to ZH$ are about 3/4%.
Once the six scale variations have been computed in inclusive bins, only the maxima of the absolute value of the six evaluated variations, named δ, are considered. For each production mode, there are therefore four relative uncertainties δ due to the bin p_{T}^V boundaries:

$$\delta_{p_{\mathrm{T}}^V \text{ range}} = \left\{\delta_{[75,\infty,]}, \delta_{[150,\infty,]}, \delta_{[250,\infty,]}, \delta_{[400,\infty,]}\right\}$$

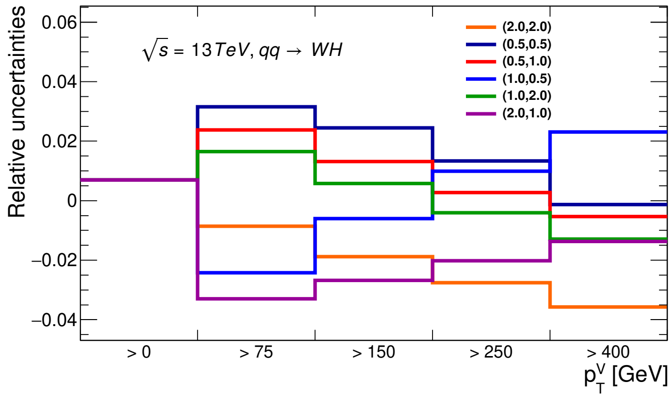

Figure 8.5: Relative QCD scale variations evaluated in inclusive p_{T}^{V} bins for WH. The represented variations are $[\mu_R, \mu_F] : [0.5, 1][1, 0.5][2, 1][1, 2][0.5, 0.5][2, 2]$. The overall scale uncertainties (bin $p_{\mathrm{T}}^{V} > 0$ GeV) are not computed with the same method, but taken from Ref. 8.3.

The QCD relative variations computed in inclusive p_T^V bins are then propagated to the STXS bins. In order to propagate the uncertainties on the STXS bins the absolute uncertainties are computed. The absolute uncertainties Δs are defined as the maximum relative variations δs times the *yields* in the inclusive p_{T}^{V} bins times a scaling factor $K = 0.5$:

$$\begin{aligned} \Delta^{y} &= y_{tot} \times \delta_{y}; \\ \Delta_{75} &= y_{[75,\infty]} \times \delta_{[75,\infty]}; \\ \Delta_{150} &= y_{[150,\infty]} \times \delta_{[150,\infty]} \times K; \\ \Delta_{250} &= y_{[250,\infty]} \times \delta_{[250,\infty]} \times K; \\ \Delta_{400} &= y_{[400,\infty]} \times \delta_{[400,\infty]} \times K; \end{aligned} \tag{8.2}$$

Here y are the yields in each inclusive p_{T}^{V} bin and the scaling factor K avoids uncertainties overestimation, as described in more detail later. Each Δ_x represents the migration uncertainty due to the splitting at $p_{\mathrm{T}}^{V} = x$ GeV and should be fully anti-correlated between bins with $p_{\mathrm{T}}^{V} > x$ GeV and $p_{\mathrm{T}}^{V} < x$ GeV, as previously described. For example the impact of Δ_{250} is:

$$\begin{aligned} -\Delta_{250}/y_{[0,250]} &\text{ for STXS bins with } p_T^V < 250 \text{ GeV} \\ \Delta_{250}/y_{[250,\infty]} &\text{ for STXS bins with } p_T^V > 250 \text{ GeV} \end{aligned}$$

where $y_{[0,250]}$ and $y_{[250,\infty]}$ are the yields for the bins $p_T^V < 250$ GeV and $p_T^V > 250$ GeV respectively. Using this definition, the migration uncertainties Δ_{75}, Δ_{150}, Δ_{250} and Δ_{400} have a null effect when all STXS bins are merged to a single bin.

production mode	δ_y
WH	$\pm 0.7\%$
$qq \to ZH$	$\pm 0.6\%$
$gg \to ZH$	$\pm 25\%$

Table 8.3: Overall QCD scale cross-section uncertainties on WH, $qqZH$ and $ggZH$ from Ref. [20] and [72].

Following this approach for the p_{T}^{V} bins, each Δ_i parameter includes a contribution from higher p_{T}^{V} boundaries. In order to avoid uncertainties overestimation, a scaling factor $K = 0.5$ is introduced starting at Δ_{150}. For $K = 1$, this effect would result on an overestimation of the uncertainties, especially at high p_{T}^{V}[1]. The chosen value for the K factor is a best guess that has been discussed and chosen within the LHC Higgs cross-section working group (LHCHXSWG) [132]. The described approach to the uncertainties induced by the scale variations is one of the possible strategies and has been agreed within the same group.

The overall cross-section scale uncertainties δ_y are not computed with the method described above but are taken from the most precise inclusive cross-section uncertainties available [20, 72]. A summary of the inclusive cross-section uncertainties used is shown in Table 8.3.

Finally, all the scale uncertainties on the STXS bins due to p_{T}^{V} boundaries are shown in Figure 8.6 for the WH and $gg \to ZH$ production modes (the equivalent plot for $qq \to ZH$ can be found at Ref. [11]). The quadrature sum of all the represented scale uncertainties (Δ_{75}, Δ_{150}, Δ_{250}, Δ_{400} and Δ^{y}) in a STXS bin is shown as well, to give an idea of the impact of the scale uncertainties (black line). The scale uncertainties for $qq \to ZH$ are not shown as their behaviour is almost identical to $qq \to WH$, as the production mechanism is similar. The uncertainties are instead higher for $gg \to ZH$. In fact, as mentioned in the previous section, the $gg \to ZH$ `Powheg` predictions are computed at LO in QCD. All the computed uncertainties (Δ_{75}, Δ_{150}, ...) are kept uncorrelated among them, while the $qq \to WH$ and $qq \to ZH$ uncertainties are kept correlated. By construction, the Δ_i parameters of the p_{T}^{V} migration uncertainties are the same for the STXS bins with 0, 1 or ≥ 2 additional jets, therefore Figure 8.6 shows no dependence on n_{jet}.

To compute the migration uncertainties due to n_{jet} boundaries, the six scale variations are evaluated in bins inclusive in the number of jets and exclusive in p_{T}^{V}. The inclusive bins used are $n_{jet} \geq 1$ and $n_{jet} \geq 2$. These uncertainties are computed following the same procedure described for the uncertainties due to p_{T}^{V} boundaries.

[1] For $K = 1$, the relative uncertainty for $p_{\mathrm{T}}^{V} > 400$ GeV would be equal to $\sqrt{\delta_y^2 + \delta_{[75,\infty]}^2 + \delta_{[150,\infty]}^2 + \delta_{[250,\infty]}^2 + \delta_{[400,\infty]}^2}$, which is higher than the actual estimate: $\delta_{[400,\infty]}^2$.

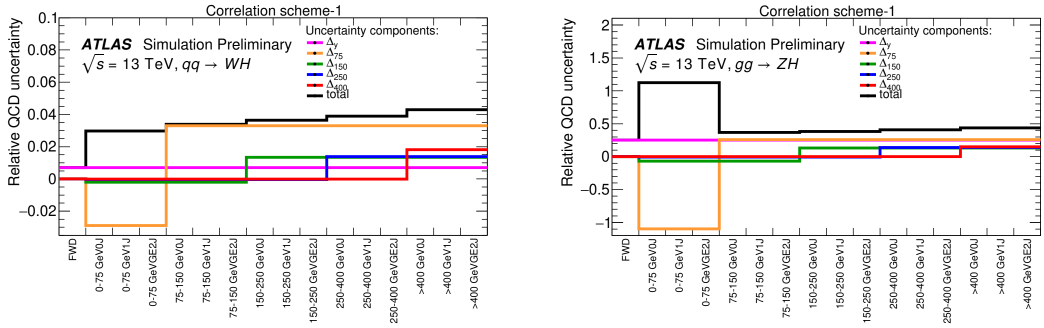

(a) **(b)**

Figure 8.6: Relative uncertainties for the STXS bins due to the p_{T}^{V} splitting and overall uncertainty for $qq \to WH$ (a) and $gg \to ZH$ (b). Δ_{75}, Δ_{150}, Δ_{250} and Δ_{400} are the four migration uncertainties due to the split in p_T^V, Δ^y is the overall scale uncertainty on the cross-section. The black line is the quadrature sum of all the represented scale uncertainties (Δ_{75}, Δ_{150}, Δ_{250}, Δ_{400} and Δ^y) in a STXS bin [11].

In each bin the maximum of the six relative variations is computed and propagated to the STXS bins, which are exclusive in n_{jet}. The impact of Δ^1 (due to the cut on 1 extra jet) and Δ^2 (due to the cut on 2 extra jet) on the STXS bins for $qq \to WH$ and $gg \to ZH$ is shown in Figure 8.7. Also in this case the $qq \to WH$ and $qq \to ZH$ uncertainties are kept correlated. The quadrature sum of all the

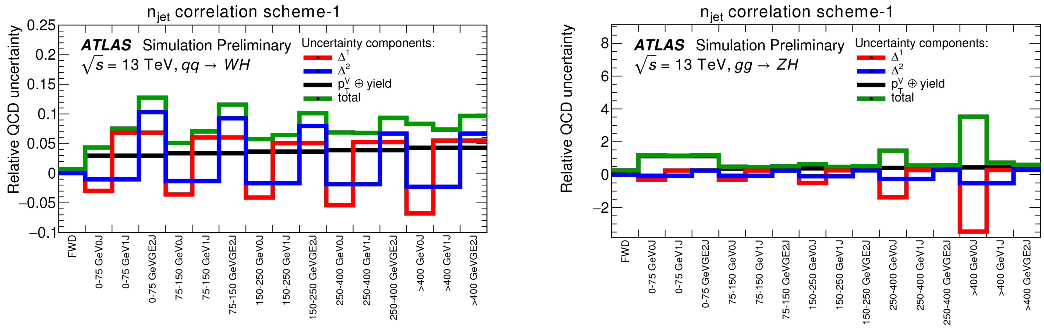

(a) **(b)**

Figure 8.7: Impact of the Δ on the STXS bins for $qq \to WH$ (a) and $gg \to ZH$ (b). Δ^1 and Δ^2 are the migration uncertainties due to the split in n_{jet}. The green line is the quadrature sum of all the uncertainties in a STXS bin: the overall uncertainties, the p_T^V migration uncertainties and the Δ^1 and Δ^2 uncertainties [11].

scale uncertainties in a STXS bin is shown in the same plot (green line). The uncertainties contributing to the quadrature sum are the overall uncertainties, the p_T^V migration uncertainties and the Δ^1 and Δ^2. The n_{jet} migration uncertainties are the largest source of uncertainties in all the bins and production modes.

8.1.4 Summary

Thanks to the work described in the previous sections the cross-sections predictions and uncertainties, that were only available for the inclusive cross-sections, are now available for all the 16 bins (STXS *maximum splitting* scheme) for each VH production mode ($qq \to WH$, $qq \to ZH$, $gg \to ZH$), including differential NLO EW corrections. In the new scheme, 30 uncertainty contributions are introduced for the PDF, one for the EW corrections[2], one for the choice of α_s and 7 for missing higher-order in QCD for $q\bar{q}-$ initiated and $gg-$ initiated processes each. The uncertainties scheme is very flexible and it is possible to easily merge the regions to obtain theoretical predictions and uncertainties on coarser binning schemes. Furthermore, these uncertainties can be used to parametrise the residual theoretical uncertainties necessary for the STXS measurement, as described in Section 8.3.2.

8.2 $VH(H \to b\bar{b})$ analyses uncertainties

The PDF and QCD scale variation uncertainties presented in the previous section affect the theoretically predicted cross-section for the signal. They are therefore not directly related to the measurement and do not include any information on the analyses acceptance or on the detector.
An overview of the main sources of the analysis systematic uncertainties is given in this section for the *resolved* and *merged* cross-section measurements. Most of the sources of systematic uncertainties affecting the *resolved* analysis also affect the *merged* analysis. The *merged* analysis is additionally affected by the uncertainties on the large-R jet and the modelling uncertainty estimate is adapted to the *merged* selection (as described in Section 8.2.2). In Section 8.3, the signal modelling uncertainties are described in the context of the STXS framework. A more detailed description of the systematic uncertainties considered in this thesis can be found in Ref. [8, 11, 16, 21].

The sources of systematic uncertainties affecting the measurements can be divided into two broad groups: uncertainties related to experimental aspects and uncertainties related to the modelling of the simulated signal and background samples. The next two sub-sections follow this subdivision.

[2]The systematic uncertainty for the EW corrections on the STXS predictions is assumed to be of the same order of the one obtained for the EW correction on the inclusive cross-section.

8.2.1 Experimental uncertainties

The main sources of experimental uncertainties in the *resolved* analysis are the b-tagging simulation-to-data efficiency correction factors, the jet energy scale corrections and the modelling of the jet energy resolution. The uncertainties on the jet energy scale and resolution are based on their respective measurements in data and have already been described in Chapter 5. The b-tagging simulation-to-data efficiency corrections are instead described in more details in this section. The large-R jet uncertainties, which are among the main sources of systematic uncertainties for the *merged* analysis, are described in this Section as well.
The uncertainties on the reconstruction, identification, isolation efficiencies of muons and electrons, which have a less relevant impact both in the *resolved* and *merged* analyses, are anyhow included in the fit and have been described in Chapter 5. Uncertainties on the E_{T}^{miss} are briefly described in the same chapter. Uncertainties are included both for the E_{T}^{miss} and for the single-lepton triggers and have a minor impact on the measurements. The luminosity uncertainty and the pile-up reweighting uncertainty are described in this section.

b-tagging uncertainties

In order to correct for different tagging efficiencies observed between data and simulation, a scaling factor is applied to the simulation. The uncertainty on this factor introduces a systematic uncertainty in the analyses [111]. Many effects are studied to evaluate this uncertainty and it is found that the largest source of uncertainties is related to the modelling of the $t\bar{t}$ sample used to compute the scale factors. As an example, the modelling of the initial and final state radiation (affecting the flavour composition), the variation of jet flavour composition between data and simulation, and the size of the simulated sample affect the scaling factor. The systematic uncertainty associated with the various components of the b-tagging is one of the largest sources of uncertainty and is considered for both small-R jets and track-jets. Separated scale factors and corresponding systematic uncertainties are provided for b-, c-, τ- and light-flavor-induced jets. The total number of uncertainties for b-tagging would be about 40 nuisance parameters per flavour. In an effort to alleviate the burden of accounting all the variations a principal component analysis has been done to reduce the number of systematic variations from ~ 160 to a total of about 30 nuisance parameters. For the nuisance parameters of the reduced set, the information on the origin of the systematic uncertainty is lost, as the new variations are given by a combination of various components.

Luminosity

As mentioned in Chapter 2 the luminosity is determined by combining the luminosity measurements of several detectors. The systematic uncertainties affecting the absolute luminosity value is obtained by comparing the measurements from the various detectors. The main contribution to the uncertainty comes from the extrapolation of the calibration from the low-luminosity regime, used during the Van der Meer scans, to the high-luminosity regime, used during data-taking. For the *resolved* and *STXS* analysis, using the data collected between 2015 and 2017, the uncertainty on the luminosity is 2.0% [133]. For the *merged* analysis, exploiting the full Run 2 dataset, the luminosity uncertainty is 1.7% [134].

Pile-up reweighting

The in-time and out-of-time pile-up is described in Section 2.1.1 and the measured average number of interaction per bunch crossing for each year of data collection is shown in Table 2.1. However, the simulated samples are produced before or during the data-taking. As a consequence, only a best-guess of the data pile-up conditions are considered in the simulation. Thus, it is necessary to correct the simulated pile-up conditions to match the condition found in the collected data. The simulated samples are reweighted to correctly reproduce the distribution of the average number of interactions per bunch crossing (μ). The μ value is rescaled by 3% to improve agreement between simulation and data. This procedure is the named pile-up reweighting. An uncertainty, as large as the correction, is included [135] in the fit.

Large-R jet uncertainties (*merged* only)

The uncertainties that mostly affect the *merged* analysis are those related to the large-R jets. They can be roughly classified into *scale uncertainties*, which take into account systematic uncertainties on the jet mass scale, and *resolution uncertainties*, which take into account the uncertainty on the jet mass resolution and on the jet p_T resolution. Both sources of uncertainty are described in Section 5.3.5. Four nuisance parameters related to the jet scale uncertainty are included in the fit, one for each of the components of the scale uncertainty: the *baseline* component accounting for the differences between data and the nominal PYTHIA 8 simulation; the *modelling* component estimated by computing the differences between the nominal PYTHIA 8 simulation to HERWIG 7 and `Sherpa` simulations; the *tracking* component taking into account various tracking uncertainty sources and the *statistical* component accounting for the statistical uncertainty of the simulated samples and of the data sample. Three nuisance parameters related to the jet mass resolution are included, each one describing the uncertainty in the mass resolution for one of the main processes of the fit: $t\bar{t}$, V+jets, and VV (including the diboson and signal processes). Finally, a nuisance parameter accounts for the jet p_T resolution.

8.2.2 Modelling uncertainties for signal and background processes

The number of simulated events fulfilling the event selection, for each process and each category (SR or CR), can be written as:

$$N_{evts} = \mathcal{L} \cdot \sigma \cdot A$$

where $\mathcal{L}$ is the luminosity, σ is the total cross-section and A is the acceptance of the event selection. The modelling uncertainties may affect both the number of events and/or the shape of the template used in the fit. These uncertainties can be broadly divided into three areas: the total cross-section uncertainties on σ; the acceptance uncertainties on A, the uncertainty on the shape of the simulated distribution.

Total cross-section uncertainties

The total cross-section uncertainties for the minor background processes are obtained from the uncertainty on the currently most accurate calculations. Instead, uncertainties on the cross-section of the main background processes, $t\bar{t}$, $W + HF$ and $Z + HF$, are not considered, as the normalisations of the simulated samples are left unconstrained in the fit.

Acceptance uncertainties

The acceptance A is defined as the fraction of events passing the full event selection in a given analysis category. In order to decouple acceptance uncertainties from the total cross-section uncertainties, the acceptance uncertainties are computed as differences in acceptance between samples normalised to the same cross-section. The systematic uncertainties on the acceptances (and on the shapes) are derived

either from comparisons between nominal and *alternative simulated samples* or from comparisons to data in control regions. The *alternative simulated samples* are simulations of either the signal or background events that are not used as *nominal samples* in the fit. These alternative samples are either produced by using a different generator or by altering parameters of the nominal generator. The final uncertainty results from the sum in quadrature of the computed variations.
The variation in acceptance for different analysis categories when using the alternative MC samples are included as well and named *extrapolation uncertainties*. Extrapolation uncertainties among two categories are computed through double ratios. For each variation the computed ratio is:

$$\frac{\text{Yields}_{\text{cat. A}}[\text{nominal}]}{\text{Yields}_{\text{cat. B}}[\text{nominal}]} \bigg/ \frac{\text{Yields}_{\text{cat. A}}[\text{alternative}]}{\text{Yields}_{\text{cat. B}}[\text{alternative}]} \tag{8.3}$$

Here $\text{Yields}_{\text{cat. A}}$ and $\text{Yields}_{\text{cat. B}}$ are the weighted number of selected events in the categories A and B. The computed nuisance parameters control the relative acceptances between two categories. The alternative samples in equation 8.3 are either alternative MC samples, or MC samples with varied parameters (e.g. QCD scale parameters). The total uncertainty is the result of the sum in quadrature of the studied variations.

Shape uncertainties

The uncertainty on the shape of the simulated distributions is also computed from the comparisons between nominal and alternative simulated samples. In order to decouple this uncertainty from the cross-section and acceptance uncertainties, which are already accounted for, all distributions are normalised to the same area. Shape uncertainties are considered in each of the analysis categories separately and are only derived for the m_{bb} and p_{T}^{V} variables, which mainly contribute to the BDT discriminant.

The strategy followed to assess each kind of modelling uncertainty is summarised in Table 8.4. These three groups of systematic uncertainties are evaluated for each signal and background process. A detailed description of the background modelling uncertainties for the *resolved* analysis can be found in Ref. [8, 16] and is not reported in this thesis.
Instead, most of the uncertainties affecting the signal modelling have been already described in Section 8.1. They include (i) the uncertainties on the branching ratio; (ii) QCD scale uncertainties; (iii) PDF and α_s uncertainties; and (iv) EW corrections. Additionally, signal uncertainties on the Parton shower (PS) and underlying events (UE) modelling have been included. Variations of the PS and

Uncertainties	Strategy
Total cross-section	uncertainty on most accurate calculation available
Acceptance	compare simulated samples normalised to the same cross-section
Shape	compare simulated distributions normalised to the same area

Table 8.4: Summary of the strategy followed to estimate the normalisation, acceptance and shape uncertainties

UE modelling affects both the acceptance and shape. The strategy followed to compute these uncertainties has been updated for the STXS and is described in Section 8.3.1. This is slightly different and more complete with respect to the one used for the $H \to b\bar{b}$ observation paper. More details about the PS/UE uncertainties derived for the observation are available at Ref. [8, 16].

8.2.3 Modelling uncertainties for the *merged* analysis

The set of modelling uncertainties described above should be computed both for the *resolved* and *merged* analysis. However, the timeline for the full computation of the modelling uncertainties and for their implementation in the fit for the *merged* analysis does not match the timeline of this thesis. For this reason, such detailed modelling studies have not been included in the fit results here presented. The differences between the full implementation in the *resolved* analysis and the preliminary estimate for the *merged* analysis are described in this section.
Shape uncertainties are not included in the *merged* fit results presented in this thesis, but will be included in the final results. While in the *resolved* analysis shape uncertainties are computed as a function of p_{T}^{V} and m_{bb}, which mainly contribute to the BDT discriminant, in the *merged* analysis the variables used in the fit is m_{J} and the shape uncertainties will be only computed as a function of this variable.
The presented *merged* fit results include a preliminary version of extrapolation uncertainties as explained in the following. In the *resolved* analysis the two extrapolation categories are the 2-jets and 3(3+)-jets categories, the SRs vs CRs or the different leptonic channels (when relevant). In the *merged* analysis the extrapolations are computed among:

- high-purity vs low-purity SRs;
- medium-energy vs low-energy categories;

- SRs vs CRs;
- different lepton channels (if relevant).

These uncertainties are computed and applied separately for each one of the main background processes. The estimation of the extrapolation uncertainties is based on the results of the previous studies performed for the *resolved* analysis. A 20% extrapolation uncertainty between the medium energy (250 GeV $< p_{\mathrm{T}}^{V} <$ 400 GeV) and high energy categories (p_{T}^{V} >400 GeV) has been included for all the samples. A 20% extrapolation uncertainty has been included for the $t\bar{t}$ and single-top samples to account for the modelling differences between the signal regions and the control regions. Finally, a 20% extrapolation uncertainty between the high purity and the low purity categories has been included for all the samples. The preliminary detailed modelling studies for the *merged* analysis are in good agreement with the estimated uncertainties that have been temporarily included in the fit.

8.3 Signal uncertainties for the STXS measurement

One of the purposes of the STXS framework is to move the dominant signal theory uncertainties to the interpretation step providing fiducial cross-section measurements [130]. The theory uncertainties on the SM and BSM predictions are in fact only required at the interpretation level and are therefore not included in the STXS cross-section measurement. However, not all the signal theory uncertainties can be moved to the interpretation level. In the cross-section measurement, the kinematic distribution within each bin is assumed to follow the SM predictions, therefore residual theory uncertainties on the kinematic distribution inside each STXS bin need to be considered.
While all the experimental and background modelling uncertainties for the STXS measurement are the same as those used for the single cross-section measurement, most of the signal modelling uncertainties need to be re-evaluated according to the STXS scheme. Two sources of signal uncertainties have not been re-evaluated: i) the one on the shape of the m_{bb} distribution due to the parton shower and underlying events modelling, and ii) the one on the p_{T}^{V} shape from the NLO EW correction. The first one has been evaluated by comparing the m_{bb} shape for different PS/UE models. This was found to be dominated by the difference between POWHEG + PYTHIA 8 and POWHEG + HERWIG 7, and it is assumed to have little dependence on the STXS bin. The second one has been evaluated following the prescription in equation 8.1 as the $max\left\{1\%, \delta_{EW}^{2}(p_{\mathrm{T}}^{V}), \Delta_{\gamma}\right\}$, and it is of the order of 1-2%. All the other signal systematic uncertainties have been re-evaluated for

the STXS measurement. The re-evaluation of the signal modelling uncertainties is described in this section. The parton shower and underlying events uncertainties for the STXS measurement are described in Section 8.3.1. In Section 8.3.2 the technique exploited to compute the residual theoretical uncertainties is described.

8.3.1 Parton-Shower and Underlying Event modelling uncertainties

The uncertainty related to the parton-shower and underlying events modelling affects the acceptance of the STXS categories and are assessed by using the STXS bin yield obtained with different simulations at truth level, as described below. The nominal POWHEG + PYTHIA 8 prediction is compared to the AZNLO [136] tune variations, and to the prediction obtained with POWHEG + HERWIG 7. 5 NPs, one for each variation, have been included to account for these uncertainties in the fit. This new calculation also allows to fully correlate the PS / UE uncertainties across the STXS bins and reconstructed categories.
The parton-shower variations are only used to define acceptance uncertainties, for each reconstructed category, in each STXS bin of the maximum splitting categorization[3]. Since the PS / UE/UE variation samples have been generated without the simulation of the detector effects, the evaluation of the uncertainties have been done emulating the event selection and the reconstructed categories at truth level. In this context, considering an alternative sample S, the uncertainty $\sigma^S_{C,i}$ in each reconstructed category C and in each STXS bin i is calculated using:

$$\sigma^S_{C,i} = \frac{N_S(C,i)}{N_S(i)} \bigg/ \frac{N_{\text{nominal}}(C,i)}{N_{\text{nominal}}(i)}$$

where $N_S(i)$ is the number of events for the sample S in the bin i before applying any selection cut, and $N_S(C,i)$ the one after applying the cuts of the category C. Given the low statistics on the bins with the lowest acceptances, the uncertainties are bound to 70%. The obtained uncertainty distributions are shown in Figure 8.8 for the 2-jet SR in the 1-lepton channel, together with the acceptance times cross-section times branching ratio. In most cases, the uncertainty is led by the difference between the nominal prediction and the POWHEG + HERWIG 7 one. In the $qq \to WH$ and $qq \to ZH$ cases, this leading component is of the order of 1% in most of the more relevant bins, except for the 3+-jet categories of the 2-lepton-channel where the uncertainty reaches 10%. The $gg \to ZH$ samples are harder to control due to the lower number of events and suffer from a LO calculation of the

[3]Using the PS / UE variation to define an uncertainty on the STXS bins prediction would in fact only add small uncertainties and partially lead to double counting.

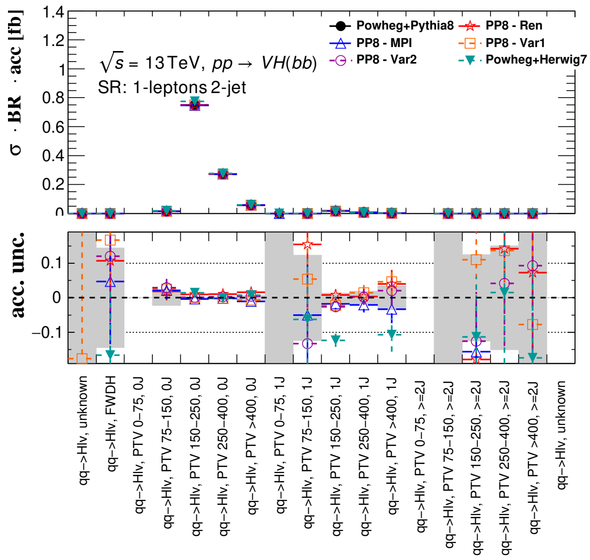

Figure 8.8: Comparison of the various predictions for the acceptance times cross-section times branching ratio in the upper pads, and corresponding acceptance uncertainty ($\sigma^{S}_{C,i}$) in the lower pads, across the STXS bins corresponding to the WH production. The distribution is shown for the 2-jet SRs of the 1-lepton channel. The statistical uncertainty on the nominal prediction is also shown as the grey area in the lower pads.

matrix element with no additional jet to the VH system. As such, the associated PS / UE uncertainties are larger, between 5% and 30%.

8.3.2 Residual theoretical uncertainties

The maximum splitting categorisation scheme introduced in Section 8.1.1 has not only the advantage of providing high flexibility but at the same time allows to take into account a coarse shape uncertainty within the bins chosen to measure the cross-section (e.g. the 5-POI scheme). A simplified example showing the meaning of such residual theoretical uncertainty is presented in the following, together with the procedure followed to subtract the overall theory uncertainties, which depends on the chosen categorisation scheme.

In Figure 8.9 the subtraction scheme is represented very schematically. The bin A and B represent two of the bins of the maximum splitting scheme. Let's suppose that with the given dataset it is only possible to meaningfully measure the cross-section in the bin given by the sum of A and B (σ_{A+B}). The black curves represent the nominal distribution, e.g. the p_{T}^{V} distribution, within the measured bin. The red curves represent the varied distribution. The horizontal dashed curve represents the value of the nominal (black) and varied (red) variable in the bins A and B. As the goal is to measure the fiducial cross-sections, the variation on the overall

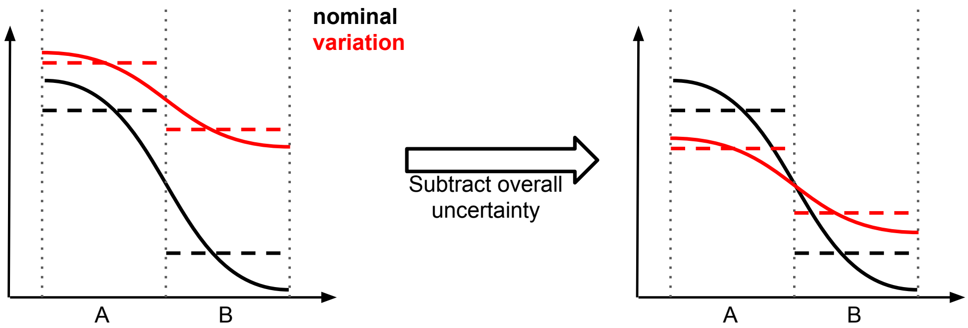

Figure 8.9: Schematic example of the systematic uncertainties on the STXS bin of the maximum splitting scheme before and after subtracting the overall uncertainty. The black curve represents the nominal distribution and the red curve represents the varied distribution. A and B represent two bins of the maximum splitting scheme and in this example, the cross-section is measured in the bin A+B.

cross-section in the measured bin (A+B) has to be removed. The scheme on the left represents the variation before the subtraction of the overall effect, while the scheme on the right represents the variation after the subtraction. As shown in the figure, after the subtraction of the overall effect, there is a residual shape uncertainty within the bin. If the events in bin A and in bin B have the same acceptance, the residual shape uncertainty has a null effect (as the uncertainties are anticorrelated and built to be null in this case). On the other hand, if the acceptance of the two bins is different a residual uncertainty is present. In all cases the uncertainties are always included in the fit through the bins of the maximum splitting scheme. For example the uncertainties for the 3-POI and 5-POI scheme only differ in the values of the overall theoretical uncertainty that is subtracted to the uncertainties of the maximum splitting bins.
In the following the procedure adopted to remove the overall theoretical uncertainty is described. Calling δ_t the theoretical systematic uncertainty on bin t of the maximum splitting STXS scheme, if the cross-section is measured on a coarser bin g that contains a set of bins t, the overall uncertainty on bin g can be removed from δ_t. The overall uncertainty δ_{g} on the coarser bin is given by:

$$\delta_{\mathrm{g}} = \frac{\sum\limits_{t\in g} \delta_t \sigma_t}{\sum\limits_{t\in g} \sigma_t}$$

where σ_t is the cross-section of the bin t. This overall uncertainty should be removed from the uncertainty δ_t, and therefore the residual uncertainty on the bin

t is

$$\delta_{t\text{ residual}} = \delta_t - \delta_{\text{group}}$$

E.g. if t is the bin $150 < p_T^V < 250$ GeV ($t = [150 - 250]$), and the measured bin is $p_T^V > 150$ GeV($g = [> 150]$), the uncertainty to be removed is:

$$\delta_{\text{g}} = \frac{\delta_{150-250}\sigma_{150-250} + \delta_{250-400}\sigma_{250-400} + \delta_{>400}\sigma_{>400}}{\sigma_{>150}}$$

And the residual uncertainty is:

$$\delta_{\text{[150-250], residual}} = \delta_{150-250} - \delta_{\text{group}}$$

The described subtraction procedure is repeated separately for each component of the PDF, α_s, and QCD scale uncertainties.

Chapter 9

Results of the $VH(H \to b\bar{b})$ *resolved* analysis

The results obtained with the resolved analysis, using a data sample of 79.8 fb^{-1}, are described in this chapter. When I joined the $VH(H \to b\bar{b})$ analysis team, the event selection and the fit strategy were already in an advanced state. Therefore the main part of my work focused on new developments directed to measure the STXS and the cross-section in the high energy region. I gave smaller contributions to the $VH(H \to b\bar{b})$ cross-section measurement for the resolved analysis, however it is the basis on which I developed the following work and for this reason a brief summary of this measurement, which led to the $H \to b\bar{b}$ and VH observations, is given in the first section of this chapter. In the second section, the results of the Simplified Template Cross-Sections measurement are presented with more details. Finally, an interpretation of the STXS results within the Effective Field Theory parametrization is described.

9.1 $H \to b\bar{b}$ and VH observation

The first observation of the $H \to b\bar{b}$ decay and VH production, obtained from a 79.8 fb^{-1} data sample, was announced by the ATLAS collaboration in summer 2018. The $VH(H \to b\bar{b})$ measurement, here presented, was combined with other production processes and same Higgs boson decay in order to reach the sensitivity necessary for the $H \to b\bar{b}$ decay observation. Similarly, other Higgs boson decays were combined with this analysis using the same production process to obtain the

VH production observation. These results are briefly summarized in this section, while a more detailed description can be found in Reference [8].
The general procedure followed to measure the cross-section has already been described in Section 7.1. Additional information concerning the *resolved* fit strategy is described here. In this analysis, the fit is used to extract a single parameter of interest (μ), which represents the ratio between the measured and the predicted cross-sections time the branching ratios. The parameter of interest is measured through a global likelihood fit to the data in the distributions of eight SRs and six CRs. The variable used as a discriminant in the SRs is the BDT multivariate discriminant outputs. Instead, only the event yields are used in the two $W + HF$ control regions of the 1-lepton channel, due to the lack of statistics. In the four top control regions of the 2-lepton channel, the m_{bb} distributions are used as input to the fit, except for the 2-jet category of the high-p_V^T region, where the event yield is used. The information about the distributions used in each category is summarised in Table 9.1.

Channels	SR/CR	Categories			
		75 <p_{T}^V < 150 GeV		p_{T}^V >150 GeV	
		2-jets	3-jets	2-jets	3-jets
0-lepton	SR	-	-	BDT	BDT
1-lepton	SR	-	-	BDT	BDT
2-lepton	SR	BDT	BDT	BDT	BDT
1-lepton	W+HF CR	-	-	Yield	Yield
2-lepton	top CR	m_{bb}	m_{bb}	Yield	m_{bb}

Table 9.1: The distributions used in the global likelihood fit for the SRs and CRs for all the categories in each channel, for the *resolved* analysis.

The resulting post-fit BDT distributions for the 0-, 1- and 2-lepton channels in the 2-jets SRs are shown in Figure 9.1 for data overlayed with the prediction obtained by the simulation. Only the high-p_T^V regions, which are the most sensitive to the measurement, are shown.
The background prediction in all post-fit distributions is obtained by setting the nuisance parameters according to the results extracted from the fit. Instead, the dashed histogram shows the total pre-fit background prediction. The signal is shown in red, both on top of the fitted background and unstacked as an unfilled histogram scaled by a factor indicated in the legend. The bins with the highest signal over background ratio are at values of the BDT close to 1.
The normalisation factors of the main background processes are left unconstrained

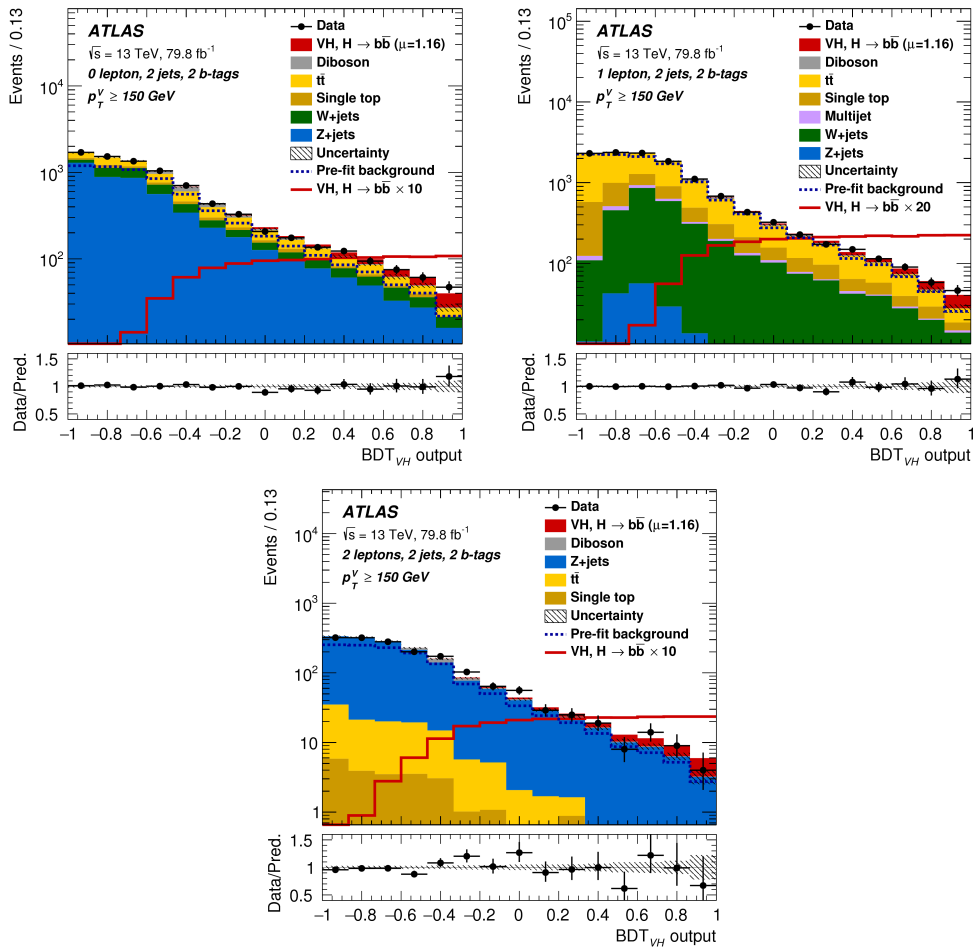

Figure 9.1: The BDT post-fit distributions in the 0-lepton (left), 1-lepton (right) and 2-lepton (bottom) channels, in the 2-jet categories in the high p_T^V region. The data are shown as black dots. The background contributions are shown as filled histograms. The signal is shown as a filled histogram on top of the fitted backgrounds and unstacked as an unfilled histogram, scaled by a factor indicated in the legend. The dashed histogram shows the total pre-fit background. The hatched band includes the combined statistical and systematic uncertainty for the sum of the fitted signal and background. The ratio of the data to the sum of the fitted signal and background is shown in the lower panel [8].

in the fit. The W+HF and Z+HF normalisation factors, unconstrained, are extracted separately in the 2-jet and 3-jet regions. The $t\bar{t}$ background in the 0- and 1-lepton channels is considered independently from the $t\bar{t}$ background in the 2-lepton channel, due to the significantly different regions of phase space probed. Three normalisation factors are thus extracted for the $t\bar{t}$ background. One in the 0-lepton and 1-lepton channels, and two in the 2-lepton channel: one in the 2-jet region and one in the 3-jet region. The values of these normalisation factors extracted from the fit to data are shown in Table 9.2. The uncertainty on all the

Process	Normalisation factor
$t\bar{t}$ 0- and 1-lepton	0.98 ± 0.08
$t\bar{t}$ 2-lepton 2-jet	1.06 ± 0.09
$t\bar{t}$ 2-lepton 3-jet	0.95 ± 0.06
W+HF 2-jet	1.19 ± 0.12
W+HF 3-jet	1.05 ± 0.12
Z+HF 2-jet	1.37 ± 0.11
Z+HF 3-jet	1.09 ± 0.09

Table 9.2: Factors applied to the nominal normalisations of the $t\bar{t}$, W+HF and Z+HF backgrounds, as obtained from the fit to data. The errors represent the combined statistical and systematic uncertainties.

normalisation factors shown in the table are of the order of 10%.
The dominant systematic uncertainty sources of this analysis are the unprecise knowledge of simulated samples modelling and of the b-tagging. A summary of the uncertainties mainly affecting the signal strength is presented in Appendix C, which also includes additional details of how the main uncertainties are derived and some considerations on the observed features. More details on the impact of the main sources of systematic uncertainties can be found in Reference [8].
The observed signal strength corresponds to an excess with a significance of 4.9σ, to be compared with an expectation of 4.3σ. The fitted value of the signal strength is:

$$\mu_{bb}^{VH} = 1.16^{+0.27}_{-0.25} = 1.16 \pm 0.16(stat.)^{+0.21}_{-0.19}(syst.),$$

in good agreement with the expected SM value (1). Systematic uncertainties have a slightly larger impact with respect to statistical uncertainties.
To validate the result of the multivariate analysis a second analysis, the *cut-based analysis* is performed. In the cut-based analysis, the multivariate discriminants are replaced by the invariant mass of the two b-tagged jets, m_{bb}, and tighter selection criteria are applied to select the events. The distribution of m_{bb} in data after subtraction of all the predicted background processes (normalised to

the normalisations extracted from the fit), except for the WZ and ZZ diboson processes, is shown in Figure 9.2. The observed (expected) excess has a significance

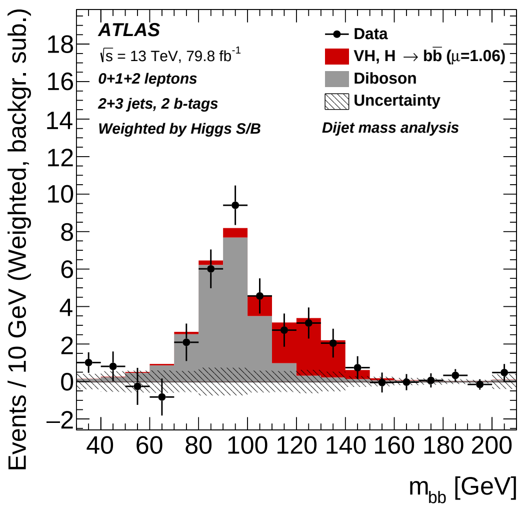

Figure 9.2: The distribution of m_{bb} in data for the cut-based analysis after subtraction of all backgrounds except for the WZ and ZZ diboson processes. The contributions from all lepton channels, p_{T}^{V} regions and number-of-jets categories are summed and weighted by their respective S/B, with S being the total fitted signal and B the total fitted background in each region. The expected contribution of the associated VH production is shown scaled by the measured signal strength. The combined statistical and systematic uncertainty for the fitted background is indicated by the hatched band [8].

of 3.6σ (3.5σ) and is in good agreement with the signal observed in the multivariate analysis. For the sake of brevity, the cut-based analysis is not described in this thesis, but a detailed description can be found in references [8, 16].
The results of the statistical analysis performed on the 13 TeV data have been combined with those obtained from the data recorded at 7 TeV and 8 TeV [137]. The result of the combination is an excess with a significance of 4.9σ, compared with an expectation of 5.1σ. The measured signal strength is:

$$\mu_{bb}^{VH} = 0.98^{+0.22}_{-0.21} = 0.98 \pm 0.14(stat.)^{+0.17}_{-0.16}(syst.)$$

9.1.1 Observation of $H \to b\bar{b}$ decay

The VH measurement has been further combined with results of the searches for the $H \to b\bar{b}$ decay in other production channels, to perform a search for the $H \to b\bar{b}$ decay. The analyses used for the combination are the search for the $H \to b\bar{b}$ decay produced in association with a $t\bar{t}$ pair and the search for $H \to b\bar{b}$

in vector boson fusion production for both Run 1 and Run 2 [121, 138, 139, 140]. Assuming that the relative production cross-sections are those predicted by the SM, the observed significance for the $H \to b\bar{b}$ decay is 5.4σ, to be compared with an expectation of 5.5σ. This corresponds to the first observation of the Higgs decay into two b-quarks. The signal strength for the combined measurement is shown in Figure 9.3a, together with the individual signal strengths for the different decay modes. As expected VH is the production mode giving the largest contribution to the combined measurement.

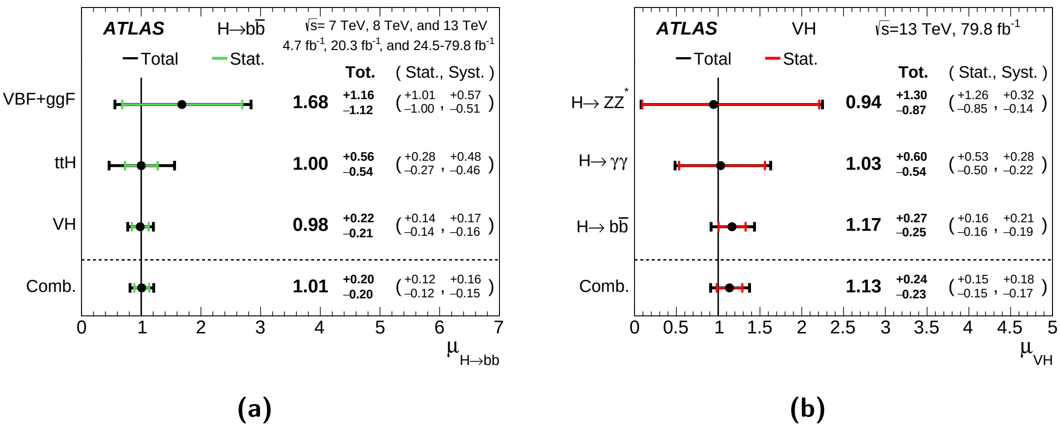

Figure 9.3: (a) The fitted values of the Higgs boson signal strength for the VH, ttH and VBF+ggF analyses along with their combination. The individual values for the different production modes are obtained from a simultaneous fit with the signal strengths for each of the processes floating independently [8].
(b) The fitted values of the Higgs boson signal strength for the $H \to b\bar{b}$, $H \to \gamma\gamma$ and $H \to ZZ^* \to 4l$ decay modes, along with their combination. The individual values for the different decay modes are obtained from a simultaneous fit with the signal strengths for each of the processes floating independently [8].

9.1.2 Observation of the VH production

The $VH(H \to b\bar{b})$ Run 2 results have also been combined with the results of other Run 2 searches for the Higgs boson produced in the VH production mode. The other two searches select the Higgs decay into two photons and into four leptons via ZZ^*. The relative branching fractions of the three decay modes have been assumed to be as predicted by the SM. Using this assumption the fitted value of the VH signal strength for the combined channels is:

$$\mu_{VH} = 1.13^{+0.24}_{-0.23} = 1.13 \pm 0.15(stat.)^{+0.18}_{-0.17}(syst.),$$

in good agreement with the SM predicted value. The combined observed significance is 5.3 standard deviations, to be compared with an expectation of 4.8 standard deviations. This constitutes the first direct observation of the VH associated production. The measured signal strength for the combined measurement is shown in Figure 9.3b, together with the value of the signal strengths for the individual decay modes. Also in this case, as expected, the $H \to b\bar{b}$ channel is giving the largest contribution to the combined measurement.

9.1.3 $VH(H \to b\bar{b})$ results obtained by the CMS collaboration

The ATLAS announcement of the $H \to b\bar{b}$ decay observation in summer 2018 was shortly followed by the announcement of the same observation by the CMS collaboration [18]. A comparison of the analysis strategy and of the results obtained by both collaborations is briefly described here.

In many aspects, the ATLAS and CMS analyses chose a similar approach to isolate $H \to b\bar{b}$ events. In both cases, multivariate techniques are employed to isolate signal events (Deep Neural Network in the CMS case), and events are classified in the 0-lepton, 1-lepton, and 2-lepton channel according to the number of charged leptons. Nonetheless, there are some key differences in the event selection and in the analysis strategy. First, the event selection in the ATLAS analysis is more consistent across the three lepton channels, while in the CMS analysis the cuts are more optimised for each channel. For example, the cuts on the jets transverse momentum from the candidate Higgs decay are uniform across the three channels in the ATLAS event selection while they vary in the CMS case. Second, the two analyses differ in the selection of the decay products of the candidate Higgs boson. While in both cases two jets compatible with having been produced by a b-hadron are selected, ATLAS uses a fixed value of the b-tagging discriminant to select such jets, while CMS takes the two jets with the maximum value the b-tagging multivariate discriminant. The values of the discriminant for the two jets are then among the input variables for the multivariate discriminant used by the CMS analysis. Finally, events in the ATLAS selection are categorised according to the number of jets, while in the CMS case the number of jets is an input variable for the multivariate discriminant.

The expected and observed significances and the measured signal strength for the two analyses are shown in Table 9.3. Both analyses are quoting not only the combined results but also the results for the individual leptonic channels. Unfortunately, it is not possible to directly compare the results for the individual channels. In fact, the CMS collaboration quotes the results only for the data

Channels	Signal strength		Significance			
			ATLAS		CMS	
	ATLAS	CMS	Exp.	Obs.	Exp.	Obs.
0-lepton	$1.04^{+0.34}_{-0.32}$	0.73 ± 0.65	3.1	3.3	1.9	1.3
1-lepton	$1.09^{+0.46}_{-0.42}$	1.32 ± 0.55	2.4	2.6	1.8	2.6
2-lepton	$1.38^{+0.46}_{-0.42}$	1.05 ± 0.59	2.6	3.4	1.9	1.9
combined (only 2017)		1.08 ± 0.34			3.1	3.3
combined (up to 2017)	$1.16^{+0.27}_{-0.25}$	1.06 ± 0.26	4.3	4.9	4.2	4.4

Table 9.3: The ATLAS and CMS measured signal strength and expected and observed significances for $VH(H \to b\bar{b})$ using the data collected at 13 TeV up to 2017 (~ 80 fb^{-1}) [8, 18]. The results are quoted both for the combined fit and for each lepton channel. The CMS results for the individual channels only take into account the data collected in 2017 (~ 41 fb^{-1}), while the ATLAS results include the full 13 TeV dataset up to 2017.

collected in 2017 while the ATLAS collaboration quotes the results for the data collected up to 2017. It is however possible to compare the relative results. While for the CMS analysis the three lepton channels are giving approximately the same contribution to the expected significance, in the ATLAS case the channel giving the largest contribution is the 0-lepton channel, followed by the 2-lepton channel. The combined observed (expected) significance for the ATLAS and CMS collaboration are 4.9 (4.3) and 4.4 (4.2), respectively. In both cases, the measured cross-section is compatible with the expected SM value.

9.2 Simplified Template Cross Sections results

The $VH(H \to b\bar{b})$ data analysis, whose results have been presented in the previous section can be re-interpreted in the STXS framework, allowing to further test the SM and to infer information on physics BSM. The statistical procedure followed to measure the STXSs has been presented in Section 7.2, and the results of the measurement are presented in this section. The results are presented both for the *5-POI* and *3-POI* schemes. However, only the first one has been used at the end to extract results on BSM parameters, as the measurement within the *5-POI* scheme is more sensitive to possible BSM deviations.

9.2.1 *5-POI* signal measurements

The cross-section measurements shown in this section have been measured using the *5-POI* scheme. Results for the *3-POI* scheme are shown in the next section. For both schemes the low p_{T}^{V} bins, namely $WH_{[0,75]}$, $WH_{[75,150]}$ and $ZH_{[0,75]}$ are fixed to the SM values, within the uncertainty that would be used for a signal strength measurement.
The measured cross-sections in the *5-POI* scheme are:

- $(\sigma \times BR)_{ZH[75,150]} = 80.5^{+46.1}_{-44.5}$ fb;
- $(\sigma \times BR)_{ZH[150-250]} = 13.7^{+12.8}_{-12.6}$ fb;
- $(\sigma \times BR)_{ZH[250-]} = 8.5^{+4.2}_{-3.8}$ fb;
- $(\sigma \times BR)_{WH[150-250]} = 19.9^{+25.0}_{-25.0}$ fb;
- $(\sigma \times BR)_{WH[250-]} = 8.8^{+5.3}_{-5.0}$ fb.

To show the comparison with the expected cross-sections, the results are normalised to the SM value and reported in Figure 9.4. The theoretical uncertainties on the SM predictions of the $\sigma \times BR$ are shown as the gray area. The uncertainties on the predicted cross-section are larger for ZH than for WH, in the same p_{T}^{V} interval. This large ZH uncertainties are due to the limited precision of the theoretical calculations of the $gg \to ZH$ process. All measured cross-section values are consistent with the Standard Model.
The expected SM cross-sections for the five STXS regions are shown in Table 9.4, and displayed in Figure 9.5, together with the measured cross-sections. The statistical and systematic uncertainties on the measured cross-sections are shown as well.
The expected and measured significance for the five measurements are reported in Table 9.5. The observed (expected) significance varies between $\sim 0.8\sigma(\sim 1\sigma)$ and $\sim 2.3\sigma(\sim 1.5\sigma)$ in a single bin, for the five regions.
The correlations between the five parameters of interest are shown in Figure 9.6a. A high anti-correlation between the regions with 150$<p_{\mathrm{T}}^{V}<$250 GeV and the regions with $p_{\mathrm{T}}^{V}>$250 GeV is observed in both the WH and ZH production modes. The observed anti-correlation is expected as there is no categorisation at reconstructed level for $p_{\mathrm{T}}^{V} > 250$ GeV, therefore all the discriminating power of the fit is obtained from the differences in the BDT shapes. This anti-correlation has been further investigated, to check whether it is due to the effect of some common systematic uncertainties. The correlation plot was therefore reproduced (Figure 9.6b) repeating the fit but including only statistical uncertainties. A high anti-correlation

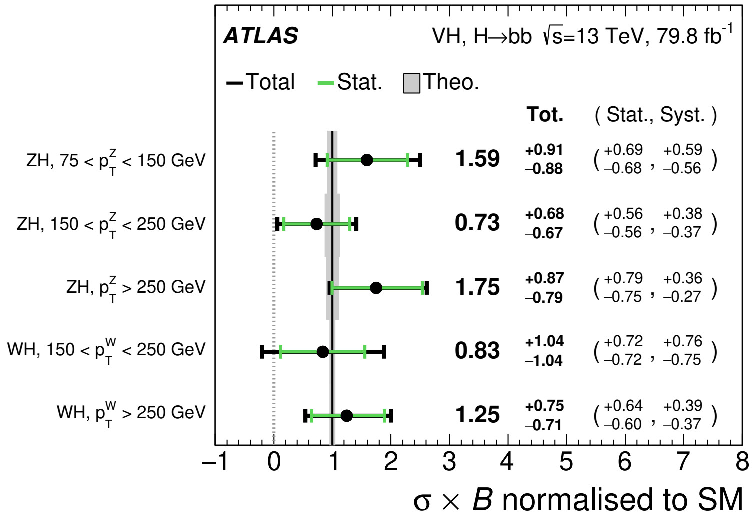

Figure 9.4: Observed values of the $\sigma \times$ BR normalized to the SM for $\text{WH}_{150-250}$, $\text{WH}_{\geq 250}$, ZH_{75-150}, $\text{ZH}_{150-250}$, and $\text{ZH}_{\geq 250}$ in the fit to data. The (black) total observed uncertainty is quoted together with its decomposition in the (green) statistical component, and systematic component. In this plot the uncertainty due to background scale factors is included in the statistical component. The theoretical uncertainty on the prediction of the $\sigma \times BR_i$ is shown as the gray area around 1.

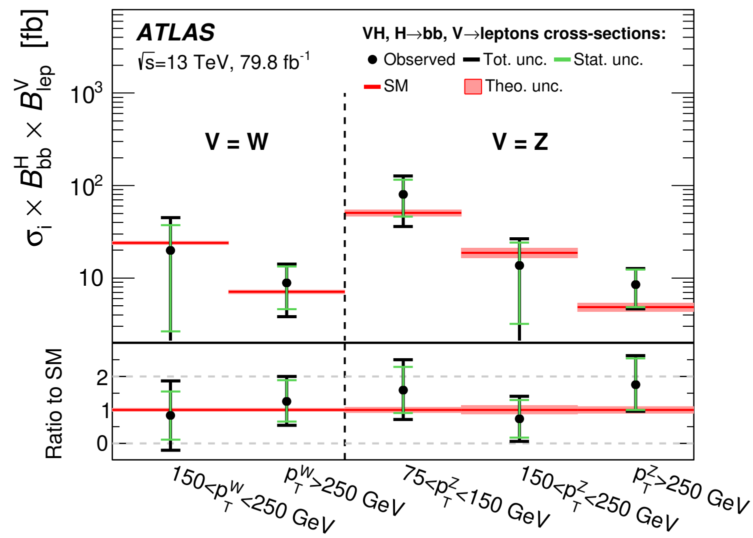

Figure 9.5: Observed values of the $\sigma \times$ BR for $\text{WH}_{150-250}$, $\text{WH}_{\geq 250}$, ZH_{75-150}, $\text{ZH}_{150-250}$, and $\text{ZH}_{\geq 250}$ in the unconditional fit to data. The (black) total observed uncertainty is quoted together with the (green) statistical component. The observation is compared to the SM prediction, marked with the red lines, and its uncertainty, represented by the red area.

Region	SM prediction		Result		Stat. Unc.	Syst. Uncertainties [fb]		
$(H \to b\bar{b})$	[fb]		[fb]		[fb]	Th. Sig.	Th. Bkg.	Exp.
$W \to \ell\nu_{150-250}$	24.00	$\pm$ 1.06	19.9	$\pm$ 25.0	$\pm$ 17.3	$\pm$ 1.6	$\pm$ 13.2	$\pm$ 9.4
$W \to \ell\nu_{\geq 250}$	7.08	$\pm$ 0.34	8.8	$\pm$ 5.2	$\pm$ 4.4	$\pm$ 0.5	$\pm$ 2.5	$\pm$ 0.9
$Z(\ell\ell,\nu\nu)_{75-150}$	50.61	$\pm$ 4.09	80.5	$\pm$ 45.2	$\pm$ 34.7	$\pm$ 10.1	$\pm$ 20.8	$\pm$ 19.3
$Z(\ell\ell,\nu\nu)_{150-250}$	18.80	$\pm$ 2.37	13.7	$\pm$ 12.7	$\pm$ 10.6	$\pm$ 1.4	$\pm$ 6.1	$\pm$ 3.3
$Z(\ell\ell,\nu\nu)_{\geq 250}$	4.85	$\pm$ 0.50	8.5	$\pm$ 4.0	$\pm$ 3.7	$\pm$ 0.8	$\pm$ 1.2	$\pm$ 0.6

Table 9.4: Expected cross-sections (SM) and measured cross-sections in the five measured regions. The contributions to the total uncertainty in the measurements from statistical or systematic uncertainties in the signal modelling (Th. sig.), background modelling (Th. bkg.), and in experimental performance (Exp.) are given separately. All leptonic decays of the V bosons are considered ($\ell = e, \mu, \tau$).

Region $(H \to b\bar{b})$	Expected significance	Observed significance
$W \to \ell\nu_{150-250}$	0.96σ	0.81σ
$W \to \ell\nu_{\geq 250}$	1.41σ	1.78σ
$Z(\ell\ell,\nu\nu)_{75-150}$	1.15σ	1.82σ
$Z(\ell\ell,\nu\nu)_{150-250}$	1.48σ	1.09σ
$Z(\ell\ell,\nu\nu)_{\geq 250}$	1.35σ	2.28σ

Table 9.5: Expected significance and observed significance for the five measured cross-sections.

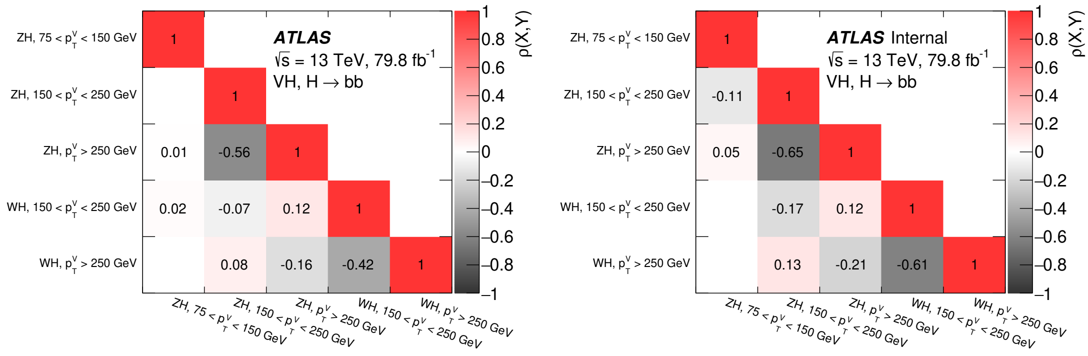

(a) **(b)**

Figure 9.6: Correlations in the measure of the ratio of the $\sigma \times$ BR over the SM for the $\mathrm{WH}_{[150-250]}$, $\mathrm{WH}_{[\geq 250]}$, $\mathrm{ZH}_{[75-150]}$, $\mathrm{ZH}_{[150-250]}$, and $\mathrm{ZH}_{[\geq 250]}$ processes in the fit to data (left). Correlations in the fit to data including only statistical uncertainties (right).

between the two regions is still present, confirming that this effect is mainly due to the correlation between the signals in these two regions.
On the other side, the correlation between the $ZH_{[0-75]}$ measurement and the other measurements is very low. This is expected as the events in this region are almost exclusively reconstructed in the 2-lepton channel.
The statistical uncertainty represents a relevant part of the cross-section uncertainty for all the five regions. The largest source of systematic uncertainty is the uncertainty on the modelling of background processes. This is due to the limited number of simulated background events and to the limited theoretical knowledge of the modelling of the background processes. The uncertainties on the theoretical modelling of the signal processes give a small contribution to the systematic uncertainty, with relative values ranging between 6% and 12%.
The origin of the uncertainty on the measured parameters is further assessed by decomposing the uncertainty into the various sources.

The ranking of the impact of the single 15 most important uncertainties, normalization scale factors, or other POIs, on each POI uncertainty is shown in Figure 9.7 for the WH regions and in Figure 9.8 for the ZH regions. The parameters are listed in decreasing order of their impact on the studied POI, as described in Section 7.1.4.

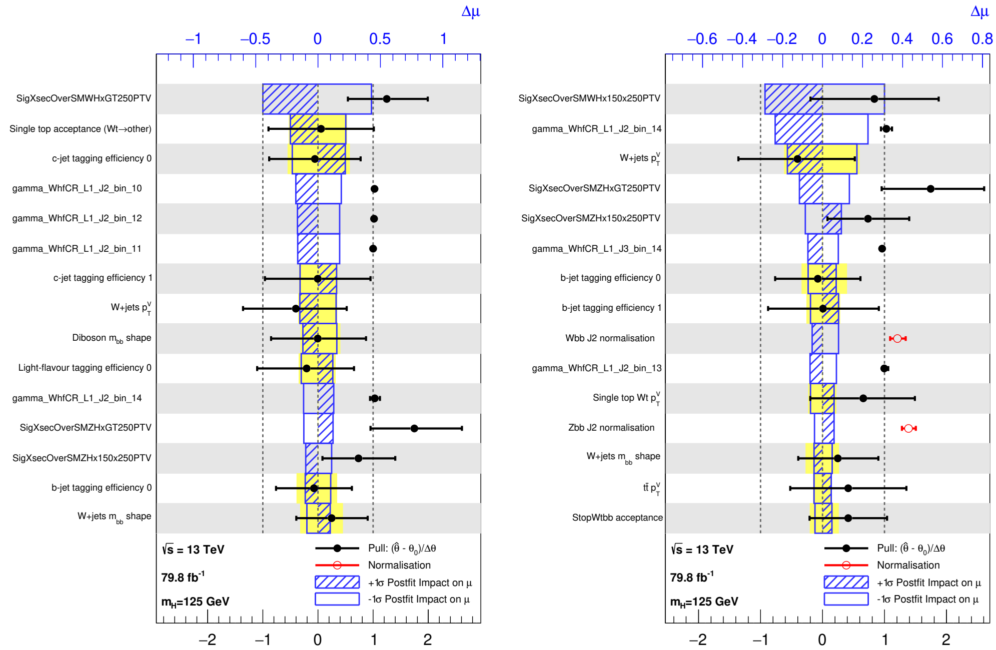

(a) WH, $150 - 250$

(b) WH, ≥ 250

Figure 9.7: Ranking of the most important systematic uncertainties according to their impact on the $\mathrm{WH}_{150-250}$, $\mathrm{WH}_{\geq 250}$ cross-sections times branching ratios. The boxes show the variations of $\hat{\mu}$, referring to the top x-axis, when fixing the corresponding individual nuisance parameter to its post-fit value modified upwards or downwards by its post-fit uncertainty, i.e. $\hat{\theta} \pm \sigma_{\hat{\theta}}$, and repeating the fit. The hatched and open areas correspond to the upwards and downwards variations, respectively. The yellow boxes show the pre-fit impact (top x-axis) by varying each nuisance parameter by $\pm 1\sigma$. The filled circles show the pulls of each nuisance parameter (bottom x-axis). The error bars show the post-fit uncertainties on $\hat{\theta}$ with respect to their nominal uncertainties. The open circles show the fitted values and uncertainties of the normalization parameters that are freely floating in the fit.

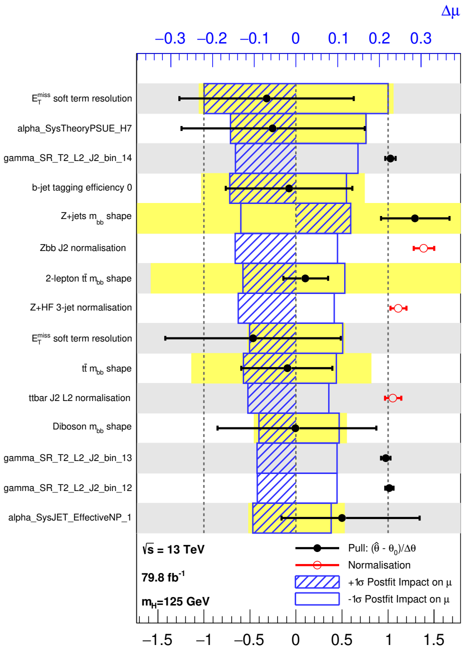

(a) ZH, 75 − 150

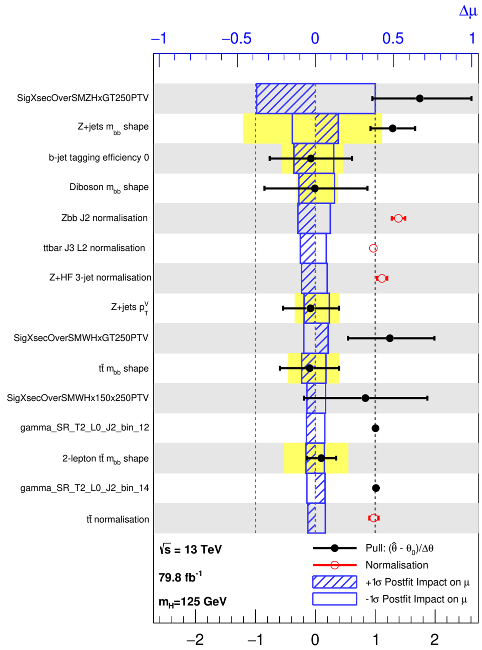

(b) ZH, 150 − 250

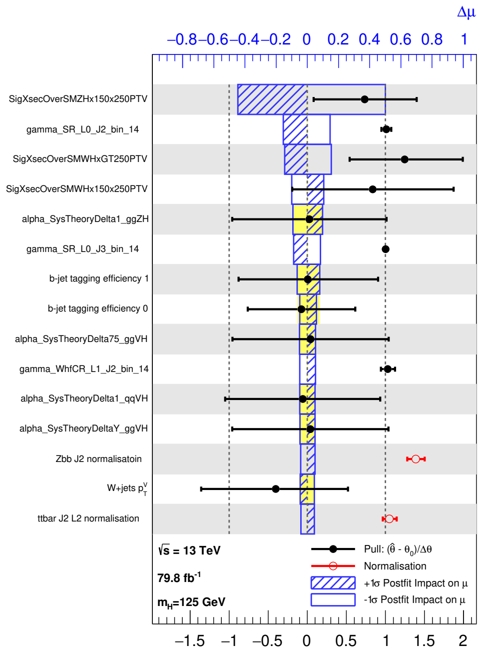

(c) ZH, ≥ 250

Figure 9.8: Ranking of the most important systematic uncertainties according to their impact on the ZH_{75-150}, $ZH_{150-250}$, $ZH_{\geq 250}$ cross-sections times branching ratios. The boxes show the variations of $\hat{\mu}$, referring to the top x-axis, when fixing the corresponding individual nuisance parameter to its post-fit value modified upwards or downwards by its post-fit uncertainty, i.e. $\hat{\theta} \pm \sigma_{\hat{\theta}}$, and repeating the fit. The hatched and open areas correspond to the upwards and downwards variations, respectively. The yellow boxes show the pre-fit impact (top x-axis) by varying each nuisance parameter by $\pm 1\sigma$. The filled circles show the pulls of each nuisance parameter (bottom x-axis). The error bars show the post-fit uncertainties on $\hat{\theta}$ with respect to their nominal uncertainties. The open circles show the fitted values and uncertainties of the normalization parameters that are freely floating in the fit.

Even though the analysis is designed to extract five cross-section values, the parameters extracted in the fit are cross section normalised to the SM. This is done just to simplify the implementation in the fit framework. Systematic uncertainties are correctly taken into account and theoretical uncertainties on the predicted cross-sections are not included. Given the high correlation between the two measured WH cross-sections, the highest NP of the WH ranking is the other WH cross-section. This is also true for $ZH_{\ 150-250}$ and $ZH_{\ \geq 250}$, as expected. Instead, no cross-section NP appears in the ranking for $ZH_{\ 0-75}$. The events in the 2-lepton channel are in fact categorised at reconstruction level with a cut at p_{T}^{V} = 75 GeV. Among the parameters with the largest impact there are the statistical uncertainties, the uncertainties related to the flavour tagging and the scale factors of the main background normalisations. The naming conventions of the parameters shown in Figure 9.7 and Figure 9.8 are depicted in Appedix C.
In order to assess the kind of systematic uncertainties that mostly affect the measurement precision, sources of systematic uncertainties are grouped by *type*. The impact of a group of systematic uncertainties is assessed by fixing all the NPs corresponding to this group to the nominal value and re-executing the fit. If the uncertainties on the measured POI obtained by this fit and by the nominal fit are indicated as $\sigma_{\hat{\mu}'}$ and $\sigma_{\hat{\mu}}$ respectively, the uncertainty impact is defined as:

$$\textit{uncertainty impact} = \sqrt{\sigma_{\hat{\mu}}^2 - \sigma_{\hat{\mu}'}^2}$$

The results obtained with this study are shown in Table 9.6. It should be noted that the sum in quadrature of all the uncertainties estimated as described above in general differs from the total uncertainty, since the correlation between nuisance parameters is not taken into account.
It should be highlighted that the *uncertainty impact* defined above quantifies how much each group of uncertainties affect the total uncertainty on the POI, and is not equivalent to the *impact* value used in the ranking of the systematics (shown e.g. in Figures 9.7 and 9.8), which instead quantify the impact of each NP on the central value of the POI.

9.2.2 *3-POI* signal measurements

In this section, the results of the fit for the *3-POI* scheme are shown. The main difference between these results and the results within the *5-POI* scheme is that, in this case, each STXS region corresponds to an analysis reconstructed region, as there is no split at p_{T}^{V} = 150 GeV. The three measured cross-sections are:

- $\sigma \times BR_{WH,150-} = 34.5^{+14.3}_{-14.0}$ fb;

Source of uncertainty	Impact on error				
	ZH_{75-150}	$ZH_{150-250}$	$ZH_{\geq 250}$	$WH_{150-250}$	$WH_{\geq 250}$
Total	±56%	±92%	±48%	±124%	±58%
Statistical	±43%	±77%	±44%	±86%	±50%
Data	±40%	±75%	±44%	±81%	±50%
Floating normalisations	±13%	±18%	±4%	±18%	±9%
Systematic	±36%	±51%	±18%	±89%	±30%
Signal modelling	±13%	±11%	±9%	±8%	±6%
Background modelling	±26%	±44%	±14%	±66%	±28%
Experimental uncertainties	±24%	±24%	±7%	±46%	±10%

Table 9.6: Breakdown of the relative uncertainty in the $\sigma \times B$ measurements in the different modelling, experimental, and statistical uncertainty sources in the 5-POI fit to 79.8 fb^{-1} of Run 2 data.

- $\sigma \times BR_{ZH,75-150} = 80.5^{+45.5}_{-44.0}$ fb;
- $\sigma \times BR_{ZH,150-} = 28.4^{+8.3}_{-7.8}$ fb.

To have an easy comparison with the expected SM cross-section values, these results have been normalised to the SM value and are reported in Figure 9.9a. Also in this case all the measured cross-section values are found compatible with the Standard Model within 1σ. The expected SM cross-sections are displayed in Figure 9.9b, together with the measured cross-sections. The statistical and systematic uncertainties on the measured cross-sections are shown in the same plot. Also in this case the statistical uncertainty gives a large contribution to the total systematic uncertainty of the three cross-sections. The main uncertainty source within the systematic uncertainties is the limited knowledge of the background modelling. The observed and measured significances for the three measurements are reported in Table 9.7. The observed significances range from ~ 1.8 to ~ 3.8.

process	p_T^V boundaries (GeV)	Expected significance	Observed significance
ZH	75-150	1.16	1.83
ZH	≥ 150	3.28	3.79
WH	≥ 150	2.24	2.50

Table 9.7: Expected significance and observed significance for the three measured cross-sections.

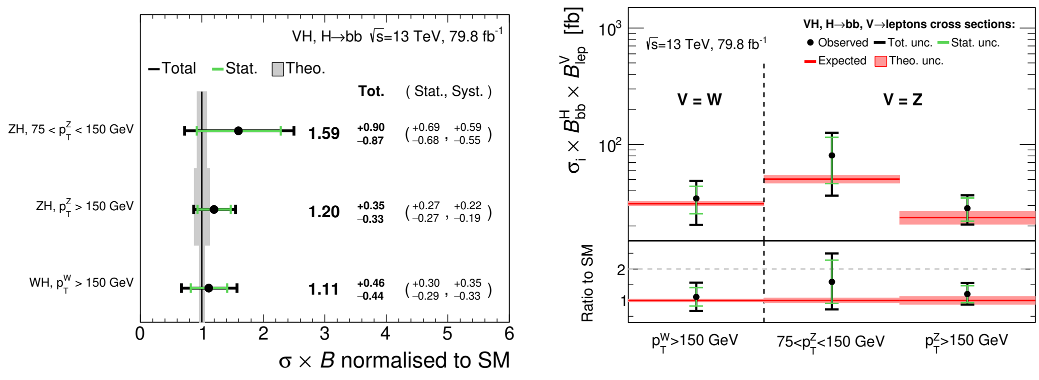

(a) (b)

Figure 9.9: Observed values of the $\sigma \times$ BR normalized to the SM for $\mathrm{WH}_{\geq 150}$, ZH_{75-150}, $\mathrm{ZH}_{\geq 150}$ in the unconditional fit to data.
(a) The (black) total observed uncertainty is quoted together with its decomposition in the (green) statistical component, and systematic component. In this plot the uncertainty due to background scale factors is included in the statistical component. The theoretical uncertainty on the SM prediction of the $\sigma \times BR_i$ is shown as the gray area around 1.
(b) The (black) total observed uncertainty is quoted together with the (green) statistical component. The observation is compared to the SM prediction, marked with the red lines, and its uncertainty, represented by the red area.

The correlations between the three measured cross-section are shown in Figure 9.10. No significant correlation between them is observed. This is expected, looking at the correlation plot for the 5-POI scheme. Regions that are highly correlated in the 5-POI scheme are in fact merged in the 3-POI scheme. As in this case the STXS bins follow the reconstructed level categorisation no large correlation are observed.

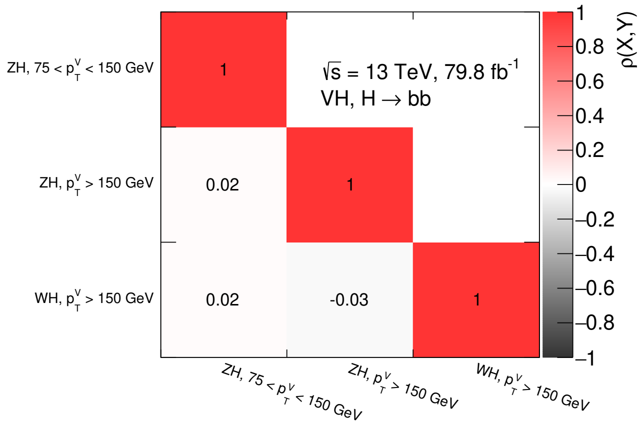

Figure 9.10: Correlations in the measure of the ratio of the $\sigma \times$ BR over the SM for the $\mathrm{WH}_{\geq 150}$, ZH_{75-150}, $\mathrm{ZH}_{\geq 150}$ processes in the unconditional fit to data.

9.3 BSM interpretations

BSM physics could lead to large deviations from the SM predictions in some phase space regions. As shown in Chapter 1 one possibility to extract information on BSM physics from the cross-section measurements is to use the EFT formalism. Measuring or constraining the values of the EFT parameters, makes it possible to infer information on a broad class of BSM theories. The STXS measurements are designed to extract information on the EFT parameters. To do so the STXSs are parametrized as a function of the EFT parameters, including only the most sensitive parameters involved in the VH processes. This parametrization, shown in Chapter 1, has been used to extract limits in the EFT parameters. The parameters that can be studied are $\bar{\mathtt{c}}_{\mathtt{HW}}$, $\bar{\mathtt{c}}_{\mathtt{HB}}$, $\bar{\mathtt{c}}_{\mathtt{W}} - \bar{\mathtt{c}}_{\mathtt{B}}$ and $\bar{\mathtt{c}}_{\mathtt{d}}$. $\bar{\mathtt{c}}_{\mathtt{HW}}$ and $\bar{\mathtt{c}}_{\mathtt{W}}$ modify both the HWW and HZZ vertices, and $\bar{\mathtt{c}}_{\mathtt{HB}}$ and $\bar{\mathtt{c}}_{\mathtt{B}}$ affect only the HZZ and $H \to \gamma\gamma$ vertices. The $\bar{\mathtt{c}}_{\mathtt{d}}$ parameter modifies the coupling between the Higgs boson and down-type, in this case in the $H \to b\bar{b}$ decay.

The regions used in the fit are the five regions identified for the *5-POI* scheme in Section 9.2.1. The *5-POI* scheme is preferred to the *3-POI* scheme since, even if it leads to measurements affected by higher uncertainty, it has a higher sensitivity to potential anomalous couplings thanks to the finer binning in the high p_{T}^{V} region. A complete procedure for fitting measurements of STXS to the EFT operators has been developed and documented in Reference [25].

No EFT effects are considered in the low energy regions (p_{T}^{V} <150 GeV for the WH production and p_{T}^{V} <75 GeV for the ZH production) as they are not measured in the fit.

9.3.1 EFT parameters measurement

The constraints on the four EFT parameters $\bar{c}_{HW}$, $\bar{c}_{HB}$, $\bar{c}_W - \bar{c}_B$ and $\bar{c}_d$ are extracted using one-dimensional POI parametrizations, where a single parameter is varied while all the others are kept constant to the SM values (zero). The five measured cross-sections of the *5-POI* scheme are therefore parametrized as a function of a single parameter per time. 68% and 95% confidence level (CL) one-dimensional intervals are inferred for the four varied parameters by performing a likelihood fits to the data yields. As already pointed out in Section 1.5 the parameters $\bar{c}_W$ and $\bar{c}_B$ are not measured individually but as a difference, because the sum of the two is strongly constrained by previous measurements [28].
A more complete fit model, with the simultaneous fit of several parameters, can only be implemented combining this analysis with other analyses sensitive to some of these parameters but aiming at selecting other Higgs decay modes.
The observed profiled negative log-likelihood functions for the one-dimensional POI fits are shown in Figure 9.11 for the four considered parameters. The red solid lines are the likelihood functions if both the interference between SM and non-SM amplitudes and the SM-independent effects are considered while the green dashed lines only shows the likelihood if the interference between SM and non-SM amplitudes are considered. The functions including the SM-independent effects show a typical shape with two minima due to the parabolic parametrization used (depicted in Tables 1.2,1.3,1.4).
The expected and observed intervals for the fitted EFT coefficients are reported in Table 9.8 with 68% and 95% of confidence level (CL).
The parameters $\bar{c}_{HW}$ and $\bar{c}_W - \bar{c}_B$ are constrained at 95% CL to be no more than a few percent, while the constraint on $\bar{c}_{HB}$ is about five times worse, and the constraint on $\bar{c}_d$ is of order unity.
The expected effect of the EFT parameters on the SM cross-sections for the STXS bins is shown in Figure 9.12. The variations, expressed in terms of

$$\frac{\sigma_i \times \mathrm{BR}_{bb}}{\sigma_i^{\mathrm{SM}} \times \mathrm{BR}_{bb}^{SM}}$$

are obtained by assuming for each parameter the value of the upper limit of the corresponding interval measured with 95% of CL. From the parametrization introduced in Chapter 1 variations of the $\bar{c}_{HW}$ and $\bar{c}_{WW}$ parameters should modify the HWW and HZZ vertices, and therefore have an effect mainly on the value of both the WH and ZH measured cross sections. Instead, the $\bar{c}_{HB}$ and $\bar{c}_B$ parameters only modify the HZZ vertex and are only expected to have an effect on the ZH cross sections. The $\bar{c}_d$ parameter is linked to the $H \to b\bar{b}$ decay and therefore has a uniform effect on all the measured cross sections. The variations shown in Figure 9.12 for the four measured parameters are coherent with the expected

Coefficient	Expected Interval	Observed Interval
Results at 68% Confidence Level		
$\bar{c}_{HW}$	[-0.003, 0.002]	[-0.001, 0.004]
(interference only	[-0.002, 0.003]	[-0.001, 0.005])
$\bar{c}_{HB}$	[-0.066, 0.013]	[-0.078, -0.055] $\bigcup$ [0.005, 0.019]
(interference only	[-0.016, 0.016]	[-0.005, 0.030])
$\bar{c}_{W} - \bar{c}_{B}$	[-0.006, 0.005]	[-0.002, 0.007]
(interference only	[-0.005, 0.005]	[-0.002, 0.008])
$\bar{c}_{d}$	[-1.5, 0.3]	[-1.6, -0.9] $\bigcup$ [-0.3, 0.4]
(interference only	[-0.4, 0.4]	[-0.2, 0.65])
Results at 95% Confidence Level		
$\bar{c}_{HW}$	[-0.018, 0.004]	[-0.019, -0.010] $\bigcup$ [-0.005, 0.006]
(interference only	[-0.005, 0.005]	[-0.003, 0.008])
$\bar{c}_{HB}$	[-0.078, 0.024]	[-0.090, -0.032]
(interference only	[-0.033, 0.033]	[-0.022, 0.049])
$\bar{c}_{W} - \bar{c}_{B}$	[-0.034, 0.008]	[-0.036, 0.024] $\bigcup$ [-0.009, 0.010]
(interference only	[-0.009, 0.010]	[-0.006, 0.014])
$\bar{c}_{d}$	[-1.7, 0.5]	[-1.9, 0.7]
(interference only	[-0.8, 0.8]	[-0.6, 1.1])

Table 9.8: The expected and observed 68% CL (four top rows) and 95% CL (four bottom rows) intervals for the effective Lagrangian coefficients $\bar{c}_{HW}$, $\bar{c}_{HB}$, $\bar{c}_{W} - \bar{c}_{B}$ and $\bar{c}_{d}$ when the other coefficients are assumed to vanish. Each row is composed of two sub-rows: the first one uses the interference between SM and non-SM amplitudes and the SM-independent contributions, while the second sub-row uses only the interference between SM and non-SM amplitudes.

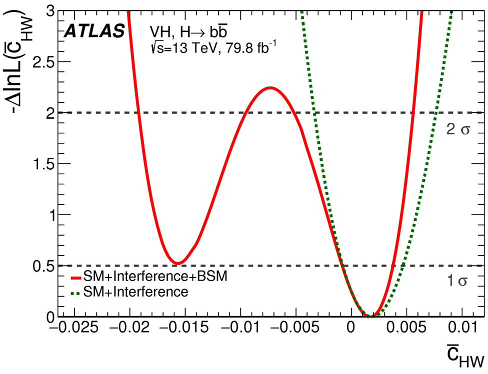

(a) Profile likelihood fit for $\bar{c}_{HW}$.

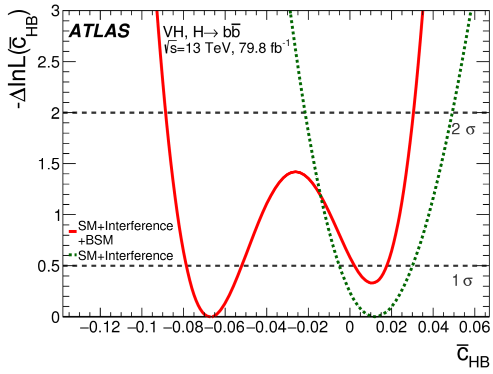

(b) Profile likelihood fit for $\bar{c}_{HB}$.

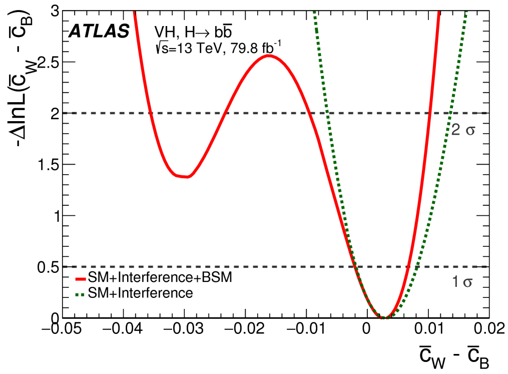

(c) Profile likelihood fit for $\bar{c}_{W} - \bar{c}_{B}$.

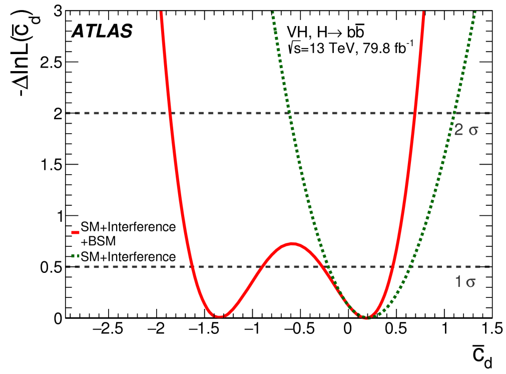

(d) Profile likelihood fit for $\bar{c}_{d}$.

Figure 9.11: The observed profiled negative log-likelihood functions for the one-dimensional fits to constrain the coefficients (a) $\bar{c}_{HW}$, (b) $\bar{c}_{HB}$, (c) $\bar{c}_{W} - \bar{c}_{B}$ and (d) $\bar{c}_{d}$, when the other coefficients are set to 0, if both the interference between SM and non-SM amplitudes and the SM-independent effects are considered (solid line) or only the interference between SM and non-SM amplitudes is considered (dashed line) [127].

behavior, the parameters $\bar{c}_{W}$ and $\bar{c}_{B}$ are only measured as a difference that potentially modifies both the WH and ZH cross section values.

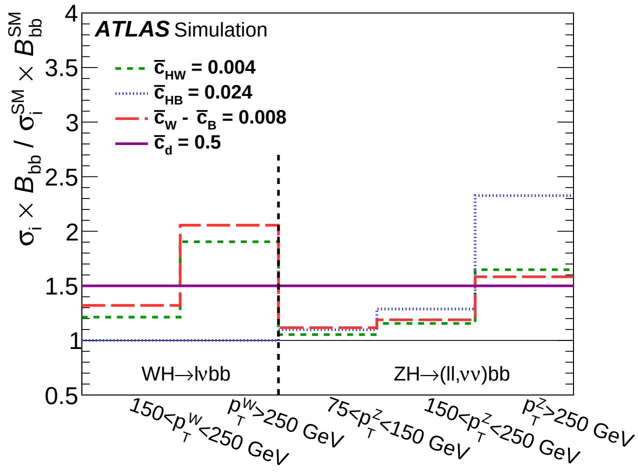

Figure 9.12: Effect of the EFT parameters on the SM cross-sections in the *5-POI* scheme, for the values of the coefficients $\bar{c}_{HW}$, $\bar{c}_{HB}$, $\bar{c}_{W} - \bar{c}_{B}$ and $\bar{c}_{d}$ that are expected to be excluded at 95% confidence level [127].

9.3.2 Future prospects

The $VH(H \to b\bar{b})$ search can be developed on three fronts:

- repeating an analysis with a selection and an analysis strategy close to the *resolved* selection described in this thesis, but using the full Run 2 data sample;
- combining the STXS results of the $VH(H \to b\bar{b})$ analysis with the results of analysis studying other Higgs decay modes. This would allow implementing a more complete fit model including several EFT parameters at the same time;
- implementing a *merged* analysis optimised to select high energy events. As seen in Figure 9.12 EFT parameter values different from 0, except for $\bar{c}_{d}$, produce deviations of the cross-section that increase as the vector boson transverse momentum increases and the *merged* analysis could contribute to measuring these parameters, or set tighter limits. The results for the *merged* analysis are presented in the next chapter.

Chapter 10

Results of the $VH(H \to b\bar{b})$ *merged* analysis

The strategy for the $VH(H \to b\bar{b})$ cross-section measurement performed with a data-sample of 139.0 fb^{-1} with the merged analysis is presented in this chapter. The analysis is close to final, therefore the data region most sensitive to signal is still "blinded" to avoid biases in the analysis design. Hence, the performance of the analysis is assessed using the expected sensitivity. The distributions used as input to the fit are shown in the first section. All the details about the sensitivity and sanity check of the fit are discussed in the second section, together with the expected results for the cross-section measurement. In the last section, the expected result for the measurement of the STXSs in the merged analysis is shown.

10.1 Fit inputs

The main reason to develop the *merged* analysis lies in the possibility to improve the sensitivity to BSM physics effects. Additionally, the availability of an increased data sample, including the p-p collision data collected in 2018, and of the techniques developed to select high energy events, allowed attempting a measurement of the $VH(H \to b\bar{b})$ cross-section with the *merged* analysis.
The general procedure followed to measure the $VH(H \to b\bar{b})$ cross-section has been already described in Chapter 7, and is very similar to the procedure adopted for the *resolved* analysis, described in Chapter 9. The main difference between the *resolved* and *merged* fit strategy is that for the *merged* analysis the final discriminating

variable is the large-R jet mass, m_{J}, while in the *resolved* it is the output of the BDT. The SRs and CRs used for the *merged* analysis are summarised in Figure 10.1. A total of ten signal regions and four control regions are used. For all the regions

		0L		1L		2L
		# add. small-R jets		# add small-R jets		
		0	>=1	0	>=1	
250-400 GeV	no add b-tagged jets	SR	SR	SR	SR	SR
	add b-tagged jets	CR		CR		
>400 GeV	no add b-tagged jets	SR	SR	SR	SR	SR
	add b-tagged jets	CR		CR		

Figure 10.1: Schematic summary of the signal regions and control regions for the *merged* analysis.

the variable used as discriminant is the large-R jet mass.
As already mentioned in the introduction, the *merged* analysis presented in this thesis has been obtained by a group of people working within the ATLAS collaboration, with a relevant contribution from my side. Although the status of the *merged* analysis is almost complete, some studies are still ongoing (e.g. the computation of more detailed modelling uncertainties), and, moreover, the results need to be carefully scrutinized by the collaboration before proceeding with the unblinding. As for the *merged* analysis, this phase is not yet completed, only the expected results will be shown. A publication with the measured cross-section is already in preparation and will likely follow in the next months. For this reason, in the plots of the signal regions shown in this chapter, the data point in the bins with $m_{\mathrm{J}} = [80, 140]$ GeV are not shown.

In this section, the shape and normalisation comparisons between data and the simulated samples are presented. The m_{J} distributions input to the fit (pre-fit plots) are shown for all the signal and control regions.
The 0-lepton channel distributions are shown in Figure 10.2. The main background for this channel is the Z+jets process, shown in blue. Differently from the *resolved* analysis, in the *merged* analysis no CR has been designed to control the Z+jets process, which is constrained by the sidebands of the 0-lepton and 2-lepton signal regions. Sizable contributions from the W+jets and $t\bar{t}$ processes, shown in green and yellow, are present as well. The $t\bar{t}$ process is constrained by dedicated control regions (Figure 10.4) while the W+jets process normalisation is mainly constrained in the 1-lepton signal regions. The contribution of the multijet backgrounds has been studied in this channel and has been verified to be negligible, it has therefore

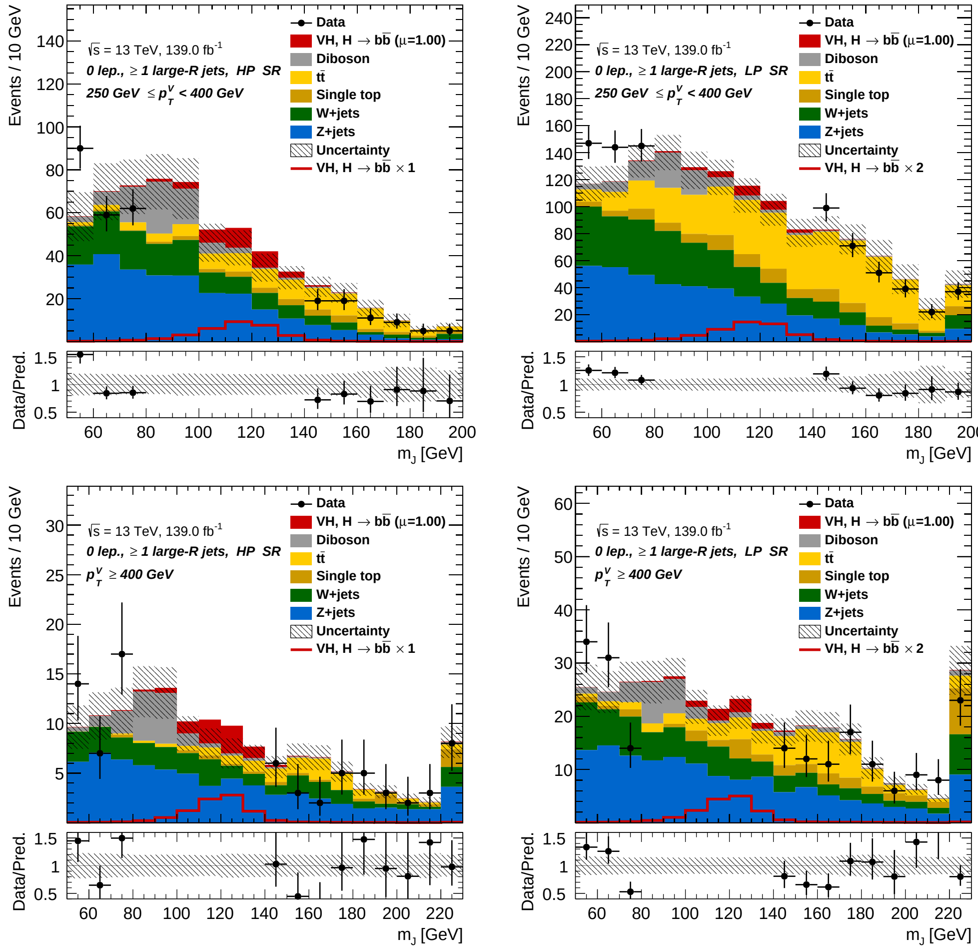

Figure 10.2: 0L pre-fit plots for the SR in the kinematic region 250 GeV $< p_{\mathrm{T}}^{V} <$ 400 GeV (top plots) and $p_{\mathrm{T}}^{V} >$ 400 GeV (bottom plots). The plots on the left are for the high purity signal region (HP SR) and the plots on the right for the low purity signal region (LP SR). The data are shown as back dots, except for the region m_{J} = [80,140] GeV, where they are not shown. The signal and background contributions before the global likelihood fit are shown as filled histograms. The Higgs boson signal is also shown unstacked as an unfilled histogram, scaled by the factor indicated in the legend. The size of the combined statistical and systematic uncertainty for the sum of the signal and background is indicated by the hatched band. The ratio of the data to the sum of the signal ($\mu = 1$) and background is shown in the lower panel.

not been included.
Given the large blinding window, it is not possible to have a precise comparison between data and simulation for the $m_{\rm J}$ distribution. For the non-blinded bins of the distributions fair agreement is observed. The larger differences are observed in the region 250 GeV $< p_{\rm T}^{V} <$ 400 GeV for events in the low purity signal region (Figure 10.2, bottom right).

The pre-fit plots for the 1-lepton channel are shown in Figure 10.3. The main background processes in this channel are W+jets (green) and $t\bar{t}$ (yellow). For both processes, the normalisation is left unconstrained in the fit to data. The $t\bar{t}$ background has a dedicated control region in the 1-lepton channel (Figure 10.4), while the W+jets is controlled through the sidebands in the signal regions. The agreement between data and the simulation is fairly good in the non-blinded bins. There is an overestimation of the predicted background in the low purity signal regions (Figure 10.3, plots on the right).
The contribution of the multijet background in this channel is under investigation. The expected impact is small and its contribution is not included in the results presented in this thesis.

The $t\bar{t}$ control regions for the 0-lepton and 1-lepton channels are shown in Figure 10.4. The events in the CRs are not categorised according to the number of additional jets, but only according to $p_{\rm T}^{V}$. In fact, as the CRs only include events that have at least an additional b-tagged track jets outside of the large-R jets, a categorisation on the jet multiplicity in these regions would leave the category with 0 additional jets with a very low number of selected events. The CRs for the 0-lepton are shown on the top row. The number of events in this channel is low and therefore a coarser binning is used. However, the region is quite pure in $t\bar{t}$ and this process seems to be well modelled. The $m_{\rm J}$ distribution for the CRs in the 1-lepton channel (Figure 10.4 bottom row) show a peak close to the expected top mass.

Finally, the signal regions for the 2-lepton channel are shown in Figure 10.5. The number of events in this channel is much lower with respect to the events in the 0-lepton and 1-lepton channels, especially in the high energy kinematic region. For this reason events are categorised only in $p_{\rm T}^{V}$ and no further categorisation is applied nor request on the number of b-tagged track jets. The main background is the Z+jets process that is controlled through the sidebands of the 2-lepton signal regions.

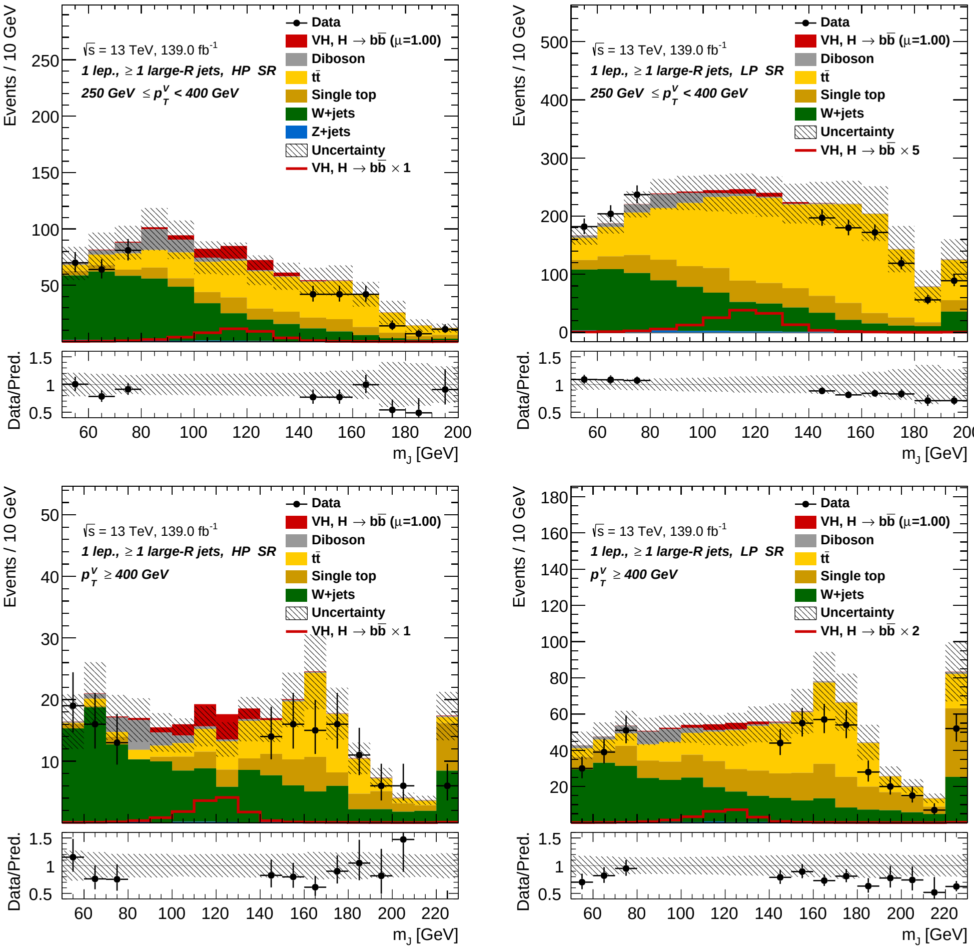

Figure 10.3: 1L pre-fit plots for the SR in the kinematic region 250 GeV $< p_{\mathrm{T}}^{V} <$ 400 GeV (top plots) and $p_{\mathrm{T}}^{V} >$ 400 GeV (bottom plots). The plots on the left are for the high purity signal region (HP SR) and the plots on the right for the low purity signal region (LP SR). The data are shown as back dots, except for the region m_{J} = [80,140] GeV, where they are not shown. The signal and background contributions before the global likelihood fit are shown as filled histograms. The Higgs boson signal is also shown unstacked as an unfilled histogram, scaled by the factor indicated in the legend. The size of the combined statistical and systematic uncertainty for the sum of the signal and background is indicated by the hatched band. The ratio of the data to the sum of the signal ($\mu = 1$) and background is shown in the lower panel.

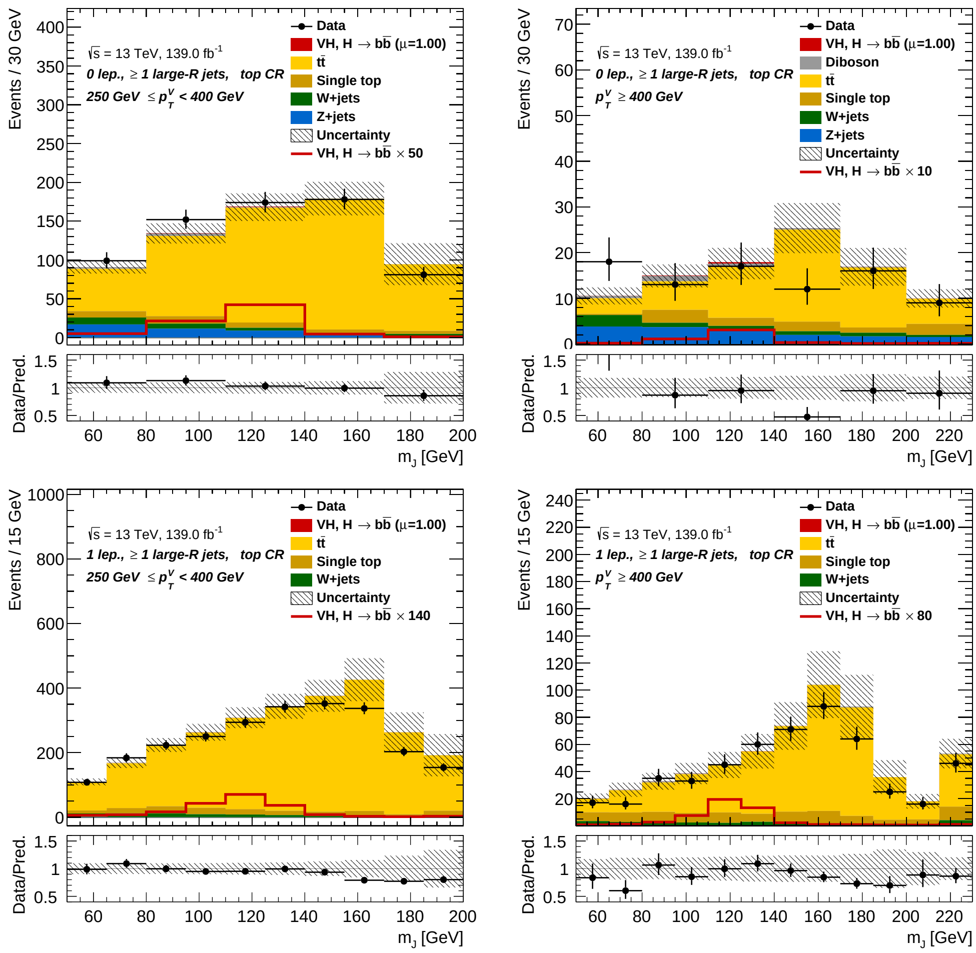

Figure 10.4: Pre-fit plots for the CR in the 0-lepton (top plots) and 1-lepton channels (bottom plots). The plots on the left are for the kinematic region 250 GeV $< p_T^V <$ 400 GeV and the plots on the right for the region $p_T^V >$ 400 GeV. The data are shown as back dots. The signal and background contributions before the global likelihood fit are shown as filled histograms. The Higgs boson signal is also shown unstacked as an unfilled histogram, scaled by the factor indicated in the legend. The size of the combined statistical and systematic uncertainty for the sum of the signal and background is indicated by the hatched band. The ratio of the data to the sum of the signal ($\mu = 1$) and background is shown in the lower panel.

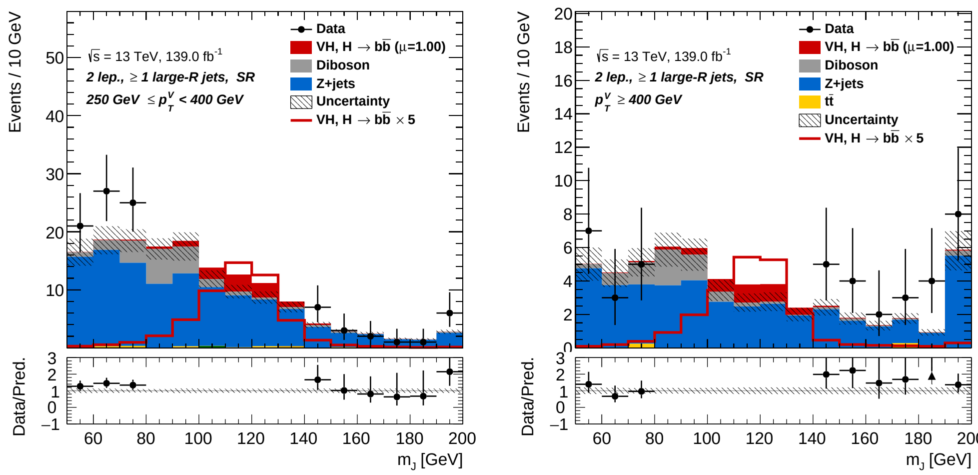

Figure 10.5: 2L pre-fit plots for the SR in the kinematic region 250 GeV $< p_{\mathrm{T}}^{V} <$ 400 GeV (top plots) and $p_{\mathrm{T}}^{V} >$ 400 GeV (bottom plots). The plots on the left are for the kinematic region 250 GeV $< p_{\mathrm{T}}^{V} <$ 400 GeV and the plots on the right for the region $p_{\mathrm{T}}^{V} >$ 400 GeV. The data are shown as back dots, except for the region m_{J} = [80,140] GeV, where they are not shown. The signal and background contributions before the global likelihood fit are shown as filled histograms. The Higgs boson signal is also shown unstacked as an unfilled histogram, scaled by the factor indicated in the legend. The size of the combined statistical and systematic uncertainty for the sum of the signal and background is indicated by the hatched band. The ratio of the data to the sum of the signal ($\mu = 1$) and background is shown in the lower panel.

10.2 Cross-section measurement

10.2.1 Fit procedure validation

One of the key steps to validate the fit procedure is the scrutiny of the nuisance parameter pulls (defined in Chapter 7), as they can help to point out potential bugs and features that need further investigation. A large number of systematic uncertainties are included in the fit, and the pulls of the systematic uncertainties are grouped by type in plots designed to scrutinise the main features. In this section, only the pull plots for the NPs describing the large-R jet uncertainties, which are among the main sources of systematic uncertainties, are shown as an example. Other plots showing the nuisance parameters pulls for the *merged* analysis are shown in Appendix F.
The pull plot for the large-R jet uncertainties is shown in Figure 10.6. Two pull values are shown in the plot for each large-R jet uncertainty: the Asimov fit result, shown in black, and the conditional fit to data with $\mu = 1$, shown in red. As in the first case, an Asimov dataset is used, the pull is exactly 0 by definition.

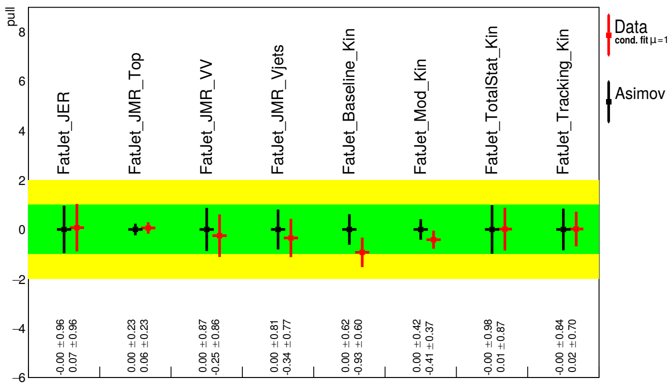

Figure 10.6: Nuisance parameter pulls for the large-R jet uncertainties corresponding to a conditional fit ($\mu = 1$) performed to Run 2 data (red) and a conditional fit to Asimov data (black), fitting simultaneously the three leptonic channels.

The uncertainties on the large-R jet are divided into two main components: the resolution uncertainties and the mass scale uncertainty. The resolution uncertainties are further divided in jet energy resolution uncertainties, indicated in the plot with the label FatJet_JER, and the jet mass resolution uncertainties, indicated in the plot with the label FatJet_JMR. These uncertainties are expected to have a significant impact on the fit result, as the large-R jet mass distribution is used as a final discriminant. The JMR uncertainty is decorrelated between the top samples, the V+jets samples and the VV samples (including signal + diboson processes).

The JMR_top NP is constrained by the fit. This is likely due to the shape of the $t\bar{t}$ distribution in the 1-lepton channel, peaking at the top mass value both in the high energy signal region and in the control regions. The four components of the large-R jet mass scale uncertainties (*Baseline*, *Modelling*, *Total statistic* and *Tracking*), depicted in Section 5.3.5, are shown as well. Both the *Baseline* and the *Modelling* components are shifted and a bit constrained in the conditional fit to data. In both cases, the shift is less than 1σ from the central value. The overall indication from these results is that the fit is correctly behaving since the parameters are either mildly/not constrained or constrained when the selected data provide information to do so.

Another useful way to study the behaviour of the NPs in the fit is to look at the correlation coefficients. The correlation coefficients among the NPs are shown in the correlation matrix in Figure 10.7. The matrix, which has been obtained from the conditional fit to data with $\mu = 1$, is symmetric by construction. Only

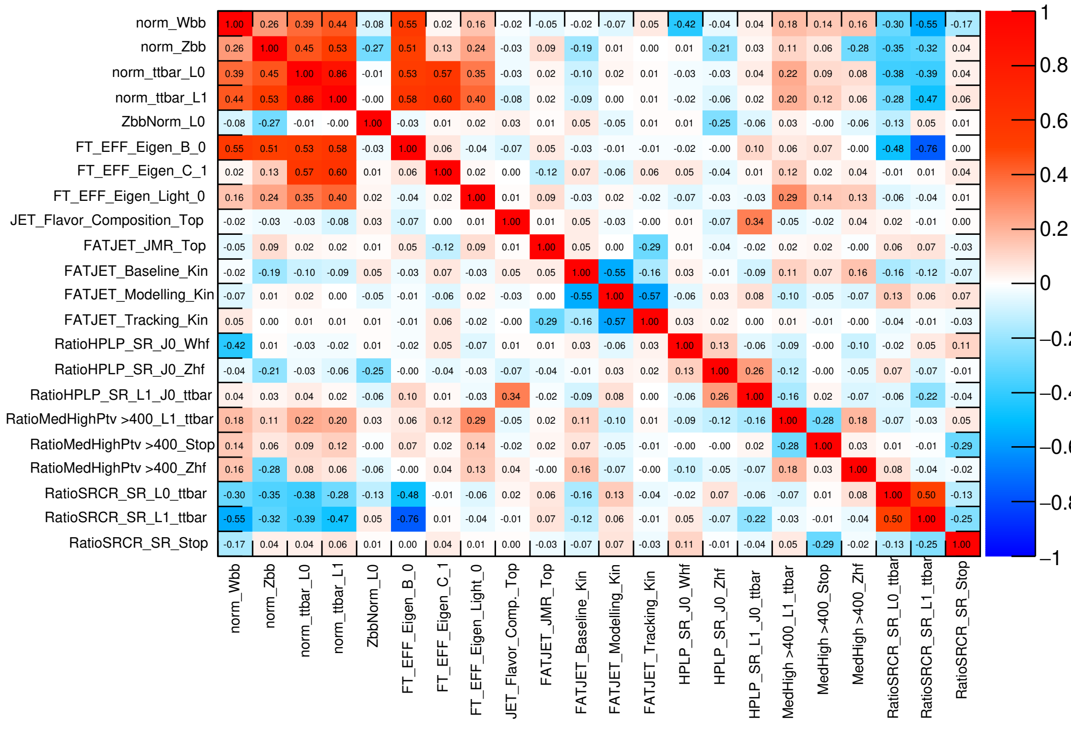

Figure 10.7: Correlation matrices from the conditional fit to data with $\mu = 1$. Only nuisance parameters that have at least one correlation of magnitude 0.25 or higher with another nuisance parameter than themselves are shown.

nuisance parameters with at least one correlation coefficient equal to 0.25 or larger are shown. No regions of large correlations are observed apart from the ones

specified in more detail in the following. A high level of correlation is observed among the parameters describing the main background processes normalisation (W+HF, Z+HF and $t\bar{t}$ both in the 0-lepton and 1-lepton channel, shown in the top-left region of the correlation matrix). This may sound as counter-intuitive but it is explained by the fact that all these parameters have high correlation or anti-correlation values with other NPs.
The nuisance parameters parametrising the differences of the $t\bar{t}$ modelling between the signal regions and the control regions are correlated among them and anti-correlated with the floating normalisations, and with one of the b-tagging nuisance parameters (top-right and bottom-left regions of the correlation matrix). This large anti-correlation introduces a correlation between the main background normalisations.
All the main background normalisation parameters, and in particular the $t\bar{t}$ normalisations, are also highly correlated with some of the flavour tagging uncertainties (top-left region of the matrix). The flavour tagging NPs are expected to have a similar effect on all the main background processes because by design a variation of these parameters changes the number of events for all processes (as the candidate Higgs is selected through two b-tagged track jets).
The main large-R jet uncertainties are anti-correlated (central region of the matrix).

10.2.2 Expected performance

As the analysis is blinded, only expected results are computed, meaning that instead of using the collected data a fit to the Asimov dataset is performed (or in some cases a conditional fit to data with $\mu = 1$).
The measured signal strength uncertainty for the fit to Asimov data of all the three leptonic channels is ± 0.35. This uncertainty can be split to assess the impact of the statistical and systematic uncertainties:

$$\mu = 1.00 \pm 0.24 \text{ (data stat.) } {}^{+0.28}_{-0.24} \text{ (syst.)}$$

The contributions from the statistical uncertainty on data and the systematic uncertainties are approximately the same.
The expected significance, measured with the Asimov fit in the three leptonic channel, is 3.1σ. This analysis could therefore provide evidence of the $VH(H \to b\bar{b})$ process measured with the large-R jets techniques. The quoted expected significance is not the final estimate since, as discussed in the introduction, the analysis is still being finalized and studies are on-going on the uncertainties that should be attributed to the background modelling. A more solid estimate of the expected significance is therefore expected in the next month. However, these last checks

are not expected to have a large impact on the final significance value.
In order to assess the contribution to the significance of each lepton channel, the fit to Asimov data has been performed also in single lepton channels separately. The expected significance for each lepton channel is reported in Table 10.1. The 0-lepton

Channel	Expected significance
0-lepton	2.04σ
1-lepton	1.94σ
2-lepton	1.26σ

Table 10.1: Expected significance for each lepton channel from the fit to Asimov data.

and 1-lepton channel give the largest contribution to the expected significance. This behaviour is different with respect to what was observed in Table 9.3 for the *resolved* analysis. At higher energies, targeted by the *merged* analysis, the 2-lepton channel is the one with the lowest number of signal events and giving the lowest contribution to the overall significance. In fact, the fraction of events with $Z \to e^+e^-, \mu^+\mu^-$ decays is lower with respect to $Z \to \nu\nu$, and a lower number of selected signal events is expected. This difference is less significant at lower energies, where the presence of two charged leptons in the 2-lepton channel allows to easily identify the signal events and use triggers with lower energy thresholds, while it is not possible in the 0-lepton channel, for which a cut at E_{T}^{miss} >150 GeV is applied. A more comprehensive comparison between the expected results for the *resolved* and *merged* analysis is presented in Appendix E.

The m_{J} SR post-fit distributions are shown in Figure 10.8, 10.9 and 10.10 for the 0-lepton, 1-lepton and 2-lepton channels, respectively. In these plots, data are compared to post-fit predictions obtained using the normalisations ad NP values extracted from the conditional fit to data with $\mu = 1$. The systematic uncertainty bands are also obtained with the uncertainties extracted from the fit. In all plots, the dashed line indicates the sum of all the pre-fit predictions.
The data/MC agreement outside of the blinding windows is good in all the lepton channels. The fluctuations in the shape of the background distributions, especially in the high energy regions, show that an increased number of events could be beneficial for the measurement. This is observed, for example, in the Z+jets distributions in the high-energy region of the 0-lepton channel (Figure 10.8, bottom row).
From the post-fit distributions it is possible to extract the m_{J} distribution for the signal, shown in Figure 10.11. This is done by subtracting from the sum of the data distributions on all channels and regions the post-fit sum of all the background distributions. The vector diboson processes, WZ and ZZ, is not included as a

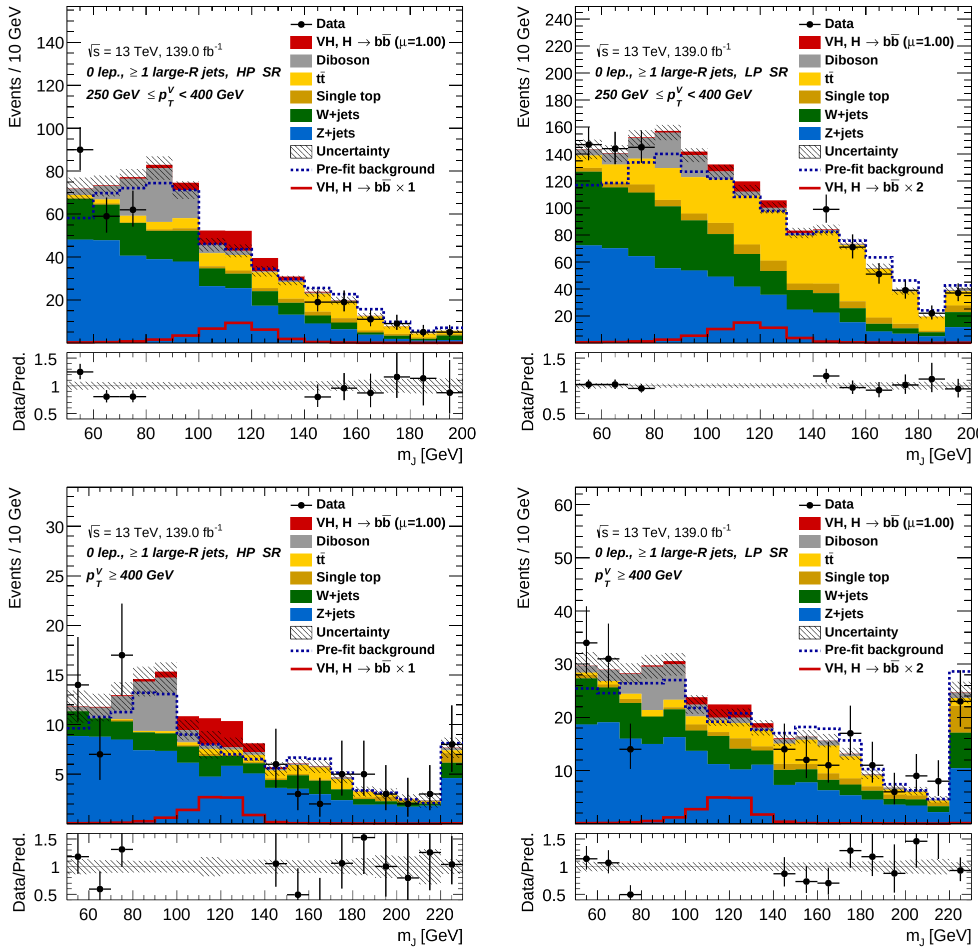

Figure 10.8: 0L post-fit plots for the SR in the kinematic region 250 GeV $< p_{\mathrm{T}}^{V} <$ 400 GeV (top plots) and $p_{\mathrm{T}}^{V} >$ 400 GeV (bottom plots). The plots on the left are for the high purity signal region (HP SR) and the plots on the right for the low purity signal region (LP SR). The data are shown as black dots. The background contributions are shown as filled histograms. The signal is shown as a filled histogram on top of the fitted backgrounds and unstacked as an unfilled histogram, scaled by a factor indicated in the legend. The dashed histogram shows the total pre-fit background. The hatched band includes the combined statistical and systematic uncertainty for the sum of the fitted signal and background. The ratio of the data to the sum of the fitted signal and background is shown in the lower panel.

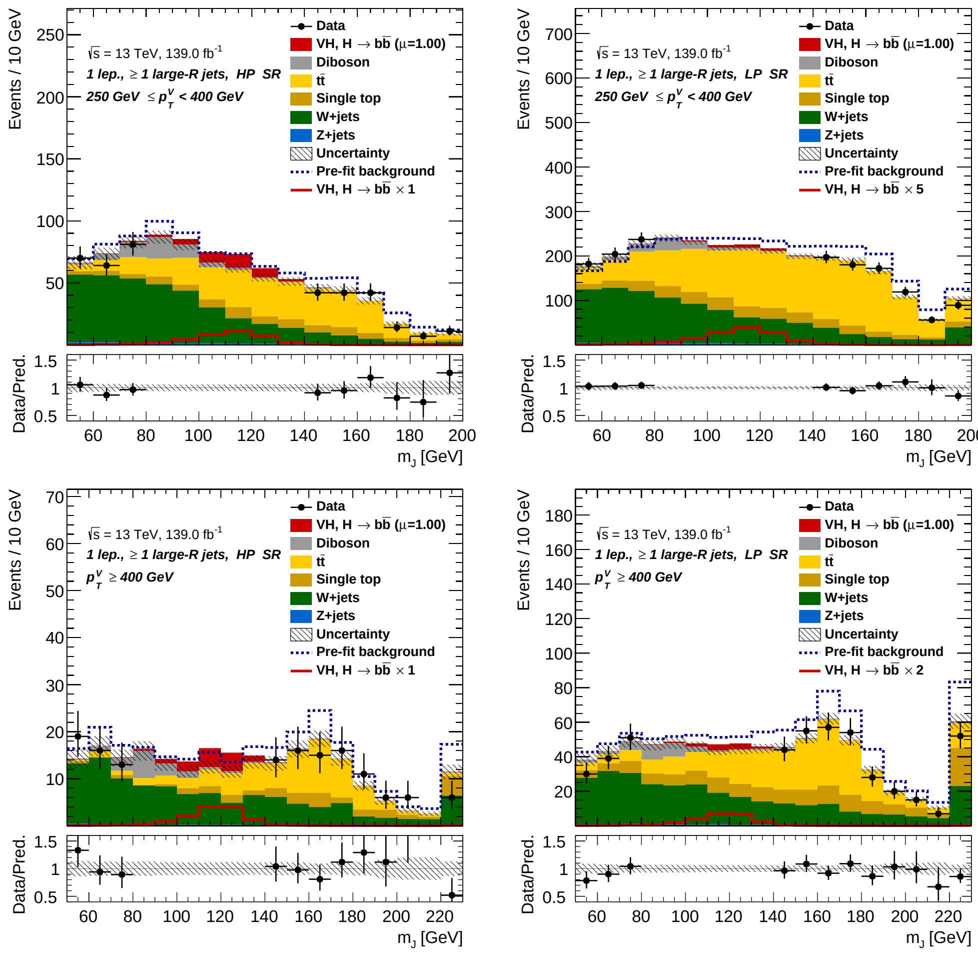

Figure 10.9: 1L post-fit plots for the SR in the kinematic region 250 GeV $< p_T^V <$ 400 GeV (top plots) and $p_T^V >$ 400 GeV (bottom plots). The plots on the left are for the high purity signal region (HP SR) and the plots on the right for the low purity signal region (LP SR). The data are shown as black dots. The background contributions are shown as filled histograms. The signal is shown as a filled histogram on top of the fitted backgrounds and unstacked as an unfilled histogram, scaled by a factor indicated in the legend. The dashed histogram shows the total pre-fit background. The hatched band includes the combined statistical and systematic uncertainty for the sum of the fitted signal and background. The ratio of the data to the sum of the fitted signal and background is shown in the lower panel.

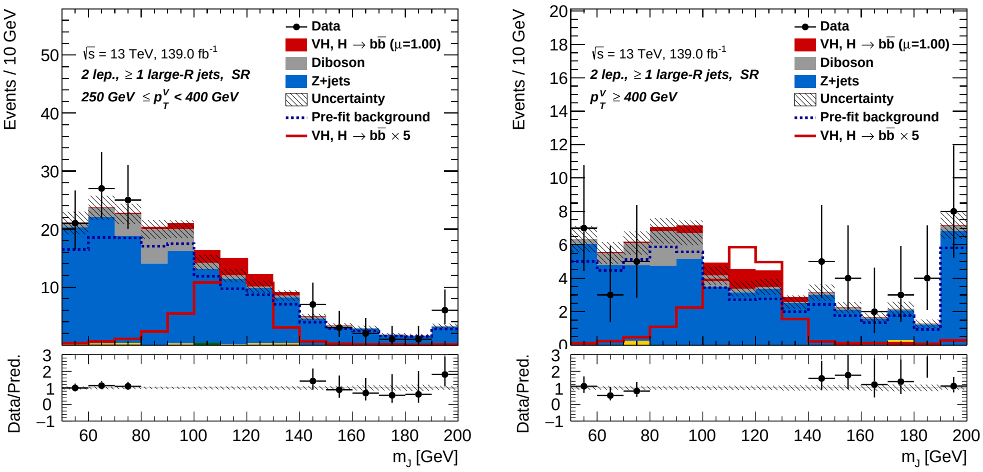

Figure 10.10: 2L post-fit plots for the SR in the kinematic region 250 GeV $< p_{\mathrm{T}}^{V} <$ 400 GeV (top plots) and $p_{\mathrm{T}}^{V} >$ 400 GeV (bottom plots). The plots on the left are for the kinematic region 250 GeV $< p_{\mathrm{T}}^{V} <$ 400 GeV and the plots on the right for the region $p_{\mathrm{T}}^{V} >$ 400 GeV. The data are shown as black dots. The background contributions are shown as filled histograms. The signal is shown as a filled histogram on top of the fitted backgrounds and unstacked as an unfilled histogram, scaled by a factor indicated in the legend. The dashed histogram shows the total pre-fit background. The hatched band includes the combined statistical and systematic uncertainty for the sum of the fitted signal and background. The ratio of the data to the sum of the fitted signal and background is shown in the lower panel.

background process to highlight the presence of the V boson peak in the m_{J} distribution.

The ranking of the impact of the single 15 most important uncertainties on the signal strength is shown in Figure 10.12. The systematic uncertainties are listed in decreasing order of their impact on μ, as explained in Section 7.1. Among the higher contributions in the ranking there are the large-R jet uncertainties. All the four parameters describing the normalisations of the main background processes are present among the 15 NP with the highest impact.

The contribution of systematic uncertainties can be split, allowing the identification of the main sources of systematic uncertainty. The breakdown of the uncertainties, defined in previous chapter as the impact of each group of NPs on the signal strength uncertainty, is shown in Table 10.2. The sources of uncertainty with the largest impact are the statistical uncertainties on the simulated distributions (0.102), the large-R jet uncertainties (0.102), the uncertainties on the floating normalisations (0.094) and acceptance ratios taking into account the uncertainties on the modelling of the signal and background processes (0.052 and 0.079).

Source of uncertainty		Signed impact	Avg. impact
Total		+0.369 / -0.337	0.353
Statistical		+0.243 / -0.238	0.240
Systematic		+0.277 / -0.239	0.258
Experimental uncertainties			
small-R jets		+0.055 / -0.049	0.052
large-R jets		+0.117 / -0.087	0.102
E_{T}^{miss}		+0.007 / -0.007	0.007
Leptons		+0.023 / -0.016	0.020
b-tagging	b-jets	+0.059 / -0.026	0.042
	c-jets	+0.005 / -0.004	0.004
	light-flavour jets	+0.007 / -0.007	0.007
	extrapolation	+0.009 / -0.009	0.009
Pile-up		+0.009 / -0.006	0.008
Luminosity		+0.020 / -0.009	0.015
Acceptance ratios			
SR to CR		+0.063 / -0.041	0.052
HP to LP		+0.098 / -0.060	0.079
med. to high p_T^V		+0.032 / -0.030	0.031
Theoretical and modelling uncertainties			
Signal		+0.073 / -0.037	0.055
Floating normalisations		+0.099 / -0.090	0.094
Diboson		+0.038 / -0.030	0.034
Z + jets		+0.010 / -0.010	0.010
W + jets		+0.011 / -0.011	0.011
Single top quark		+0.003 / -0.003	0.003
$t\bar{t}$		+0.001 / -0.001	0.001
MC statistical		+0.102 / -0.101	0.102

Table 10.2: Breakdown of the contribution to the uncertainty on the signal strength $\hat{\mu}$ obtained from a conditional $\mu = 1$ fit to the Asimov data set. The sum in quadrature of the individual contributions differs from the total uncertainty due to correlations between the nuisance parameters.

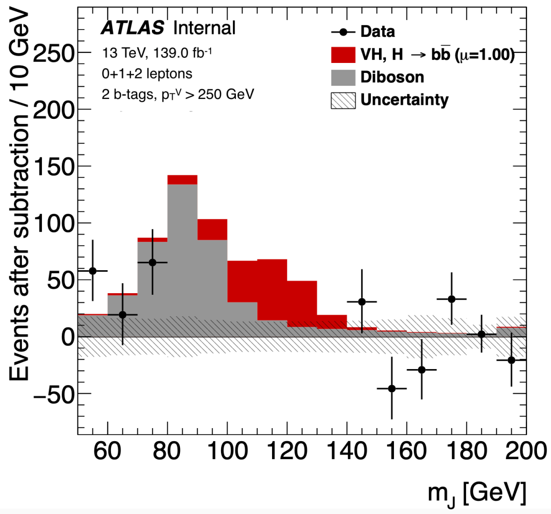

Figure 10.11: m_{J} distribution for the full Run 2 dataset after the subtraction of the histogram of all the background processes except for WZ and ZZ (diboson). The diboson processes are depicted in light grey, the Higgs signal in red. The signal region around the expected nominal Higgs mass is blinded. The size of the combined statistical and systematic uncertainty for the fitted background is indicated by the hatched band.

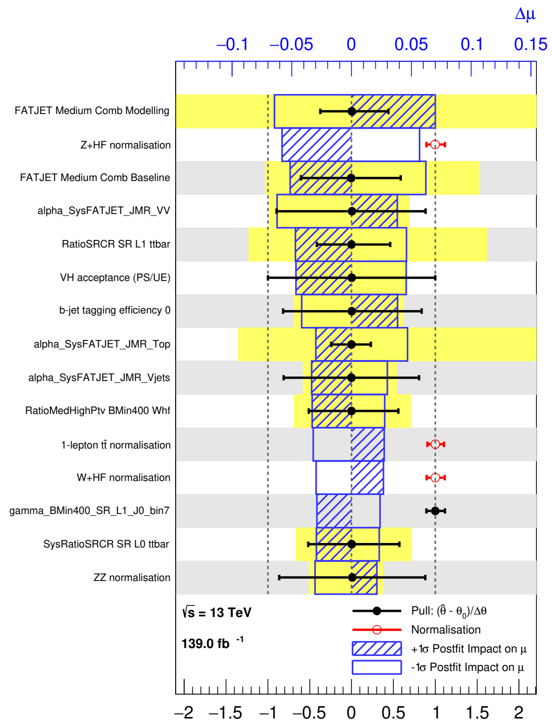

Figure 10.12: Ranking of the most important systematic uncertainties according to their impact on the signal strength parameter $\hat{\mu}$ for the *merged* analysis. The boxes show the variations of $\hat{\mu}$, referring to the top x-axis, when fixing the corresponding individual nuisance parameter to its post-fit value modified upwards or downwards by its post-fit uncertainty, i.e. $\hat{\theta} \pm \sigma_{\hat{\theta}}$, and repeating the fit. The hatched and open areas correspond to the upwards and downwards variations, respectively. The yellow boxes show the pre-fit impact (top x-axis) by varying each nuisance parameter by $\pm 1\sigma$. The filled circles show the pulls of each nuisance parameter (bottom x-axis). The error bars show the post-fit uncertainties on $\hat{\theta}$ with respect to their nominal uncertainties. The open circles show the fitted values and uncertainties of the normalization parameters that are freely floating in the fit.

10.3 STXS

10.3.1 Expected performance

The main goal of the *merged* analysis is to select the very high energy events in order to measure the cross-section as a function of the vector boson transverse momentum and measure (or constrain) the physics BSM parametrisation. The expected results for the STXS measurements are presented in this section. The categorisation scheme adopted for the *merged* selection is schematically summarised in Figure 10.13. The scheme chosen is naturally a *4-POI* categorisation, with the

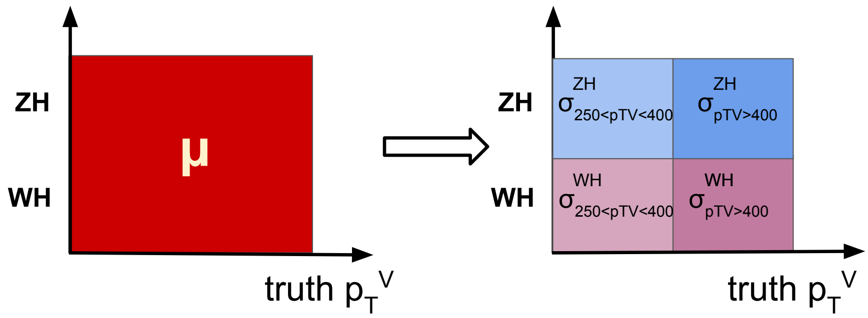

Figure 10.13: Standard signal strength measurement (left) compared with the STXS binning scheme used for the *merged* analysis (right). p_T^V is the truth-level V-boson transverse momentum.

cross-section measured separately for the WH and ZH production modes and separately for the medium-energy (250 GeV $< p_T^V <$ 400 GeV) and high-energy (p_T^V >400 GeV) regions. As for the *resolved* analysis, also in this case the forward Higgs region ($|y_H| > 2.5$) has not been included in the measurement as the acceptance for these events is too small. The STXS bins, built at truth level, follow the reconstructed categories, which have been specifically designed to isolate high energy events. For this reason, no large correlations are expected among the four measured parameters of interest.
The number of events of each STXS bin selected in each SR is shown in Figure 10.14a. Additionally to the four measured STXS bins, also events with 150 GeV$<p_T^V$ <250 GeV are shown, to study possible migrations. Nonetheless, as expected, the number of signal events with 150 GeV$<p_T^V$ <250 GeV reconstructed in the SRs is low, as the *merged* analysis is designed to measure events with p_T^V >250 GeV. Among the remaining regions, the one with the lowest number of signal events is ZH, p_T^V >400 GeV with $\sim$ 20 signal events.
Inside each reconstructed category, the fraction of signal events belonging to a

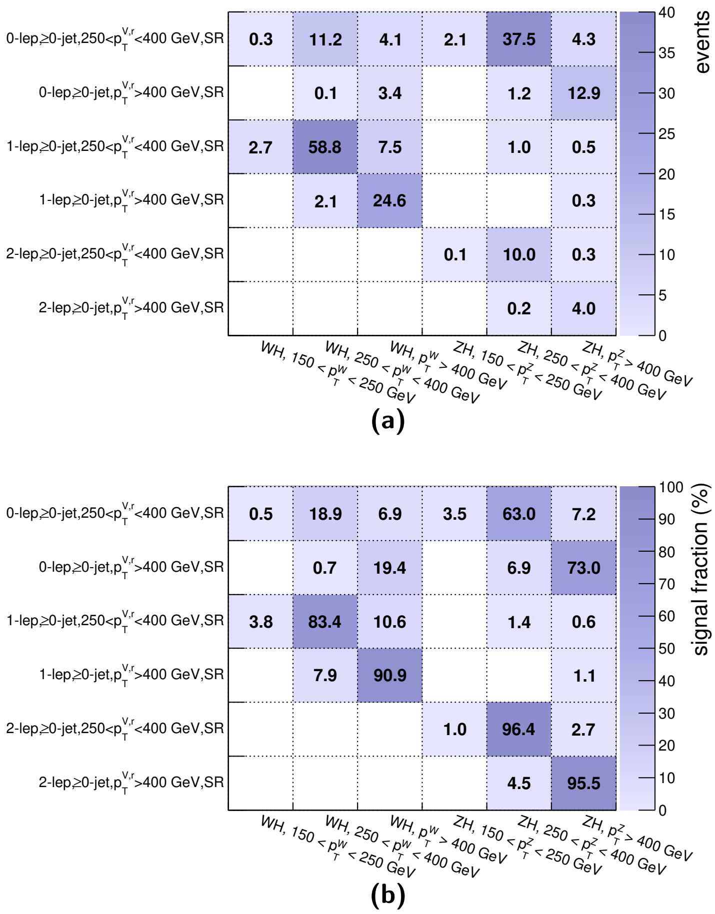

Figure 10.14: With the 4-POI splitting categorisation scheme, (a) the surviving events from each STXS signal region (x-axis) in every reconstructed category (y-axis); (b) the fraction of signal (in percent) from each STXS signal region (x-axis) in every reconstructed category (y-axis). The control regions are not shown due to negligible contributions. Entries with acceptance times efficiency below 0.01% or signal fractions below 0.1% are not shown.

specific STXS bin is shown in Figure 10.14b. Similarly to what was observed in the *resolved* analysis (Section 7.2.3), in the 0-lepton SRs a significant fraction of events belongs to a WH STXS bin ($\sim 20/26\%$). In the 1-lepton signal regions, a small amount of events belongs to a ZH STXS bin ($\sim 1/2\%$). Differently, in the 2-lepton signal regions the fraction of events that belong to a WH STXS bin is negligible.
The measurement of the STXSs in the *merged* analysis is accomplished with the same procedure adopted for the *resolved* analysis. Obviously, also for this measurement, the analysis is still blinded, therefore only the expected results are shown in this section. The expected significances of the four measured cross-sections are shown in Table 10.3. In all cases, the significance is between 1σ and 2σ.

Region ($H \to b\bar{b}$)	Expected significance
$W \to \ell\nu_{250-400}$	1.32 σ
$W \to \ell\nu_{\geq 400}$	1.24 σ
$Z(\ell\ell, \nu\nu)_{250-400}$	1.60 σ
$Z(\ell\ell, \nu\nu)_{\geq 400}$	1.31 σ

Table 10.3: Expected significance for the four measured STXSs in the *merged* analysis.

The plot summarizing the expected result for STXS measurements for both the *resolved* and *merged* analysis is shown in Figure 10.15. The uncertainties on the four cross-sections are reported in the figure, together with the predicted values of the cross-sections. The expected cross-sections and uncertainties for the *merged* analysis are reported in blue. The results obtained with the *resolved* analysis are reported in the same plot to have an easy visual comparison. The STXS bin measured in the *resolved* for p_{T}^{V} >250 has been split in the *merged* analysis at p_{T}^{V} = 400 GeV.
The uncertainties on the cross-section for the two analyses are not easily comparable as they are not measuring the same STXS bins and because the presented results for the *resolved* analysis are obtained with a 79.8 fb^{-1} data sample, while the results of the *merged* analysis are already updated to a 139.0 fb^{-1} data sample. Nonetheless, some interesting aspects can already be highlighted. While the *resolved* analysis is expected to perform better in the region between 250 GeV $< p_{\mathrm{T}}^{V} <$ 400 GeV, the *merged* analysis is expected to extract a more precise measurement in the region with $p_{\mathrm{T}}^{V} >$ 400 GeV. This measurement is expected to improve the sensitivity to some of the BSM parameters.

The values of the correlations among the four measured parameters of interest is shown in Figure 10.16. As each STXS bin corresponds to different categories of the analysis, the correlations are expected to be low, as confirmed by the plot.

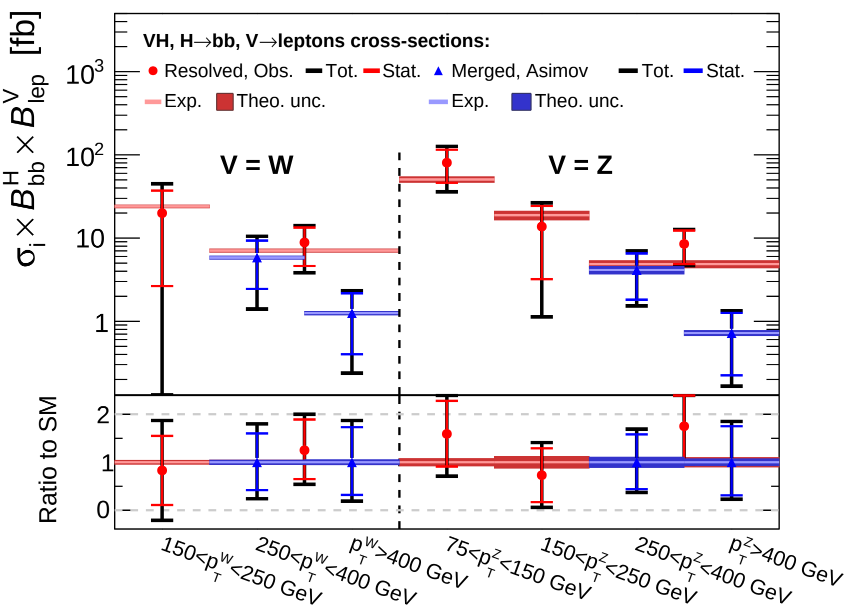

Figure 10.15: Expected cross-sections in the 4-POI scheme for the *merged* analysis, using the 139.0 fb^{-1} data sample (blue), shown together with the measured cross-section in the 5-POI scheme with the *resolved* analysis, using the 79.8 fb^{-1} data sample (red). For the *resolved* results the observation is compared to the SM prediction, marked with the light red lines, and its uncertainty, represented by the darker red area. The SM predicted cross-section are shown also for the regions $250 < p_{\mathrm{T}}^{V} < 400$ GeV and $p_{\mathrm{T}}^{V} > 400$ GeV (and they overlap, by definition, with the cross-section measured by the *merged* analysis with the fit to the Asimov data set). They are marked with a light blue line overlaid to the theoretical uncertainty represented by a darker blue area.

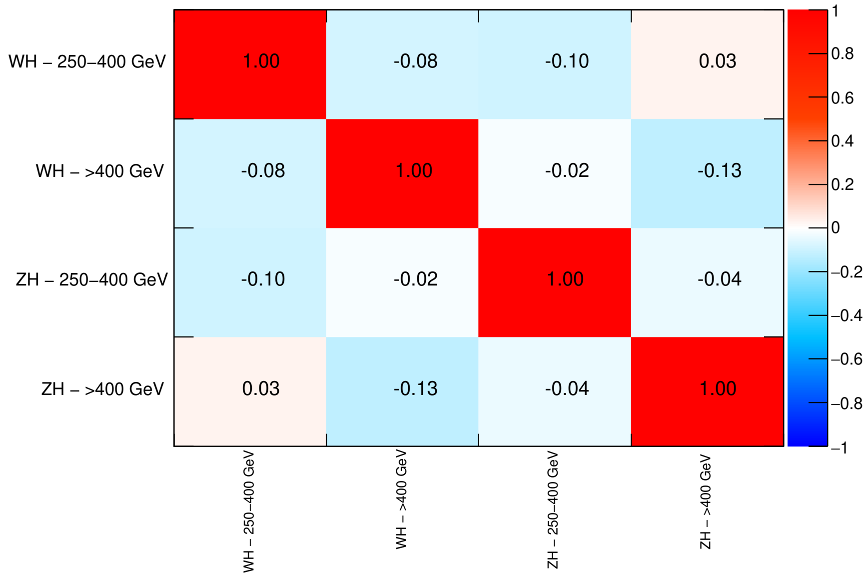

Figure 10.16: Correlations in the measure of the ratio of the $\sigma \times BR$ over the SM for the $WH_{250-400}$, $WH_{\geq 400}$, $ZH_{250-400}$, $ZH_{\geq 400}$ processes in the unconditional fit to Asimov data.

10.3.2 Future development for the STXS in $VH(H \to b\bar{b})$

As already shown in Figure 6.7 the efficiency for the *resolved* analysis drops at ~ 500 GeV, while the *merged* analysis has a higher signal efficiency starting at ~ 350 GeV. As at high p_{T}^{V} the *merged* analysis gives better performance w.r.t. the *resolved* analysis, it is also expected to provide better measurements or tighter constraints on the EFT parameters. One possibility for the future could be to combine the two analyses, *merged* and *resolved*, to perform the fit simultaneously. There are several possibilities to combine the two analyses, and the choice will depend on the expected performance and on the technical difficulties of the implementation. In order to draft the combination strategy a study of the number of signal events selected by both the *merged* and the *resolved* analysis (*overlap events*) was performed in the 1-lepton channel. For this preliminary study, only the signal process WH has been considered. First, the p_{T}^{V} distributions at truth level have been studied for the WH signal events selected by the *resolved* and *merged* analyses, and for the *overlap events*. The p_{T}^{V} distributions for the three cases are shown in Figure 10.17a assuming an integrated luminosity of 139 fb^{-1} both for the *resolved* and the *merged* analyses. In order to compare them, they have been obtained using in all cases the truth level selection $p_{\mathrm{T}}^{V} > 150$ GeV. The same distributions are shown in Figure 10.17b normalised to unitary area in order to highlight the difference in shapes. For the *resolved* analysis the p_{T}^{V} distribution shows a sharply falling shape

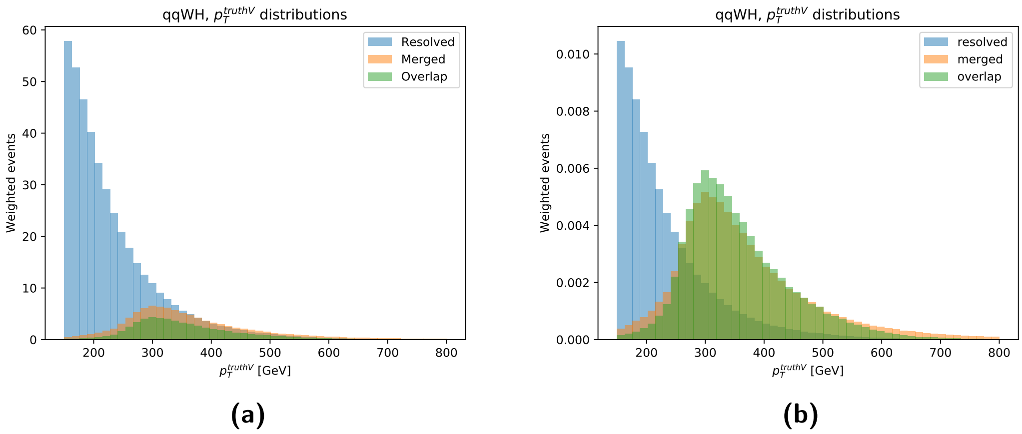

Figure 10.17: p_{T}^{V} distributions at truth level for the WH signal events selected in the *merged* and *resolved* 1-lepton signal regions and for the overlap events. In the plot on the left the expected number of signal events assume an integrated luminosity of 139 fb^{-1} both for the *resolved* and the *merged* analyses, while in the plot on the right all the distributions are normalised to unitary area.

while for the *merged* analysis the distribution peaks at around 300 GeV. The shape of the distribution for the overlap events (also shown in Figure 10.17b normalised to unit area) is similar to the shape of the distribution of the *merged* events, as the overall number of signal events is much larger for the *resolved* analysis w.r.t. the *merged* analysis.
Among all the selected events, the fractions of events selected exclusively by the *resolved* and by the *merged* analysis are shown in Figure 10.18a together with the fraction of overlap events (the sum of the three curves is equal to one). Of all the events selected in the signal regions, about 40% is selected by both the *resolved* and the *merged* analysis, in the p_{T}^{V} range between $\sim$ 300 and $\sim$ 500 GeV. For lower energies most events are only selected by the *resolved* analysis and for higher energies most of the events are only selected by the *merged* analysis. The crossing point between the *merged* and the *resolved* curve is at about 350 GeV, meaning that above this point the fraction of events only selected by the *merged* analysis is larger than the number of events only selected by the *resolved* analysis. While this study provides useful information on the number of selected signal events, no information about the number of selected background events is present. As the final goal is to measure some EFT parameters, in order to assess which analysis strategy will give the best sensitivity the signal efficiency study needs to be completed with the study of the sensitivity of each analysis to the EFT parameters. Therefore, for a more complete test the parametrisation of the EFT in all STXS bins is needed. This is one of the next step foreseen for the analysis.

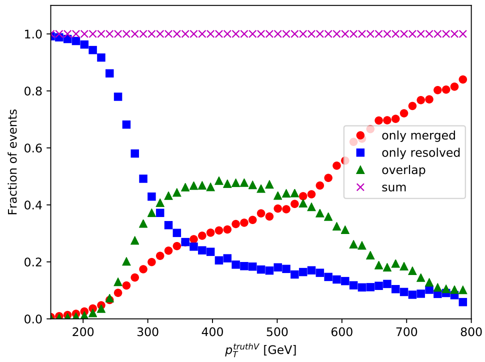

(a)

Figure 10.18: Fraction of WH signal events selected only by the *resolved* analysis, only by the *merged* analysis, and selected by both analyses, as a function of p_{T}^{V} at truth level.

One of the simplest strategies to combine the two analyses could be to sharply divide the events based on $p_{\mathrm{T}}^{V} = 400$ GeV and use the *resolved* analysis below this value and the *merged* analysis above. This implementation allows increasing the analysis sensitivity to BSM deviations and, at the same time, the implementation is extremely simple. Nonetheless, for the bin at $p_{\mathrm{T}}^{V} \geq 400$ GeV, 20% for the signal events would be lost. A more complex possibility could be to give priority to the *merged* analysis in the region $p_{\mathrm{T}}^{V} \geq 400$ GeV. Events not passing the *merged* selection would be tested again with the *resolved* event selection. This implementation is more complex but would exploit all the selected signal events. The final strategy is not set yet and will be decided in the next months.

Chapter 11

Conclusions

The search for the $VH(H \to b\bar{b})$ process with the ATLAS detector has been presented in this thesis. The data sample used corresponds to an integrated luminosity of 79.8 fb^{-1} collected at a centre-of-mass energy of $\sqrt{s} = 13$ TeV. An excess over the expected Standard Model (SM) background is observed, with a significance of 4.9σ (4.3σ expected). This result has been combined with previous results based on Run 1 data collected at $\sqrt{s} = 7$ TeV and $\sqrt{s} = 8$ TeV, measuring an excess with a significance of 4.9σ (5.1σ expected).

The first observation of the $H \to b\bar{b}$ decay has been obtained by combining the $H \to b\bar{b}$ search in VH with the searches with ttH and $VBF - ggF$ production modes. In all cases all available data has been used, using events collected at $\sqrt{s} = 7$ TeV, 8 TeV and 13 TeV. This combination allowed measuring an excess over the expected background, with a significance of 5.4 σ (5.5 σ expected), providing the first observation of the $H \to b\bar{b}$ decay mode.

Similarly, the first observation of the VH production mode has been obtained combining the Run 2 $VH(H \to b\bar{b})$ result with the results of other Run 2 searches for the Higgs boson decaying into either four leptons (via ZZ^*) or diphotons in the VH production mode. The result is an excess over the expected background with a significance of 5.3σ(4.8σ expected), providing the first VH production observation.

The encouraging results and the relatively large data sample available favoured performing the measurement of the $VH(H \to b\bar{b})$ production as a function of the vector-boson transverse momentum. This measurement allows further testing of the SM and provides information to search for effects of physics beyond the Standard Model (BSM). The measurement has been carried out within the

Simplified Template Cross Section (STXS) framework, which provides an efficient structure to constrain or measure effects of BSM physics. Measurements done in the STXS framework also allow a coherent combination of results from different decay channels, a very useful feature for future measurements.
Five cross-sections have been measured in a fiducial volume with rapidity $|y_H| < 2.5$: $WH_{150-250}$, $WH_{>250}$, ZH_{75-150}, $ZH_{150-250}$, $ZH_{>250}$. The relative uncertainties on the cross-sections vary between 50% and 125%. All the measurements are in agreement with the SM predictions, even in high p_{T}^{V} ($>$ 250 GeV) regions, which are most sensitive to potential anomalous couplings between the Higgs boson and the V bosons.
One-dimensional limits on four linear combinations of the coefficients of the Effective Lagrangian operators affecting the Higgs boson couplings to the V bosons and to down-type quarks have also been set. For two of these parameters, the constraint has a precision of a few percents.

Given the excellent performances of the LHC and the relatively large data sample collected in 2018, it is possible to further develop the $VH(H \to b\bar{b})$ measurement using the full Run 2 data sample, corresponding to an integrated luminosity of 139 fb^{-1}.
Two main developments are possible, the first possibility is to repeat the analysis with improvements aimed, above all, at augmenting the sensitivity to BSM effects. This is possible for example designing the event categorisation specifically to improve the measurement within the STXS framework.
On the other side, as the parameters modelling BSM physics are particularly sensitive to deviations at high energies, a search for the $VH(H \to b\bar{b})$ production in the very high energy regime has been developed and presented in this thesis. Within this analysis, named *merged* analysis, the candidate Higgs boson is reconstructed through a single large-R jet, differently from the standard reconstruction mode where the Higgs candidate is reconstructed through two jets (*resolved* analysis). The expected significance for the $VH(H \to b\bar{b})$ cross-section in the *merged* analysis is 3.1σ, the analysis could therefore potentially lead to evidence of the $VH(H \to b\bar{b})$ production at high energies. The measured cross-section value will be published in the next months, as soon as the analysis is complete.
Also for the *merged* analysis, the measurement of the $VH(H \to b\bar{b})$ production as a function of the vector-boson transverse momentum, within the STXS framework, has been presented. The expected uncertainties on four cross-sections, in a fiducial volume with rapidity $|y_H| < 2.5$, have been measured: $WH_{250-400}$, $WH_{>400}$, $ZH_{250-400}$, $ZH_{>400}$.

Since at high energies the *merged* analysis gives better performance w.r.t. the *resolved* analysis, it is also expected to provide better measurements or tighter

constraints on the parameters modelling BSM effects. In order to extract additional information, the cross-section at $p_{\mathrm{T}}^{V} > 400$ GeV needs to be parameterized as a function of such parameters. This is one of the most important next steps for this analysis.
Another future development will be to combine the two analyses (*merged* and *resolved*) to perform the fit simultaneously. There are several possibilities to implement such a combination, and the choice will depend on the expected performance and on the technical difficulties of the implementation. A preliminary study showing the fraction of WH events selected by both the *resolved* and *merged* analysis has been presented. The fraction of events selected by both analyses is about 40% at $p_{\mathrm{T}}^{V} = 400$ GeV and decreases to about 20% at $p_{\mathrm{T}}^{V} = 700$ GeV, where most events are only selected by the *merged* analysis. More detailed studies, exploiting the parametrisation of BSM effects in the region with p_{T}^{V} >400 GeV, will be needed to decide the combination strategy.

As I am finalizing the thesis, the decision on the date for analysis unblinding is being discussed. If results will be as expected they will soon be public and will provide the first measurement of the $VH(H \to b\bar{b})$ cross-section in a very high energy phase space for the first time with an experimental analysis using large-R jets.

Appendices

Appendix A

FTK and the associative memory system

In this appendix, the FTK system, introduced in Chapter 2, is described in more detail. Particular attention is given to the associative memory system and its components and to the procedure followed to test and validate the boards composing the system.

A.1 Hardware for the FTK system

In order to cope with event rates of up to 100 kHz the tracking performed by FTK has to be several orders of magnitude faster than tracking at reconstruction level. Hence, the processing of the data is organised as parallel as possible. The information from the ID is divided in 64 $\eta \times \phi$ regions, so-called towers, processed independently in parallel by custom electronics boards (FTK slice). The numbering of the 64 towers is shown in Figure A.1a.
A diagram of an FTK slice, showing the connections between the electronic boards, is presented in Figure A.1b. The boards receiving inputs from the ID are the **Input Mezzanines** (IM): these boards handle the inputs and perform the hit clustering. This operation consists in decreasing the data volume by a custom clustering algorithm defining *hits*, which are considered later on instead of the full pixel/strip information. The **Data Formatter** boards (DF) receive the clusters and geometrically group them into the 64 independent $\eta - \phi$ towers. For each tower, the information is distributed to the corresponding processing unit, which consists of two **Auxiliary cards** (AUX) and their **Associative Memory Boards** (AMB).

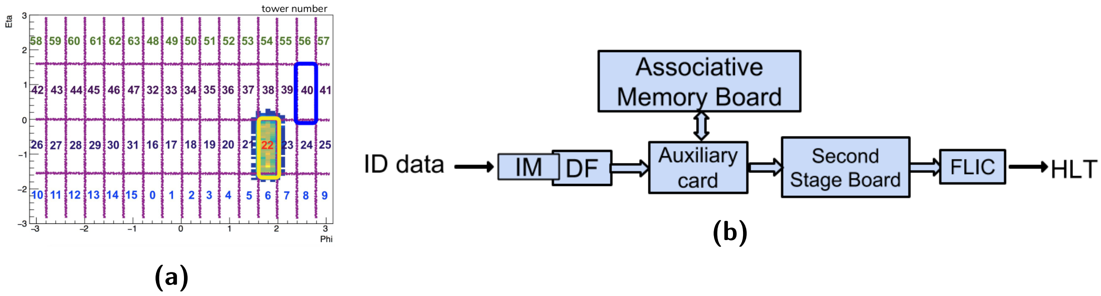

Figure A.1: a) $\eta \times \phi$ position of the 64 ID towers.
b) Diagram of the electronic boards forming FTK slices.

Clusters are then reclustered by the AUX into coarse resolution hits that are sent to the AMB. In the AMB, the coarse cluster information is compared simultaneously to O(10^9) patterns determined from simulation. The hits matching a pattern are used by AUX cards to perform a first-stage fit with 8 out of the 12 silicon detector layers. A cut on the fit quality helps to further reduce the data-flow to **Second Stage Board** (SSB). The SSB retrieves the hit information on four additional silicon detector layers from the DF and performs a 12-layer fit. The second fit, performed with 12 layers, strongly reduces the number of fake tracks and increases the final track quality. Finally, the tracks are converted to the ATLAS format and sent to the HLT by the **FTK to Level-2 Interface Card** (FLIC).

A.2 Associative Memory System

The Associative Memory (AM) system is a key part of the FTK project. It is a real-time pattern matching processor customly developed for FTK [141]. This system is mainly composed of three elements:

- The Associative Memory Chip (AM-chip).
- The Little Associative Memory Board, a daughter-board.
- The Associative Memory Board, the mother-board that hosts four daughter-boards and 64 AM-chips.

The **AM-chip** is an Application Specific Integrated Circuit (ASIC) designed to execute a particular pattern matching algorithm [142]. It is made of a matrix of Content Addressable Memory (CAM) cells. The CAM is a type of memory that returns in output the list of addresses where the input data is stored [143]. A schematic of the architecture of the chip is shown in Figure A.2. Each row is made

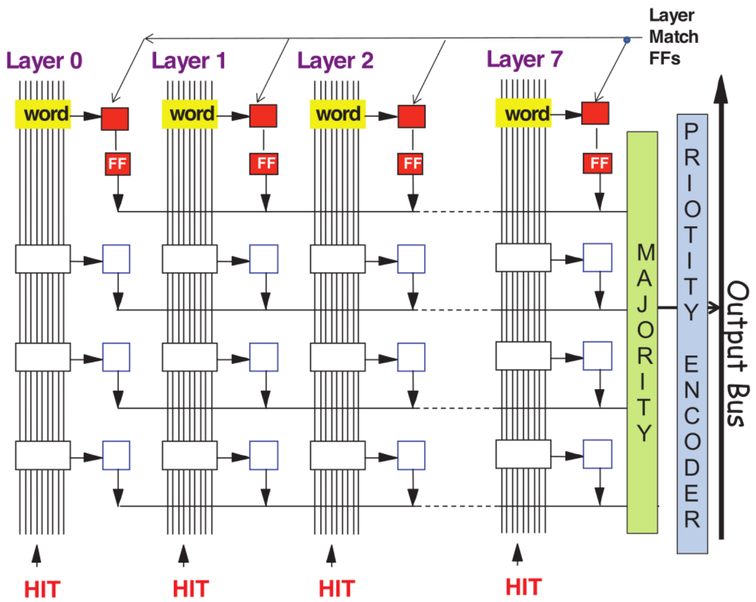

Figure A.2: Architecture of the Associative Memory chip [141]. Each row represents a pattern, the first one on the top is shown in more detail.

of eight CAM cells of one word each, and they form a pattern. Each AM-chip stores about 100 k patterns. In the AM-chip a pattern is not stored in a single memory location, like in the commercial CAM, but it consists of 8 independent words of 16 bits each. The coordinate locations of where the particle hits the silicon detector are stored in these words, one word for each detector layer. The innovative characteristic of the AM is that each one of these 8 words has a comparator and a *layer match flip-flop* (FF), shown in red in the figure, to continuously compare the stored data with its own input data stream and remember the result.

As previously written, the FTK system is highly parallelised to allow using a high trigger rate. The data flow rate is increased by exploiting the parallel readout of eight detector layers on eight buses, one for each detector layer. The eight buses are represented by the columns of Figure A.2. All words in the AM are independently and simultaneously compared with the data serially presented on their own bus. Every time a match is found, the layer match FF is set and remains set until the end of the event processing. This part of the chip is called the *pattern bank*, where all input hits are processed. A second part of the chip, called the *readout logic*, includes the second row of flip-flops for each pattern, the majority logic, and the priority encoder. In Figure A.2 the second row of flip-flops is only shown for the

pattern at the top. A pattern matches inside the majority logic when a predefined number of the flip-flops is set. Finally, the priority encoder reads the matched patterns in order.
This complex AM architecture has many advantages: first of all, it is possible to analyze and look for coincidences among asynchronous data-streams. Data can arrive at the chip at a different time since partial results are recorded and kept as much as needed. Another important feature is that the matching of detector words is accomplished during their data reading, reducing the total latency.

The AM system has been designed to pack AM-chips as much as possible. The elementary block of the system is composed of one mother-board, the AMB, and four daughter-boards, called **Little Associative Memory Board** (LAMB), plugged on the AMB. Each LAMB hosts 16 AM-chips, so a total of 64 AM-chips are installed on each AMB. The LAMB was designed in order to simplify the I/O operations and increase the system modularity. The LAMB is a printed circuit board (PCB) hosting 16 AM-chips. Its main function is to distribute the input data from the mother-board to the 16 AM-chips and to send back their output to the mother-board. Input data must be distributed at 2 Gbit/s on each serial link with a very large fan-out: eight words from eight detector layers reach eight million patterns in parallel in one clock cycle (10 ns). Another important function implemented by the LAMB is the configuration of the AM-chips. First of all, since the memory locations are SRAM, the patterns have to be stored after each power on. Additionally, the AM-chips have other configuration registers that need to be set up.

The **Associative Memory Board** (AMB) motherboard is a 9U VME board, made of 12 layers. It has been designed to hold 4 LAMBs [141]. The LAMB and the motherboard communicate through a high frequency and high pin-count connector placed in the centre of the LAMB.
A network of high-speed serial links handles the data distribution from the input to the four LAMB connectors and back. Twelve input serial links carry the data of the Inner Detector to the LAMBs, and 16 output serial links carry the fired patterns from the LAMBs. Events are loaded on the board at a maximum rate of 100 kHz corresponding to a maximum input bandwidth of 1.6 GB/s. 100 kHz corresponds to the Level 1 output rate, as described in Chapter 2. An even larger number of output words per link can be collected and sent back. Each board can readout up to 8000 matched patterns per average event, for a maximum output bandwidth of $\sim$ 3.2 GB/s, thanks to 16 parallel output links (four links per LAMB). The data traffic is handled by two FPGAs, one handling the input data and the other handling the output data. Two other FPGAs implement data control logic and configuration.

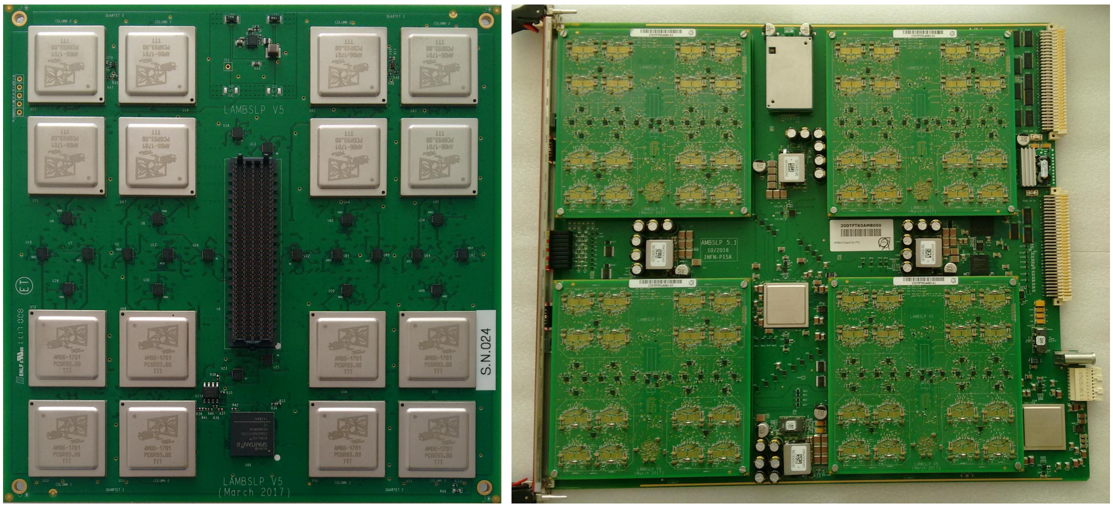

(a) (b)

Figure A.3: a) Picture of a LAMB. The 16 AM-chips mounted on it are visible.
(b) Picture of an AMB with four LAMBs mounted on it, the AM-chips are not visible as they are facing the AMB.

A.2.1 Test of the Associative Memory System components

The final FTK system will include a total of 64 AMB, one per FTK tower, 256 LAMB and 4096 AMB. Once installed the boards will stay in place during the full Run 3. Each of the produced boards needs therefore to be carefully tested before the installation, as described in this section for the AMBs and LAMBs.
The AM-chips and LAMBs are produced by two different private companies and are later assembled, together with the FPGAs and the rest of the component, by a third company. A similar procedure is followed for the AMB. The assembled LAMBs and AMBs are then tested at the University of Pisa before being finally delivered at CERN.
The first tests are simple mechanical and electronic tests. Each LAMB and AMB board is visually analysed to verify that all components have been mounted correctly. Electronic test are performed to verify that there are no shorts among all power supply test points and among the power supply test points and the ground. New boards are labelled and the information on the board are saved on a shared database (EDMS).
The LAMBs are then mounted on the AMBs, which in turn are inserted in the crate, connected to an AUX board and powered up. At this point the AMB and LAMBs firmware is installed, and after some basic checks a long series of software tests is performed. The goal of the tests is to check the correct functioning of all the lines on the boards, including the connection between the AMB and the AUX,

between the AMB and the LAMB, the link between the AM-chips and between the AM-chips and the LAMB. The boards are tested both in the "rest condition" and under "stress condition", simulating the handling of a large number of events and checking that the power consumption and the temperatures are kept under control. Boards passing all tests successfully are marked as GOOD on the database and delivered at CERN. Defective boards are marked as BAD with details of the issue, they are further tested and debugged to understand which part is defective and if the issue is fixable.
The described software procedure is fully automated and takes about one hour. I have debugged, improved and automated the test procedure starting from a set of single tests. The various steps of the test procedure can also be run singularly, as it is typically done to debug boards that are found defective. The test procedure has been used not only to test new boards, but also to test new AMB firmware versions, by running the test on validated boards. Additionally, some AMBs found defective at CERN have been brought back in Pisa to be further tested to locate the problematic components. Last but not least, the described test procedure was used in January 2018 to validate more than one hundred newly produced LAMBs in a short time (three weeks), as was requested by the project timeline. I organised the testing in Pisa, which was carried on by a team of six people working in couples and including several non-experts. The automated test procedure, combined by a short set of instructions and a first shift with a test expert, allowed all the people involved to give a relevant contribution in the testing. Four of the 103 tested LAMBs have been found defective and have been further tested.

Appendix B

Matrix element and Monte Carlo event generators

A brief description of the MC event generators used in this analysis is given in this appendix.

Not all the event generators [144] include all steps from matrix element to hadronisation and decay. Some generators, like `MadGraph5_aMC@NLO` and `Powheg`, only generate the hard process, without the parton shower and hadronisation steps. The output of these generators can be the input of an event generator designed to simulate the showering and decays (e.g. POWHEG + PYTHIA 8).

MadGraph5

`MadGraph5_aMC@NLO` is a leading-order matrix element generator extended to include loop diagrams [145]. `MadGraph5_aMC@NLO` generates Feynman diagrams and calculates matrix elements for user-specified processes. The framework aims at providing all the elements necessary for SM and BSM phenomenologies, such as the computations of cross-sections and the generation of hard events. `MadGraph5_aMC@NLO` does not simulate parton shower and hadronisation, but it can be interfaced to other event generators to simulate this part.

POWHEG BOX

Powheg-BOX (Positive Weight Hardest Emission Generator) is a general framework for implementing NLO calculations in shower Monte Carlo programs according to the Powheg method. In the Powheg method, the hardest radiation is generated first using the exact NLO matrix elements [146, 147]. The algorithm does not depend on a specific parton shower and its output can be easily interfaced to any modern shower generator (e.g. Pythia 8).

MiNLO

MiNLO (Multi-scale improved NLO) is a procedure for the choice of factorisation and renormalisation scales that improve the prediction for inclusive quantities in any NLO calculation, and allow to reach NLO accuracy in the production of associated jets [148].

Pythia 8

Pythia 8 is a general-purpose event generator. It contains an extensive list of hardcoded subprocesses and is designed such that it facilitates the use of external input (e.g. from MadGraph for the simulation of parton showering, hadronisation and underlying event) [70]. Pythia 8 includes elastic, single and double diffractive and non-diffractive soft processes, providing an inclusive description of the total pp interaction cross-section. Hence, it is also well-suited for the generation of pile-up events. The subprocess cross-sections have to be convoluted with PDFs to obtain the event rates. Several proton PDFs are hardcoded in this event generator.

Sherpa

Sherpa is a general-purpose event generator, capable of simulating the physics of lepton-lepton, lepton-hadron, and hadron-hadron collisions as well as photon-induced processes [149]. Sherpa covers both the matrix element calculation and the parton shower description. It is considered to be one of the most advanced programmes for the automated generation of tree-level matrix elements for both SM and new physics processes. Apart from parton shower and hadronisation, Sherpa provides modelling of hadron and tau decays as well as electromagnetic final state radiation and the simulation of multiple parton scattering. Multiple parton scattering is the scattering of more than one couple of partons, from the same colliding couple of hadrons. These interactions can cause non-trivial changes to the final state.

Appendix C

Additional information on the more relevant systematic uncertainties in the *resolved* analysis

An overview of the systematic uncertainties affecting the resolved and the merged analysis is presented in Chapter 8. The first section of this appendix provides additional material on the systematic uncertainties with a large impact on the signal strength in the resolved analysis. The second section clarifies the naming convention for the parameters with the largest impact on the measured STXS.

C.1 Uncertainties with largest impact on the signal strength for the *resolved* analysis

A useful tool to identify the more relevant sources of uncertainty is to measure the impact of the related parameters on the signal strength. This is done through the *ranking plots*, introduced in Chapter 7. The ranking plot for the *resolved* analysis is shown in Figure 7.3 and the highest-ranked systematic uncertainties are described in this section. The 15 parameters with the largest impact on the signal strength have an impact varying between $\sim 3\%$ to $\lesssim 6\%$. These parameters are related to the uncertainties on the background modelling, followed by the signal modelling uncertainties and the b-tagging uncertainties.
The first three uncertainties in the raking are the W+HF shape uncertainty as a function of p_{T}^{V}, the Z+HF shape uncertainty as a function of m_{bb} and the diboson

shape uncertainty as a function of m_{bb}. All three are described in the following.

The W+HF shape uncertainties are computed as briefly described in Section 8.2.2, and they are derived only for the most important physical variables used in the BDT: m_{bb} and p_{T}^{V}.
Since it is very hard to isolate a high purity W+jets sample not biased to a particular region of phase space, the modelling uncertainties are completely derived from MC simulations. They are derived from the comparisons of the `Sherpa` samples with varied scales settings and from the comparison of the `Sherpa` sample to the `MadGraph` sample. Shape uncertainties are computed fitting a functional form through the largest variation and symmetrising it. If variations are found to be similar for several analysis regions then a common uncertainty is derived and implemented for those regions. In all the channels, the largest variation is produced by the comparison between the `Sherpa` and the `MadGraph` predictions and the effect of the `Sherpa` internal scale variations is found to be negligible in comparison.
From the comparisons it is found that the shape uncertainties for the p_{T}^{V} distributions can be parametrised by a straight line. A summary of the linear fits used to parametrise the uncertainties in the 2 and 3-jet regions for the 0 and 1-lepton channels is shown in Figure C.1. As the shape effects are in a consistent direction

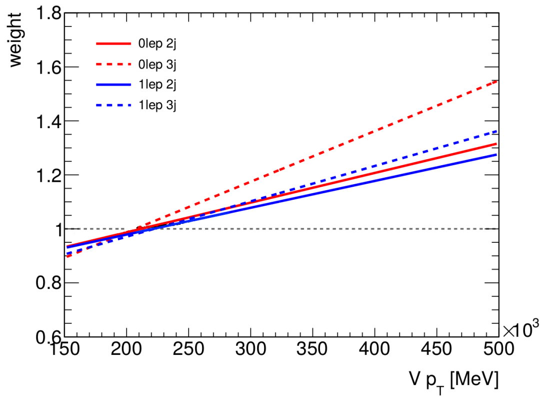

Figure C.1: W+HF shape uncertainties as a function of p_{T}^{V}: comparison of the linear fit to the ratio of `MadGraph` and `Sherpa` predictions in the 2-jets (solid lines) and 3-jets (dotted lines) categories in the 0-lepton (blue lines) and 1-lepton (red lines) channels.

and of a similar magnitude in all the regions, the variation in the 1-lepton 3-jet region has been adopted for all of them.
It can be noticed that the W+HF p_{T}^{V} shape uncertainty has high variations in the high p_{T}^{V} regions. These regions correspond to high BDT bins and are more enriched in signal events. Considering also that W+jets is one of the main background processes, the relatively large impact from the W+HF uncertainty on the signal

strength is thus not surprising.

The second uncertainty in the ranking plot is the Z+HF shape uncertainty as a function of m_{bb}. This highly-ranked uncertainty is constrained and has a pull of $\sim 1.4\sigma$. In fact, the large data sample in the 0- and 2-lepton mass sidebands allows the fit to pull and constrain the nuisance parameter on the m_{bb} shape of the Z+HF background. The pull is thus correcting a simulation mismodelling of the m_{bb} distribution, observed in Z+HF enriched sideband regions.
The Z+HF uncertainties are derived similarly to what is described above for W+HF. Additionally, the highly pure control regions dominated by the Z+jets background allow to directly extract shape uncertainties from the comparison of data to MC simulations. In the CRs the total MC background is compared to data for the distributions for which the shape uncertainties are being derived. The Z+HF shape uncertainties are studied in the 2-lepton channel. Additionally to the event selection described in Chapter 6, a MET significance cut < 3.5 is applied to reduce the contribution of $t\bar{t}$. The Z+jets background is then scaled to the data after subtracting off the non-Z+jets backgrounds. The distributions are studied in the 0, 1 and 2 tag categories, with 0, 1 or 2-b tagged jets, respectively. In addition, the tag categories are studied for different jet multiplicities: 2-jets and 3+jets. For the 2 tags category only events outside the region with 110 GeV $< m_{bb} <$ 140 GeV have been used.

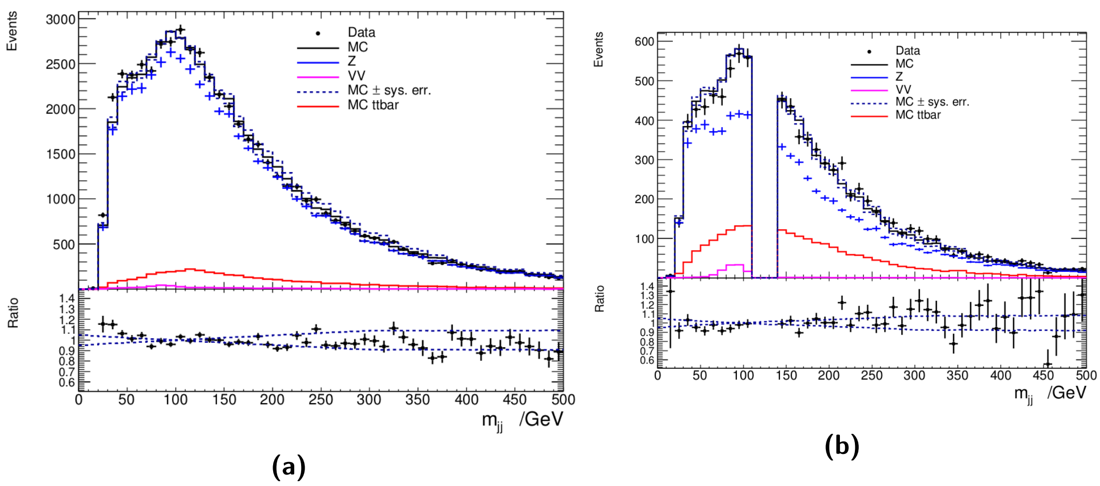

Figure C.2: The m_{jj} distribution for the medium p_T^Z region (75 GeV $< p_T^Z <$ 150 GeV) 2-lepton control region for the 3+jets regions with 1 (left) and 2 tags (right). The data are indicated as black dots with the associated error bars. The blue, red and magenta lines represent the Z+jets, $t\bar{t}$ and diboson simulated distributions, respectively. The shape uncertainties are indicated by the blue dotted lines the lower panels.

The data/MC comparisons for m_{bb} in the medium (75 GeV $< p_T^Z <$ 150 GeV) p_T^Z

region is shown in Figure C.2 as an example. For both the p_T^Z and m_{bb} distributions the shape uncertainty was derived by assigning functions to include the observed data/MC differences. The shape uncertainties are indicated by the blue dotted lines in the figures. The data in the figures only include the 2015 and 2016 data. The study was updated including the data collected in 2017 obtaining the same results, the uncertainty derived in Figure C.2 have been therefore used.

The diboson m_{bb} shape uncertainty is the third uncertainty in the ranking plot. It has large uncertainty in the tail of the m_{bb} distribution, close to the simulated signal peak, so a relatively large impact on the signal strength is expected. For all diboson processes, uncertainties in the shapes of the variables m_{bb} and p_T^V have been considered. Shape uncertainties have been computed considering effects from the parton shower variation, scale variations (considering the single scale variation that shows the largest impact), and from comparing `Powheg` +PYTHIA 8 with `Sherpa` 2.2.1. Scale variations are found to have a smaller impact and are in general well-covered by the parton-shower variation, therefore the shape systematics are extracted from the parton-shower variations and the `Powheg` +PYTHIA 8 versus `Sherpa` 2.2.1 comparison. Also in this case the shapes are approximated by a suitable functional form. For the m_{bb} distribution, the shape variation is described by a tanh function in the 2-jets region, and by a third-degree polynomial with range capped at 250 GeV for the 3-jet region. The shape variation from `Sherpa` versus `Powheg` in the m_{bb} variable is shown as an example in Figure C.3 for the 1-lepton 2-jets region.

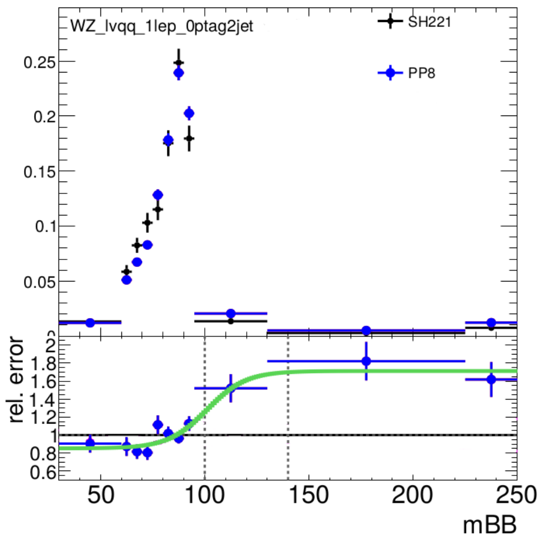

Figure C.3: Example diboson shape variations from `Sherpa` (black dots) versus `Powheg` (blue dots) in the m_{bb} variable, shown for the 1-lepton 2-jets region, approximated by tanh.

Other uncertainties with a large impact on the signal strength are the uncertainties due to limited knowledge of the signal shape, already described in Chapter 8, and the b-tagging uncertainties, described as well in Chapter 8.

C.2 Naming conventions for the uncertainties with largest impact on the STXS measurement

For each one of the 5 POI measured within the STXS framework, the uncertainties with the largest impact on each POI have been studies. The ranking plots showing these uncertainties are presented in Figures 9.7 and 9.8 of Section 9.2.1. The naming convention utilized in these Figures is given in this section.
In all the ranking plots, except for the one describing the impact on ZH [75-150] GeV, the other POI have a large impact on the studied POI. E.g. the POI for WH with p_{T}^{V} >250 GeV is on top of the ranking plot for the POI WH with 150 GeV< p_{T}^{V} <250 GeV. These parameters are named in the ranking plots in the following way:

- SigXsecOverSMWHx150x250PTV for WH with 150 GeV $< p_{\mathrm{T}}^{V} <$ 250 GeV
- SigXsecOverSMWHxGT250PTV for WH with $p_{\mathrm{T}}^{V} >$ 250 GeV
- SigXsecOverSMZHx75x150PTV for ZH with 75 GeV $< p_{\mathrm{T}}^{V} <$ 150 GeV
- SigXsecOverSMZHx150x250PTV for ZH with 150 GeV $< p_{\mathrm{T}}^{V} <$ 250 GeV
- SigXsecOverSMZHxGT250PTV for ZH with $p_{\mathrm{T}}^{V} >$ 250 GeV

In most of the ranking plots shown the statistical uncertainties have a large impact on the POI. The nuisance parameters associated with the statistical uncertainty are named *gamma* and are followed by indications on the histogram and bin of the specific NP with large impact. E.g. SR indicates that the relevant histogram is in the signal region, while Whf indicates that the relevant distribution is in the control region. $L0$, $L1$ and $L2$ specify the relevant leptonic channel and $J2$ and $J3$ specify if the distribution is in the 2-jets or 3-jets region. Finally the name contains the indication of the relevant bin number.
The uncertainties related to the flavour tagging also have a relevant impact on all the measured POIs. As described in Section 8.2.1, separated scale factors and corresponding systematic uncertainties are provided for b-, c- and light-flavor-induced jets. These uncertainties are indicated in the ranking plots as:

- b-jet tagging efficiency
- c-jet tagging efficiency
- Light-flavour tagging efficiency

As for each kind there are several components, the name in the ranking plot is associated to a number indicating the relevant component (e.g. b-jet tagging efficiency 0).
The residual theoretical uncertainties on the signal cross section and the signal modelling uncertainties, described in Chapter 8, are indicated in the ranking plots as $alpha\_SysTheory$. The $PSUE$ uncertainties are related to the parton shower and underlying events modelling. The uncertainties including $Delta$ in the name are related to the QCD scale uncertainty (e.g. $alpha\_SysTheoryDelta1\_ggZH$ is the NP related to the impact of Δ^1 on $gg \to ZH$).
The parameters indicated with *normalisation* are the scale factors applied to the normalisation of the main background processes, and are left unconstrained in the fit. They are indicated as red open circles in the ranking plots.
The NPs including p_{T}^{V} in the name are shape uncertainties as a function of p_{T}^{V}, e.g. the W+HF and Z+HF p_{T}^{V} uncertainties, already depicted in the previous section. The uncertainties named m_{bb} shape are related to the background shape uncertainty as a function of m_{bb}.
The NPs named *acceptance* are related to the acceptance uncertainties of the background processes.
The NPs named E_T^{miss} soft term resolution are related to the uncertainties on the soft term of the E_T^{miss} computation.
Finally, the NP named $SysJet$ is related to the uncertainty on the small-R calorimetric jets.

Appendix D

Validation of the STXS inputs for the *resolved* analysis

The measurement of the STXS in the $VH(H \to b\bar{b})$ channel required a split of the signal simulated events and an update of the signal systematic uncertainties, with respect to the systematic uncertainties used in the single signal strength measurement. In order to validate the STXS approach, the merging procedure has been applied to all the STXS , and a fit to a global signal strength has been performed. This validation is described in this appendix.

The measurement of the STXS in the $VH(H \to b\bar{b})$ channel implied a split of the signal simulated events and an update of the signal systematic uncertainties, with respect to the systematic uncertainties used in the single signal strength measurement. The uncertainties have first been computed using the *maximum splitting scheme*, and then propagated to match the *3-POI* and *5-POI* categorisation schemes used for the cross-section measurements. In order to validate the STXS approach and the signal uncertainties, all the STXS bins have been merged in a single bin, and a fit to a global signal strength has been performed (referred to as one-μ fit). The merging procedure applied to compute the uncertainty is the same described in Chapter 8. This fit differ from the single signal strength fit performed in the $H \to b\bar{b}$ observation paper only by the new definition of the signal uncertainties.
The signal strength measured using the STXS fit inputs is shown in Table D.1, together with the signal strength measured in the $H \to b\bar{b}$ observation paper [8]. The results are very compatible, both for the central value and for the overall uncertainty, with a shift smaller than 3% of the central value for a relative uncertainty of ±22%. The expected and observed significance, shown in the same table,

Analysis	μ central value	μ uncertainty		Significance	
		stat	syst	exp.	obs.
Observation paper	1.16	±0.16	$^{+0.21}_{-0.19}$	4.33	4.88
STXS measurement	1.19	±0.16	$^{+0.22}_{-0.20}$	4.25	4.93

Table D.1: Comparison of the measured signal strengths, expected significance and observed significance of the $VH(H \to b\bar{b})$ signal in the one-μ fit to data for the $H \to b\bar{b}$ observation paper and using the STXS inputs and uncertainties.

are also compatible.
The impact on the signal uncertainty of potential changes brought by the STXS uncertainty scheme, has been further scrutinized studying the breakdown of the uncertainty in its various components. The ranking of the impact of the uncertainty on the final result has been compared as well and is shown in Table D.2, comparing the results of the one-μ fit in the STXS scheme and the results of the $H \to b\bar{b}$ observation paper. The overall effect from the data and MC statistics, as well as the systematic uncertainties, is almost unchanged. This is also true for the signal systematic uncertainties. However, some small differences are present, e.g. the impact of the W+jets modelling on the signal uncertainty is increased by 12%.
A further breakdown in the individual sources of systematic uncertainties is shown in the ranking Figure D.1. The plot shows the ranking of the impact of the 15 most important uncertainties and normalisation scale factors on the signal strength uncertainty. As for the background, the STXS ranking is very compatible the result of the observation paper, with relatively small increase of the W+jets p_{T}^{V} uncertainty for example, which contributes to the changes observed in the breakdown table.
Such changes are compatible with the increase of flexibility in the STXS nuisance parameter model, in particular for the signal uncertainty along p_{T}^{V} in the STXS binning. A reduction of the presence of the PS / UE uncertainties, compatible with the overall reduction of the uncertainty from a better treatment of Powheg + Herwig 7, is also observed. Figure D.2 overviews the comparison of the pulls and constraints on the uncertainties after the full one-μ fit to data in the STXS measurement and observation paper. The post-fit values of the uncertainties are very compatible between the two fits.

NP set	Impact on error			
	STXS measurement		Observation paper	
	signed	unsigned	signed	unsigned
Total	+0.272 / -0.254	±0.263	+0.268 / -0.249	±0.259
DataStat	+0.164 / -0.162	±0.163	+0.162 / -0.159	±0.161
FullSyst	+0.217 / -0.196	±0.206	+0.214 / -0.191	±0.203
Floating normalizations	+0.033 / -0.041	±0.037	+0.032 / -0.038	±0.035
Multi Jet	+0.005 / -0.006	±0.006	+0.005 / -0.005	±0.005
Modelling: single top	+0.029 / -0.026	±0.027	+0.030 / -0.027	±0.028
Modelling: ttbar	+0.049 / -0.051	±0.050	+0.050 / -0.050	±0.050
Modelling: W+jets	+0.068 / -0.066	±0.067	+0.060 / -0.059	±0.060
Modelling: Z+jets	+0.053 / -0.055	±0.054	+0.055 / -0.054	±0.055
Modelling: Diboson	+0.055 / -0.053	±0.054	+0.056 / -0.052	±0.054
Modelling: VH	+0.110 / -0.074	±0.092	+0.114 / -0.074	±0.094
Detector: lepton	+0.009 / -0.008	±0.008	+0.010 / -0.009	±0.009
Detector: MET	+0.019 / -0.018	±0.018	+0.017 / -0.010	±0.014
Detector: JET	+0.045 / -0.031	±0.038	+0.041 / -0.028	±0.035
Detector: FTAG (b-jet)	+0.062 / -0.062	±0.062	+0.062 / -0.059	±0.061
Detector: FTAG (c-jet)	+0.044 / -0.037	±0.040	+0.046 / -0.037	±0.042
Detector: FTAG (l-jet)	+0.004 / -0.004	±0.004	+0.008 / -0.009	±0.009
Detector: FTAG (extrap)	+0.009 / -0.008	±0.008	+0.007 / -0.008	±0.008
Detector: PU	+0.010 / -0.007	±0.008	+0.007 / -0.006	±0.007
Lumi	+0.026 / -0.017	±0.022	+0.029 / -0.018	±0.023
MC stat	+0.072 / -0.074	±0.073	+0.070 / -0.071	±0.070

Table D.2: Breakdown of the uncertainty on the $VH(H \to b\bar{b})$ signal strength in the different modelling, experimental, and statistical components. The table corresponds to the one-μ fit to 79.1 fb^{-1} of Run 2 data in the (second/third columns) STXS analysis and in the (fourth/fifth column) observation paper.

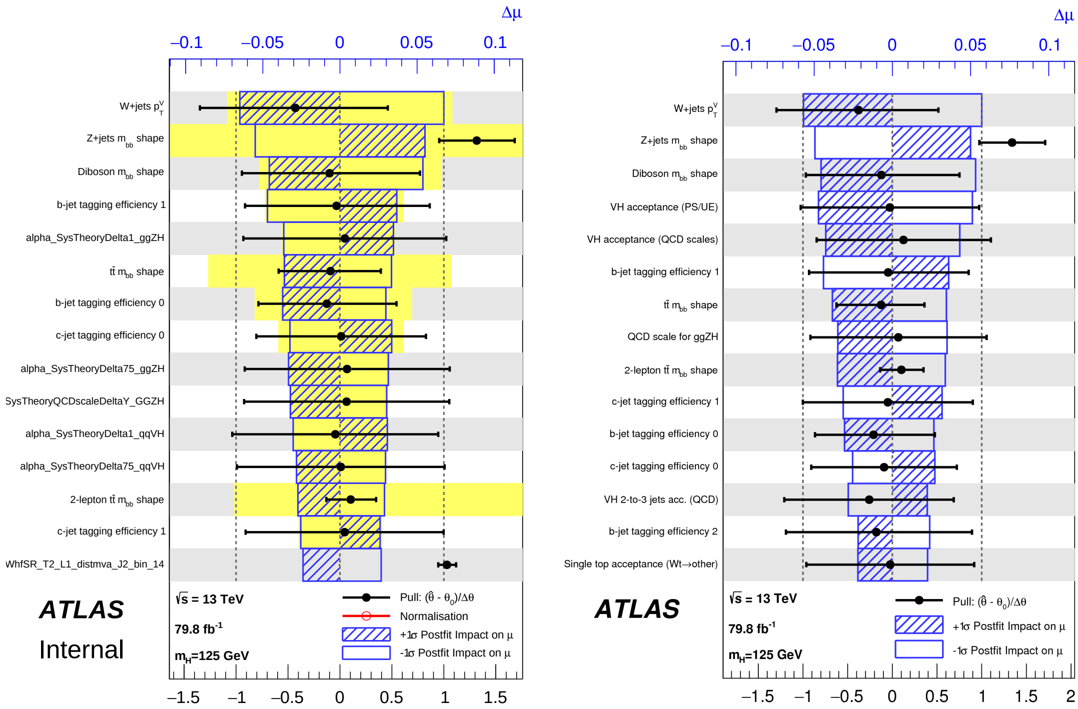

Figure D.1: Impact of systematic uncertainties on the fitted signal strength μ using STXS inputs (left) and from the observation paper (right) [60]. The systematic uncertainties are listed in decreasing order of their impact on μ. The boxes (yellow area) show the variations of μ, referring to the top x-axis, when fixing the corresponding individual nuisance parameter θ to its fitted value $\hat{\theta}$ modified upwards or downwards by its fitted uncertainty (pre-fit uncertainty), and performing the fit again, with all the other parameters allowed to vary, so as to take correlations between systematic uncertainties properly into account. The hatched and open areas correspond to the upwards and downwards variations, respectively. The filled circles, referring to the bottom x-axis, show the deviations of the fitted nuisance parameters $\hat{\theta}$ from their nominal values θ_0, expressed in terms of standard deviations with respect to their nominal uncertainties $\Delta\theta$. The associated error bars show the fitted uncertainties of the nuisance parameters, relative to their nominal uncertainties.

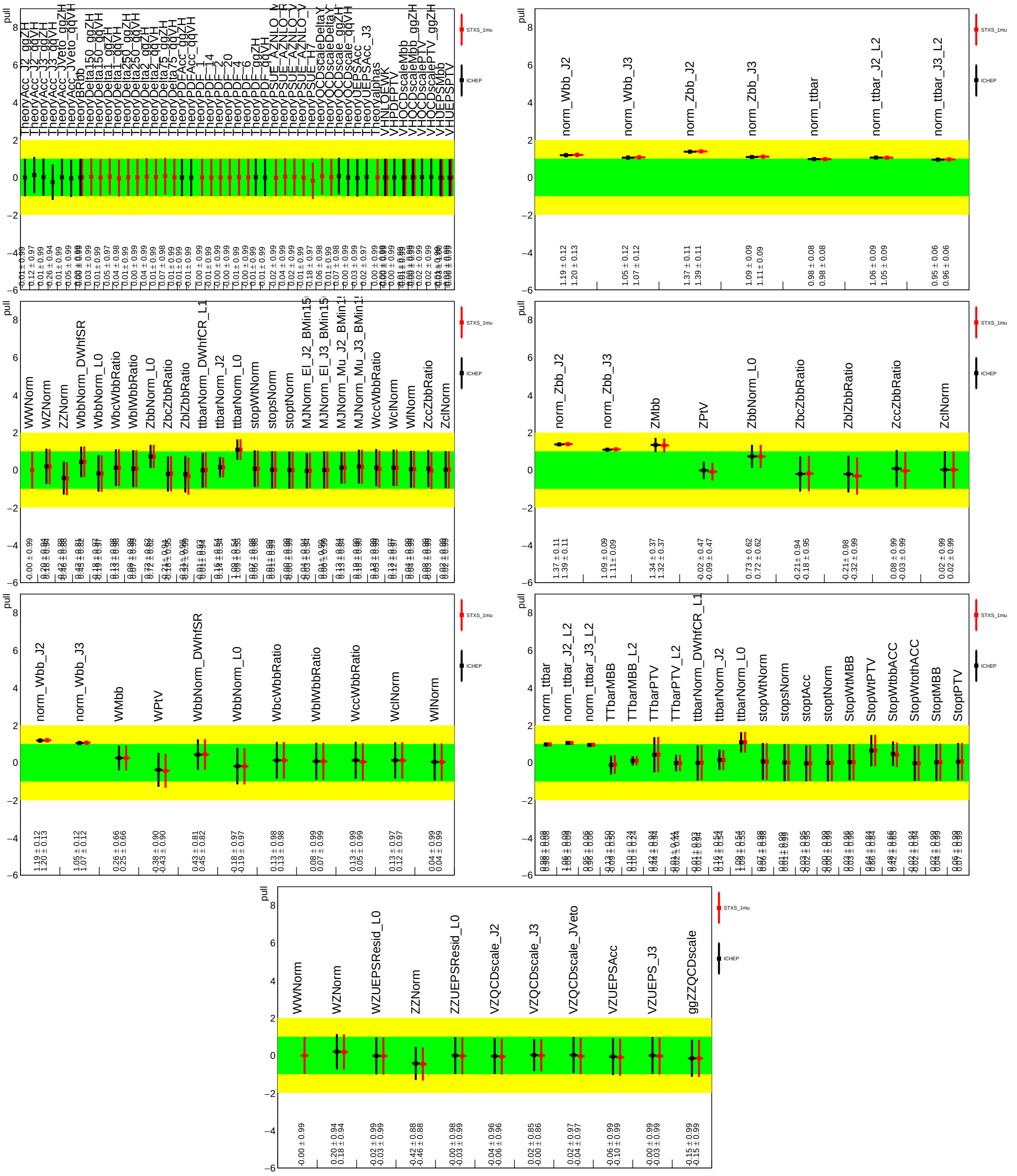

Figure D.2: Comparison of the STXS one-μ and the observation paper results. Pulls and constraints of the MC modelling nuisance parameters and floating scale factors for the unconditional fit to Run 2 data in the (black) observation paper and (red) STXS approach. The first plot displays the uncertainties on the signal prediction, and the following ones are for the unchanged background uncertainties

Appendix E

Expected significance comparison between *merged* and *resolved* analysis

In this appendix, a comparison between the expected significances for the resolved analysis that led to the $H \to b\bar{b}$ observation and merged analysis described in this thesis is presented.

No exact comparison between the expected results of the of the *merged* analysis presented in this thesis and the *resolved* analysis that led to the $H \to b\bar{b}$ observation is possible. However, an approximate comparison among the two is attempted in this appendix, highlighting the limitations of this comparison. In order to proceed with the comparison three differences should be taken into account:

- the luminosity;
- the chosen p_{T}^{V} range;
- the Asimov dataset used to measure the expected significance.

The observed and expected results of the *resolved* analysis are obtained using the data collected up to 2017, with an integrated luminosity of 79.8 fb^{-1}. On the other hand the integrated luminosity of the data used in the *merged* analysis is 139.0 fb^{-1}. An approximate comparison between the two can be done by scaling the *resolved* expected results by a factor $\sqrt{139.0/79.8} \simeq 1.32$.
Another difference is that the expected significances quoted in Chapter 10 for the

merged analysis are obtained with a fit to Asimov data, whereas the expected results quoted for the *resolved* analysis are the so called post-fit expected results. To obtain the post-fit expected results the normalisation of the background processes are first scaled by doing a fit to data. The artificial dataset is then built with the same technique used for the Asimov dataset, but using the background normalisation obtained from the fit to data.
Finally, the *merged* analysis only takes into account events in the range p_T^V >250 GeV, while in the *resolved* analysis events are included starting at p_T^V >150 GeV (75 GeV in 2-lepton channel). For the comparison it is therefore preferable to take into account the STXS results of the *resolved* analysis, and to only consider the bins with p_T^V >250 GeV (Table 9.5). The STXS *resolved* results are divided according to the production mode (WH and ZH). These results can be approximately compared to the *merged* expected results for the 0-lepton and 1-lepton channels, assuming that most WH events are reconstructed in the 1-lepton channel (thus neglecting the 0-lepton contribution) and assuming that most ZH events are reconstructed in the 0-lepton channel for p_T^V >250 GeV (neglecting the 2-lepton contribution). The expected significance for $W \to \ell\nu H \to b\bar{b} \geq 250$ is 1.41σ and for $Z(\ell\ell,\nu\nu)H \to b\bar{b}_{\geq 250}$ is 1.35σ.
Another difference between the two analyses is that the uncertainties in the *resolved* analysis are obtained from detailed studies, not completed yet for the *merged* analysis. Additionally, the results that we could expect from the *resolved* analysis using the full Run 2 dataset (139.0 fb^{-1}) will likely include further optimisations in the data analysis, not included in this comparison.

The expected post-fit significances for the *merged* analysis are reported in Table E.1, together with the Asimov fit results already presented in the main body of this thesis (Table 10.1). The post-fit significances are slightly higher with respect to the significances from the fit to Asimov data.

Channel	pre-fit expected significance	post-fit expected significance
0-lepton	2.04σ	2.05σ
1-lepton	1.94σ	2.12σ
2-lepton	1.26σ	1.07σ
combined	3.10σ	3.12σ

Table E.1: Expected significance from the fit to Asimov data (middle column) and post-fit expected significance (right column) for each lepton channel in the *merged* analysis using the full Run 2 dataset (139.0 fb^{-1}).

The post-fit significances are then presented in Table E.2 side by side to the *resolved* expected results rescaled by a factor $\sqrt{139.0/79.8} \simeq 1.32$. In both cases the expected significances are higher ($+\sim 10/20\%$) in the *merged* analysis.

Channel	*resolved* expected significance	*merged* expected significance
$ZH_{\ >250}$ / 0-lepton	1.86σ	2.05σ
$WH_{\ >250}$ / 1-lepton	1.78σ	2.12σ

Table E.2: Expected significances for $W \to \ell\nu H \to b\bar{b} \geq 250$ and for $Z(\ell\ell, \nu\nu)H \to b\bar{b}_{\geq 250}$ in the *resolved* analysis [8] (middle column) using the data collected up to 2017 (79.8 fb^{-1}) rescaled by a factor $\sqrt{139.0/79.8} \simeq 1.32$. Expected significances for the *merged* analysis, using the data collected up to 2018 (139.0 fb^{-1}) for the 0-lepton and 1-lepton channels (right column).

It should be reminded that the presented comparison includes several approximations. However the results are encouraging, and indicate that the *merged* analysis could lead to similar significances with respect to the *resolved* analysis ones.

Appendix F

Pull plots for the *merged* analysis

One of the key steps to validate the fit procedure is the scrutiny of the nuisance parameter pulls. In this appendix, the pull plots for all the systematic uncertainties considered in the merged analysis are shown.

The pull plots shown in this appendix have been derived for the simultaneous fit of the three lepton channels. The pulls are shown both for a *conditional fit* to data with $\mu = 1$ and for the *Asimov fit*. In the second case the pull values are by definition 1, and the only relevant information is the constraints of the pull uncertainties.
The NP pulls for the normalisation uncertainties are shown in Figure F.1 on the left. Wbb_{L0} is a NP describing a 5% uncertainty on the $W \to b\bar{b}$ normalisation

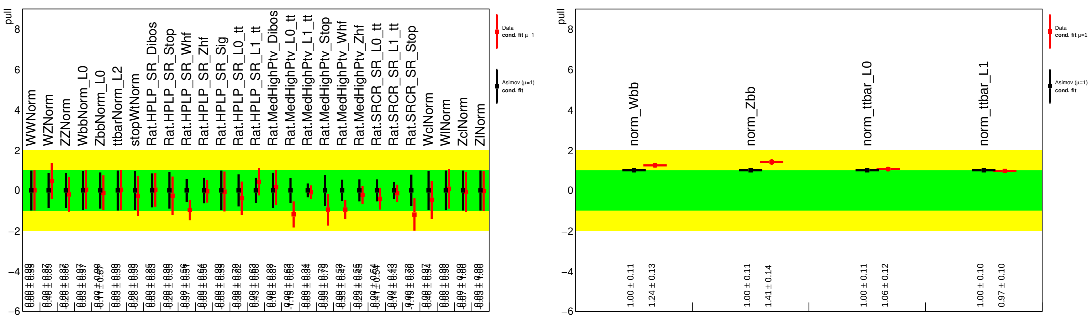

Figure F.1: Nuisance parameter pulls and the free parameter scale factors corresponding to a conditional fit ($\mu = 1$) performed to Run 2 data (red) and a conditional fit to Asimov data (black), fitting simultaneously the three leptonic channels.

in the 0-lepton channel. This systematic uncertainty accounts for the differences of the $W \to b\bar{b}$ normalisation in the 0-lepton and 1-lepton channels. Similarly

Zbb_{L0} is a 7% uncertainty on the ratio of the $Z \to b\bar{b}$ normalisation in 0-lepton and 2-lepton. The uncertainties named HPLP are 20% extrapolation uncertainties between the high purity and low purity signal regions. The high purity (HP) signal region is the one with 0 additional jets, and it is richer in signal. The low purity (LP) signal region has one or more additional jets. These HP/LP NPs accounts for the differences that could be present among the modelling of each process in the two categories. They are applied to the $t\bar{t}$, W+HF, Z+HF, diboson and single top processes. Similarly the MedHighPtv extrapolation uncertainties are 20% uncertainties that take into account the differences between the medium energy (250 GeV $< p_{\mathrm{T}}^{V} <$ 400 GeV) and high energy (p_{T}^{V} >400 GeV) categories. They are applied to the $t\bar{t}$, W+HF, Z+HF, diboson and single top processes. Finally, RatioSRCR are 20% extrapolation uncertainties taking into account the difference in the modelling between the SR and the CR for the $t\bar{t}$ and single top processes. No strong pulls are observed for these uncertainties. Some components of the Ratio uncertainty between the medium energy and the high energy channels are constrained, together with some component of the ratio uncertainties between the SR and the CR. As mentioned in Section 8.2.3 the modelling uncertainties included in the *merged* analysis fit are not the results of detailed modelling studies, that will be finalised in the next months. They are instead evaluated from previous studies performed with the *resolved* analysis. These uncertainties will be further studied in the next month, substituting the preliminary numbers with the results of the studies in the *merged* analysis.

The remaining uncertainties on Figure F.1, left, are normalisation uncertainties on the minor background processes. The value of these uncertainties, obtained from the most updated cross section uncertainties computations, are shown in Table F.1a.

The normalisations of the main background processes, W+HF, Z+HF and $t\bar{t}$, are instead simply determined from the fit. No auxiliary measurement is used to infer these normalisation values. The fitted value of the cross section normalisation for these processes is shown in Figure F.1 on the right. The value of the $t\bar{t}$ normalisation measured separately in the 0-lepton and 1-lepton channels, as both have a dedicated control region. The normalisation factors for the main background processes are also reported on Table F.1b, together with the measured uncertainty in the conditional fit with $\mu = 1$.

The pull plots for the small-R jet uncertainties and the flavour tagging uncertainties are shown in Figure F.2. The uncertainties on the small-R jets are shown on the left. They are uncertainties on the JES (jet energy scale) and JER (jet energy resolution) of the small-R calo jets. No unexpected behavior is observed for these uncertainties. As the analysis is mainly based on the selection of a large-R jet, the small-R jet uncertainties are expected to have a minor impact (mainly due to the additional jet categorisation and to the contribution to the E_{T}^{miss}).

Process	Normalisation syst. uncertainty
Single top+s	4.6%
Single top+t	4.4%
Single top+Wt	6.2%
WW	25.0%
ZZ	20.0%
WZ	26.0%
Wl	32.0%
Zl	18.0%
Wcl	37.0%
Zcl	23.0%

(a)

Process	Norm. factor
W+HF	1.25 ± 0.13
Z+HF	1.41 ± 0.14
$t\bar{t}_{L0}$	1.06 ± 0.12
$t\bar{t}_{L1}$	0.97 ± 0.10

(b)

Table F.1: (a) Systematic uncertainties on the cross section normalisation for the minor background processes.
(b) Scale factors applied to the nominal normalisations of the $t\bar{t}$, W+HF, Z+HF processes, as obtained from the conditional fit to the data with $\mu = 1$. The errors include the statistical and systematic uncertainties.

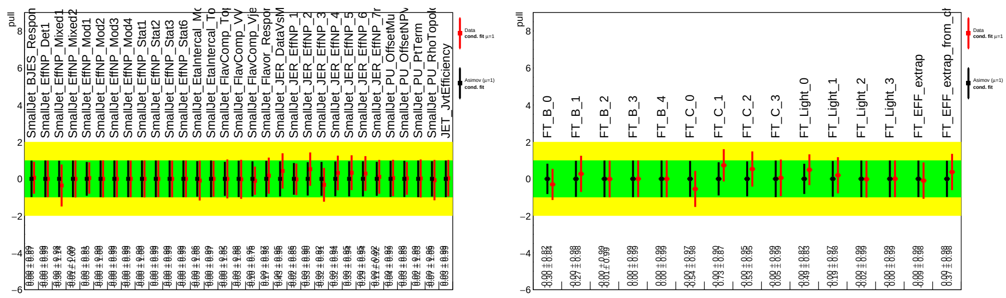

Figure F.2: Nuisance parameter pulls, for the jet uncertainties and the flavour tagging uncertainties, corresponding to a conditional fit ($\mu = 1$) performed to Run 2 data (red) and a conditional fit to Asimov data (black), fitting simultaneously the three leptonic channels.

The uncertainties shown in the plot on the right in Figure F.2 are the flavor tagging uncertainties on the track jets depicted in Section 8.2.1. Some of these uncertainties are shifted from the central value, but always for less than 1σ. A non negligible impact of these uncertainty is expected, as b-tagged jets are used to define the SRs and CRs.
The pull plots for the lepton, luminosity and E_{T}^{miss} uncertainties are shown in Figure F.3. None of the shown NPs is particularly pulled or constrained. The

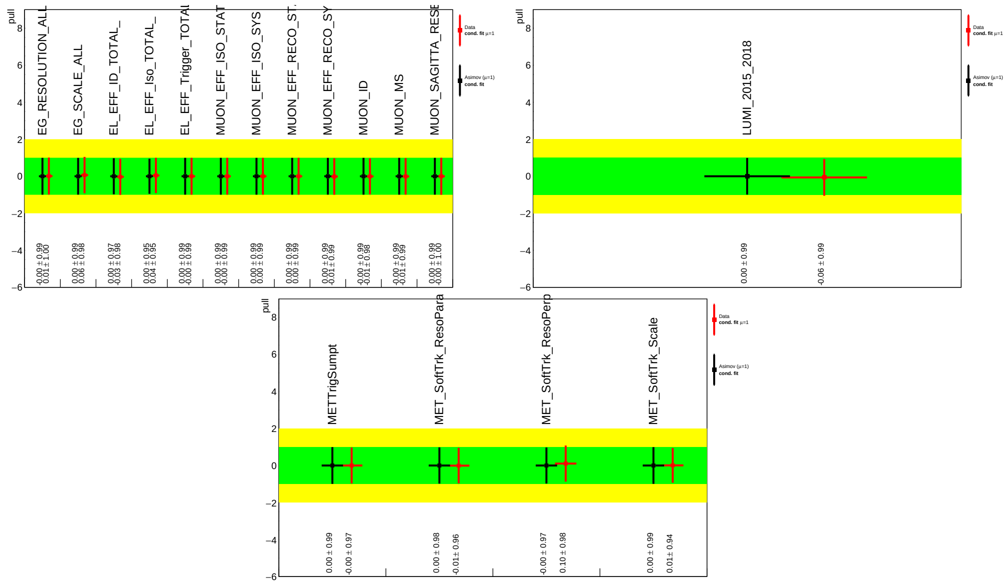

Figure F.3: Nuisance parameter pulls, for the leptons, E_{T}^{miss} and luminosity uncertainties, corresponding to a conditional fit ($\mu = 1$) performed to Run 2 data (red) and a conditional fit to Asimov data (black), fitting simultaneously the three leptonic channels.

pull plots for the lepton uncertainties are shown in the plot on the left. The electron uncertainties, named *EL* include the uncertainties on the reconstruction, identification, trigger and isolation. The uncertainties on the electron calibration are named *EG_SCALE_ALL*, which involves scale variations, and *EG_RESOLUTION_ALL*, which involves resolution variations. The muon uncertainties are named *MUON* and take into account the uncertainties on the isolation, reconstruction and identification efficiency. The NP linked to the luminosity uncertainty is shown in the plot on the right. The E_{T}^{miss} uncertainties are shown on the bottom plot. *METTrigSumPt* accounts for the kinematic dependence of the E_{T}^{miss} trigger efficiency on the offline scalar sum of all final state jets within the event, known as *SumPt*. The *SoftTrk* terms account for the propagation of the uncertainties on the calo-jets and track-jets to the E_{T}^{miss}.
Finally, the pulls on the statistical uncertainties are shown in Figure F.4 for the 2-lepton channel in the category with p_{T}^{V} >400 GeV. The NPs represent the sta-

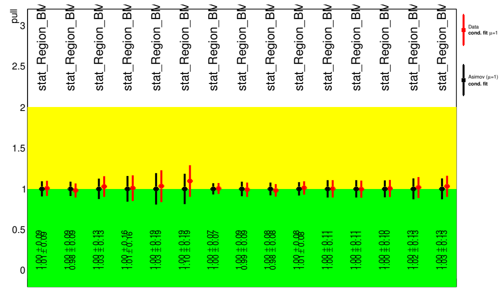

Figure F.4: Nuisance parameter pulls, for the statistical uncertainties, corresponding to a conditional fit ($\mu = 1$) performed to Run 2 data (red) and a conditional fit to Asimov data (black), fitting simultaneously the three leptonic channels. The uncertainties are shown for the 2-lepton channels for the category with p_{T}^{V} >400 GeV.

tistical uncertainty in single bins of one m_{J} histogram. These plots can be used to check that the uncertainty due to the MC statistics is not too large in single bins, helping in the binning optimisation and eventually in choosing to increase the MC statistics, by producing larger samples. From the plots it is observed that the 2-lepton sample could benefit for larger MC samples in the high energy region. Similar plots have been produced and scrutinized for the other SRs and CRs.

Bibliography

[1] Mark Thomson. *Modern particle physics*. New York: Cambridge University Press, 2013. ISBN: 9781107034266. URL: http://www-spires.fnal.gov/spires/find/books/www?cl=QC793.2.T46::2013.

[2] ATLAS Collaborationn. "Observation of a new particle in the search for the Standard Model Higgs boson with the ATLAS detector at the LHC". In: *Phys. Lett.* B716 (2012), pp. 1–29. DOI: 10.1016/j.physletb.2012.08.020. arXiv: 1207.7214 [hep-ex].

[3] The CMS Collaboration. "Observation of a New Boson at a Mass of 125 GeV with the CMS Experiment at the LHC". In: *Phys. Lett.* B716 (2012), pp. 30–61. DOI: 10.1016/j.physletb.2012.08.021. arXiv: 1207.7235 [hep-ex].

[4] Lyndon Evans and Philip Bryant. "LHC Machine". In: *JINST* 3 (2008), S08001. DOI: 10.1088/1748-0221/3/08/S08001.

[5] Gianfranco Bertone, Dan Hooper, and Joseph Silk. "Particle dark matter: Evidence, candidates and constraints". In: *Phys. Rept.* 405 (2005), pp. 279–390. DOI: 10.1016/j.physrep.2004.08.031. arXiv: hep-ph/0404175 [hep-ph].

[6] LHC Higgs Cross Section Working Group. *SM Higgs Branching Ratios and Total Decay Widths*. URL: https://twiki.cern.ch/twiki/bin/view/LHCPhysics/CERNYellowReportPageBR.

[7] LHC Higgs Cross Section Working Group. *Picture Gallery*. URL: https://twiki.cern.ch/twiki/bin/view/LHCPhysics/LHCHXSWGCrossSectionsFigures.

[8] ATLAS Collaboration. "Observation of $H \to b\bar{b}$ decays and VH production with the ATLAS detector". In: *Phys. Lett.* B786 (2018), pp. 59–86. DOI: 10.1016/j.physletb.2018.09.013. arXiv: 1808.08238 [hep-ex].

[9] ATLAS Collaboration. "Combination of searches for heavy resonances decaying into bosonic and leptonic final states using 36 fb^{-1} of proton-proton collision data at $\sqrt{s} = 13$ TeV with the ATLAS detector". In: *Phys. Rev.* D98 (2018), p. 052008. DOI: 10.1103/PhysRevD.98.052008. arXiv: 1808.02380 [hep-ex].

[10] Anke Biekötter et al. "Vices and virtues of Higgs effective field theories atlarge energy". In: *Phys. Rev.* D91 (2015), p. 055029. DOI: 10.1103/PhysRevD.91.055029. arXiv: 1406.7320 [hep-ph].

[11] ATLAS Collaboration. *Evaluation of theoretical uncertainties for simplified template cross section measurements of V-associated production of the Higgs boson*. Tech. rep. ATL-PHYS-PUB-2018-035. Geneva: CERN, Nov. 2018. URL: http://cds.cern.ch/record/2649241.

[12] P. Aurenche. "The Standard model of particle physics". In: *Cinquieme Seminaire Rhodanien, Symetries en Physique Dolomieu, France, March 17-21, 1997*. 1997. arXiv: hep-ph/9712342 [hep-ph].

[13] Peter W. Higgs. "Broken symmetries, massless particles and gauge fields". In: *Phys. Lett.* 12 (1964), pp. 132–133. DOI: 10.1016/0031-9163(64)91136-9.

[14] Peter W. Higgs. "Broken Symmetries and the Masses of Gauge Bosons". In: *Phys. Rev. Lett.* 13 (1964). [,160(1964)], pp. 508–509. DOI: 10.1103/PhysRevLett.13.508.

[15] F. Englert and R. Brout. "Broken Symmetry and the Mass of Gauge Vector Mesons". In: *Phys. Rev. Lett.* 13 (1964). [,157(1964)], pp. 321–323. DOI: 10.1103/PhysRevLett.13.321.

[16] ATLAS Collaboration. "Evidence for the $H \to b\bar{b}$ decay with the ATLAS detector". In: *JHEP* 12 (2017), p. 024. DOI: 10.1007/JHEP12(2017)024. arXiv: 1708.03299 [hep-ex].

[17] CMS Collaboration. "Evidence for the Higgs boson decay to a bottom quark–antiquark pair". In: *Phys. Lett.* B780 (2018), pp. 501–532. DOI: 10.1016/j.physletb.2018.02.050. arXiv: 1709.07497 [hep-ex].

[18] CMS Collaboration. "Observation of Higgs Boson Decay to Bottom Quarks". In: *Phys. Rev. Lett.* 121 (12 Sept. 2018), p. 121801. DOI: 10.1103/PhysRevLett.121.121801. URL: https://link.aps.org/doi/10.1103/PhysRevLett.121.121801.

[19] J. R. Andersen et al. "Les Houches 2015: Physics at TeV Colliders Standard Model Working Group Report". In: *9th Les Houches Workshop on Physics at TeV Colliders (PhysTeV 2015) Les Houches, France, June 1-19, 2015*. 2016. arXiv: 1605.04692 [hep-ph]. URL: http://lss.fnal.gov/archive/2016/conf/fermilab-conf-16-175-ppd-t.pdf.

[20] LHC Higgs Cross Section Working Group. "Handbook of LHC Higgs Cross Sections: 4. Deciphering the Nature of the Higgs Sector". In: *CERN Yellow Reports* (2016). DOI: 10.23731/CYRM-2017-002. arXiv: 1610.07922 [hep-ph].

[21] ATLAS Collaboration. "Measurement of VH, H $\rightarrow$ b$\bar{\text{b}}$ production as a function of the vector-boson transverse momentum in 13 TeV pp collisions with the ATLAS detector". In: *JHEP* 05 (2019), p. 141. DOI: 10.1007/JHEP05(2019)141. arXiv: 1903.04618 [hep-ex].

[22] G. F. Giudice et al. "The Strongly-Interacting Light Higgs". In: *JHEP* 06 (2007), p. 045. DOI: 10.1088/1126-6708/2007/06/045. arXiv: hep-ph/0703164 [hep-ph].

[23] ATLAS Collaboration. *Constraints on an effective Lagrangian from the combined $H \rightarrow ZZ^* \rightarrow 4\ell$ and $H \rightarrow \gamma\gamma$ channels using 36.1 fb^{-1} of $\sqrt{s}$ = 13 TeV pp collision data collected with the ATLAS detector*. Tech. rep. ATL-PHYS-PUB-2017-018. Geneva: CERN, Nov. 2017. URL: https://cds.cern.ch/record/2293084.

[24] Adam Alloul, Benjamin Fuks, and Verónica Sanz. "Phenomenology of the Higgs Effective Lagrangian via FEYNRULES". In: *JHEP* 04 (2014), p. 110. DOI: 10.1007/JHEP04(2014)110. arXiv: 1310.5150 [hep-ph].

[25] Chris Hays, Veronica Sanz Gonzalez, and Gabija Zemaityte. *Constraining EFT parameters using simplified template cross sections*. Tech. rep. LHCHXSWG-2019-004. Geneva: CERN, May 2019. URL: http://cds.cern.ch/record/2673969.

[26] John Ellis, Verónica Sanz, and Tevong You. "Complete Higgs sector constraints on dimension-6 operators". In: *Journal of High Energy Physics* 2014.7 (2014). ISSN: 1029-8479. DOI: 10.1007/jhep07(2014)036. URL: http://dx.doi.org/10.1007/JHEP07(2014)036.

[27] Christophe Grojean et al. "Renormalization Group Scaling of Higgs Operators and Γ(h -> γ γ)". In: *JHEP* 04 (2013), p. 016. DOI: 10.1007/JHEP04(2013)016. arXiv: 1301.2588 [hep-ph].

[28] John Ellis et al. "Updated Global SMEFT Fit to Higgs, Diboson and Electroweak Data". In: *JHEP* 06 (2018), p. 146. DOI: 10.1007/JHEP06(2018)146. arXiv: 1803.03252 [hep-ph].

[29] ATLAS Collaboration. "Measurement of the Higgs boson coupling properties in the $H \rightarrow ZZ^* \rightarrow 4\ell$ decay channel at $\sqrt{s} = 13$ TeV with the ATLAS detector". In: *JHEP* 03 (2018), p. 095. DOI: 10.1007/JHEP03(2018)095. arXiv: 1712.02304 [hep-ex].

[30] ATLAS Collaboration. "Measurements of Higgs boson properties in the diphoton decay channel with 36 fb^{-1} of pp collision data at $\sqrt{s} = 13$ TeV with the ATLAS detector". In: *Phys. Rev.* D98 (2018), p. 052005. DOI: 10.1103/PhysRevD.98.052005. arXiv: 1802.04146 [hep-ex].

[31] Philippe Mouche. *Overall view of the LHC*. General Photo. June 2014. URL: http://cds.cern.ch/record/1708847.

[32] ATLAS Collaboration. "The ATLAS Experiment at the CERN Large Hadron Collider". In: *JINST* 3 (2008), S08003. DOI: 10.1088/1748-0221/3/08/S08003.

[33] CMS Collaboration. "The CMS Experiment at the CERN LHC". In: *JINST* 3 (2008), S08004. DOI: 10.1088/1748-0221/3/08/S08004.

[34] LHCb collaboration. "The LHCb Detector at the LHC". In: *JINST* 3 (2008), S08005. DOI: 10.1088/1748-0221/3/08/S08005.

[35] ALICE collaboration. "The ALICE experiment at the CERN LHC". In: *JINST* 3 (2008), S08002. DOI: 10.1088/1748-0221/3/08/S08002.

[36] ATLAS Collaboration. *Run II luminosity public plots*. URL: https://twiki.cern.ch/twiki/bin/view/AtlasPublic/LuminosityPublicResultsRun2.

[37] ATLAS Collaboration. *Run I luminosity public plots*. URL: https://twiki.cern.ch/twiki/bin/view/AtlasPublic/LuminosityPublicResults.

[38] Simon White et al. "First Luminosity Scans in the LHC". In: *Conf. Proc.* C100523 (2010), MOPEC014.

[39] S van der Meer. *Calibration of the effective beam height in the ISR*. Tech. rep. CERN-ISR-PO-68-31. ISR-PO-68-31. Geneva: CERN, 1968. URL: https://cds.cern.ch/record/296752.

[40] ATLAS Collaboration. "Luminosity determination in pp collisions at $\sqrt{s} = 8$ TeV using the ATLAS detector at the LHC". In: *Eur. Phys. J.* C76.12 (2016), p. 653. DOI: 10.1140/epjc/s10052-016-4466-1. arXiv: 1608.03953 [hep-ex].

[41] G. Avoni et al. "The new LUCID-2 detector for luminosity measurement and monitoring in ATLAS". In: *JINST* 13.07 (2018), P07017. DOI: 10.1088/1748-0221/13/07/P07017.

[42] Dan Green, ed. *At the leading edge*. Singapore: World Scientific, 2010. ISBN: 9789814304672. URL: http://www.worldscibooks.com/physics/7349.html.

[43] ATLAS Collaboration. "ATLAS magnet system: Technical design report". In: (1997).

[44] "ATLAS inner detector: Technical design report. Vol. 1". In: (1997).

[45] ATLAS Collaboration. "ATLAS Insertable B-Layer Technical Design Report". In: (2010). URL: http://cds.cern.ch/record/1291633.

[46] ATLAS Collaboration. "The ATLAS Inner Detector commissioning and calibration". In: *Eur. Phys. J.* C70 (2010), pp. 787–821. DOI: 10.1140/epjc/s10052-010-1366-7. arXiv: 1004.5293 [physics.ins-det].

[47] ATLAS Collaboration. *Impact Parameter Resolution Plots*. URL: https://atlas.web.cern.ch/Atlas/GROUPS/PHYSICS/PLOTS/IDTR-2015-007.

[48] ATLAS Collaboration. *Basic Inner Detector Tracking Performance Plots at 13 TeV*. URL: https://atlas.web.cern.ch/Atlas/GROUPS/PHYSICS/PLOTS/IDTR-2015-001.

[49] Karolos Potamianos. "The upgraded Pixel detector and the commissioning of the Inner Detector tracking of the ATLAS experiment for Run-2 at the Large Hadron Collider". In: *PoS* EPS-HEP2015 (2015), p. 261. arXiv: 1608.07850 [physics.ins-det].

[50] ATLAS Collaboration. "Observation of a new particle in the search for the Standard Model Higgs boson with the ATLAS detector at the LHC". In: *Phys. Lett.* B716 (2012), pp. 1–29. DOI: 10.1016/j.physletb.2012.08.020. arXiv: 1207.7214 [hep-ex].

[51] Christian W. Fabjan and Fabiola Gianotti. "Calorimetry for particle physics". In: *Rev. Mod. Phys.* 75 (4 Oct. 2003), pp. 1243–1286. DOI: 10.1103/RevModPhys.75.1243. URL: https://link.aps.org/doi/10.1103/RevModPhys.75.1243.

[52] A. Henriques. "The ATLAS tile calorimeter". In: *Proceedings, 4th International Conference on Advancements in Nuclear Instrumentation Measurement Methods and their Applications (ANIMMA 2015): Lisbon, Portugal, April 20-24, 2015*. 2015, p. 7465554. DOI: 10.1109/ANIMMA.2015.7465554.

[53] ATLAS Collaboration. "Measurement of the photon identification efficiencies with the ATLAS detector using LHC Run 2 data collected in 2015 and 2016". In: *Submitted to: Eur. Phys. J.* (2018). arXiv: 1810.05087 [hep-ex].

[54] ATLAS Collaboration. "Studies of the performance of the ATLAS detector using cosmic-ray muons". In: *Eur. Phys. J.* C71 (2011), p. 1593. DOI: 10.1140/epjc/s10052-011-1593-6. arXiv: 1011.6665 [physics.ins-det].

[55] ATLAS Collaboration. "Muon reconstruction performance of the ATLAS detector in proton–proton collision data at $\sqrt{s}$ =13 TeV". In: *Eur. Phys. J.* C76.5 (2016), p. 292. DOI: 10.1140/epjc/s10052-016-4120-y. arXiv: 1603.05598 [hep-ex].

[56] ATLAS Collaboration. "Measurement of the Inelastic Proton-Proton Cross Section at $\sqrt{s} = 13$ TeV with the ATLAS Detector at the LHC". In: *Phys. Rev. Lett.* 117.18 (2016), p. 182002. DOI: 10.1103/PhysRevLett.117.182002. arXiv: 1606.02625 [hep-ex].

[57] ATLAS Collaboration. "Technical Design Report for the Phase-I Upgrade of the ATLAS TDAQ System". In: (2013).

[58] A. Annovi et al. "Design of a hardware track finder (Fast TracKer) for the ATLAS trigger". In: *JINST* 9.01 (2014), p. C01045. DOI: 10.1088/1748-0221/9/01/C01045.

[59] ATLAS Collaboration. *FTK public results*. URL: https://twiki.cern.ch/twiki/bin/view/AtlasPublic/FTKPublicResults.

[60] ATLAS Collaboration. "Observation of $H \to b\bar{b}$ decays and VH production with the ATLAS detector. Figure, Tables and Auxiliary material." In: (2018). URL: https://atlas.web.cern.ch/Atlas/GROUPS/PHYSICS/PAPERS/HIGG-2018-04/.

[61] *Trigger Menu in 2017*. Tech. rep. ATL-DAQ-PUB-2018-002. Geneva: CERN, June 2018. URL: https://cds.cern.ch/record/2625986.

[62] *Trigger Menu in 2016*. Tech. rep. ATL-DAQ-PUB-2017-001. Geneva: CERN, Jan. 2017. URL: https://cds.cern.ch/record/2242069.

[63] ATLAS Collaboration. "Performance of the ATLAS Trigger System in 2015". In: *Eur. Phys. J.* C77.5 (2017), p. 317. DOI: 10.1140/epjc/s10052-017-4852-3. arXiv: 1611.09661 [hep-ex].

[64] ATLAS Collaboration. *Pile-up Suppression in Missing Transverse Momentum Reconstruction in the ATLAS Experiment in Proton-Proton Collisions at sqrts = 8 TeV*. Tech. rep. ATLAS-CONF-2014-019. Geneva: CERN, May 2014. URL: http://cds.cern.ch/record/1702055.

[65] *Simulations*. Tech. rep. SLAC. URL: https://theory.slac.stanford.edu/our-research/simulations.

[66] Zachary Marshall. "Simulation of Pile-up in the ATLAS Experiment". In: *J. Phys. Conf. Ser.* 513 (2014), p. 022024. DOI: 10.1088/1742-6596/513/2/022024.

[67] GEANT4 collabortion. "GEANT4: A Simulation toolkit". In: *Nucl. Instrum. Meth.* A506 (2003), pp. 250–303. DOI: 10.1016/S0168-9002(03)01368-8.

[68] ATLAS Collaboration. "The ATLAS Simulation Infrastructure". In: *Eur. Phys. J.* C70 (2010), pp. 823–874. DOI: 10.1140/epjc/s10052-010-1429-9. arXiv: 1005.4568 [physics.ins-det].

[69] Gionata Luisoni et al. "$HW^{\pm}$/HZ + 0 and 1 jet at NLO with the POWHEG BOX interfaced to GoSam and their merging within MiNLO". In: *JHEP* 10 (2013), p. 083. DOI: 10.1007/JHEP10(2013)083. arXiv: 1306.2542 [hep-ph].

[70] Torbjörn Sjöstrand et al. "An Introduction to PYTHIA 8.2". In: *Comput. Phys. Commun.* 191 (2015), pp. 159–177. DOI: 10.1016/j.cpc.2015.01.024. arXiv: 1410.3012 [hep-ph].

[71] Richard D. Ball et al. "Parton distributions for the LHC Run II". In: *JHEP* 04 (2015), p. 040. DOI: 10.1007/JHEP04(2015)040. arXiv: 1410.8849 [hep-ph].

[72] LHC Higgs Cross Section Working Group. *SM Higgs production cross sections at 13 TeV*. URL: https://twiki.cern.ch/twiki/bin/view/LHCPhysics/CERNYellowReportPageAt13TeV.

[73] Oliver Brein, Abdelhak Djouadi, and Robert Harlander. "NNLO QCD corrections to the Higgs-strahlung processes at hadron colliders". In: *Phys. Lett.* B579 (2004), pp. 149–156. DOI: 10.1016/j.physletb.2003.10.112. arXiv: hep-ph/0307206 [hep-ph].

[74] Oliver Brein et al. "Top-Quark Mediated Effects in Hadronic Higgs-Strahlung". In: *Eur. Phys. J.* C72 (2012), p. 1868. DOI: 10.1140/epjc/s10052-012-1868-6. arXiv: 1111.0761 [hep-ph].

[75] Ansgar Denner et al. "Electroweak corrections to Higgs-strahlung off W/Z bosons at the Tevatron and the LHC with HAWK". In: *JHEP* 03 (2012), p. 075. DOI: 10.1007/JHEP03(2012)075. arXiv: 1112.5142 [hep-ph].

[76] ATLAS Collaboration. *Monte Carlo Generators for the Production of a W or Z/γ^* Boson in Association with Jets at ATLAS in Run 2*. Tech. rep. ATL-PHYS-PUB-2016-003. Geneva: CERN, Jan. 2016. URL: https://cds.cern.ch/record/2120133.

[77] Richard D. Ball et al. "Parton distributions with LHC data". In: *Nucl. Phys.* B867 (2013), pp. 244–289. DOI: 10.1016/j.nuclphysb.2012.10.003. arXiv: 1207.1303 [hep-ph].

[78] J Butterworth et al. *Single Boson and Diboson Production Cross Sections in pp Collisions at sqrts=7 TeV*. Tech. rep. ATL-COM-PHYS-2010-695. Geneva: CERN, Aug. 2010. URL: https://cds.cern.ch/record/1287902.

[79] Keith Hamilton, Peter Richardson, and Jon Tully. "A Positive-Weight Next-to-Leading Order Monte Carlo Simulation for Higgs Boson Production". In: *JHEP* 04 (2009), p. 116. DOI: 10.1088/1126-6708/2009/04/116. arXiv: 0903.4345 [hep-ph].

[80] M. Beneke et al. "Hadronic top-quark pair production with NNLL threshold resummation". In: *Nucl. Phys.* B855 (2012), pp. 695–741. DOI: 10.1016/j.nuclphysb.2011.10.021. arXiv: 1109.1536 [hep-ph].

[81] Federico Demartin et al. "tWH associated production at the LHC". In: *Eur. Phys. J.* C77.1 (2017), p. 34. DOI: 10.1140/epjc/s10052-017-4601-7. arXiv: 1607.05862 [hep-ph].

[82] ATLAS Collaboration. *Multi-Boson Simulation for 13 TeV ATLAS Analyses*. Tech. rep. ATL-PHYS-PUB-2017-005. Geneva: CERN, May 2017. URL: https://cds.cern.ch/record/2261933.

[83] ATLAS Collaboration. "Reconstruction of primary vertices at the ATLAS experiment in Run 1 proton–proton collisions at the LHC". In: *Eur. Phys. J.* C77.5 (2017), p. 332. DOI: 10.1140/epjc/s10052-017-4887-5. arXiv: 1611.10235 [physics.ins-det].

[84] ATLAS Collaboration. *Vertex Reconstruction Performance of the ATLAS Detector at "$\sqrt{s} = 13$ TeV"*. Tech. rep. ATL-PHYS-PUB-2015-026. Geneva: CERN, July 2015. URL: http://cds.cern.ch/record/2037717.

[85] ATLAS Collaboration. *Performance of the ATLAS Inner Detector Track and Vertex Reconstruction in the High Pile-Up LHC Environment*. Tech. rep. ATLAS-CONF-2012-042. Geneva: CERN, Mar. 2012. URL: http://cds.cern.ch/record/1435196.

[86] ATLAS Collaboration. *Electron and photon reconstruction and performance in ATLAS using a dynamical, topological cell clustering-based approach*. Tech. rep. ATL-PHYS-PUB-2017-022. Geneva: CERN, Dec. 2017. URL: https://cds.cern.ch/record/2298955.

[87] ATLAS Collaboration. "Electron and photon energy calibration with the ATLAS detector using 2015–2016 LHC proton-proton collision data". In: *JINST* 14.03 (2019), P03017. DOI: 10.1088/1748-0221/14/03/P03017. arXiv: 1812.03848 [hep-ex].

[88] ATLAS Collaboration. "Electron reconstruction and identification in the ATLAS experiment using the 2015 and 2016 LHC proton-proton collision data at $\sqrt{s} = 13$ TeV". In: *Submitted to: Eur. Phys. J.* (2019). arXiv: 1902.04655 [physics.ins-det].

[89] W. Lampl et al. "Calorimeter clustering algorithms: Description and performance". In: (2008).

[90] ATLAS Collaboration. "Electron efficiency measurements with the ATLAS detector using 2012 LHC proton–proton collision data". In: *Eur. Phys. J.* C77.3 (2017), p. 195. DOI: 10.1140/epjc/s10052-017-4756-2. arXiv: 1612.01456 [hep-ex].

[91] ATLAS Collaboration. "Measurement of the muon reconstruction performance of the ATLAS detector using 2011 and 2012 LHC proton–proton collision data". In: *Eur. Phys. J.* C74.11 (2014), p. 3130. DOI: 10.1140/epjc/s10052-014-3130-x. arXiv: 1407.3935 [hep-ex].

[92] ATLAS Collaboration. *Electron efficiency measurements in 2017 data and electron identification discriminating variables from 2016 data*. URL: https://atlas.web.cern.ch/Atlas/GROUPS/PHYSICS/PLOTS/EGAM-2018-002/index.html.

[93] ATLAS Collaboration. "Electron efficiency measurements with the ATLAS detector using the 2015 LHC proton-proton collision data". In: (2016).

[94] Johannes Josef Junggeburth and Nicolas Maximilian Koehler. *Muon reconstruction efficiency on full 2018 pp data set evaluated using $Z \to \mu\mu$ events*. Tech. rep. ATL-COM-PHYS-2018-1624. Geneva: CERN, Nov. 2018. URL: https://cds.cern.ch/record/2648573.

[95] W Lampl et al. *Calorimeter Clustering Algorithms: Description and Performance*. Tech. rep. ATL-LARG-PUB-2008-002. ATL-COM-LARG-2008-003. Geneva: CERN, Apr. 2008. URL: https://cds.cern.ch/record/1099735.

[96] ATLAS Collaboration. "Topological cell clustering in the ATLAS calorimeters and its performance in LHC Run 1". In: *Eur. Phys. J.* C77 (2017), p. 490. DOI: 10.1140/epjc/s10052-017-5004-5. arXiv: 1603.02934 [hep-ex].

[97] ATLAS Collaboration. *Selection of jets produced in 13TeV proton-proton collisions with the ATLAS detector*. Tech. rep. ATLAS-CONF-2015-029. Geneva: CERN, July 2015. URL: https://cds.cern.ch/record/2037702.

[98] Matteo Cacciari, Gavin P. Salam, and Gregory Soyez. "The anti-k_t jet clustering algorithm". In: *JHEP* 04 (2008), p. 063. DOI: 10.1088/1126-6708/2008/04/063. arXiv: 0802.1189 [hep-ph].

[99] ATLAS Collaboration. *Jet Calibration and Systematic Uncertainties for Jets Reconstructed in the ATLAS Detector at $\sqrt{s} = 13$ TeV*. Tech. rep. ATL-PHYS-PUB-2015-015. Geneva: CERN, July 2015. URL: http://cds.cern.ch/record/2037613.

[100] ATLAS Collaboration. *Monte Carlo Calibration and Combination of In-situ Measurements of Jet Energy Scale, Jet Energy Resolution and Jet Mass in ATLAS*. Tech. rep. ATLAS-CONF-2015-037. Geneva: CERN, Aug. 2015. URL: https://cds.cern.ch/record/2044941.

[101] ATLAS Collaboration. "Jet energy scale measurements and their systematic uncertainties in proton-proton collisions at $\sqrt{s} = 13$ TeV with the ATLAS detector". In: *Phys. Rev.* D96.7 (2017), p. 072002. DOI: 10.1103/PhysRevD.96.072002. arXiv: 1703.09665 [hep-ex].

[102] ATLAS Collaboration. "Performance of pile-up mitigation techniques for jets in pp collisions at $\sqrt{s} = 8$ TeV using the ATLAS detector". In: *Eur. Phys. J.* C76.11 (2016), p. 581. DOI: 10.1140/epjc/s10052-016-4395-z. arXiv: 1510.03823 [hep-ex].

[103] ATLAS Collaboration. "Tagging and suppression of pileup jets". In: (2014).

[104] ATLAS Collaboration. *JVT Public Plots for ICHEP 2016.* Tech. rep. Geneva: CERN. URL: https://atlas.web.cern.ch/Atlas/GROUPS/PHYSICS/PLOTS/JETM-2016-011/.

[105] The ATLAS collaboration. "Data-driven determination of the energy scale and resolution of jets reconstructed in the ATLAS calorimeters using dijet and multijet events at $\sqrt{s} = 8\ TeV$". In: (2015).

[106] David Krohn, Jesse Thaler, and Lian-Tao Wang. "Jet Trimming". In: *JHEP* 02 (2010), p. 084. DOI: 10.1007/JHEP02(2010)084. arXiv: 0912.1342 [hep-ph].

[107] ATLAS Collaboration. "Performance of jet substructure techniques for large-R jets in proton-proton collisions at $\sqrt{s} = 7$ TeV using the ATLAS detector". In: *JHEP* 09 (2013), p. 076. DOI: 10.1007/JHEP09(2013)076. arXiv: 1306.4945 [hep-ex].

[108] ATLAS Collaboration. "In situ calibration of large-radius jet energy and mass in 13 TeV proton–proton collisions with the ATLAS detector". In: *Eur. Phys. J.* C79.2 (2019), p. 135. DOI: 10.1140/epjc/s10052-019-6632-8. arXiv: 1807.09477 [hep-ex].

[109] ATLAS Collaboration. "Jet mass and substructure of inclusive jets in $\sqrt{s} = 7$ TeV pp collisions with the ATLAS experiment". In: *JHEP* 05 (2012), p. 128. DOI: 10.1007/JHEP05(2012)128. arXiv: 1203.4606 [hep-ex].

[110] Nazar Bartosik. *B-tagging diagram.* Tech. rep. May 2016. URL: https://commons.wikimedia.org/wiki/File:B-tagging_diagram.png.

[111] ATLAS Collaboration. "Performance of b-Jet Identification in the ATLAS Experiment". In: *JINST* 11.04 (2016), P04008. DOI: 10.1088/1748-0221/11/04/P04008. arXiv: 1512.01094 [hep-ex].

[112] ATLAS Collaboration. *Optimisation and performance studies of the ATLAS b-tagging algorithms for the 2017-18 LHC run.* Tech. rep. ATL-PHYS-PUB-2017-013. Geneva: CERN, July 2017. URL: https://cds.cern.ch/record/2273281.

[113] ATLAS Collaboration. "ATLAS b-jet identification performance and efficiency measurement with $t\bar{t}$ events in pp collisions at $\sqrt{s} = 13$ TeV". In: (2019). arXiv: 1907.05120 [hep-ex].

[114] ATLAS Collaboration. *Flavor Tagging with Track Jets in Boosted Topologies with the ATLAS Detector*. Tech. rep. ATL-PHYS-PUB-2014-013. Geneva: CERN, Aug. 2014. URL: http://cds.cern.ch/record/1750681.

[115] ATLAS Collaboration. "Boosted Higgs ($\rightarrow b\bar{b}$) Boson Identification with the ATLAS Detector at $\sqrt{s} = 13$ TeV". In: (2016).

[116] David Krohn, Jesse Thaler, and Lian-Tao Wang. "Jets with Variable R". In: *JHEP* 06 (2009), p. 059. DOI: 10.1088/1126-6708/2009/06/059. arXiv: 0903.0392 [hep-ph].

[117] *Variable Radius, Exclusive-k_T, and Center-of-Mass Subjet Reconstruction for Higgs($\rightarrow b\bar{b}$) Tagging in ATLAS*. Tech. rep. ATL-PHYS-PUB-2017-010. Geneva: CERN, 2017. URL: https://cds.cern.ch/record/2268678.

[118] Matteo Cacciari and Gavin P. Salam. "Pileup subtraction using jet areas". In: *Phys. Lett.* B659 (2008), pp. 119–126. DOI: 10.1016/j.physletb.2007.09.077. arXiv: 0707.1378 [hep-ph].

[119] ATLAS Collaboration. "Performance of missing transverse momentum reconstruction with the ATLAS detector using proton-proton collisions at $\sqrt{s} =$ 13 TeV". In: *Eur. Phys. J.* C78.11 (2018), p. 903. DOI: 10.1140/epjc/s10052-018-6288-9. arXiv: 1802.08168 [hep-ex].

[120] Andreas Hocker et al. "TMVA - Toolkit for Multivariate Data Analysis". In: (2007). arXiv: physics/0703039 [physics.data-an].

[121] ATLAS Collaboration. "Search for the Standard Model Higgs boson produced in association with top quarks and decaying into $b\bar{b}$ in pp collisions at $\sqrt{s} = 8$ TeV with the ATLAS detector". In: *Eur. Phys. J.* C75.7 (2015), p. 349. DOI: 10.1140/epjc/s10052-015-3543-1. arXiv: 1503.05066 [hep-ex].

[122] Kyle Cranmer. "Practical Statistics for the LHC". In: *Proceedings, 2011 European School of High-Energy Physics (ESHEP 2011): Cheile Gradistei, Romania, September 7-20, 2011*. [,247(2015)]. 2015, pp. 267–308. DOI: 10.5170/CERN-2015-001.247,10.5170/CERN-2014-003.267. arXiv: 1503.07622 [physics.data-an].

[123] Roger J. Barlow and Christine Beeston. "Fitting using finite Monte Carlo samples". In: *Comput. Phys. Commun.* 77 (1993), pp. 219–228. DOI: 10.1016/0010-4655(93)90005-W.

[124] S. S. Wilks. "The Large-Sample Distribution of the Likelihood Ratio for Testing Composite Hypotheses". In: *Annals Math. Statist.* 9.1 (1938), pp. 60–62. DOI: 10.1214/aoms/1177732360.

[125] Glen Cowan et al. "Asymptotic formulae for likelihood-based tests of new physics". In: *Eur. Phys. J.* C71 (2011). [Erratum: Eur. Phys. J.C73,2501(2013)], p. 1554. DOI: 10.1140/epjc/s10052-011-1554-0,10.1140/epjc/s10052-013-2501-z. arXiv: 1007.1727 [physics.data-an].

[126] E. Gross. "Practical Statistics for High Energy Physics". In: *CERN Yellow Rep. School Proc.* 3 (2018), pp. 199–221. DOI: 10.23730/CYRSP-2018-003.199.

[127] ATLAS Collaboration. "Measurement of VH, H $\to$ b$\overline{\text{b}}$ production as a function of the vector-boson transverse momentum in 13 TeV pp collisions with the ATLAS detector, Auxiliary material". In: (2019). URL: http://atlas.web.cern.ch/Atlas/GROUPS/PHYSICS/PAPERS/HIGG-2018-50/#auxstuff.

[128] Ansgar Denner et al. "HAWK 2.0: A Monte Carlo program for Higgs production in vector-boson fusion and Higgs strahlung at hadron colliders". In: *Comput. Phys. Commun.* 195 (2015), pp. 161–171. DOI: 10.1016/j.cpc.2015.04.021. arXiv: 1412.5390 [hep-ph].

[129] Jon Butterworth et al. "PDF4LHC recommendations for LHC Run II". In: *J. Phys.* G43 (2016), p. 023001. DOI: 10.1088/0954-3899/43/2/023001. arXiv: 1510.03865 [hep-ph].

[130] J. R. Andersen et al. "Les Houches 2017: Physics at TeV Colliders Standard Model Working Group Report". In: *10th Les Houches Workshop on Physics at TeV Colliders (PhysTeV 2017) Les Houches, France, June 5-23, 2017*. 2018. arXiv: 1803.07977 [hep-ph]. URL: http://lss.fnal.gov/archive/2018/conf/fermilab-conf-18-122-cd-t.pdf.

[131] Iain W. Stewart and Frank J. Tackmann. "Theory Uncertainties for Higgs and Other Searches Using Jet Bins". In: *Phys. Rev.* D85 (2012), p. 034011. DOI: 10.1103/PhysRevD.85.034011. arXiv: 1107.2117 [hep-ph].

[132] LHC Higgs cross-section Working group. *LHC Higgs cross-section Working group main web page*. URL: https://twiki.cern.ch/twiki/bin/view/LHCPhysics/LHCHXSWG.

[133] ATLAS Collaboration. "Luminosity determination in pp collisions at $\sqrt{s}$ = 8 TeV using the ATLAS detector at the LHC". In: *Eur. Phys. J.* C76.12 (2016), p. 653. DOI: 10.1140/epjc/s10052-016-4466-1. arXiv: 1608.03953 [hep-ex].

[134] ATLAS Collaboration. "Luminosity determination in pp collisions at $\sqrt{s} = 13$ TeV using the ATLAS detector at the LHC". In: (2019).

[135] ATLAS Collaboration. "Measurement of the Inelastic Proton-Proton Cross Section at $\sqrt{s} = 13$ TeV with the ATLAS detector at the LHC". In: *Phys. Rev. Lett.* 117.18 (2016), p. 182002. DOI: 10.1103/PhysRevLett.117.182002. arXiv: 1606.02625 [hep-ex].

[136] ATLAS Collaboration. "Measurement of the Z/γ^* boson transverse momentum distribution in pp collisions at $\sqrt{s} = 7$ TeV with the ATLAS detector". In: *JHEP* 09 (2014), p. 145. DOI: 10.1007/JHEP09(2014)145. arXiv: 1406.3660 [hep-ex].

[137] ATLAS Collaboration. "Search for the bb decay of the Standard Model Higgs boson in associated W/ZH production with the ATLAS detector". In: (2013). URL: {https://arxiv.org/abs/1409.6212}.

[138] ATLAS Collaboration. "Search for the standard model Higgs boson produced in association with top quarks and decaying into a $b\bar{b}$ pair in pp collisions at $\sqrt{s} = 13$ TeV with the ATLAS detector". In: *Phys. Rev.* D97.7 (2018), p. 072016. DOI: 10.1103/PhysRevD.97.072016. arXiv: 1712.08895 [hep-ex].

[139] ATLAS Collaboration. "Search for the Standard Model Higgs boson produced by vector-boson fusion and decaying to bottom quarks in $\sqrt{s} = 8$ TeV pp collisions with the ATLAS detector". In: *JHEP* 11 (2016), p. 112. DOI: 10.1007/JHEP11(2016)112. arXiv: 1606.02181 [hep-ex].

[140] ATLAS Collaboration. "Search for Higgs bosons produced via vector-boson fusion and decaying into bottom quark pairs in $\sqrt{s} = 13$ TeV pp collisions with the ATLAS detector". In: *Phys. Rev.* D98.5 (2018), p. 052003. DOI: 10.1103/PhysRevD.98.052003. arXiv: 1807.08639 [hep-ex].

[141] S. Citraro et al. "Highly Parallelized Pattern Matching Hardware for Fast Tracking at Hadron Colliders". In: *IEEE Trans. Nucl. Sci.* 63.2 (2016), pp. 1147–1154. DOI: 10.1109/TNS.2016.2529718.

[142] A. Annovi et al. "AM06: the Associative Memory chip for the Fast TracKer in the upgraded ATLAS detector". In: *Journal of Instrumentation* 12.04 (Apr. 2017), pp. C04013–C04013. DOI: 10.1088/1748-0221/12/04/c04013. URL: https://doi.org/10.1088%2F1748-0221%2F12%2F04%2Fc04013.

[143] Kostas Pagiamtzis and A Sheikholeslami. "Content-Addressable Memory (CAM) Circuits and Architectures: A Tutorial and Survey". In: *Solid-State Circuits, IEEE Journal of* 41 (Apr. 2006), pp. 712 –727. DOI: 10.1109/JSSC.2005.864128.

[144] Andy Buckley et al. "General-purpose event generators for LHC physics". In: *Phys. Rept.* 504 (2011), pp. 145–233. DOI: 10.1016/j.physrep.2011.03.005. arXiv: 1101.2599 [hep-ph].

[145] J. Alwall et al. "The automated computation of tree-level and next-to-leading order differential cross sections, and their matching to parton shower simulations". In: *JHEP* 07 (2014), p. 079. DOI: 10.1007/JHEP07(2014)079. arXiv: 1405.0301 [hep-ph].

[146] Paolo Nason. "A New method for combining NLO QCD with shower Monte Carlo algorithms". In: *JHEP* 11 (2004), p. 040. DOI: 10.1088/1126-6708/2004/11/040. arXiv: hep-ph/0409146 [hep-ph].

[147] Carlo Oleari. "The POWHEG-BOX". In: *Nucl. Phys. Proc. Suppl.* 205-206 (2010), pp. 36–41. DOI: 10.1016/j.nuclphysbps.2010.08.016. arXiv: 1007.3893 [hep-ph].

[148] Keith Hamilton, Paolo Nason, and Giulia Zanderighi. "MINLO: Multi-Scale Improved NLO". In: *JHEP* 10 (2012), p. 155. DOI: 10.1007/JHEP10(2012)155. arXiv: 1206.3572 [hep-ph].

[149] T. Gleisberg et al. "Event generation with SHERPA 1.1". In: *JHEP* 02 (2009), p. 007. DOI: 10.1088/1126-6708/2009/02/007. arXiv: 0811.4622 [hep-ph].